1st INTERNATIONAL PhD SYMPOSIUM ON ENGINEERING AND SPORT SCIENCE

UNIVERSITÀ DI CASSINO E DEL LAZIO MERIDIONALE
10–12 October 2023

edited by
Fabrizio Marignetti – Salman Ali – Romolo Di Bernardo

EUC - EDIZIONI UNIVERSITÀ DI CASSINO

Il volume raccoglie gli atti del Simposio Internazionale del Dottorato di Ricerca in Ingegneria e Scienze Motorie, che si è svolto all'Università degli Studi di Cassino e del Lazio Meridionale dal 10 al 12 ottobre 2023. Studenti di Dottorato di diversi settori scientifici, provenienti da 7 diverse nazioni hanno presentato i risultati delle loro ricerche. I lavori presentati hanno fornito una panoramica dello stato della ricerca nei vari settori dell'Ingegneria e delle Scienze Motorie.

This volume collects the proceedings of the International PhD Symposium in Engineering and Sport Sciences, which was held at the University of Cassino and Lazio Meridionale from Oct. 10 to 12, 2023. Doctoral students of different scientific fields from 7 different countries presented the results of their research. The papers presented provided an overview of the state of research in the various fields of Engineering and Motor Sciences.

Copyright © **EUC**
EDIZIONI UNIVERSITÀ DI CASSINO

CENTRO EDITORIALE DI ATENEO
Università degli Studi di Cassino e del Lazio meridionale
Campus universitario – Palazzo degli Studi – Località Folcara,
03043 Cassino (FR), Italia

ISBN **978-88-8317-129-1**

Impaginazione a cura di EUC, Alfiero Klain.

L'immagine di copertina è stata realizzata dalla commissione Logo della conferenza. La foto del rettorato in copertina è stata scattata dai curatori. L'immagine di copertina è libera da diritti.

Pubblicato in versione digitale su archivi online in *open access* nel luglio 2024.

COLLANA SCIENTIFICA – EBOOK

1st INTERNATIONAL PhD SYMPOSIUM ON ENGINEERING AND SPORT SCIENCE

UNIVERSITÀ DI CASSINO E DEL LAZIO MERIDIONALE
10-12 October 2023

edited by
Fabrizio Marignetti – Salman Ali – Romolo Di Bernardo

ebook

EDIZIONI UNIVERSITÀ DI CASSINO
Centro Editoriale di Ateneo – Università degli Studi di Cassino e del Lazio meridionale | 2024

1st International PhD Symposium on Engineering and Sport Sciences

Website **Linkedin**

10 - 12 October 2023

Aula Magna di Ingegneria
Università degli Studi di Cassino e del Lazio Meridionale
Via Gaetano di Biasio, 43, Cassino (FR)
www.internationalphdsymposium.com

Civil, Electrical, Environmental, Information, Managment and Mechanical **Engineering**

Environments and Technologies for **Motor Activity and Health**

sponsored by:

UNIVERSITÀ DEGLI STUDI DI CASSINO E DEL LAZIO MERIDIONALE – 1979 –
SOL PER NOCTEM

dIE

Scienze Motorie

VISIO ELECTRIC

Editors:

Fabrizio Marignetti

Salman Ali

Romolo Di Bernardo

Table of Contents

II Section
Civil and Environmental Engineering

III Section
Information Engineering

V Section
Mechanical and Management Engineering

Message from the Chair

This book collects the contributions presented at the 1st International PhD Symposium that was held at the University of Cassino and South Lazio from 10 to 12 October 2023. This Symposium represents an effort of the PhD program in Methods, Models and Technologies for Engineering, together with the three Departments supporting the PhD program, i.e.: the Department of Electrical and Information Technology "Maurizio Scarano", the Department of Civil and Mechanical Engineering and the Department of Humanities, Social Sciences and Health Sciences.

The collection aims at sharing the state-of-the-art of a wide range of topics connected to the design and engineering, with a special emphasis on innovation, sustainable development, urbanism and mobility, circular economy, and health and education. The contributions were selected through a rigorous international peer-review process. The Proceedings will be of interest to academics, professionals, industry representatives, and local government officials.

International Students from EU and non-EU universities have been invited also to present their works and their manuscripts are also collected in this Proceedings book. The book is structured into five Sections, each one dedicated to one subject.

General Chair of ISSES

Fabrizio Marignetti

International Ph.D. Symposium

Steering Committee

General Chair:	Fabrizio Marignetti
General Co-Chair:	Salman Ali
Coordinators:	Romolo Di Bernardo, Lidia Piccerillo

Program Committee

Romolo Di Bernardo	Hedieh Taremizadeh
Salman Ali	Alessia Tescione
Lidia Piccerillo	Carmine Bourelly

Advertisement Committee

Mirko Sgambetterra	Hamza Mustafa

Logo and Format Committee

Emanuele Nardone	Ciro Russo
Giorgio Grossi	Sara Perna
Marco Cantone	Hamza Mustafa

International Reviewer Committee

Ghent University, Belgium:	Muhammad Azeem
COMSATS University Abbottabad, Pakistan:	Faisal Khan
Sapienza University Rome, Italy:	Naseer Ahmad
Aarhus University, Denmark:	Asim ul haq
COMSATS University Abbottabad, Pakistan:	Mohammad Yousaf
Ecole de technnologie superieure, ETS Montreal, Canada:	Sangrez Khan
University of Cassino, Italy:	Alessia Tescione
University of Cassino, Italy:	Simone Palazzo
University of Cassino, Italy:	Romolo Di Bernardo
University of Cassino, Italy:	Hedieh Taremizadi
Strythclade University, Scotland:	Muhammad Bin Younas

Photo Gallery


AULA MAGNA
LUIGI PAPA


Abstract Submission:
30 September 2023
1st International PhD Symposium on
Engineering and Sport Sciences
10 - 12
October 2023
Civil, Electrical,
Environmental,Information,
Management and Mechanical
Engineering
Environments and Technologies for
Motor Activity and Health
website
LinkedIn
1:27 PM
10/12/2023


UAV-based Video Surveillance in cities
Using UAVs to keep watch on a city:
the UAVs fly around the city to monitor a set of points of interest
UAVs ADVANTAGES
- less expensive to deploy
- mobile surveillance
- easy substitution of camera types (normal, infrared, thermal, etc).
HOWEVER, UAVs pose the problem of energy management of batteries
Chair

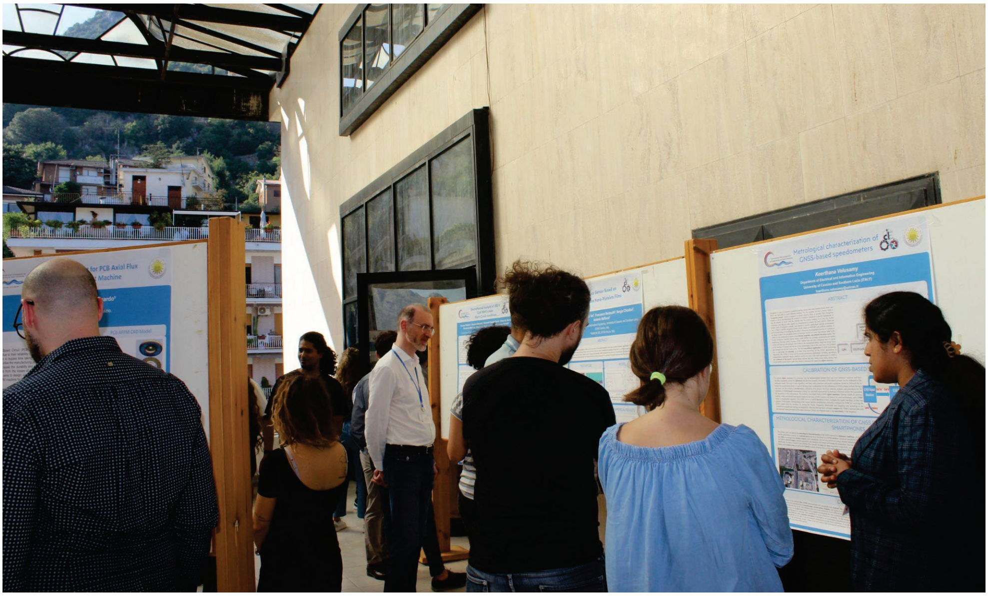
for PCB Axial Flux
Machine
Metrological characterization of
GNSS-based speedometers
Keerthana Velusamy
Department of Electrical and Information Engineering
University of Cassino and Southern Lazio (ITALY)
ABSTRACT
CALIBRATION OF GNSS-BASED

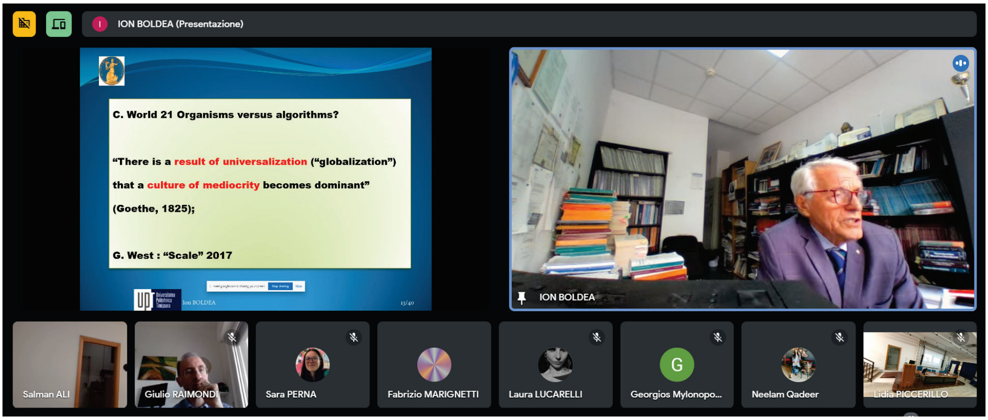
ION BOLDEA (Presentazione)
C. World 21 Organisms versus algorithms?
"There is a result of universalization ("globalization")
that a culture of mediocrity becomes dominant"
(Goethe, 1825);
G. West : "Scale" 2017
ION BOLDEA
Salman ALI
Giulio RAIMONDI
Sara PERNA
Fabrizio MARIGNETTI
Laura LUCARELLI
Georgios Mylonopo...
Neelam Qadeer
Lidia PICCERILLO

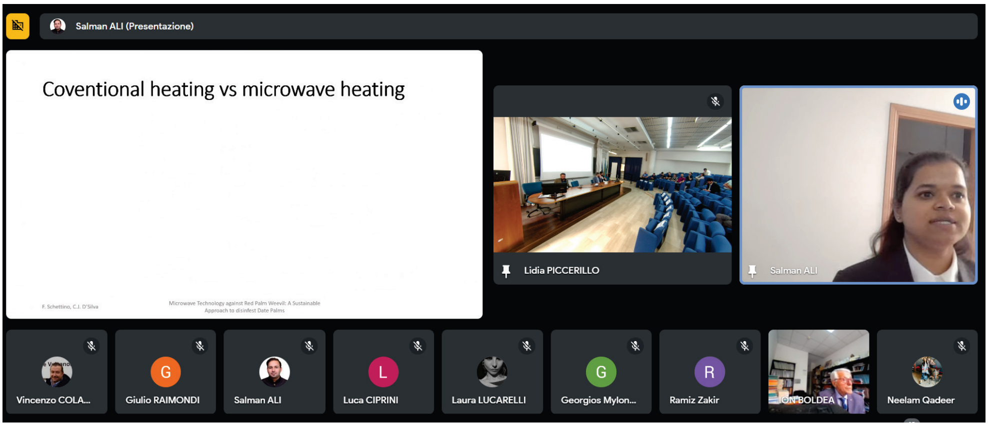
Salman ALI (Presentazione)
Coventional heating vs microwave heating
F. Schettino, C.J. D'Silva
Microwave Technology against Red Palm Weevil: A Sustainable Approach to disinfest Date Palms
Lidia PICCERILLO
Salman ALI
Vincenzo COLA...
Giulio RAIMONDI
Salman ALI
Luca CIPRINI
Laura LUCARELLI
Georgios Mylon...
Ramiz Zakir
ION BOLDEA
Neelam Qadeer

Cogging Torque Comparison of Different Permanent Magnet Profiles for Axial Flux Permanent Magnet Machine

Salman Ali[1], Raja Asfand Munir[2], Roberto Giacomobono[1], Junaid Ikram[2], Fabrizio Marignetti[1]

[1]Department of Electrical and Information Engineering- University of Cassino and Southern Lazio Cassino, Italy 03043

[2]Department of Electrical and Computer Engineering, COMSATS University Islamabad, Pakistan. 44000

Corresponding author

Email: salmanalibajwa@outlook.com

Abstract

The research aims to improve the performance of axial flux permanent magnet (AFPM) machines by reducing cogging torque and improving output torque quality. Noise in the AFPM machine is prominently due to cogging torque, and it can cause problems in starting and reduce the machine's life. Stator side modifications and rotor side modifications can reduce cogging torque. This research presents a new sine with a third harmonic permanent magnet (PM) shape to reduce the cogging torque. Finite element analysis (FEA) simulations are performed on the proposed PM-shaped, trapezoidal, arc-shaped, and conventional third harmonics-shaped PM. AFPM machine and their cogging torque are compared. Time-stepped 3D-FEA is used for the cogging torque comparison of the AFPM machine models.

Index Terms

AFPM, Cogging Torque, Torque Ripples.

I. Introduction

With increasing eco-friendly and energy concerns, progress and research on high performance permanent magnet machines are gaining increasingly supplementary attention. The AFPM machines have proved to have better performance in terms of higher torque to volume density ratio than their radial flux permanent magnet (RFPM) counterparts [1-3].

AFMs have many topologies depending on arrangements of stators and rotors. These topologies are single stator single rotor (SSSR), double stator single rotor (DSSR), single stator double rotor (SSDR) and multidisc AFM [4-8]. Every topology have its own importance according to the need of the application. The use of double stator configuration helps to maximize the flux linkage in the back iron of single stator topology through the double magnetic circuit. The DSSR topology is preferred over other topologies due to balanced axial forces, less cogging torque, better torque quality and better cooling characteristics. The weight of machine, winding resistance and copper losses are also reduced in DSSR topology.

Different methods used to enhance the performance of AFMs are modification in the shapes of magnet, winding configuration, changes in parameters (air gap, slot/pole ratio) and magnet skewing. Different types of windings that can be used for the construction of stator of AFPM machine are integral slot winding, fractional slot winding, drum winding, ring winding, concentrated winding (single layer, double layer) and distributed winding.

Single layer concentrated winding is used for the construction of stator of DSSR due to which magnetic flux is distributed in whole coil.

The AFPM machines are used in various application like wind turbines, electric vehicles, elevation industry, ship propulsion, computer hard disc drives and in robots [9-12].

This paper presents a design of slotless DSSR topology which is suitable for the application that need high power, high torque density, high efficiency and low noise. Previously used shapes of magnets are tested in this topology and a proposed shape of magnet is also applied which shows better results. Special attention is paid to torque ripple and torque ripple is minimized by using a proposed shape of magnet.

II. MAGNET SHAPES

In this research a comparison between flat trapezoidal, arc trapezoidal, conventional sine + 3rd harmonics and proposed shaped PM is carried out.

A. Flat Trapezoidal Shaped Model

This model consists of three phase, double sided AFPM machine. In this case DSSR AFPM machine have flat trapezoidal magnet shape as shown in Figure 1. Machine consists of two disc type slotless stators and a rotor having magnets on both sides is placed between these two outer slotless stators. Rotors have magnets aligned on both sides of the disc. Rotors consist of 20 magnets on each side and stator have 24 coils on side of disk facing internal rotor.

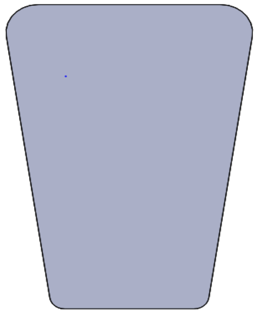

Fig. 1: Trapezoidal Shaped Magnet

B. Arc Shaped Model

In this model arc trapezoidal shape of magnet is used. 20 magnets are fitted on each side of rotor. In this shape the region of trapezoidal magnet facing towards stator is arc shape as presented in Figure 2. Arc trapezoidal shaped magnet was adopted to reduce the cogging torque and increase efficiency of the machine. Use of arc shaped magnet reduces the cogging torque as air-gap flux is reduced. With the reduction of air gap flux the back emf also slightly descends.

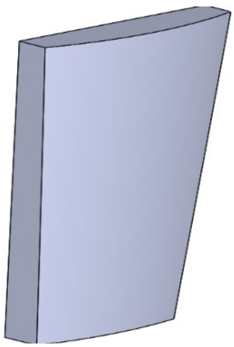

Fig. 2 : Arc Shaped Magnet

C. Conventional Sine with Third Harmonic Shaped Model

The conventional sine + 3rd harmonics shape is sketched as shown in figure 3 by using the equation (1)

$$y(x) = A.\sin(\frac{\pi .x}{w}) + B.\sin(\frac{3\pi .x}{w}) \tag{1}$$

where, A represents the maximum peak of sine shape and B is value of dip that is due to third harmonics. In this model conventional sine + 3rd harmonics shape magnets are fitted on disc of rotor and there is slight increase in axial length of machine.

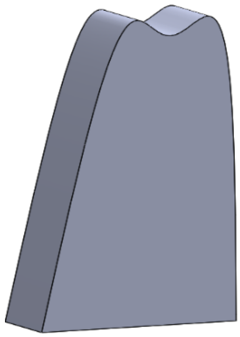

Fig. 3: Trapezoidal Shaped Magnet

D.Proposed Shaped Model

In this shape the top of magnet is made by adding factor of third harmonics in sine shape but in this case negative amplitude of third harmonics is lesser than positive amplitude as shown in Figure 4. This modification cause increase in the airgap. The main advantage of this shape of magnet is that interaction between coils of stator and magnets of stator become gradual which results in reduction of cogging torque.

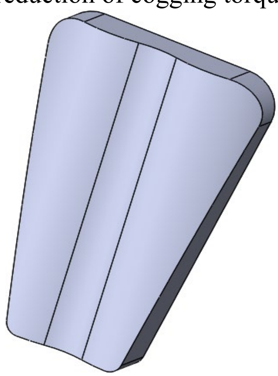

Fig. 4: Proposed Magnet

III. Magnet Shape Comparison

Comparison between flat trapezoidal, arc, conventional sine with third harmonics and proposed shaped PM is performed to show that which magnet shape is best for reduction of cogging torque. Volume of magnets are kept constant but height of magnet vary from shape to shape. Air gap of all machines are kept same but due to different shape geometry of magnets there is difference of air gap and flux density is also different.

Cogging torque can be find out by means of the formula as shown in eq. 1.2 [2][3]:

$$T_{cogg} = -\frac{1}{2}\phi_g^{\,2}\frac{dR}{d\theta} \tag{2}$$

Where,

ϕ_g Indicates flux of air gap, R shows reluctance of air gap and rotor's position is denoted by θ.

According to this equation, T_{cogg} should be maximum in proposed shape and minimum in proposed shaped PM. There is small difference of air gap length in trapezoidal, arc shape and conventional sine with third harmonic shape with proposed shape as presented in Figure 5 but this small difference play an important role in minimization of T_{cogg}. As shown in equation 2, T_{cogg} shows direct relation with air-gap flux Φ_g and the factor ${dR}/{d\theta}$,that is change in air-gap reluctance with respect to change in position of rotor. The factor ${dR}/{d\theta}$ is maximum in arc shape PM model and least in flat trapezoidal PM model, whereas midway in conventional and proposed shaped model**.**

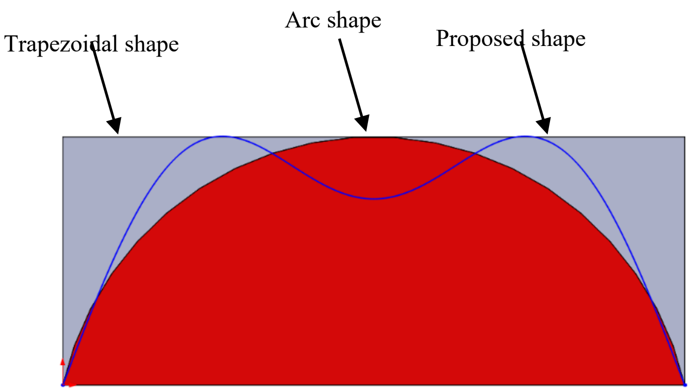

Fig. 4: Comparison of Different Magnet Shapes

IV. Results

Results of finite element analysis illustrate that the cogging torque is reduced significantly in proposed PM shaped AFPM machine due to the sine shaped surface of PM facing the airgap and stator, which causes the airgap to change throughout the surface of PM and provides significant reduction in cogging torque. Maximum peak to peak cogging torque in flat trapezoidal magnet model is calculated as 13.5 Nm, arc shaped magnet model shows maximum peak to peak cogging torque of 9.9 Nm, conventional sine with 3rd harmonic shaped model exhibits 7.41 Nm and our proposed magnet AFPM model mitigates the torque the least of all which is 4.15 Nm. Hence flat trapezoidal magnet model has the most peak to peak cogging torque and proposed magnet model reduces the peak to peak cogging torque significantly

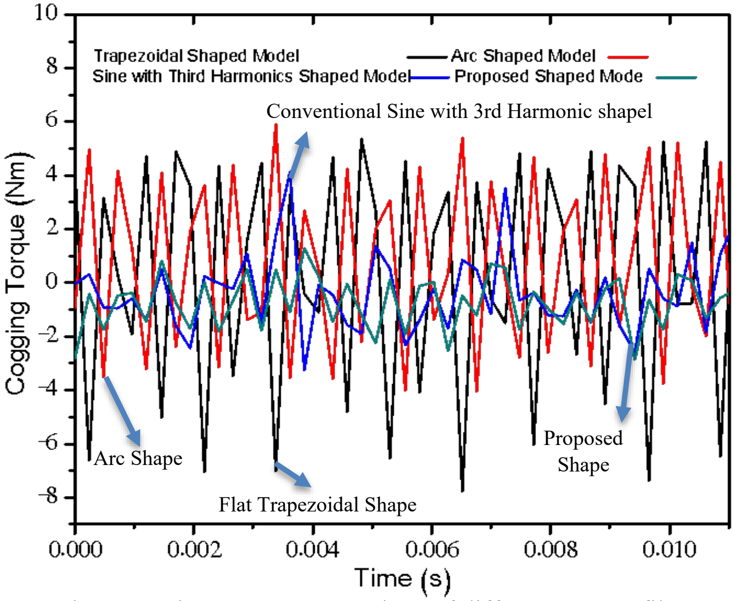

Fig.5 Cogging Torque comparison of different PM profiles

Acknowledgement

This study was carried out within the MOST – Sustainable Mobility Center and received funding from the European Union Next-GenerationEU (PIANO NAZIONALE DI RIPRESA E RESILIENZA (PNRR) – MISSIONE 4 COMPONENTE 2, INVESTIMENTO 1.4 – D.D. 1033 17/06/2022, CN00000023). This manuscript reflects only the authors' views and opinions, neither the European Union nor the European Commission can be considered responsible for them.

REFERENCES

[1] Liu, C. T. and S. C. Lee, "Magnetic field modeling and optimal operational control of a single-side axial-flux permanent magnet motor with center poles,"*Journal of Magnetism and Magnetic Materials,* Vol. 304, No. 1, 454–456, September 2006.

[2] Di Gerlando, A., Foglia, G., Iacchetti, M.F., Perini, R.: 'Axial flux PM machines with concentrated armature windings: design analysis and test validation of wind energy generators', *IEEE Trans. Ind. Electron*., 2011, 58, (2), pp. 3795–3805

[3] Curiac, P., Kang, D.H.: 'Preliminary evaluation of a MW-class low-speed AFPMSM with self-magnetisation function of the armature coils', *IEEE Trans. Energy Convers.,* 2007, 22, (3), pp. 621–628.

[4] Patterson, D., and R. Spee, "The design and development of an axial flux permanent magnet brushless DC motor for a wheel drive in a solar powered vehicle*," Proc. IEEE Ind. Apps. Society Conf.,* Denver, 1994, vol. 1, pp. 188–195.

[5] Brown, N., L. Haydock, and J.R. Bumby, "Foresight vehicle: A toroidal, axial flux generator for hybrid IC engine/battery electric vehicle applications*." Proc. SAE Conf. paper 2002-01-089*, Detroit, March 2002.

[6] Spooner, E. and B.J. Chalmers, "TORUS: A slotless, toroidal-stator permanent magnet generator," *IEE Proc. Electr. Power Appl.*, Nov. 1992, pp. 497–506.

[7] Huang, S., M. Aydin, and T.A. Lipo, "TORUS concept machines: pre-prototyping design assessment for two major topologies," 2001 *IEEE Industry Applications Conference,* vol. 3, no. 30, Sept. 2001, pp. 1619–125.

[8] Kessinger, R., and S. Robinson, "SEMA-based permanent magnet electric motors for high torque, high performance," *Naval Symposium on Electric Machines, Newport*, RI, 1997, pp. 151–155.

[9] F.Profuma, Z.Zhang and A.Tenconi, ''Axial Flux Machine Drive: New Viable Solution for Electric Cars''*, IEEE Trans. Ind. Electron*, Vol. 44, No. 1, pp. 39--45, Feb. 1997.

[10] R.J.Wang, M.J.Kamper, K.V.westhuizen and J.F.Gieras, ''Optimal Design of a Coreless Stator Axial Flux Permanent-Magnet Generator'', *IEEE Trans. Magn*, Vol. 41, No. 1, pp. 55--64, Jan. 2005.

[11] B.Xia, M.J.Jin, J.X.Shen and A.G.Zhang, ''Design and Analysis of an Air-Cored Axial Flux Permanent Magnet Generator for Small Wind Power Application'', *in Proc.IEEE Int. Sustainable Energy Technologies Conf*., 2005, pp. 1--5.

[12] J.F.Eastham, F.Profumo, A.Tenconi, R.H.cottingham, P.Coles and G.Gianolio, ''Novel Axial Flux Machine for Aircraft Drive: Design and Modeling'', *IEEE Trans. Magn*, Vol. 38, No. 5, pp. 3003--3005, Sep. 2002

[13] T. Simpson, T. Mauery, J. Korte, and F. Mistree, "Kriging models for global approximation in simulation-based multidisciplinary design optimization," *AIAA Journal*, vol. 39, no. 12, pp. 2233-2241, 2001.

[14] Y. Ahn, J. Park, C. Lee, J. Kim, and S. Jung, "Novel memetic algorithm implemented with GA (genetic algorithm) and MADS (mesh adaptive direct search) for optimal design of electromagnetic system," *IEEE Transactions on Magnetics*, vol. 46, no. 6, pp. 1982-1985, 2010.

[15] N. Rostami, M. R. Feyzi, J. Pyrhonen, A. Parviainen, and V. Behjat, "Genetic algorithm approach for improved design of a variable speed axial-flux permanent-magnet synchronous generator," *IEEE Transactions on Magnetics*, vol. 48, no. 12, pp. 4860-4865, 2012.

Single-Phase Low-Voltage Regulation Device for Enhanced Distributed Generation Integration

Andrea Danzo, Giovanni Mercurio Casolino Department of Electrical and Information Engineering
University of Cassino and Southern Lazio, Cassino, Italy Email: andrea.danzo, casolino@unicas.it

Abstract

To achieve significant national climate objectives, many countries worldwide have adopted ambitious goals to promote wide-spread use of Distributed Generation. Con- sequently, there has been a substantial increase in the installation of renewable energy sources, both on a large scale and within residential scale.

Since the network was originally designed for centralized power distribution and was not configured to accommodate a large number of micro-sources, this has brought about novel challenges for the distribution system operator. One of them is the necessity to maintain voltage levels in accordance with the specifications defined in the European norm EN50160. During periods of high power demand, the electrical lines face voltage drops. In contrast, in case of excess of power generation, reverse power flow can occur causing an increase in voltage along the electrical lines. In these critical scenarios, where electrical parameters deviate from standard regulatory levels, the untimely tripping of electrical protections can result in disconnection of renewable energy production and so leading to a reduction in the economic revenue of producers.

Various methods are used to restore the voltage profile inside the prescribed limits and this research focuses on a novel Single-Phase Low-Voltage Regulation Device (LVRD) for active users. The realized device is based on a two-winding transformer which is switched by a H-bridge of IGBT to step-up or step-down the voltage at the Point of Common Coupling. In case of no regulation required or in case of fault, the LVRD deactivates automatically with a bypass switch, without interrupting the supply of the costumer. The control is managed by a 32-bit microcontroller which select the appropriate configuration accordingly to the measured voltage.

Laboratory tests show the effectiveness of the regulator and the low THD voltage indices measured demonstrate that the regulator does not affect the harmonic content of the supply voltage.

The proposed regulator has several advantages over other solutions as it uses a simple control logic, has low operational losses, is compact and inexpensive and can be easily extended to three-phase systems, by using a device for each phase and thus also realizing phase balancing.

Index Terms

low-voltage network, voltage profile, single-phase voltage regulator, active users

The role of aggregation in the Italian Electricity Market

Luca Del Greco[1]

[1] DIEI, Univerity of Cassino and Southern Lazio, Cassino, Italy

Email: luca.delgreco@unicas.it

Abstract

This paper presents a view of the Italian electricity market from the point of view of the aggregation of resources for participation in the markets. In I an excursus is made of the current regulation which will lead from 1 January 2025 to the definition of aggregate units in Italian dispatching. Section II describes the operation of the UVAM pilot project, which - in an experimental manner - introduced these units into the Italian regulation, allowing for analyzes and assessments to be made on the effectiveness of the aggregation and on the necessary interventions by the Regulator. In III the changes introduced by Testo Integrato del Dispacciamento Elettrico (TIDE) are illustrated with the description of the different units defined and introduced. In IV there is a mention of the local ancillary services markets, currently still in the experimental stage, which will introduce further needs for aggregation on the distribution networks.

Index Terms

UVAMN, Aggregation, Ancillary Market, Flexibility

I. Introduction

The electricity system is going through a phase of profound changes: the extensive development of renewable sources, especially non-programmable, the ever-increasing diffusion of Distributed Generation and the expected increase in final demand, caused by strong electrification of consumption, are leading to a complete revision of the system management paradigm, which inevitably has repercussions on the functioning of the electricity markets and ancillary services. During 2022, the Italian Authority (ARERA) published document no. 685/2022/R/eel containing the consultation of the articulation of the TIDE. The document, which follows the previous n.322/2019, aims to define the structure and rules of the Italian electricity market, in order to introduce the reform from 01/01/2025. This intervention is dictated by the need to guarantee the security of the electricity system, efficiently and at the lowest cost, in the current context of rapid and continuous evolution, characterized by the growing diffusion of non-programmable renewable sources and distributed generation, as well as by the progressive reduction in the use of programmable plants, increased the level of uncertainty in the planning phase of the operation, making additional resources necessary for ancillary services. In this scenario, the role of the aggregation of resources appears to be central, used both for the purposes of the energy markets and for the markets of dispatching and balancing services.

II. UVAM PILOT PROJECT

One of the first aggregation precedents introduced in the Italian regulation is given by the Unità Virtuali Abilitate Miste (UVAM). UVAM is a pilot project launched in 2017 by the Italian Regulator with the aim of investigating technical and economic feasibility of the provision of ancillary services for Terna by units not already enabled. The pilot provides for the voluntary participation in the MSD, in aggregate form, of small-scale power plants, loads, large production units in the availability of a final consumer not subject to mandatory participation, stationary energy storage systems and electric vehicles.

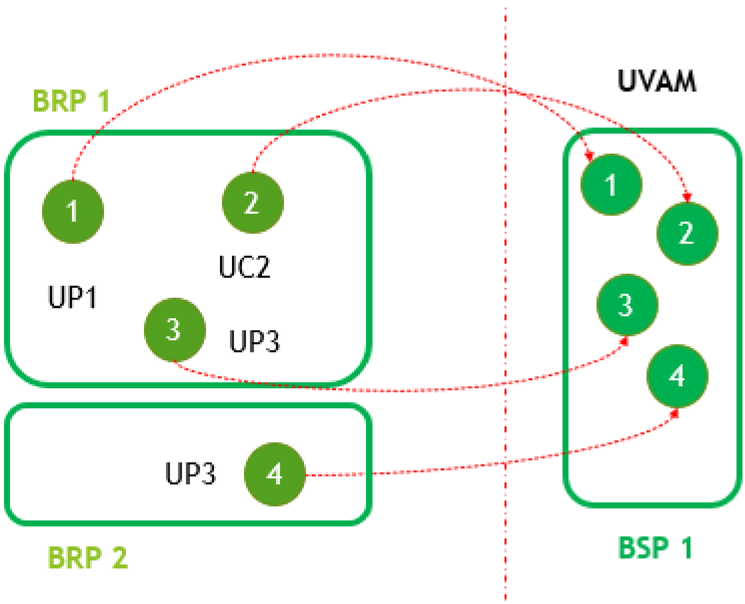

Fig. 1: Example of the structure of a UVAM and the BSP/BRP relationship.

As shown in Figure 1, the elementary units, production units (UP) and consumption units (UC), not authorized for the Dispatching Services markets, belonging to different Balance Responsible Parties (BRP) can be aggregated in a virtual unit of competence by a third, the Balancing Service Providers (BSP), thus enabling it voluntarily in the Dispatching Services markets as a single enabled unit. The BRP will therefore be responsible for delivering the energy of the single UCs/UPs of its portfolio, while the BSP will operate the aggregated unit in the Services market according to the rules of the pilot project [1].

III. TESTO INTEGRATO DEL DISPACCIAMENTO ELETTRICO

With the approval of the TIDE [2], which will enter into force on 01/01/2025, the level of aggregation of the distributed resources present in the electricity system becomes much more stringent. This regulation provides for the overcoming of the UVAM pilot project and the definition of different forms of aggregation of resources both as regards the energy markets and the services markets. For the purposes of the energy markets, the Unità Virtuali Zonali (UVZ) and the Unità Virtuali Nodali (UVN) are defined, while, for the purposes of the services and balancing markets, the Unità Virtuali Abilitate Zonali (UVAZ) and the the Unità Virtuali Abilitate Nodali (UVAN). These units have a link with each other according to the type of service they offer, which defines their nodal or zonal characteristic, as well as the type and association with the related BRPs and BSPs.

A. *Nodal units*

The UVANs represent aggregates of elementary units for movements with a nodal value (or services with a wider scope of delivery) and in particular:

- aggregate of UPs and UCs directly connected to the same node of the relevant network.
- aggregate of UPs only directly connected to the same node of the relevant network.
- aggregate of UPs and UCs connected to the network of a DSO and attributable to the same node of the relevant network or to a set of neighboring nodes of the relevant network falling within the same nodal supply perimeter.

UVN represent the subdivisions into which the UVAN is divided to consider the coexistence of several BRPs or several types of UPs: the UVANs are, therefore, subsets of the UVANs under the responsibility of the same BRP.

Within the UVN, injections and withdrawals must be kept separate: the injection UVNs and the withdrawal UVNs are therefore identified. Furthermore, only UPs belonging to a given type can be included in each input UVN.

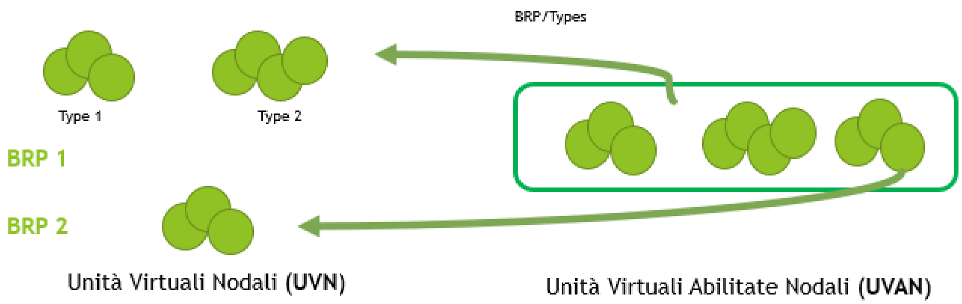

Fig. 2: Example of the structure of UVN and UVAN and the BSP/BRP relationship.

B. Zonal units

The UVZs are the aggregates into which all the UPs and UCs managed by the same BRP converge, not included in the additional typologies defined by the TIDE (UAS, UnAP and UVN) . The UVZ of injection is unique for each type, for each BRP and for each bidding zone. The units contained in the UVZs can qualify for the provision of zonal services by accessing, individually and voluntarily, a UVAZ. The UVAZ in fact represent the aggregates for global national ancillary services with zonal value. They can include only UPs, only UCs, or both UPs and UCs. The only requirement is the ability to deliver global national ancillary services in an aggregate manner with a zonal delivery perimeter.

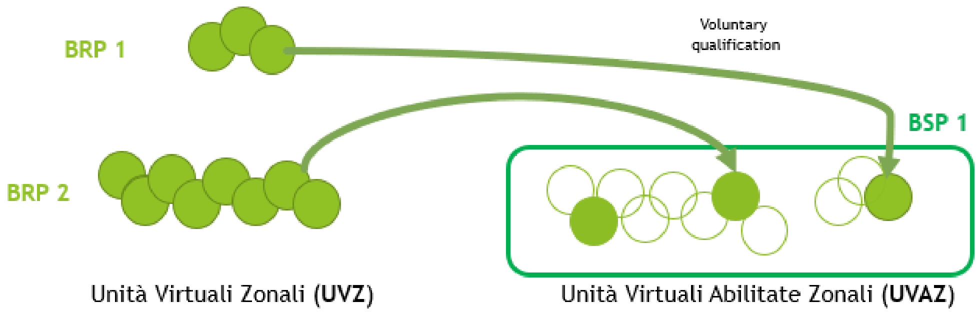

Fig. 3: Example of the structure of UVZ and UVAZ and the BSP/BRP relationship.

C. The scenario outlined by TIDE

The TIDE therefore defines a structure of the electricity markets where the aggregated units will have a central role and the individual units will be able to contract in various forms with different BRPs and BSPs. The "single" units will be divided into UAS (enabled to provide services and therefore managed by both a BRP and a BSP) and UnAP (not authorized to provide services and therefore managed only by the BRP). The aggregated units will instead be of different types and compositions: the UVZ and UVN will be available to the BRP for offers on the energy markets, while the BSPs will constitute the UVAN, in turn aggregating the UVN of different BRPs and the UVAZ by aggregating individual UP /UC pertaining to different UVZs of different BRPs.

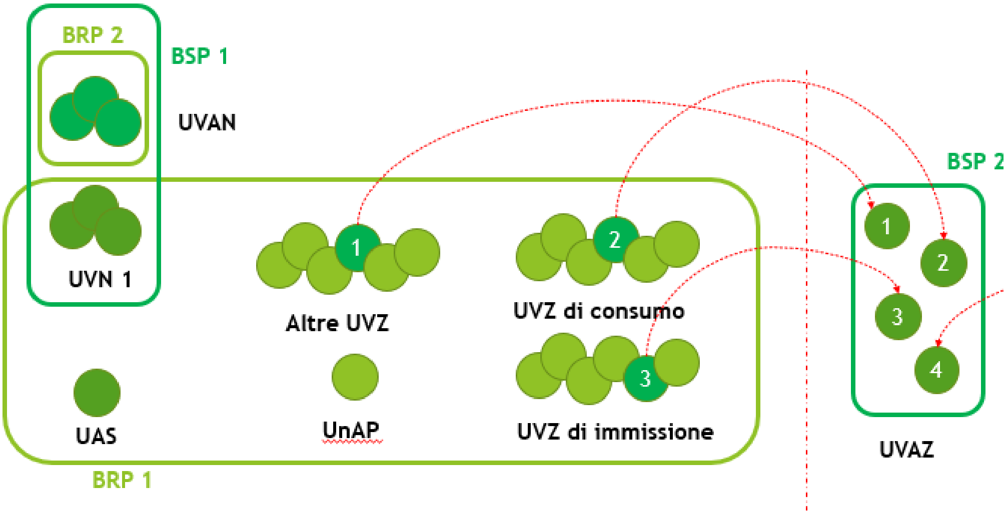

Fig. 4: Example of the scenario outlined by TIDE

IV. DSO LOCAL MARKET

A further element that will be added to the regulation is that of the local markets of the DSO, introduced into the Italian regulation with the resolution and the related pilot projects (Edge, RomeFlex and MindFlex). On this aspect, the results that these pilot projects will highlight will be important. In the literature there are some works on studies on the use of the Load Area concept for the definition of the aggregation perimeters of the distributed resources involved in these markets. [3] [4]

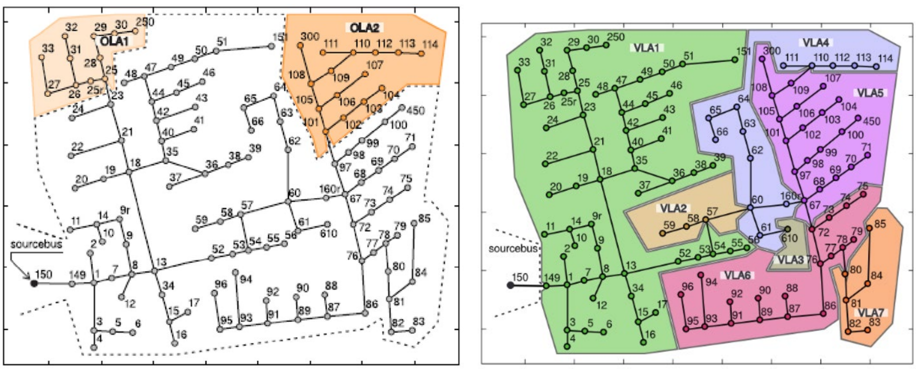

Fig. 5: Flexibility Aggregation Perimeter for Ancillary Services in Radial Distribution Systems: An Application of Load Area

a) Overload Load Area b) Voltage Load Area

V. CONCLUSION

This paper shows that the role of the aggregation of electricity markets in Italy will be increasingly greater. It is therefore essential to direct future research work on how these aggregation processes can make a greater contribution to the electricity system, increasing its efficiency and safety.

3

REFERENCES

[1] Luca Del Greco, Arturo Losi, Michele Mauro, “Demand Response in Italian regulation and first results”, L’Energia elettrica supplement journal, October 2022

[2] ARERA, Consultation document n.685/2022/R/eel, Testo integrato del dispacciamento elettrico (TIDE) - Consultazione dell'articolato, December 2022

[3] ARERA, Resolution n.352/2021/R/eel, Progetti pilota per l’approvvigionamento di servizi ancillari locali, August 2021

[4] Giovanni Mercurio Casolino, Luca Del Greco, Arturo Losi, “Flexibility Aggregation Perimeter for Ancillary Services in Radial Distribution Systems: An Application”, IEEE Eurocon, 2023

Microwave Technology against Red Palm Weevil: A Sustainable Approach to disinfest Date Palms

F. Schettino[1,2], C.J. D'Silva[2]
[1]ICEmB-Inter-University research Center on the study of the interactions between ElectroMagnetic fields and Biosystems; [2]Dep. of Electrical and Information Engineering "Maurizio Scarano", Un. of Cassino and Southern Lazio, Cassino, Via G. Di Biasio, 43 – 03043 – Cassino (FR), Italy;

Abstract

The Red palm weevil, *Rhynchophorus ferrugineus* (Olivier) (Coleoptera: Curculionidae), is considered as one of the most serious pest insects currently threatening the sustainability of the date palm sector (*Phoenix dactylifera* L.). Several control methods have been applied to treat the red palm weevil (RPW); however, these treatments are known to cause significant environmental pollution. The microwave heating method is a promising and eco-compatible solution to fight the spread of RPW. The effectiveness of the microwave treatment strongly depends on an appropriate modeling of the heating process, and on the design of the entire microwave system. The microwave heating system depends on the precise electromagnetic and thermal characterization of all the materials involved, that is the RPW and the date palm in present work. In a previous study on the feasibility to combat the RPW in *Phoenix canariensis* Hort. ex Chabaud (Red palm), in order to disinfest the palm, a microwave heating system and an electromagnetic-thermal model were developed to better control the temperature profile inside the palm tissues. The aim of this paper is to present our approach on a feasibility study, on the use of microwaves to disinfest RPW in a wider scenario by extending the results obtained with *Phoenix Canariensis* (red palm) to *Phoenix dactylifera* (date palm). The study will provide information for the development of a microwave heating strategy as an additional tool that, in an Integrated Pest Management (IPM) approach, could contain or hopefully eliminate RPW that poses a serious threat to date palm cultivation.

Index Terms

Microwave heating, Rhynchophorus ferrugineus, Phoenix dactylifera, electromagnetic-thermal model, integrated pest management.

III. INTRODUCTION

The Date palm, *Phoenix dactylifera* L. (*Arecaceae*, or *Palmae*) has a high socioeconomic importance due to its fruit, and in its capacity as shelter, fiber, clothing, aesthetic beauty, and furniture [1]. It is an important perennial and dioecious species cultivated mostly in the Middle East and North Africa, but date palms have also been introduced in Australia, India, Mexico, Southern Africa, South America, Pakistan, and the USA [2]. In particular, the Gulf region of the Middle East accounts for about 30% of the world's date production, with Saudi Arabia and the United Arab Emirates being the region's top producers [3].

As per a recent review by El-Shafie [4], there are 112 species of mites and insects worldwide associated with date palms. Among the arthropod pests listed in this report, only ten are classified as major, of which *Rhynchophorus ferrugineus* (Olivier) (Coleoptera: Curculionidae), or Red Palm Weevil (RPM) is currently considered as one of the most dangerous. The Food and Agriculture Organization of the UN has identified RPW as a category-1 pest of date palm in the Middle East.

The RPW completes its metamorphosis, through a four-stage life cycle: egg, larva, pupa, and adult which takes about 3-4 months to be completed. Adult females live for several weeks during which they lay as many as 300 eggs in the crevices of the soft palm tissue. In coconuts and date palms, oviposition usually occurs in young palms below 20 years old. The eggs hatches in about 6 days and the newborn larvae start feeding and moving towards the interior of the palm. In fact, the larva is the most destructive stage of the RPW, which causes serious damage to the palm tree by tunneling the tissue of the trunk, eventually leading to the date palms death. Moreover, the larvae are inaccessible, hard to detect, and difficult to treat with chemical pesticides. They are characterized by dark prominent heads, and pass through three to seven instars, growing into mature grubs that migrate to the periphery of the trunk where they build cocoons, entering the pupal stage. Finally, adults emerge from the cocoons a few weeks later.

The concealed nature of the larval and pupal stages infestation of the date palm stem is often hard to detect in the early stages. Early clues of an infestation are provided by the drying of the youngest fronds due to larvae feeding, which damages the meristem, resulting in larval excrement accumulation at the base of fronds or at a point of injury.

RPW can only be effectively fought by an IPM strategy, defined as an ecosystem approach to crop production and protection, which combines different management strategies and practices to grow healthy crops, and to minimize the use of pesticides [3]. A successful IPM program requires proper identification of the pest and knowledge of its biology, ecology, sampling and monitoring of its population for developing appropriate actions and identifying thresholds [5].

Microwave heating is proposed as an eco-friendly green protocol [6]. The basic idea of the microwave approach is very simple: increasing the temperature of the palm tissues and/or insect until it dies, or it is strongly affects the RPW's ability of reproduce. Advantages of microwave disinfestation include speed, efficiency, and the absence of toxic, hazardous, or polluting residues. Moreover, insects are not likely to develop a resistance to radiation as they often do to chemical insecticides. Finally, the technique was recognized to be harmless for the environment, the workers, and the plants [7].

The aim of this paper is to present a feasibility study, on the use of microwaves to disinfest RPW in a wider scenario by extending the results obtained with *Phoenix Canariensis* (red palm) to *Phoenix dactylifera* (date palm). A precise estimation of the thermal and electromagnetic parameters is necessary to set up an electromagnetic-thermal model that will aid in identifying the power, time, and schedule necessary to obtain the RPW lethal temperature at a certain depth, depending on the assumed date palm infestation level [8].

IV. PARAMETERS TO DEVELOP THE ELECTROMAGNETIC MODEL

A. Microwaves

Microwaves are non-ionizing electromagnetic waves operating in the frequency range between 0.3 GHz and 300 GHz, or equivalently, with wavelengths of a range from 1 m to 1 mm. In air they travel with the speed of light and they interact with any medium by means of reflection, transmission, and absorption.

The motivation of using microwaves against RPW is that microwave radiation should be able to induce a lethal thermal dose in the pest, or impair their reproductivity or longevity, without harming the plant tissues.

Microwave heating is based on the transformation of alternating electromagnetic field energy into thermal energy by affecting polar molecules of a material. All the matter is made up of atoms and molecules that are electrically neutral, but in a polar medium the electric charge distribution is not symmetric. In presence of an electromagnetic field, these molecules can move, oscillate and / or rotate in order to align themselves with the electromagnetic field (polarization). According to the Debye interpretation [9], the heat is generated by frictional forces occurring between polar molecules, whose rotational velocity has been increased by coupling it with the microwave radiation. When using microwaves, the heating source is inside the material, and an increase of temperature occurs in the area where the radiation can propagate (volumetric heating), but the heat flux would successively spread in the rest of the material by means of thermal conduction; while in conventional heating the thermal increase, induced by an external source, is related to the heat flux into the material from the surface. The efficiency of conversion of microwave energy into thermal energy that in turn raises the temperature in the medium depends upon both the dielectric and thermal properties of the material such as thermal conductivity, specific heat capacity, and material density.

Dielectric properties depend on the frequency of the applied electric field, the temperature of the material and the number of polar molecules in the volume of the material. Relative permittivity (ε_r'), and equivalent electric conductivity (σ) are commonly used to describe the electromagnetic properties of the materials of interest. Relative permittivity (ε_r') is related to the ability of materials to 'store' electromagnetic energy, and it is reported as a value relative to that of free space ($\varepsilon 0 = 8.85 \times 10^{-12}$ F/m), the equivalent electric conductivity (σ) measures the capacity of a material to dissipate the electromagnetic energy, due to all operating dielectric relaxation mechanisms and ionic conduction, transforming it into heat. Both depend on frequency, moisture content and temperature. Analysis by [10][11] provides more insight on the basic theory of these processes.

To summarize, an electromagnetic wave incident on a material will be partially reflected, but part of the radiation will penetrate the material and will transfer a percentage of its energy, that will be dissipated and converted into heat according to the electrical conductivity (σ) and electric field intensity. The dissipation process takes away power from the electromagnetic wave, that will attenuate rapidly with greater σ. The penetration depth indicates the depth from the surface of incidence, over which the 63.2% of the traveling wave energy (or power) is deposited in the material. The relative rate of increase of temperature ($\Delta T/\Delta t$ [°C/s]) is strictly related to the electric field strength, and the electric conductivity, specific heat, and mass density of the medium.

B. Dimension of the Palm

P. canariensis, red palm is described as having a thick trunk or stipe (50–120 cm in diameter) of columnar aspect and of uniform thickness, and a height of 12–15 m, although centennial palms can reach more than 30 m [12].

P. dactilifera date palm tree commonly grows to a height of about 10 to 15m and features a slender trunk of a diameter (about 60 cm) from the base to the crow (Table I). These results can be useful for determining the size, reach and general requirements of a special date palm services machine [13].

TABLE I: Date palm dimensions for different ages (data from Jahromi et al, 2007)

Age (year)	Bottom circumference (cm)	Mid circumference (cm)	Top circumference (cm)
10	194.07	-	-
15	183.30	194.40	-
16	194.00	186.80	-
20	185.40	175.40	173.10
22	203.60	170.68	162.80
25	215.00	189.20	198.00

31	175.80	175.80	172.60
40	185.40	166.40	134.20
45	178.20	169.60	171.60

C. *biological parameters*

The adult insects were much more sensitive to heat than the larger larvae. LT100 resulted 20 min at 50°C and only 4 min at 80°C, while 30 min at 50°C were necessary for larvae weighing 5-6 g [14]. This data is consistent with that reported in [15]. It was observed that, in general, the longevity of adult RPW decreased with increasing temperature: both female and male longevity declined at 36 °C, in addition it suppresses mating frequency and sperm transfer, as well as fertility.

In the case of *Phoenix Canariensis* Palm, the equivalent conductivity and heat capacity able to simulate the heating and the cooling process, including the effect of several processes such as change of conductivity due to some slow water diffusion in the palm tissue, were estimated in [6]. The data of a low thermal diffusion confirm that the palm tree protects itself from the external extremes [16].

In the case of date palm, the palm can adapt to a temperature range from zero to 50 °C. Temperatures allowing vegetative activity of the date palm, are between 10 and 40 °C, 18 °C for flowering and 25 °C for maturity. The internal temperature of the apical bud varies from 4 to 5 °C during the day. It can be 11 to 14 °C higher than the lowest external temperatures and 17 to 18 °C lower than the highest temperatures, with the safeguard of internal tissues from high thermal excursions.

III. MEASUREMENTS FOR THE ELECTROMAGNETIC CHARACTERIZATION OF THE MATERIALS

Measurements of dielectric constant and conductivity of the Canariensis Palm tissues and of RPW were carried out with the open-ended coaxial line method. This is a noninvasive, simple, and reliable technique employed for measuring electromagnetic properties of liquid, solid and gel alike media as well as biological systems (tissue, cells) within a wide radiofrequency/microwave frequency band, at different temperatures. Measurements were made in the 500 MHz -20 GHz band [17]. The moisture content (MC) of the palm tissues was calculated as

$$MC = \frac{M_{water}}{M_{sample}} * 100$$

Where M_{water} and M_{sample} is the mass of water in the sample and the oven-dried sample respectively.

Moisture content is a parameter that can be subject to the season of the treatment and/or the phase of the treatment. Since the sample was non homogenous, measurement was an average of the values obtained with the probe located in different positions either on the healthy/damaged slice of palm as observed in Fig 1.

Fig. 1. Measurement of the palm wood slice with the probe at different locations.

IV. NUMERICAL SIMULATION

Electromagnetic and thermal simulations have been performed in CST Microwave Studio, which implements the Finite Integration Technique (FIT). The purpose of the model is to assess the power distribution in the palm, and consequently the temperature distribution.

The computational volume is discretized with a hexahedral mesh, where Maxwell equations are solved. Mesh dimensions have been chosen to be one twentieth of the wavelength, which is appropriate for an accurate description of electromagnetic phenomena.

The radiating system has been designed as a flanged rectangular waveguide (WR340) placed at 50 mm from the trunk of the palm, modeled as a dielectric cylinder. Two different models have been considered (Fig 2), differentiated on the health of the palm.

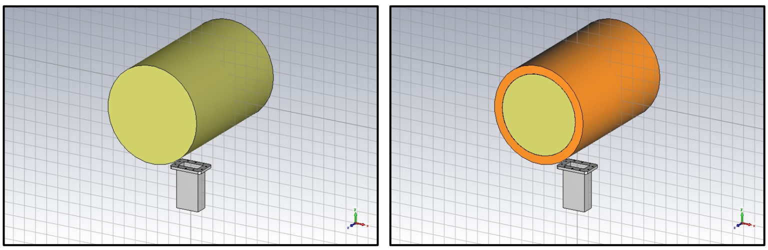

Fig 2. Numerical model. Left: healthy palm; right: damaged palm.

The healthy palm is modeled to be a homogeneous dielectric cylinder with a radius of 20 cm with electromagnetic characteristics depending on the moisture content; whereas the damaged palm has been modeled as concentric cylinders (fig 2). In the damaged palm model, the radius of the inner cylinder (healthy) is 16.5 cm and the outer cylinder's (damaged) thickness is 3.5cm. The stimulated power of the incident wave on the palm was 500 W, whereas dissipated power has been calculated by CST.

Thermal simulations have been realized by means of the thermal transient solver of CST. The output power loss of electromagnetic simulations represents the heat source of thermal simulation. The thermal parameters of the palm tissues have been taken as in [6].

V. TEMPERATURE DEPENDENT MODEL

The permittivity of the date palm tissues was modeled after the complex permittivity of vegetation model by [18]. In the vegetation model the complex permittivity (ε_v) is presented as the sum of three components in equation (2)

$$\varepsilon_v = \varepsilon_r + v_{fw}\varepsilon_f + v_b\varepsilon_b$$

Where ε_r is the non dispersive residual component; ε_f and ε_b are the permittivity of the free water and bound water respectively, v_{fw} and v_b are the volume fraction of free water and bound water respectively.

The free water components in the model refer to the water molecules that can move within the vegetation with relative ease, its dielectric permittivity is described by the Debye model of saline water. The bound water component refers to the water molecules that are held tightly to the organic compound by physical forces, its dielectric permittivity is modelled by the Cole-Cole model of sucrose water. With an ambient temperature of 22°C and a salinity ≤10‰ in [18]:

$$\varepsilon_v = \varepsilon_r + v_{fw}\left[4.9 + \frac{75}{1 + \frac{jf}{18}} - j\frac{18\sigma}{f}\right] + v_b\left[2.9 + \frac{55}{1 + \left(\frac{jf}{0.18}\right)^{0.5}}\right]$$

Where, f is the frequency in GHz and σ is the ionic conductivity in S/m.

The unknowns in the above equation were determined by fitting it with the measurements of the date palm trunk. The above equation works only at room temperature and not at temperatures close to 60°C.

To estimate the permittivity as a function of temperature also at temperatures up to 60°C, the Ulaby-Rayes model must be modified with data from [19]. The modification was made in the square bracket of the second term of the Ulaby-Rayes model, which was replaced by a corresponding temperature dependent expression from [19]. The unknown parameters in the modified Ulaby-Rayes model were determined by fitting it with the measurements of the date palm trunk.

The unknown in both the models determined after the fitting are displayed in the table II.

TABLE II

Model	ε_r	v_{fw}	$v_b = 1 - v_{fw}$	σ
Ulaby-Rayes Model	1.96	0.33	0.67	0.67
Modified Model	1.57	0.34	0.66	0.60

The complex fitting obtained by means of the Measured data (Experimental data), Ulaby-Rayes model, and modified model at an ambient temperature of 20°C are presented in the fig 3.

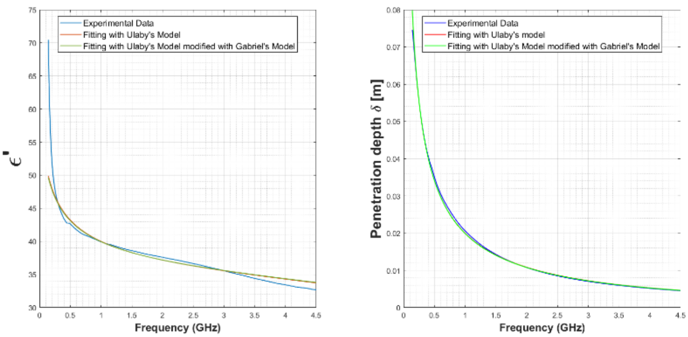

Fig .3. Complex permittivity of Date Palm trunk at room temperature(20°C). Blue line- measured data. Red line – Ulaby-Rayes model fitted data. Green line – Modified model fitted data.

VI. RESULTS AND DISCUSSIONS

From previous measurements on healthy and damaged *Phoenix Canariensis* palm tissues it was observed that in the damaged tissues the volume fraction of free water resulted higher than that of the bulk vegetation-bound water mixture. At 2.45 GHz the penetration depth was about 2.5 cm for the healthy palm and about 1 cm in the damaged palm tissue, due to the equivalent conductivity that is lower in the healthy tissues compared to that in the damaged tissues.

Regarding the insect, the penetration depth was higher in the adult (few centimeters) with respect to the pupa chamber and the larva again due to the different water content in the three different life stage. These results were confirmed in laboratory tests. Larvae at 2.45 GHz absorb more microwave power than adults. Exposures for different times up to 20 minutes at 0.06 W/cm^2 impaired larvae and not adults, while 5 s to 30 s at 2 W/cm^2 an ablation occurred on the larvae and reproductivity ability, of both male and female adults, was reduced [8].

The temperature dependent permittivity model mentioned in the previous section is applied for the saline component of the permittivity. In fig 4 the temperature dependent permittivity model is compared to a model with a constant permittivity for the healthy palm. In both the models the distance of the waveguide from the trunk is varied from 5cm (50mm) to 15cm (150mm) in steps of 2.5cm. As observed in the figure, neglecting the dependence of permittivity on the temperature can lead to an underestimation of the efficiency of the heating the palm.

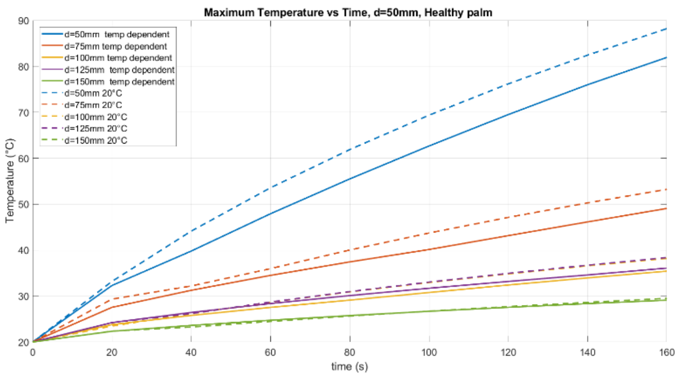

Fig. 4. Maximum temperature versus time, for a homogenous healthy date palm, with a constant permittivity model (solid lines) and with a temperature dependent permittivity (dashed lines) for different distances of the waveguide from the trunk of the date palm.

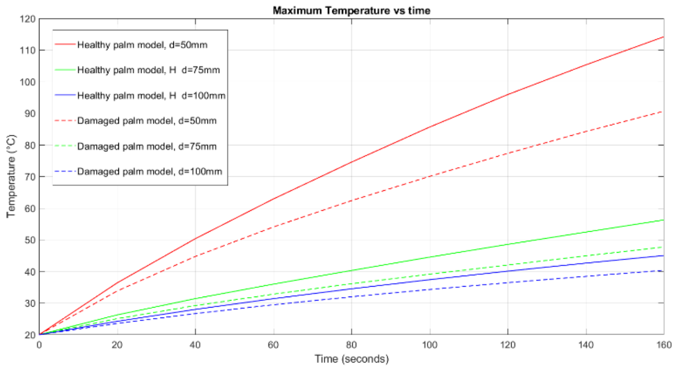

Fig 5: Maximum temperature versus time, for a homogenous healthy date palm (solid line) and a damaged palm model (dashed line) with different distances of the waveguide from the trunk of the date palm, for a temperature dependent permittivity model.

In fig 5 the temperature dependent model is used in a healthy palm model and a damaged palm model, where the waveguide is shifted from 5cm (50mm) to 10 cm (100mm) in steps of 2.5cm. As observed, a higher temperature is reached in the homogenous healthy palm model in comparison to the damaged palm model; this is due to the higher real permittivity of damaged tissues, that in turn results in a higher reflection of the electromagnetic waves that are incident on it. Power transfer to the healthy tissues is more, whereas in the damaged tissues the power reflected is more. The RPW live within the healthy tissues hence rendering this model useful.

The temperature distribution along the radial and longitudinal directions for a temperature dependent permittivity is presented in fig 6 and fig 7 respectively, for the homogenous healthy palm model and the damaged palm model, when the distance of the waveguide is 5cm (50mm) and 10cm (100mm), for a duration of the exposure of 120s.

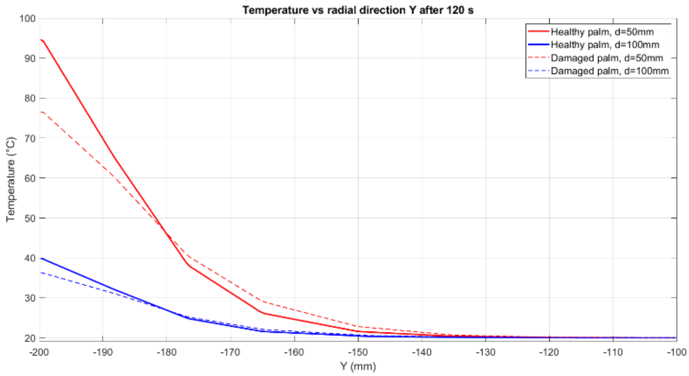

Figure 6: Temperature distribution along the radial direction for the palm models with the two waveguide distances from the trunk of the palm, after 120s of continuous incident electromagnetic waves.

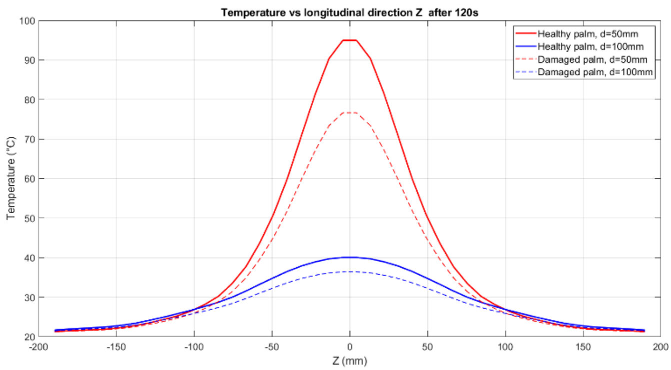

Figure 7: Temperature distribution along the longitudinal direction for the palm models with the two waveguide distances from the trunk of the palm, after 120s of continuous incident electromagnetic waves

VII. CONCLUSIONS

In this paper a feasibility study on the use of microwaves to disinfest RPW in date palms was presented with the aid of some models. The difference in the constant permittivity model and the temperature dependent model for the date palm were discussed. The importance of considering the temperature dependance in the palm modulization was established, as the constant permittivity model underestimates the temperature in the palm as depicted in this paper. With the preliminary results from a good model as presented in this paper, a protocol to disinfest the date palm from RPW can be developed as part of an IPM strategy.

REFERENCES

[1] Al-Shawaf, Abdul Moneim, et al. "A quarantine protocol against red palm weevil Rhynchophorus ferrugineus (Olivier) (Coleptera: Curculiondae) in date palm." *Journal of plant protection research* 53.4, 2013.

[2] Wakil, Waqas, Jose Romeno Faleiro, and Thomas A. Miller, eds. *Sustainable pest management in date palm: current status and emerging challenges*. Springer, 2015.

[3] FAOSTAT. Food and agricultural commodities production. Available at: https://www.fao.org/faostat/en/#home. 2012.

[4] El-Shafie, Hamadttu Abdel Farag, and Jose Romeno Faleiro. "Red palm weevil Rhynchophorus ferrugineus (Coleoptera: Curculionidae): Global invasion, current management options, challenges and future prospects." *Invasive Species-Introduction Pathways, Economic Impact, and Possible Management Options:* 1-30, 2020.

[5] Bouhssini M. El, and Faleiro J. R. (Editors). Date Palm Pests and Diseases- Integrated Management Guide. Beirut, Lebanon: International Center for Agriculture Research in the Dry Areas, 2018.

[6] Massa R., Panariello G., Pinchera D., Schettino F., Caprio E., Griffo R., and Migliore M. D. Experimental and numerical evaluations on palm microwave heating for Red Palm Weevil pest control. Scientific Reports, 1-8. 2017.

[7] Suffert F., Escobar Gutiérrez A., Ollivier L., Rochat D., Silvie P., et al. Stratégies de lutte contre le charançon rouge du palmier. [Autre] Anses, Agence nationale de sécurité sanitaire de l'alimentation, de l'environnement et du travail, 2018.

[8] Massa R., Panariello G., Migliore M. D., Pinchera D., Schettino F., Griffo R., Martano M., Power K., Maiolino P., and Caprio E. Microwave heating: a promising and eco-compatible solution to fight the spread of red palm weevil. Arab Society for Plant Protection, 143-148, 2019.

[9] Debye, P. J. W. Polar molecules. Dover publications, 1929.

[10] Gabriel C., Gabriel S., and Corthout E. The dielectric properties of biological tissues: I. Literature survey. Physics in Medicine & Biology, 1996.

[11] Kuang W., and Nelson S.O. Low- Frequency dielectric properties of biological tissues: A review with some new insights. American Society of Agricultural and Biological Engineers, 173-184, 1998.

[12] Sosa P. A., Saro I., Johnson D., Obon C., Alcaraz F., and Rivera D. Biodiversity and conservation of *Phoenix canariensis*: a review. Biodiversity and Conservation, 275-293, 2021.

[13] Jahromi M.K., Jafari A., and Mohtasebi S.S. A survey on some physical properties of the Date Palm tree. Journal of Agricultural Technology, 317-322, 2007.

[14] Massa R., Caprio E., De Santis M., Griffo R., Migliore M. D., Panariello G., Pinchera D., and Spigno P. Microwave treatment for pest control: the case of *Rhynchophorus ferrugineus* in *Phoenix canariensis*. EPPO Bulletin, 128-135, 2011.

[15] Peng L., Miao Y., and Hou Y. Demographic comparison and population projection of *Rhynchophorus ferrugineus* (Coleoptera: Curculionidae) reared on sugarcane at different temperatures. Scientific Report, 1-11, 2016.

[16] Faci M., and Benziouche S.E. Cointribution to monitoring the influence of the air temperature on some phenological stages of the date palm (cultivar ' Deglet Nour') in Biskra. Journal of the Saudi Society of Agricultural Sciences, 248-256, 2021.

[17] Massa R., Migliore M. D., Panariello G., Pinchera D., Schettino F., Caprio E., and Griffo R. Wide Band Permittivity Measurements of Palm (*Phoenix Canariensis*) and *Rhynchophorus ferrugineus* (Coleoptera Curculionidae) for RF Pest Control. Journal of Microwave Power and Electromagnetic Energy, 158-169, 2014.

[18] Ulaby, Fawwaz T., and MOHAMED A. El-Rayes. "Microwave dielectric spectrum of vegetation-Part II: Dual-dispersion model." *IEEE Transactions on Geoscience and Remote Sensing* 5: 550-557, 1987.

[19] Peyman, A., C. Gabriel, and E. H. Grant. "Complex permittivity of sodium chloride solutions at microwave frequencies." *Bioelectromagnetics: Journal of the Bioelectromagnetics Society, The Society for Physical Regulation in Biology and Medicine, The European Bioelectromagnetics Association* 28.4: 264-274, 2007.

Effect of Temperature on Morphology of SILAR deposited ZnO Thin Film

Faisal Baig [1,2], Yousaf Hameed Khattak[2], Bernabé Marí Soucase[1]
1School of Design Engineering, Universitat Politécnica de Valencia, Camí de Vera, Spain Electrical Engineering Department,
2Federal Urdu University of Arts, Science and Technology Islamabad, Pakistan
Email:
yousaf.hameedk@gmail.com

Abstract

In this work zinc oxide (ZnO) was deposited on ITO substrate by dipping substrate in alternate solution of zinc acetate dihydrate and water by varying solution temperature from 70°C to 90°C. The alternate dipping method called successive ionic layer adsorption and reaction (SILAR). The temperature of the solution plays a critical role on morphology and electrochemical properties of the deposited material. The results which confirm the effect of solution temperature on deposited substrate are structural analysis (XRD), scanning electron microscopy (SEM), optical analysis and photoelectrochemical (PEC) measurements. From XRD measurement with increase in solution temperature shows a shift in the peak and the formation of polycrystalline structure with high orientation along the c axis (002). SEM results shows the variation of surface morphology from nano-flakes to nano-rods and optical analysis shows a slight shift in band gap from 3.15eV to 3.22eV. PEC and solar cell capacitance simulator (SCAPS) measurement shows significant increase in photocurrent and device performance for sample deposited at 90°C.

Index Terms

Crystallites, X-ray diffraction, Polycrystalline deposition, Zinc compounds, Solar cells, SCAPS, Numerical analysis

I. Introduction

Population growth around the globe and deforestation of land has raised serious health issues around the globe. Increased industrialization is causing serious threats to the survival of bio life because of environmental pollution triggered by organic pollutants. To save environment from organic pollutants, photocatalytic degradation of organic pollutants using wideband gap semiconductor has gained much attention in recent years [1–4]. Wide band gap semiconductors with one dimensional nanorods, nanowires and nanotubes like structure has gain much attention because of their unique properties and they are considered to be the possible building blocks of future electronics, optoelectronic and life science applications [5–9]. In recent years much efforts have been devoted in the design and fabrication of 1d semiconductor with nanostructure [10–14].

Among those semiconductor materials ZnO has gained much attention because of nontoxic, earth abundant, large band gap energy (E_g=3.2 eV), transparent conductivity, high optical transmission and piezoelectricity. Because of its non-toxic nature ZnO is used in bio medical application without any passivation. Intensive research had been done in fabrication of ZnO thin films by various methods like spray pyrolysis, electrodeposition, hydrothermal, chemical bath deposition, spin coating, sol-gel, pulsed laser deposition and SILAR deposition [15–23].

In this work SILAR deposition of ZnO nanorods was demonstrated with various bath temperature for solutions used for fabrications of ZnO film. In our work we use High Z-400T CNC machine for dipping of substrate into the alternate solutions of cation and anion. A general block diagram of SILAR is given in Figure 1 below.

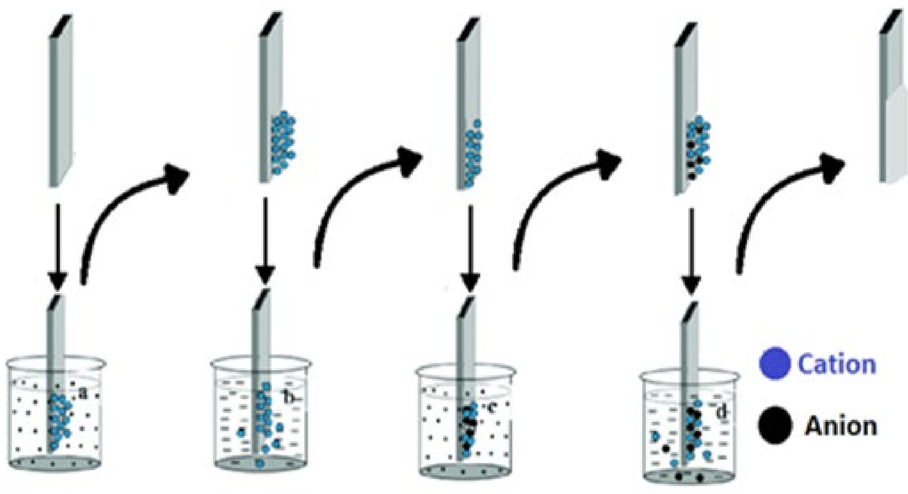

Fig. 1: SILAR diagram

The paper is organized as, experimental section contains the details of SILAR about the fabrication of ZnO nanorods and results and discussion sections contain the details about the characterization of ZnO nanorods with the aid of x-ray diffraction (XRD), scanning electron microscopy (SEM), optical analysis and photoelectrochemical (PEC) measurements. The last section contains the findings of the work presented in this paper.

I. Experimental Section

A. Materials

Analytical graded chemicals including Zinc acetate dihydrate, Citric Acid and ammonia were used without further purification.

B. Preparation of SnS thin film

Solution 1:

Solution for Cationic precursor was prepared by mixing (0.05M) of Zinc acetate dihydrate in 20 ml of water with citric acid as complexing agent to dissolve zinc acetate dihydrate in water. The solution was well stirred with magnetic stirrer and put on a temperature.

Solution 2:

Solution for Anionic precursor was prepared by adding ammonia in water and the pH of the solution was adjusted to 12. After that the aqueous ammonia solution was put on a temperature bath of 90°C.

C. Fabrication of ZnO thin film

For ZnO thin film fabrication well sanitized ITO substrate was put into the solution of (Zinc (II) acetate dihydrate, citric acid) for 10s to absorb the Zn^(2+) ions on ITO substrate. After the entanglement of Zn^(2+) on ITO substrate in the solution (Zinc (II) acetate dihydrate, citric acid), the substrate was then immersed into the solution of (aqueous ammonia) for 10s. This complete our one SILAR cycle and after every 5 cycles the substrate was washed with double distilled water to remove any precipitation and impurity on the substrate for 10s.

D. Result and discussion

To investigate the crystal structure of ZnO thin film deposited at cationic bath temperature of (70 C, 80 C, 90 C), we used diffractometer in the Bragg-Brentano configuration of Rigaku Ultima IV (the X-ray radiation is λCuKα=1.54060Å). The measured XRD peaks are plotted in Figure 1 for ZnO thin films. From Figure 1 the film with temperature 90◦C shows a large peak of crystal orientation across (002) axis [23][24], whereas this peak is smaller in other two sample which are deposited at temperature (70◦C, 80◦C). Similarly, the inset plot in Figure 1 shows a shift in peak for sample deposited at 90C towards the principal peak of (002) for ZnO with comparison to the reference card 00-036-1451.

Average value of ZnO thin film crystallite size can be obtained from Debye – Scherrer's Equation given in Equation 1 [25].

$$D = \left(\frac{K\lambda}{\beta \ Cos\theta}\right) \qquad (1)$$

θ is the diffraction angle, β is the width at half height intensity or full width half maximum (FWHM) of the peak, λ is the wavelength of the incident beam, K is Scherrer's constant and usually takes the value 0.9 and D is the crystalline size. Values for crystallite size is given in Table 1 and from Table 1 crystalline size for 2θ Peak (002) increase with bath temperature.

θ is the diffraction angle, β is the width at half height intensity or full width half maximum (FWHM) of the peak, λ is the wavelength of the incident beam, K is Scherrer's constant and usually takes the value 0.9 and D is the crystalline size. Values for crystallite size is given in Table 1 and from Table 1 crystalline size for 2θ Peak (002) increase with bath temperature.

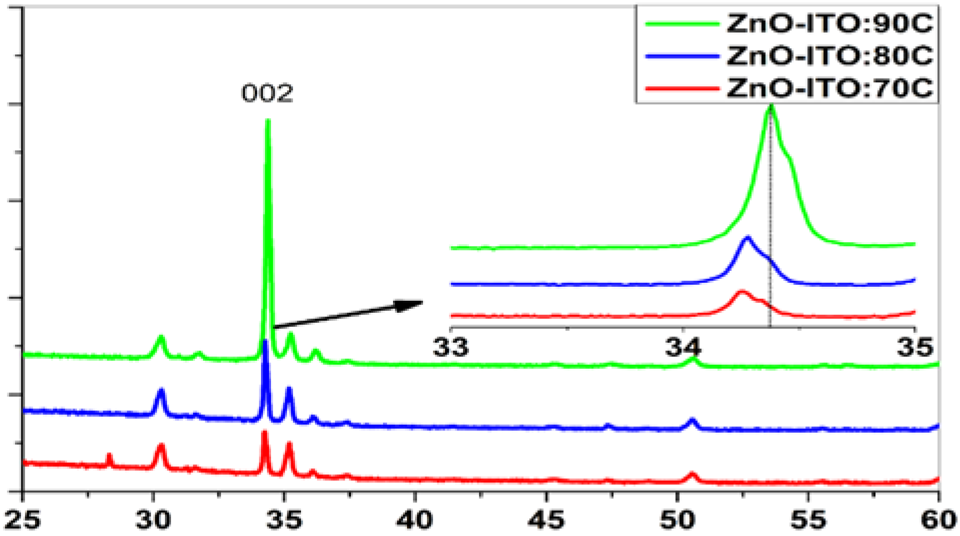

Fig. 2: ZnO thin film XRD pattern

TABLE I: Structural parameters of ZnO.

Sample Name	Peak 2θ (0,0,2)	Size of Crystallite [nm]
70C	0.22757	38.14
80C	0.20193	42.99

90C	0.1996	43.50

To find the transmission and band gap energy of ZnO thin film we used Ocean Optics HR4000 (UV-Visible spectrophotometer) fixed with an integrating sphere (to collect both specular and diffuse transmittance). Figure 3 result for transmission and the transmittance of ZnO thin film is slightly decreased by increase in temperature of the bath. This happens may be due the morphological changes in ZnO thin film. And Figure 4 shows the result for band gap energy of ZnO thin film vs photon energy and from Figure it is quite evident that bath temperature also effects the band gap energy of ZnO thin film and for bath temperature of 90◦C the band gap is around 3.22 eV. The results for variation in band gap on change in temperature is shown in table 2.

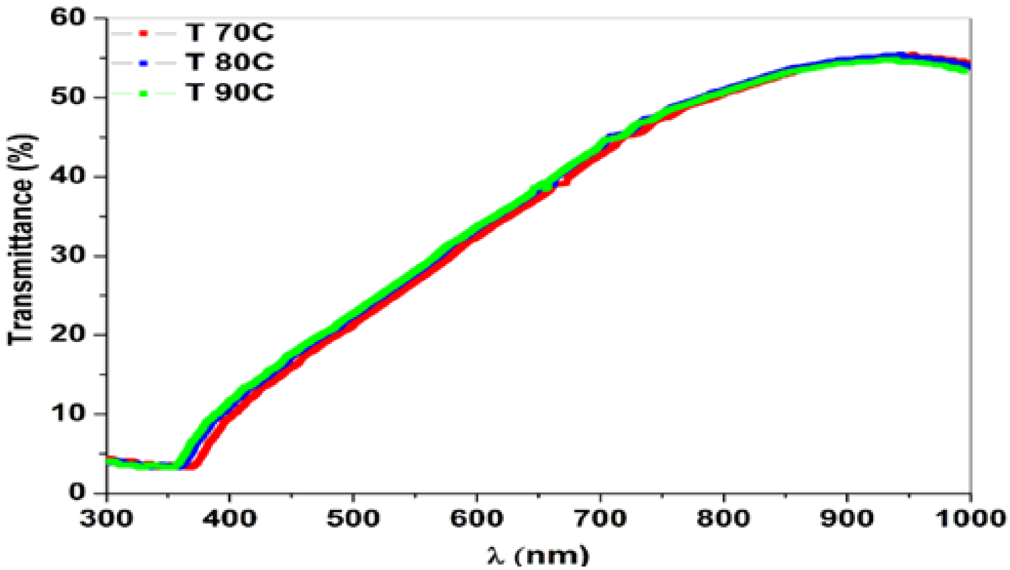

Fig. 3: Transmittance of ZnO thin film

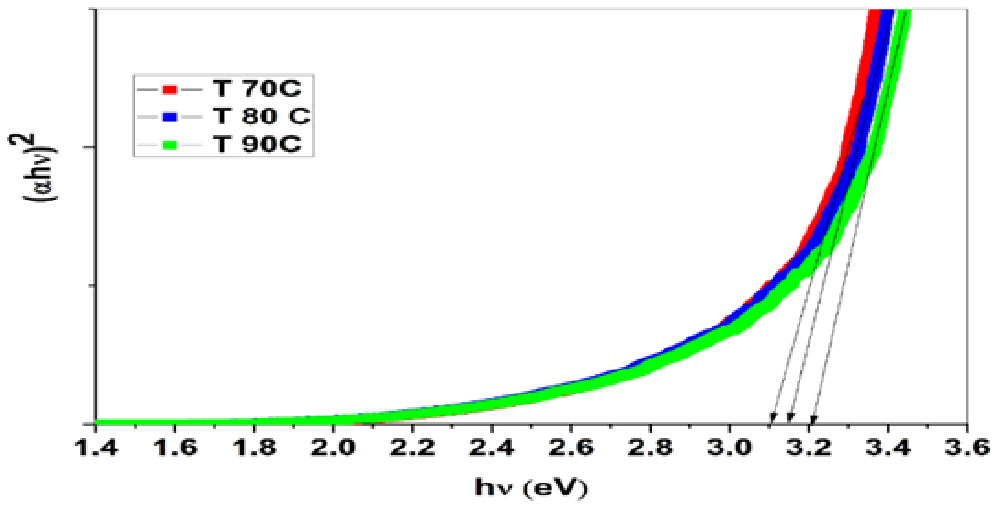

Fig. 4: ZnO thin film band gap

TABLE 2: ZnO band gap

Sample Name	Band Gap (eV)
70C	3.15
80C	3.17
90C	3.22

Figure 5 shows the scanning electron microscopy (SEM) images of ZnO thin films deposited at different temperatures (70°C, 80°C, 90°C). And based on the results from SEM as given in Figure 5 it was found that temperature bath temperature influences morphology of ZnO samples and by increase in temperature for cationic solution the morphology of the ZnO thin film changes from nano-flakes to nano-rods structure.

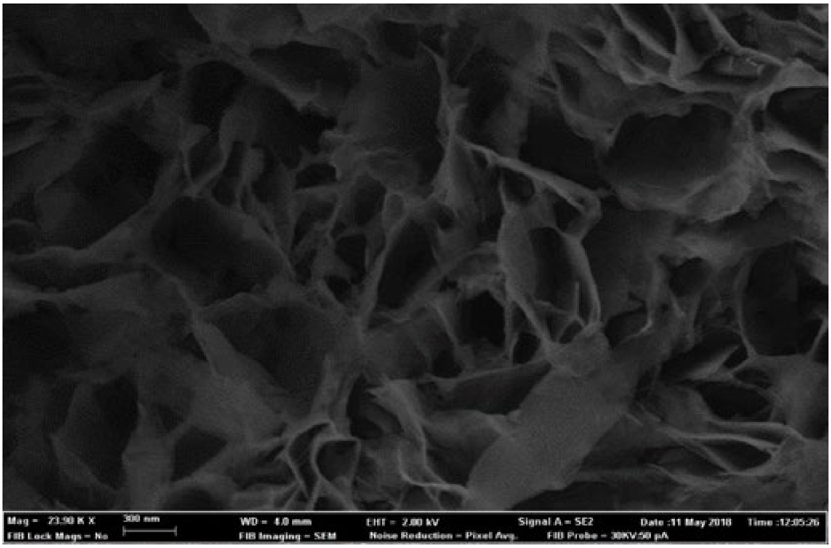

Fig. 5: (a) SEM images of films prepared at temperature 70°C

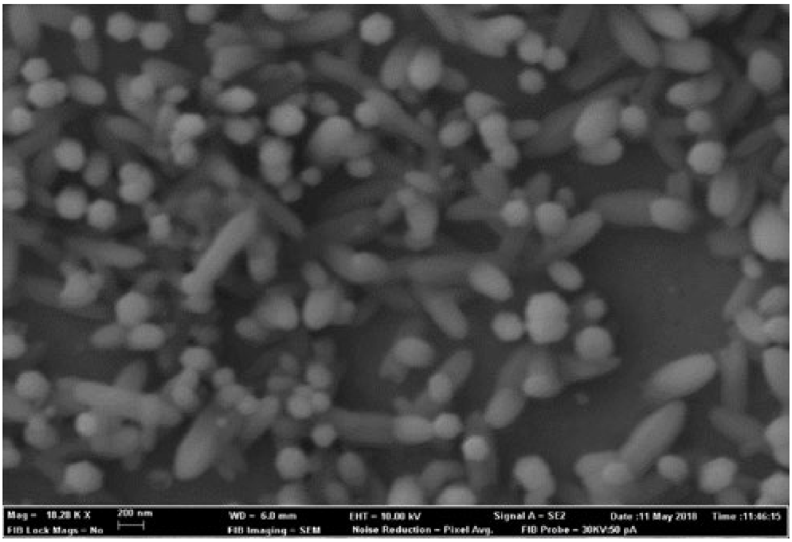

Fig. 5: (b) SEM images of films prepared at temperature 80°C

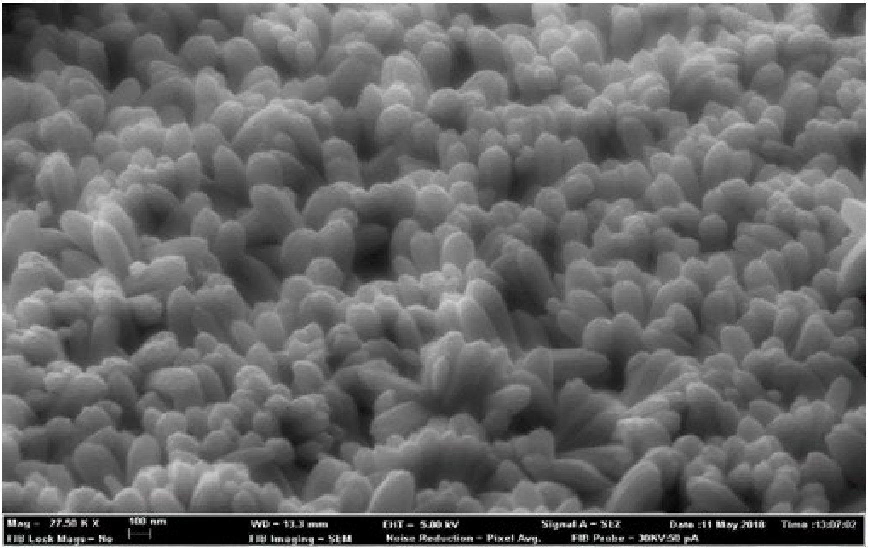

Fig. 5: (c) SEM images of films prepared at temperature 90℃

To measure the degree of photocatalytic action ZnO deposited thin film at various temperature for water splitting we used potentiostat (autolab), solar simulator and three probes photochemical cell. The artificial light intensity was calibrated at 1 SUN (100) with standard silicon photodiode. The system for measuring photocatalytic activity consists of three electrodes, ZnO work as working electrode, Ag/AgCL as reference electrode and Pt as counter electrode. The electrolyte solution used to measure the photocurrent activity for ZnO film deposited at different temperature is Na_2SO_4 with molar ratio of 0.5 M. The chronoamperometric study was performed at the chopping ON/OFF rate of ~10 s/cycle. Figure 6 shows the result for photocurrent activity of ZnO film and based on the result from photoelectrochemical (PEC) test ZnO fil deposited at temperature 90◦C has current higher than other films.

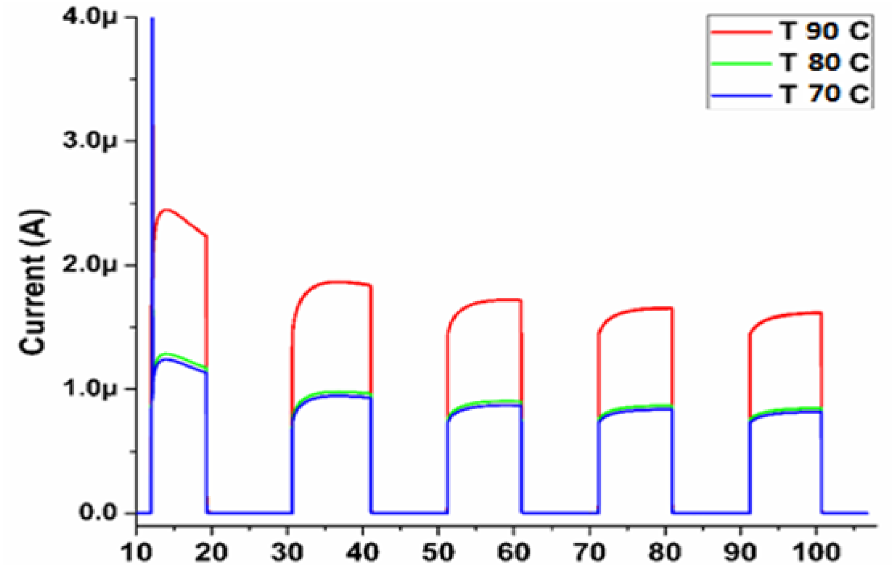

Fig. 6: Photocurrent for ZnO films deposited at different temperature

Similarly, results for variation of band gap on solar cell device performance was also analyzed using SCAPS-1D (solar cell capacitance software) with structure of solar cell SnS/CdS/ZnO as discussed in our earlier work [26]. Results for numerical simulation in SCAPS-1D, are plotted in Figure 7 and from the results with increase in band gap of ZnO layer device performance was enhanced. From Figure 7 the results for ZnO thin film deposited at bath temperature of 90C shows better performance with comparison to other samples for device structure SnS/CdS/ZnO.

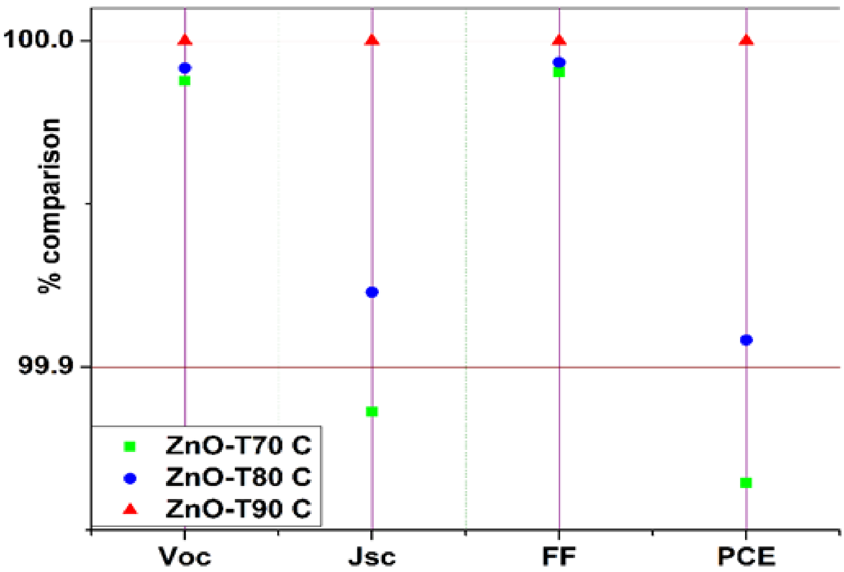

Fig. 7: SCAPS simulation for device structure SnS/CdS/ZnO

A. Conclusions

Zinc oxide (ZnO) was deposited on ITO substrate at different bath temperature ranging from 70°C to 90°C using SILAR technique. The effect of bath temperature on ZnO deposited film was analyzed by XRD, optical analysis, SEM and PEC measurements. From XRD analysis it was found that by changing bath temperature the crystal orientation along 002 is improved whereas bath temperature had a minor effect of band gap of ZnO deposited films. SEM images reveal that with increase in bath temperature ZnO nano-rods grown on ITO substrate and PEC measurement prove an enhanced current for ZnO nano-rods at temperature 90°C and whereas SCAPS-1D simulation shows that sample with band gap of 3.22 eV shows better performance for solar cell with device structure SnS/CdS/ZnO.

ACKNOWLEDGMENTS

Ministerio de Economía y Competitividad (PID2019-107137RB-C21)Ministerio de Economía y Competitividad (PID2019-107137RB-C21)

REFERENCES

[1] T.L. Thompson, J.T. Yates, Surface science studies of the photoactivation of TIO2- New photochemical processes, Chem. Rev. 106 (2006) 4428–4453. doi:10.1021/cr050172k.

[2] R. Comparelli, E. Fanizza, M.L. Curri, P.D. Cozzoli, G. Mascolo, A. Agostiano, UV-induced photocatalytic degradation of azo dyes by organic-capped ZnO nanocrystals immobilized onto substrates, Appl. Catal. B Environ. 60 (2005) 1–11. doi:10.1016/j.apcatb.2005.02.013.

[3] D. Chatterjee, S. Dasgupta, Visible light induced photocatalytic degradation of organic pollutants, J. Photochem. Photobiol. 6 (2015) 186–205. doi:10.13140/RG.2.1.3848.1364.

[4] P. Kumar, N. Singh, A. Solanki, S. Upadhyay, S. Chaudhary, V.R. Satsangi, S. Dass, R. Shrivastav, A Clean and Green Hydrogen Energy Production Using Nanostructured ZnO and Fe-ZnO via Photoelectrochemical Splitting of Water, in: Chem. Phytopotentials Heal. Energy Environ. Perspect., Springer Berlin Heidelberg, Berlin, Heidelberg, 2012: pp. 191–194. doi:10.1007/978-3-642-23394-4_40.

[5] X. Duan, Y. Huang, Y. Cui, J. Wang, C.M. Lieber, Indium phosphide nanowires as building blocks for nanoscale electronic\nand optoelectronic devices, Nature. 409 (2001) 66–69. doi:10.1038/35051047.

[6] Y. Cui, Q. Wei, H. Park, C.M. Lieber, Nanowire nanosensors for highly sensitive and selective detection of biological and chemical species., Science. 293 (2001) 1289–92. doi:10.1126/science.1062711.

[7] Y.N. Xia, P.D. Yang, Y.G. Sun, Y.Y. Wu, B. Mayers, B. Gates, Y.D. Yin, F. Kim, Y.Q. Yan, B.Y. Xia, P.D. Yang, Y.G. Sun, Y.Y. Wu, B. Mayers, B. Gates, Y.D. Yin, F. Kim, H. Yan, Y.N. Xia, P.D. Yang, Y.G. Sun, Y.Y. Wu, B. Mayers, B. Gates, Y.D. Yin, F. Kim, Y.Q. Yan, One-dimensional nanostructures: Synthesis, characterization, and applications, Adv. Mater. 15 (2003) 353–389. doi:10.1002/adma.200390087.

[8] H. Sun, Q. Zhang, J. Zhang, T. Deng, J. Wu, Electroluminescence from ZnO nanowires with a p-ZnO film/n-ZnO nanowire homojunction, Appl. Phys. B Lasers Opt. 90 (2008) 543–546. doi:10.1007/s00340-007-2900-7.

[9] W.Q. Lim, S. Shanmugan, M. Devarajan, Influence of annealed Cu–Al2O3 thin film on the performance of high power LED: thermal and optical analysis, Opt. Quantum Electron. 48 (2016) 1–14. doi:10.1007/s11082-016-0454-9.

[10] Z.L. Wang, Characterizing the structure and properties of individual wire-like nanoentities, Adv. Mater. 12 (2000) 1295–1298. doi:10.1002/1521-4095(200009)12:17<1295::AID-ADMA1295>3.0.CO;2-B.

[11] J. Wallentin, N. Anttu, D. Asoli, M. Huffman, I. Åberg, M.H. Magnusson, G. Siefer, P. Fuss-Kailuweit, F.

Dimroth, B. Witzigmann, H.Q. Xu, L. Samuelson, K. Deppert, M.T. Borgström, InP nanowire array solar cells achieving 13.8% efficiency by exceeding the ray optics limit, Science (80-.). 339 (2013) 1057–1060. doi:10.1126/science.1230969.

[12] S.H. Ko, D. Lee, H.W. Kang, K.H. Nam, J.Y. Yeo, S.J. Hong, C.P. Grigoropoulos, H.J. Sung, Nanoforest of hydrothermally grown hierarchical ZnO nanowires for a high efficiency dye-sensitized solar cell, Nano Lett. 11 (2011) 666–671. doi:10.1021/nl1037962.

[13] M.D. Kelzenberg, D.B. Turner-Evans, B.M. Kayes, M. a. Filler, M.C. Putnam, N.S. Lewis, H. a. Atwater, Single-nanowire Si solar cells, 2008 33rd IEEE Photovolatic Spec. Conf. (2008) 1–6. doi:10.1109/PVSC.2008.4922736.

[14] K. Yu, J. Chen, Enhancing solar cell efficiencies through 1-D nanostructures, Nanoscale Res. Lett. 4 (2009) 1–10. doi:10.1007/s11671-008-9200-y.

[15] S. a Studenikin, N. Golego, M. Cocivera, Fabrication of green and orange photoluminescent , undoped ZnO films using spray pyrolysis Fabrication of green and orange photoluminescent , undoped ZnO films using spray pyrolysis, J. Appl. Phys. 2287 (2012) 22–24. doi:10.1063/1.368295.

[16] E.M. Elsayed, A.E. Shalan, M.M. Rashad, Preparation of ZnO nanoparticles using electrodeposition and co-precipitation techniques for dye-sensitized solar cells applications, J. Mater. Sci. Mater. Electron. 25 (2014) 3412–3419. doi:10.1007/s10854-014-2033-9.

[17] D. Polsongkram, P. Chamninok, S. Pukird, L. Chow, O. Lupan, G. Chai, H. Khallaf, S. Park, A. Schulte, Effect of synthesis conditions on the growth of ZnO nanorods via hydrothermal method, Phys. B Condens. Matter. 403 (2008) 3713–3717. doi:10.1016/j.physb.2008.06.020.

[18] V.R. Shinde, C.D. Lokhande, R.S. Mane, S.H. Han, Hydrophobic and textured ZnO films deposited by chemical bath deposition: Annealing effect, Appl. Surf. Sci. 245 (2005) 407–413. doi:10.1016/j.apsusc.2004.10.036.

[19] S. Ilican, Y. Caglar, M. Caglar, Preparation and characterization of ZnO thin films deposited by sol-gel spin coating method, J. Optoelectron Adv. Mater. 10 (2008) 2578–2583. doi:10.1080/24701556.2016.1242627.

[20] S. Öztürk, N. Taşaltin, N. Kilinç, H. Yüzer, Z.Z. Öztürk, Fabrication of ZnO nanowires at room temperature by cathodically induced sol-gel method, Appl. Phys. A Mater. Sci. Process. 99 (2010) 73–78. doi:10.1007/s00339-009-5504-8.

[21] R.G. Nikov, A.O. Dikovska, N.N. Nedyalkov, P.A. Atanasov, G. Atanasova, D. Hirsch, B. Rauschenbach, ZnO nanostructures produced by pulsed laser deposition in open air, Appl. Phys. A Mater. Sci. Process. 123 (2017) 1–7. doi:10.1007/s00339-017-1276-8.

[22] V.L. Patil, S.A. Vanalakar, P.S. Patil, J.H. Kim, Fabrication of nanostructured ZnO thin films based NO2gas sensor via SILAR technique, Sensors Actuators, B Chem. 239 (2017) 1185–1193. doi:10.1016/j.snb.2016.08.130.

[23] A. Raidou, F. Benmalek, T. Sall, M. Aggour, A. Qachaou, L. Laanab, M. Fahoume, The influence of rinsing period on the structural and optical properties of ZnO thin films, Opt. Quantum Electron. 46 (2014) 171–178. doi:10.1007/s11082-013-9737-6.

[24] C. Yun, L.T. Chen, S.T.Y. Shen, The optical and electrical properties of F doped ZnO thin film by different post-annealing temperatures, Opt. Quantum Electron. 50 (2018) 1–8. doi:10.1007/s11082-018-1430-3.

[25] N. Soundaram, R. Chandramohan, S. Valanarasu, R. Thomas, A. Kathalingam, Studies on SILAR deposited Cu2O and ZnO films for solar cell applications, J. Mater. Sci. Mater. Electron. 26 (2015) 5030–5036. doi:10.1007/s10854-015-3020-5.

[26] F. Baig, Y.H. Khattak, S. Ullah, B.M. Soucase, S. Beg, H. Ullah, Numerical analysis a guide to improve the efficiency of experimentally designed solar cell, Appl. Phys. A. 124 (2018) 471. doi:10.1007/s00339-018-1877-x.

Numerical simulation of a voltage multiplier based three-phase CSI micro inverter for PV applications

Roberto Giacomobono[1], Salman Ali [2], and Fabrizio Marignetti[3]

[1] Department of electrical and information engineering(DIEI), University of Cassino and Southern Lazio, Cassino
Email: roberto.giacomobono@unicas.it

[2]Department of electrical and information engineering(DIEI), University of Cassino and Southern Lazio, Cassino
Email:Salman.Ali@unicas.it

[3]Department of electrical and information engineering(DIEI), University of Cassino and Southern Lazio, Cassino
Email:fabrizio.marignetti@unicas.it

Abstract

The layout with which PV strings are often arranged to be connected to a single inverter that often controls various solar panels can cause various issues. Those issues can be addressed by employing micro-inverters connected to the single panels or to smaller arrays to have better control over the system. This paper presents a topology of CSI micro inverter designed to use a voltage multiplier as a voltage boost for the DC link choke inductor using SiC switches at high frequency. The general topology is presented alongside the simulation results obtained for non-ideal components in SPICE.

Index Terms

PV, micro inverters, power quality

I. Introduction

In photovoltaic applications many known issues arise from the strategy of connecting many PV modules to the same inverter. One of those problems is partial shading of some cells or of an entire module, which can cause overheating to the module itself [1]. Another issue arises when connecting multiple PV arrays to the same inverter is the necessity of interrupting DC currents in case of fault on a single array since interrupting DC currents requires employment of specialized breakers, which are becoming more available with the increased attention on DC microgrids but are still less common than their AC counterparts [2]. Furthermore, during much of their functioning hours modules can work under mismatching irradiance conditions, and controlling the power flow with a single

inverter and a single MPPT controller can lead to non optimized results. For all those reasons micro-inverters can be employed on smaller arrays to better handle the control power flow via the employment of DMPPT [3]. Arrays with micro inverters also behave effectively as AC generators and therefore can bypass the aforementioned DC interruption problems. Another aspect of making smaller arrays is also the fact that the DC link voltage obtained this way can be rather small and so a voltage boost is required for the proper functioning of the converter. This voltage boost can be normally achieved with circuits that use transformer based topology such as a Flyback element [4] or boost converter based techniques [5] or employ a buck-boost or other kinds of transformerless operation [6] [7]
[8] This work presents a topology which employs a capacitive voltage multiplier and the natural capability of the CSI inverter of acting as a boost converter to control low DC link voltage arrays. This type of circuit has been used as a voltage equalizer in [9]. Papers [10] and [11] also present a similar conception with different application fields. The idea of this paper is to test the power capabilities and output power quality of the proposed topology to attest the feasibility of application as a power micro-inverter for PV applications.

II. Topology presented

The topology presented for this work is shown in Fig.1. The first part of the schematic is comprised of a full bridge converter that feeds a square alternating AC waveform to a capacitive voltage multiplier. Than an ideal regulated current source is realized via a chopper converter and an inductance whose aim is to provide a stabilized DC current to the last stage. The final part of the schematic is the inverter itself which is a four leg topology [12]. The fourth leg is introduced to provide a freewheeling path for the current during certain commutation stages and it serves the purpose of lowering conduction losses in the freewheeling stages.
The results of a sample simulation are shown in 2 and 3 to better explain the operation of this topology. In Fig.2 the initial voltage transient before the DC-Link inductor is shown. In the beginning the chopper is not modulating and the voltage at the node before the DC-link inductor is simply the one determined by the voltage multiplier. After that the current flowing through L1 reaches a value which is around the setpoint chosen and the M7 mosfet starts to switch to maintain the desired current.

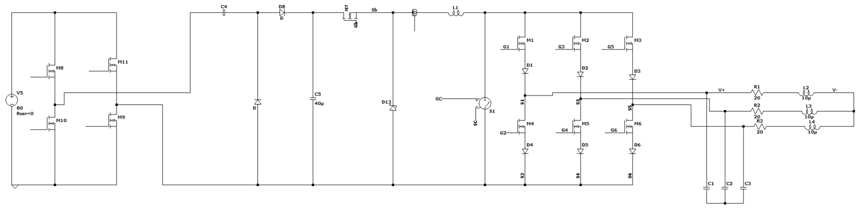

Fig. 1: Schematic of the converter presented

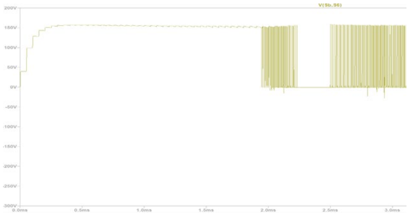

Fig. 2: Voltage transient and beginning of modulation for the chopper converter

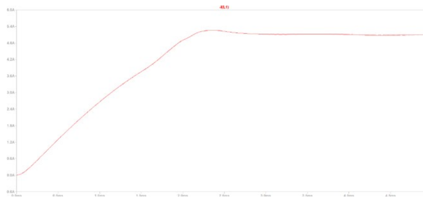

Fig. 3: DC link current transient

In Fig.3 the current transient is shown. The current modulation in the chopper starts when the current goes above the setpoint for the first time. An efficiency curve for various passive resistive loads is shown in figure 4. This curve was taken from a 100Khz switching frequency simulation with 5A stabilized DC link current Since the current implementation

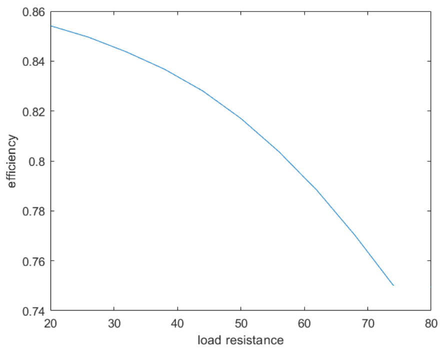

Fig. 4: Efficiency curve@100Khz switching frequency

of the topology includes three hard switching sub-topologies (a full bridge in input, a chopper and four inverter legs) all in series, the resulting final efficiency for high switching frequencies is lower than most standard solutions. Working at higher frequencies could in any case beneficial to have a smaller choke inductance for the DC link and lower THDs, which coupled with the fact that this topology doesn't use transformers, make it still a viable low cost solution. A trade off between better efficiency and a bigger choke inductance could be made to achieve a better overall performance. Finally, a sample current waveform is shown in figure 5.

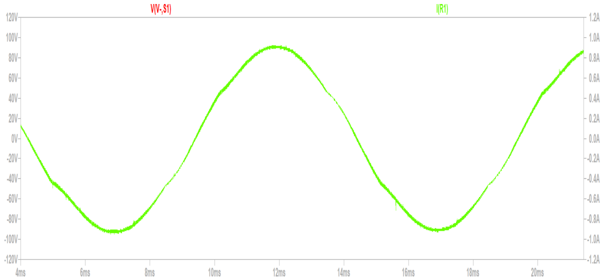

Fig. 5: Output current waveform

REFERENCES

[1] Manish Kumar, Arun Kumar, Performance assessment and degradation analysis of solar photovoltaic technologies: A review, Renewable and Sustainable Energy Reviews, Volume 78, 2017, Pages 554-587, ISSN 1364-0321, https://doi.org/10.1016/j.rser.2017.04.083.

[2] Z. Yu, R. Bai, Y. Zhang and Y. Zhu, ”Review of DC Circuit Breaker Technology Development,” 2022 7th Asia Conference on Power and Electrical Engineering (ACPEE), Hangzhou, China, 2022, pp. 621-626, doi: 10.1109/ACPEE53904.2022.9783627.

[3] Marco Balato, Luigi Costanzo, Massimo Vitelli, Chapter 5 - DMPPT PV System: Modeling and Control Techniques, Editor(s): Imene Yahyaoui, Advances in Renewable Energies and Power Technologies, Elsevier, 2018, Pages 163-205, ISBN 9780128129593, https://doi.org/10.1016/B978-0-12-812959-3.00005-8.

[4] Abdel-Rahim, O., Funato, H., & Haruna, J. (2015, November). Pseudo single stage flyback current source inverter for grid connected PV applications. In IECON 2015-41st Annual Conference of the IEEE Industrial Electronics Society (pp. 000001-000006). IEEE.

[5] Tseng, K. C., Huang, C. C., & Shih, W. Y. (2012). A high step-up converter with a voltage multiplier module for a photovoltaic system. IEEE transactions on power electronics, 28(6), 3047-3057.

[6] de Brito, M., Sampaio, L., Melo, G., & Canesin, C. A. (2015). Three-phase tri-state buck–boost integrated inverter for solar applications. IET Renewable Power Generation, 9(6), 557-565.

[7] Yang, B.; Li, W.; Gu, Y.; Cui, W.; He, X. Improved transformerless inverter with common-mode leakage current elimination for a 712 photovoltaic grid-connected power system. IEEE Transactions on Power Electronics 2012, 27, 752–762. https://doi.org/10.1109/ 713 tpel.2011.2160359.

[8] Alajmi, B.N.; Ahmed, K.H.; Adam, G.P.; Williams, B.W. Single-phase single-stage transformer less grid-connected PV system. 734 IEEE Transactions on Power Electronics 2013, 28, 2664–2676. https://doi.org/10.1109/tpel.2012.2228280.

[9] Uno, M., & Tanaka, K. (2012). Double-switch single-transformer cell voltage equalizer using a half-bridge inverter and a voltage multiplier for series-connected supercapacitors. IEEE Transactions on Vehicular Technology, 61(9), 3920-3930.

[10] Tran, T. T., Nguyen, M. K., Nguyen, H. N., Duong, T. D., Lim, Y. C., & Choi, J. H. (2020). A three-phase constant common-mode voltage inverter with triple voltage boost for transformerless photovoltaic system. IEEE Access, 8, 166692-166702.

[11] Lee, S. S., Iqbal, S., & Kamarol, M. (2011). Control of ZCS-SR inverter-fed voltage multiplier-based high-voltage DC–DC converter by digitally tuning tank capacitance and slightly varying pulse frequency. IEEE transactions on power electronics, 27(3), 1076-1083.

[12] Lorenzani, E.; Immovilli, F.; Migliazza, G.; Frigieri, M.; Bianchini, C.; Davoli, M. CSI7: A modified three-phase current- 702 source inverter for modular photovoltaic applications. IEEE Transactions on Industrial Electronics 2017, 64, 5449–5459. https: 703 //doi.org/10.1109/tie.2017.2674595.

Slice-Level Diagnostics with 2D CNNs: A Promising Approach to Alzheimer's Detection Using Structural MRI Data

Gabriele Lozupone, Alessandro Bria, Claudio De Stefano, Francesco Fontanella

Department of Electrical and Information Engineering, University of Cassino and Southern Lazio, v. Di Biasio 43, 03043 Cassino (FR), Italy

Abstract

According to the latest data collected by the Alzheimer's Disease International (ADI), Alzheimer's disease (AD) affects a significant percentage of the elderly population (approximately 50 million individuals), leading to progressive cognitive deficits, impairments in daily activities, and, finally, death due to lack of effective treatments. AD is characterized by brain atrophy and neuronal death caused by the abnormal neurotoxic accumulation of amyloid and tau proteins. In our endeavour to delve deeper into the complexities of AD, we embarked on an extensive review of the existing literature. This comprehensive study enriched our understanding and highlighted the gaps in the current research landscape, guiding our subsequent investigations. Structural magnetic resonance imaging (sMRI) represents a fundamental tool in diagnosing and evaluating AD in the clinical setting. Building on established techniques, our study aimed to investigate and extract discrimi- native features from these kind of images. Specifically, the datasets used in our research come from the Alzheimer's Disease Neuroimaging Initiative (ADNI), a renowned global effort to advance our understanding of Alzheimer's disease through neuroimaging and other methods. We split the 3D sMRI into individual slices and trained a 2D convolutional neural network (CNN), pre-trained on ImageNet, on each slice, associating each with a label of AD or CN (cognitively normal). We then used a majority voting approach as a fusion method to classify the entire brain volume. Our results were promising. The models tested and implemented have achieved good performance in terms of accuracy, MCC (Matthew's correlation coefficient), sensitivity, and specificity. In particular, we observed that models with multiple parameters only sometimes generalized well for this task. Simpler architectures like VGG-16 were better suited to this challenge than newer, more capable networks such as EfficientNet or ResNet. This study underscores the potential of a slice-level approach with pre-trained 2D CNNs for AD diagnosis, possibly rivalling the capabilities of 3D CNN methods that process data at the volume level. Our future goal is to identify more advanced fusion techniques to enhance diagnostic accuracy further.

Electromagnetic Tomography for linear and nonlinear materials

Vincenzo Mottola* and Antonello Tamburrino*†

*Dipartimento di Ingegneria Elettrica e dell'Informazione "M. Scarano", Universita` degli Studi di Cassino e del Lazio Meridionale, Cassino, Italy
Email: vincenzo.mottola@unicas.it

†Department of Electrical and Computer Engineering,Michigan State University, East Lansing, USA
Email: antonello.tamburrino@unicas.it

Abstract

In this paper, we present two non-iterative imaging methods for Electromagnetic Tomography (ET) and, specifically, for Soft-Field Tomography, that is of great interest in literature due to the low-cost operations and the absence of ionizing radiations. The first method proposed, called Kernel Method, treats linear materials, while the second one, that is a Monotonicity Principle based method, is meant for nonlinear materials. Both are feasible for real-time applications, that is a very uncommon feature in Soft-Field Tomography. Furthermore, the second method is the first real-time imaging algorithm able to deal with field-dependent electromagnetic properties.

Index Terms

Electromagnetic Tomography, Inverse Problem, Real-time imaging method, Kernel Method, Monotonicity Principle, Nonlinear materials.

I. Introduction

Electromagnetic Tomography (ET), and especially Soft-Field Tomography, is a topic of great interest, since the great flexibility of these techniques to various practical applications. Basically, ET allows to reconstruct the interior of a sample under test exciting it by a certain form of electromagnetic energy and measuring a proper electromagnetic quantity on the boundary. In other words, it is a nondestructive technique.

We are interested in the inverse obstacle problem, that is retrieving the shape of one or more anomalies embedded in a known background material, throughout boundary measurements. This is a very challenging problem, since it is an ill-posed and nonlinear problem, even in presence of linear materials.

Fig. 1. Inverse obstacle problem. Ω is the domain of interest for tomographic inspection, A the

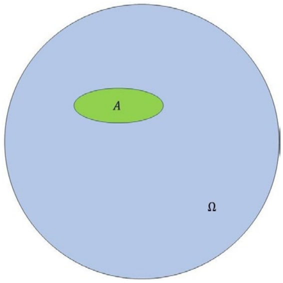

anomalous region to reconstruct.

There are two main approaches to this problem. The first one, known as iterative methods, consists in minimizing a proper error functional between the measured and the numerical computed data [1]. The main drawbacks of these methods are the high computational cost and the difficulty in guaranteeing global convergence. For these reasons, they are incompatible with real-time applications.

The non-iterative methods, instead, have their roots in the properties of the physical-mathematical model of the target problem. Starting from these properties, a proper indicator function is introduced able to give real-time reconstructions. There are very few of them available such as: Linear Sampling Method [2], Factorization Method [3], Enclosure Method [4], Monotonicity Principle Method [5], MUSIC [6].

In this work, we propose two new non-iterative imaging method. The first one, called Kernel Method, is meant for linear materials, while the second one, based on a recent generalization of the Monotonicity Principle, is able to deal with nonlinear materials.

The paper is organized as follows. In Section II we present the Kernel Method, while in Section III we treat the imaging of nonlinear materials via the Monotonicity Principle.

II. THE KERNEL METHOD

Despite the Kernel Method can be applied in different contexts, for the seek of clarity, we focus on Electrical Resistance Tomography (ERT). In ERT the aim is to infer the spatial behavior of the electrical conductivity by boundary measurements in DC operations. The excitation is represented by DC currents driven by a certain number of electrodes, while the measured quantity is represented by DC voltages resulting on the same electrodes. Let us consider a sample under test, which has an anomalous region A and hereafter termed actual configuration. Furthermore, let us introduce a second configuration, called reference configuration, with the same geometry of the actual configuration, but without the anomaly.

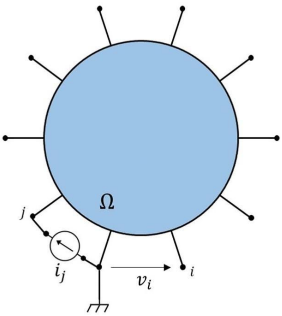

Fig. 2. System for ERT. A certain number of electrodes are attached on the boundary of the domain. Currents are imposed on the electrodes and voltages are measured.

A key role in our method is played by the resistance matrix, i.e. the matrix that maps the applied currents on the electrodes to the measured voltages. We refer to $\mathbf{R}_A$ and $\mathbf{R}_{BG}$ as the resistance matrix related to the actual and reference configuration, respectively.

The imaging method consists in evaluating the spatial behavior of the power density on the reference configuration, when the system is driven by an eigenvector of $\mathbf{R}_A\ \mathbf{R}_{BG}$ corresponding to a proper eigenvalue above the noise level. The estimate of the anomaly is given by the region where this power density is negligible.

It results that the proposed method has a very low computational cost. Indeed, the computation of eigenvalues and eigenvectors of $\mathbf{R}_A - \mathbf{R}_{BG}$ has a negligible cost. Then it is required the solution of only one direct problem to carry out reconstructions.

III. Tomography of nonlinear materials via Monotonicity Principle

The Monotonicity Principle (MP) is the foundation of the a class of non-iterative algorithms for Soft-Field Tomography. It has successfully applied in various fields such as: Electrical Resistance Tomography [5], Electrical Capacitance Tomography [7], Magnetic Inductance Tomography [7], Eddy Current Tomography [8] and so on. It has a series of peculiar characteristics such the feasibility for real-time applications, the possibility to give rigorous upper and lower bounds to the anomalous region and the capability to perfectly reconstruct the outer boundary of the anomaly in presence of noise-free data.

Basically, MP states a monotonic relationship between the values, in the interior of the domain, of an unknown material property and the boundary measurements, represented by a proper boundary operator. Recently, it has been extended to nonlinear materials, under very general assumptions [9].

In this work, we focus on the problem of retrieving an unknown nonlinear anomaly embedded in known linear background, i.e., let Ω be the domain of interest for tomographic inspection and A Ω be the anomalous region, the electrical conductivity related to the sample under test is

$$\sigma(x, E) = \begin{cases} \sigma_{NL}(E) & \text{in } A \\ \sigma_{BG} & \text{in } \Omega \setminus A. \end{cases}$$

The steady state current problem can be formulated via the introduction of an electrical scalar potential φ, i.e. $\mathbf{E} = -\nabla\varphi$

$$\begin{cases} \nabla \cdot (\sigma_A(x, |\nabla\varphi_A(x)|)\nabla\varphi_A(x)) = 0 & \text{in } \Omega \\ \varphi_A(x) = f(x) & \text{on } \partial\Omega, \end{cases}$$

where f is the imposed boundary potential. Furthermore, we denote with Λ_A the DtN (Dirichlet-to-Neumann) related to the anomaly A, that is the operator mapping the imposed boundary potential f to the measured current flux at the boundary, when the anomaly occupies the region A.

Let $T \subset \Omega$ an arbitrary region, hereafter called test domain, characterized by the nonlinear electrical conductivity σ_{NL}. The MP takes the form [9], [10]

$$T \subseteq A \Longrightarrow \bar{\Lambda}_T \leqslant \bar{\Lambda}_A, \qquad (1)$$

where $\bar{\Lambda}_A$ is the so-called *average* DtN, related to an anomaly in A. It is defined as

$$\bar{\Lambda}_A : f \mapsto \int_0^1 \Lambda_A(\alpha f)\, d\alpha$$

and $\bar{\Lambda}_T \leqslant \bar{\Lambda}_A$ is meant as $\langle \bar{\Lambda}_T(f), f \rangle \leq \langle \bar{\Lambda}_A(f), f \rangle \; \forall f$.

The Monotonicity Condition in (1) can be written equivalently as

$$\bar{\Lambda}_T \not\leqslant \bar{\Lambda}_A \Longrightarrow T \not\subseteq A \qquad (2)$$

Condition (2) is the basis of the reconstruction method. In fact, it allows to infer if T is well-included in A or not by boundary measurements. From this reasoning, introducing a certain set of test anomalies T_k, it is possible to obtain an estimate of the unknown anomaly as

$$\tilde{A} = \bigcup_k \{T_k \mid \bar{\Lambda}_{T_k} \leqslant \bar{\Lambda}_A\}.$$

Verifying in practice condition (2) poses serious problems. In order to do that, in fact, it is needed to find a boundary potential f such that $\langle \bar{\Lambda}_T(f), f \rangle > \langle \bar{\Lambda}_A(f), f \rangle$. While this task is trivial in the linear case, when $\bar{\Lambda} = \frac{1}{2}\Lambda$ and the problem can be addressed to the evaluation of eigenvalues, the same task is very challenging in the nonlinear case, since there are no such mathematical tools.

The more natural approach appears to be solving the nonlinear minimization problem

$$\min_f \langle \bar{\Lambda}_A(f) - \bar{\Lambda}_T(f), f \rangle.$$

If the minimum is negative, then $T A$. The main drawback is that, being the problem ill-posed, the number of the $i$iteration required is huge and so the number of measurements needed. In other words, the minimization is incompatible with real-time applications.

The method we propose allows to compute, before the measurements process, a set of boundary potentials to carry out the Monotonicity Test in (2). These special potentials are optimal in the sense that they are able to reveal if $T A$. The computation of these potentials, that arise from a set of linear problems, requires only the knowledge of the geometry of the domain and the conductivities involved. It follows that this approach is feasibile for real-time applications.

REFERENCES

[1] M. Cheney, D. Isaacson, and J. C. Newell, Electrical impedance tomography, SIAM Review,383 41 (1999), pp. 85–101.384

[2] D. Colton and A. Kirsch, A simple method for solving inverse scattering problems in the resonance region, Inverse Problems, 12 (1996), pp. 383-393.

[3] A. Kirsch, Characterization of the shape of a scattering obstacle using the spectral data of the far field operator, Inverse Problems, 14 (1998), pp. 1489-1512.

[4] M. Ikehata, (1999). How to draw a picture of an unknown inclusion from boundary measurements. Two mathematical inversion algorithms. Journal of Inverse and Ill-Posed Problems. 7. 255-271. 10.1515/jiip.1999.7.3.255.

[5] A. Tamburrino, G. Rubinacci, "A new non-iterative inversion method for Electrical Resistance Tomography", Inverse Problems, vol. 18, pp. 1809-29, December 2002.

[6] A. J. Devaney, Super-resolution processing of multi-static data using time-reversal and MUSIC, preprint in http://www.ece.neu.edu/faculty/devaney/ preprints/paper02n 00.pdf

[7] A. Tamburrino, G. Rubinacci, M. Soleimani, and W. R. B. Lionheart, Non iterative inversion method for electrical resistance, capacitance and inductance tomography for two phase materials, in Proc. 3rd World Congress on Industrial Process Tomography, Canada,813 2003

[8] A. Tamburrino and G. Rubinacci, Fast methods for quantitative eddy-current tomography of conductive materials, IEEE Transactions on Magnetics, 42 (2006), pp. 2017–2028

[9] Corbo Esposito, A., Faella, L., Piscitelli, G., Prakash, R., Tamburrino, A., Monotonicity Principle in tomography of nonlinear conducting materials (2021) Inverse Problems, 37 (4), art. no. 045012, DOI: 10.1088/1361-6420/abd29a

[10] Corbo Esposito, A., Faella, L., Piscitelli, G., Prakash, R., Tamburrino, A., Monotonicity Principle for the imaging of nonlinear piecewise homogeneous materials (2023), prepr

Intelligent Control for DFIG-Based Wind Farms: Neuro-Fuzzy Wavelet Approach to Power System Stability

Muhammad Abdul Basit[1], Rabiah Badar[2]
[1]Department of Electrical and Computer Engineering, COMSATS University Islamabad, Pakistan 44000.
Email: ab_basit007@hotmail.com
[2]Department of Electrical and Computer Engineering. International Islamic University Islamabad, Pakistan 44000
Email: rabiah.badar@iiu.edu.pk

Abstract

Significant interest in wind power generation has been sparked by the necessity of halting global warming and switching to renewable energy sources. Although wind energy is widely available and cost-effective, its intrinsic variability presents significant obstacles. Double Fed Induction Generators (DFIGs) have emerged as crucial components in efficiently using wind energy. This research tackles the problem of controlling variations in wind speed by incorporating different controllers into the inner voltage control loops of the Rotor Side Converter (RSC) and Static Series Synchronous Compensator (SSSC). This study investigates the utilization of Neuro-Fuzzy Wavelet Control (NFWC) to improve the stability and efficiency of DFIG-based wind power systems. The NFWC system has been developed to enhance voltage regulation in the RSC following a fault occurrence. The proposed methodology utilizes a gradient-descent optimization algorithm to integrate with power system control, enhancing stability effectively.

Index Terms

Neuro-Fuzzy, Wavelet Control, DFIG, Wind Power, Power System Stability, Voltage Regulation, FACTS Controllers, Renewable Energy.

I. Introduction

Concerns about global warming and the limited availability of fossil fuel reserves have caused an increasing focus on renewable energy sources, especially wind energy [1]. The field of wind power generation has witnessed enormous expansion, as evidenced by estimates that indicate a notable surge in global wind-generated electricity. Double Fed Induction Generators (DFIGs) have gained significant popularity as a preferred option for wind power generation owing to their cost-effectiveness and efficiency in capturing fluctuating wind speeds [2]. The effective performance of DFIG is significantly dependent on a resilient control system encompassing speed control, power control, and pitch angle control. This comprehensive control system maximizes energy capture and minimizes mechanical stress [3].

Integrating wind farms into power grids has stimulated research in power system stability, power quality, and accurate forecasting. The utilization of Flexible AC Transmission System (FACTS) controllers, specifically the Static Synchronous Compensator (STATCOM), has become crucial in addressing low-frequency oscillations in power networks that incorporate wind farms. The reactive power compensation capability of STATCOM contributes to improving power system stability, albeit at a comparatively more significant financial expenditure than alternative options [4].

The control algorithms utilized in power converters inside DFIG systems are of utmost importance in attaining optimal efficiency and reliable performance [5]. Although decoupled PI control is frequently used, the existence of uncertainties and the lack of an accurate system model can present difficulties in parameter tuning. Fuzzy logic and Artificial Neural Networks (ANNs) present alternate methodologies [6]; yet, due to their respective limitations, the emergence of NeuroFuzzy systems has been witnessed. The NeuroFuzzy approach integrates the learning capacity of ANNs with the decision-making skills of fuzzy logic, providing a robust methodology for tackling intricate nonlinear issues. Incorporating wavelet neural networks (WNN) enhances the localization capabilities of the NeuroFuzzy methodology [7].

This work proposes implementing a Neuro-Fuzzy Wavelet Controller (NFWC) to improve power systems' stability using DFIG-based wind farms. The purpose of the NFWC is to regulate the voltage of the Rotor Side Converter (RSC) during post-fault scenarios. A gradient-descent optimization approach is utilized to update the controller's parameters iteratively. This study aims to devise an algorithm that effectively enhances power system control by integrating multiple controllers into the inner voltage control loop of both the RSC and the SSSC.

II. Aerodynamics and drive train model

The wind turbine is a nonlinear complex system being the combination of three subsystems, i.e., electrical (generator), mechanical (drive train), and aerodynamics. Available aerodynamic power at the swept area (A) of rotor blades is given as:

$$P_{wind} = \frac{1}{2}\rho A v^3 \tag{1}$$

Where ρ is the air density, and v is the velocity of wind. Extracted power from available wind power is calculated as:

$$P_{extract} = \frac{P_{wind}}{\rho} C_P\left(\lambda, \beta\right);\ \lambda = \omega_r R / v \tag{2}$$

$$C_P = \frac{1}{2}\left(\frac{RC_f}{\lambda} - 0.022\beta - 2\right)e^{-0.225 RC_f / \lambda} \tag{3}$$

Where β is the pitch angle of blades, *R* is the length of blades, ω_r is the angular speed of the rotor, and $C_P(\lambda,\beta)$ is the power coefficient. It is a nonlinear function of pitch angle and tip speed ratio. C_f is the blade design constant-coefficient and λ is the blade tip ratio.

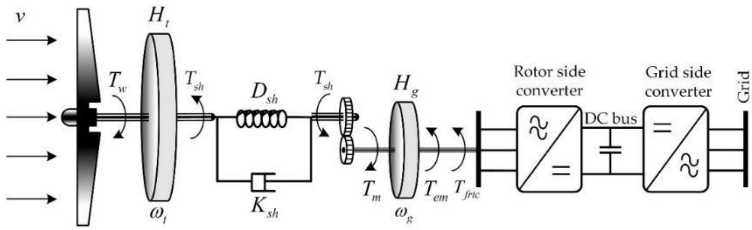

Fig 1. Wind turbine two-mass model.

The components of the drive train are a turbine, a gearbox, and a high/low-speed shaft. It acts like a conversion system which converts the low rotational speed of the turbine to a high rotational speed to drive the generator. Fig 1. shows the two-mass model used in this system, mathematically represented as follows [8]:

Change in angular speed ω_t of turbine is caused due to difference in aerodynamic torque T_w due to wind speed and shaft torque T_{sh}.

$$H_t \frac{d\omega_r}{dt} = T_w - T_{sh} \tag{4}$$

$$\frac{d\omega_t}{dt} = \frac{d^2\varphi_t}{dt^2} \tag{5}$$

The relationship between mechanical torque T_m and electromechanical T_{em} torque of a generator with losses due to friction T_{fric} is equal to the change in angular velocity.

$$H_g \frac{d\omega}{dt} = T_m - T_{em} - T_{fric} \tag{6}$$

$$\frac{d\omega_g}{dt} = \frac{d^2\varphi_g}{dt^2} \tag{7}$$

Gear ratio relates to mechanical torque and shaft torque.

$$T_m = \frac{T_{sh}}{n} \tag{8}$$

Where

$$T_{sh} = K_{sh}.\varphi + D_{sh}.\frac{d\varphi}{dt} \tag{9}$$

$$\frac{d\varphi}{dt} = d\varphi_t / dt - \frac{d\varphi_g / dt}{n} = \omega_t - \frac{\omega_g}{n} \tag{10}$$

Where, $T_m = 0.5\rho\pi R^2 C_P v^3 / \omega_t$ and $T_{em} = P_s / \omega_s$.

H_t and H_g is the inertia constant of the turbine and generator, respectively.

ω_t and ω_g are the wind turbine angle speed and generator rotor angle speed, respectively.

K_{sh} and D_{sh} is the shaft stiffness and damping coefficients, respectively.

P_s is the active power of the stator;

φ is the shaft twist angle.

III. NEUROFUZZY CONTROL ARCHITECTURE

In an adaptive network, multi-layered feedforward neural networks and TSK type inference systems are used along with an online adaptive algorithm. NeuroFuzzy structure is shown in Fig. 2. where *n* represents the inputs and *m* presents the rules. The network has *i* number of inputs, where $n = 1, 2, 3 \ldots i$. Output u_c and j number of rules where $m = 1, 2, 3 \ldots j$. The generalized kth rule from the figure can be expressed as:

$$R_k : IF\ x_1\ is\ \eta_{1k}\ AND\ x_2\ is\ \eta_{2k} \ldots AND\ x_i\ is\ \eta_{ik}\ THEN\ \zeta_k = y_k \tag{11}$$

There are seven layers in the NeuroFuzzy control. Layer 2 and layer 4 have adaptive nodes, whereas other nodes are fixed. A brief description of each layer is stated in [9]:

Layer 1: It is the input layer having *i* number of inputs.

Layer 2: This layer is called the fuzzification layer, where each numerical input is mapped using the respective membership function. Here, Gaussian membership functions are used for fuzzification and given as:

$$\eta_{nm} = e^{-0.5\left[\frac{(x_n - r_{nm})^2}{\xi_{nm}^2}\right]} \tag{12}$$

Where *r* and ξ are the mean and the variance of the membership function, respectively, that can adjust the shape of the membership function. The degree of membership can be anywhere between 0 and 1.

Layer 3: According to the firing strengths of inputs, fuzzy system rules are processed in this layer. Degree of fulfillment for each rule is calculated by using the T-norm operation.

$$\mu_m = \prod_{m=1}^{j} \eta_{nm} \tag{13}$$

Layer 4: It is the consequent part of the controller and is adaptive in nature. Wavelet neural networks having *i* inputs are used instead of polynomials. The type of the wavelet is a Mexican hat. Basically, Mexican hat is the second derivative of the Gaussian function. The gaussian derivative of the wavelet function does not have an associated scaling function. Mexican hat wavelet function is given as:

$$\psi_n = \left(p_{nm}\right)^{-\frac{1}{2}}\left(1 - z_{nm}^2\right)e^{-\frac{z_{nm}^2}{2}} \tag{14}$$

Where

$$z_{nm} = \frac{x_n - q_{nm}}{p_{nm}} \tag{15}$$

In the above Equation, p and q are the dilation and translation parameters of wavelet, respectively. The output of layer 4 is given below:

$$y_m = w_m \sum_{n=1}^{i} \psi_{nm} \tag{16}$$

Where w is the weighting factor.

Layer 5 and Layer 6: These two layers are defuzzification layers, where center of gravity method is used to translate fuzzy values again into crisp values.

Layer 7: This is the output layer having a single fixed node whose output is denoted by u_c.

$$u_c = \frac{\sum_{m=1}^{j} \mu_m y_m}{\sum_{m=1}^{j} \mu_m} \tag{17}$$

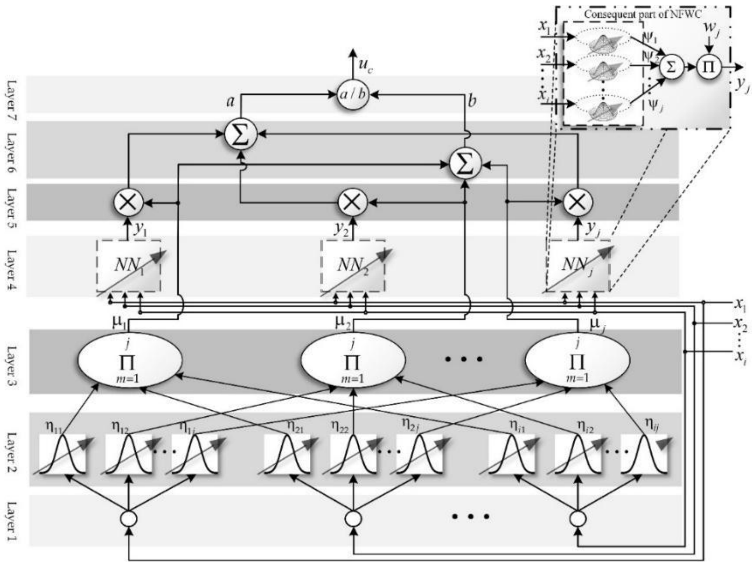

Fig. 2. Architecture of NeuroFuzzy Control

Adaptation mechanism:

NeuroFuzzy control is modeled in MATLAB/Simulink and simulated using the ode 23 solver. Evaluations of NeuroFuzzy control are simulated in a phasor-type power system. The phasor model is preferred for large power system simulation because it replaces large differential equations with simple algebraic equations and neglects the electromechanical transients, improving the simulation speed.

The back-propagation algorithm and the optimization technique are used to update the NeuroFuzzy network. It is the simplest algorithm to update network parameters.

The cost function used for updating the parameters of the controller is given as:

$$E = \frac{1}{2}\left[\left(\rho_{ref} - \rho\right)^2 + \square u_c^2\right] \tag{18}$$

Where, $e_{(k)} = \rho_{ref} - \rho$ and ρ_{ref} is the reference value and ρ is the output value of plant.

The optimization technique used in this paper is gradient descent. It is also known as the steepest decent method. Information is provided by gradient vector, that is why it is called the first-order method. The generalized update law is given below:

$$b_{nm(k+1)} = b_{nm(k)} - \alpha g_k \tag{19}$$

Where b_{nm} is the update parameters vector and is given as:

$$b_{nm} = \left[r_{nm}, \zeta_{nm}, w_m, p_{nm}, q_{nm}\right] \tag{20}$$

And g_k is the vector having derivatives of the controller parameters and given as:

$$g_k = \left[\frac{\partial E}{\partial r_{nm}}, \frac{\partial E}{\partial \zeta_{nm}}, \frac{\partial E}{\partial w_m}, \frac{\partial E}{\partial p_{nm}}, \frac{\partial E}{\partial q_{nm}}\right] \tag{21}$$

The generalized chain rule is given in Equation (22)

$$\frac{\partial E}{\partial \Phi_{nm}} = \frac{\partial E}{\partial \rho_m}\frac{\partial \rho_m}{\partial u_c}\frac{\partial u_c}{\partial \Phi_{nm}} + \frac{\partial E}{\partial u_c}\frac{\partial u_c}{\partial \Phi_{nm}} \tag{22}$$

Where, $\Phi_{nm} = \left[r_{nm}, \zeta_{nm}, w_m, p_{nm}, q_{nm}\right]$

$$\frac{\partial E}{\partial \Phi_{nm}} = \left[\frac{\partial E}{\partial \rho_m}\frac{\partial \rho_m}{\partial u_c} + \frac{\partial E}{\partial u_c}\right]\frac{\partial u_c}{\partial \Phi_{nm}} \tag{23}$$

A direct adaptive control scheme is used in this work. In the direct approach, the term $\partial \rho / \partial u_c$ called sensitivity measure is approximated to some constant [10].

Solutions of the derivative of Equation (23) are given below:

$$r_{nm(k+1)} = r_{nm(k)} - \tau\left(y_m - u_c\right)\left[\frac{\left[x_m - r_{nm}\right]}{\zeta_{nm}^2}\right] \tag{24}$$

$$\zeta_{nm(k+1)} = \zeta_{nm(k)} - \tau\left(y_m - u_c\right)\left(\frac{\left(x_n - r_{nm}\right)^2}{\left(\zeta_{nm}\right)^3}\right) \tag{25}$$

$$w_{m(k+1)} = w_{m(k)} - \tau\Psi_m \tag{26}$$

$$p_{nm(k+1)} = p_{nm(k)} - \tau\, w_m \frac{\left[-3.5z_{nm}^2 + z_{nm}^4 - 0.5\right] e^{-\frac{z_{nm}^2}{2}}}{\sqrt{p_{nm}^3}} \tag{27}$$

$$q_{nm(k+1)} = q_{nm(k)} - \tau\, w_m \frac{\left(3z_{nm} - z_{nm}^3\right)}{|\, p_{nm}|^{\frac{3}{2}}} e^{-\frac{z_{nm}^2}{2}} \tag{28}$$

Where3

$$\tau = \alpha\left(-e_{(k)} + \square u_c\right)\left(\frac{\mu_m}{\sum_{m=1}^{j}\mu_m}\right) \tag{29}$$

IV. SIMULATION MODEL

A wind farm with six turbines and a capacity of 9 MW at 575 V that operates at an 8 m/s wind speed is employed in this work. The diagram presented in Fig. 3 illustrates a single-line diagram of the system. The wind farm is interconnected with a 25 kV distribution feeder, which ultimately transfers power to a 120 kV grid that is an infinite bus. This transfer of power occurs via a transmission line that spans a distance of 30 kilometers. Each wind turbine is connected to a capacitor bank with a 400 kVAR rating. A 3 MVA SSSC is installed in the power system, connected explicitly between bus B2 and B3. The behavior of the system is examined across five different configurations. At the outset, the system lacks any auxiliary control connection. Subsequently, a post-fault study is conducted following the integration of the SSSC with NeuroFuzzy control within the system. Following this, the real control PI of the voltage loop in the RSC system is substituted by NeuroFuzzy control. The resulting results are contrasted and discussed in relation to various configurations.

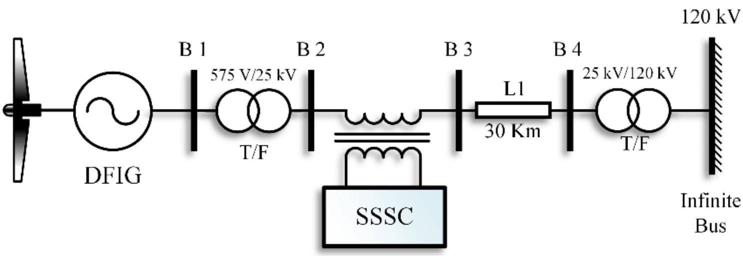

Fig. 3: Wind power system with SSSC

The validation of all damping techniques is conducted on a wind power system in the occurrence of a significant fault. A three-phase fault occurs at t=16 seconds and is automatically cleared after 0.5 seconds. The active and reactive powers of the DFIG are depicted in Fig. 4. It has been found that during the occurrence of a fault, the active power remains at a value of zero. Significant oscillations are produced as a result of abrupt situations. Comparing PI control to all other traditional and non-traditional controllers, it can be shown that it lags. The PI control system exhibits an overshoot, as seen by a spike in power reaching 27 MW, followed by sustained oscillations over an extended period. Incorporating NeuroFuzzy control in the SSSC has resulted in a considerable reduction in power overshoot. The regulation of the NFWC in the SSSC has an enhanced impact in mitigating overshoot spikes. The magnified results in the picture illustrate the effects of TSK and NFWC when used in a DFIG system. The power overshoot observed in the case of NFWC exhibits a slight improvement compared to TSK. However, it notably contributes to the substantial mitigation of oscillations.

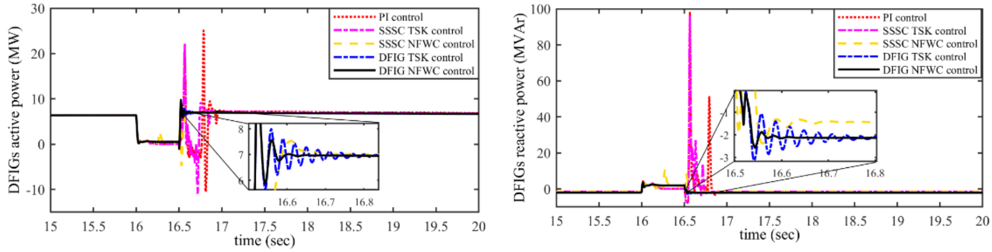

(a) (b)

Fig. 4: (a) Active power; (b) Reactive powers of wind turbine

The current and voltages of the wind turbine in *p.u.* are measured at Bus B1 and shown in Fig. 5. The figure shows that turbine voltage goes down to zero during fault time and oscillates after fault clearance. Almost the same response is observed in a power system equipped with TSK in SSSC and NFWC in SSSC. In contrast, TSK and NFWC in DFIG perform effective damping action and stabilize the voltage. The percentage of overshoot (POT) and improvement index μ is calculated from voltage. Results of POT and μ, given in Table I, show drastic improvement when NeuroFuzzy control works in DFIG, but marginal improvement is observed between TSK and NFWC in DFIG.

Moreover, it is seen that NFWC suppresses the voltage overshoot 42% w.r.t. PI control, and its overshoot value from its steady-state value is just 3%. Likewise, the post-fault behavior of the current has large oscillations. Moreover, different control schemes show the same trend in stabilizing the system as in the case of voltage-damping

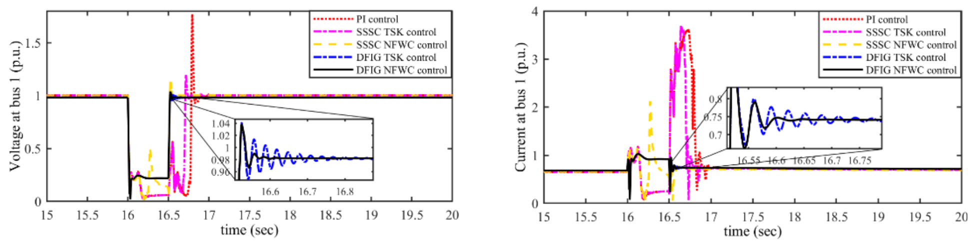

(a) (b)

Fig. 5: (a) Voltage at bus B1; (b) Current at bus B1.

The formula used to calculate POT is given below;

$$POT = \frac{y_{\max} - y_{ss}}{y_{ss}} \tag{30}$$

Table I: Performance w.r.t. PI control

Sr. #	Control scheme	Settling time (%)	POT (%)	Improvement index μ (%)
1	TSK in SSSC	0.81	73.38	56.5
2	NFWC in SSSC	3.25	78.311	60.3
3	TSK in DFIG	1.85	92.05	73
4	NFWC in DFIG	4.04	92.3143	73.2

V. Conclusion

This paper proposes a Neuro-Fuzzy Wavelet Controller (NFWC) to enhance power system stability in DFIG-based wind farms. The NFWC regulates Rotor Side Converter (RSC) voltage post-fault, utilizing gradient-descent optimization for parameter tuning. This research advances power system control by integrating multiple controllers within the inner voltage control loop of both the RSC and the SSSC.

In conclusion, this study contributes to the ongoing efforts to make wind energy a reliable and sustainable component of the global energy landscape. Adopting advanced control systems, like the NFWC, represents a significant step towards harnessing the full potential of wind power while ensuring the stability and efficiency of power systems in a renewable energy-driven future.

References

[20] M. A. Basit, S. Dilshad, R. Badar, and S. M. Sami ur Rehman, “Limitations, challenges, and solution approaches in grid-connected renewable energy systems,” *Int J Energy Res*, vol. 44, no. 6, pp. 4132–4162, May 2020, doi: 10.1002/ER.5033.

[21] R. Hemmati, H. Faraji, and N. Y. Beigvand, “Multi objective control scheme on DFIG wind turbine integrated with energy storage system and FACTS devices: Steady-state and transient operation improvement,” *International Journal of Electrical Power & Energy Systems*, vol. 135, p. 107519, Feb. 2022, doi: 10.1016/J.IJEPES.2021.107519.

[22] P. ; Singh *et al.*, “Performance Evaluation of Grid-Connected DFIG-Based WECS with Battery Energy Storage System under Wind Alterations Using FOPID Controller for RSC,” *Mathematics 2023, Vol. 11, Page 2100*, vol. 11, no. 9, p. 2100, Apr. 2023, doi: 10.3390/MATH11092100.

[23] A. Mahdy, H. M. Hasanien, W. Helmy, R. A. Turky, and S. H. E. Abdel Aleem, “Transient stability improvement of wave energy conversion systems connected to power grid using anti-windup-coot optimization strategy,” *Energy*, vol. 245, Apr. 2022, doi: 10.1016/J.ENERGY.2022.123321.

[24] S. Gupta and A. Shukla, “Improved dynamic modelling of DFIG driven wind turbine with algorithm for optimal sharing of reactive power between converters,” *Sustainable Energy Technologies and Assessments*, vol. 51, p. 101961, Jun. 2022, doi: 10.1016/J.SETA.2022.101961.

[25] R. Tabbussum and A. Q. Dar, “Performance evaluation of artificial intelligence paradigms—artificial neural networks, fuzzy logic, and adaptive neuro-fuzzy inference system for flood prediction,” *Environmental Science and Pollution Research*, vol. 28, no. 20, pp. 25265–25282, May 2021, doi: 10.1007/S11356-021-12410-

1/METRICS.
[26] R. K. Singh and N. K. Singh, “Power system transient stability improvement with FACTS controllers using SSSC-based controller,” *Sustainable Energy Technologies and Assessments*, vol. 53, p. 102664, Oct. 2022, doi: 10.1016/J.SETA.2022.102664.
[27] L. Arturo Soriano, W. Yu, and J. D. J. Rubio, “Modeling and control of wind turbine,” *Math Probl Eng*, vol. 2013, 2013, doi: 10.1155/2013/982597.
[28] J. Shair, M. A. Basit, and R. Badar, “Damping low frequency oscillations in an HVDC system using Neuro-Fuzzy SMC,” *Proceedings - 2018, IEEE 1st International Conference on Power, Energy and Smart Grid, ICPESG 2018*, pp. 1–6, Jun. 2018, doi: 10.1109/ICPESG.2018.8384502.
[29] R. Badar and L. Khan, “Online adaptive Legendre wavelet embedded neurofuzzy damping control algorithm,” *2013 16th International Multi Topic Conference, INMIC 2013*, pp. 7–12, 2013, doi: 10.1109/INMIC.2013.6731316.

Smart Protection Scheme for existing Distribution System

Muhammad Azeem[1], Muhammad Bilal Arif[2]

[1]Signatics Private limited, E11, Islamabad, Pakistan.

Email: azeem.muhammad79@email.com,

[2]Department of Engineering and Environment,
Northumbria University, Newcastle, UK

Email: muhammadbilalarif7@gmail.com,

Abstract

A smart protection scheme is proposed for the existing distribution system using multiple current and voltage sensors. Using the proposed scheme, the location of fault and its nature can be identified. After identification and localization, the faulty system is isolated from the healthy system and a backup path is provided if needed. Values from current sensors are observed continuously and based on their values decisions are made. By the results returned from the sensors in case of fault, the nature and location of fault is also identified. Alarm is generated and tripping is done in case of fault using the predefined values of currents. In case of fault circuit breaker is tripped for short period of time turned ON to check whether the fault is temporary or permanent after regular intervals. Some loads are highly sensitive like hospitals and defence departments etc. in this after one tripping the load is directly shifted to the backup path. In case of permanent fault load is disconnected from the original path and shifted to a backup path till the maintenance of the faulted section. After the successful elimination of fault load is again shifted to its original path. Continuous data acquisition is done with time along with the values of currents and conditions of breakers. A distribution model is designed to implement the proposed method. Satisfactory results were obtained.

Index Terms

Protection Scheme, fault identification, fault localisation, fault isolation.

I. Introduction

We are living in an age where a continuous supply of electric power is a necessity of life. We face interruption in electric power supply daily, due to faults in the supply system. Mostly, faults occur in the distribution system, due to which some of the connected areas have to face power outages for a long time. These faults are the cause of the failure of the distribution grid. Conventional methods for the protection of the distribution system don't involve the localisation and identification of faults. The existing protection scheme of a distribution network in Pakistan and other underdeveloped countries is a conventional and old system. This system comprises CT, PT and a circuit breaker at the distribution grid. The circuit breaker for every feeder is dedicated and separate from the other feeders. These methods only isolate the faults but do not identify and locate them. Identification and location is done by inspection method or on the complaint of the locality affected by the fault. This identification, location and elimination requires several hours, and the customer has to face power outages. These power outages cause huge losses to the small and cottage industry, which in turn affects the economy of the country.

This project is about the smart protection of the distribution system. The main idea of the project is to design a smart protection scheme for the existing distribution system that would not only reduce the time of power outages but can also provide power from a backup path in case of a fault. The aim of the project was to convert the manual system of protection to a digital system for better monitoring and protection and to compete with the world through advancements in technology.

- The objectives of the research were:
- Integration of voltage and current sensors with a distribution network.
- Fault identification.
- Fault Isolation.
- Fault localisation.
- Self-Healing
- Load prioritisation

The designed model consists of three different loads, i.e., industrial, commercial and residential. Every load has its control unit consisting of Arduino Mega 2560, all three control units are integrated. To monitor their current, a current sensor, ACS712, was used and for measurement of voltages, a three-phase voltmeter compatible with Arduino is designed. Relays are used to break and make the connections. Real-time values from current and voltage sensors are monitored and stored using PLX-DAC software to monitor the whole system.

II. RELATED WORK

A. Failure Prediction and Prevention

Vaiman et al. [1] proposed an automated method to get the real-time data of a transmission system using PMU, ROSE and SCADA to monitor and increase the stability by calculating the boundary values of voltages and thermal limits for steady-state stability. Data from PMU is gathered using SCADA and analysed by ROSE. ROSE defines the region of stability of operation and control. Chertkov et al. [2] proposed an algorithm for static load distribution networks to identify and predict the most probable modes of failure and their weak points.

Using the proposed algorithm, an error surface was developed that separates the region where no load shedding is required from the region in which some load shedding is unavoidable.

B. Failure Identification and Location

Calderaro et al.[3] proposed a method for failure identification and localisation based on the Petri net model. A PN model is constructed using the acquired data, and the system is analysed. Error is detected in the data transmitted, i.e. false signals, if no error is detected, then the location of the fault is detected by applying different matrix operations on the matrix obtained from the PN model. Mladen Kezunovic [4] proposed a method for fault location using IEDs. These sensors installed send the voltage and current values to EMS every two seconds. Initial simulated waveforms are compared for fault localisation with new waveforms gathered using IEDs. Kongming Sun [5] proposed a method to select the faulty line automatically. It can be divided into the faulted line section location method for medium-voltage distribution feeders and the faulted area identification technique for low-voltage distribution systems. In the first part, an adjacency list that shows the adjacency relationship and status of fault-indicating devices (FIDs) is developed. Then an iterative search technique is devised to traverse the adjacency list to determine the faulted line section. The second part develops a relational table showing the association relationship between smart meters, meter boxes and distribution transformers. The faulted area can be located based on the table and the voltage of smart meters received from the customer electric information acquisition system (CEIAS).

C. Self-Healing

Mohamed Eid Aljahani [6] proposed a method for Surveillance of the distribution system of the smart grid using PSCAD software. He proposed that after locating the fault in the faulty area, power is supplied using an alternative path.

III. METHODOLOGY

A. Fault Identification

The fault is identified based on the current behaviour. A three-phase fault current in all three phases will be equal and exceed the nominal value. In the case of line-to-line fault, the current value in the two phases, which are physically held together, exceeds the nominal limit, and some of the current flow through the load. In the case of a double line-to-ground fault, the current value in the two phases physically held together exceeds the nominal limit, but in this case, the load current is equal to zero, i.e., no current flows through the load. In the case of a single line fault, the value of the current in the phase in which the fault occurs exceeds the nominal value and the load current is equal to zero. In case of an overloading fault, the value of the load current will increase from the nominal value. In the case of under voltage fault, the magnitude of the voltage will be less than the nominal voltage; in the case of overvoltage, the magnitude will be greater than the nominal voltage.

B. Fault Location

When the fault occurs, the value of the sensor returned to the microcontroller is not equal to the magnitude of the nominal value. Depending on the fault, the value may be smaller or greater than the nominal value. After getting the faulted value from the sensor, the sensor is identified to locate the position of the fault. For example, a single-phase short circuit fault occurs in the middle of the distribution feeder. At the point at which the fault occurs, the current sensor before the fault will have a greater value than the nominal current value and the sensor after the fault will have a current value of zero. The region between these two sensors is the faulty region. Based on the location of the sensors, the location of the fault is identified.

C. Fault Isolation

Once the fault is identified and located, it has to be isolated or separated from the rest of the network for its proper working. The faulty section is isolated by tripping the circuit breakers through the microcontroller. Two breakers operate for the isolation of fault. One breaker is before the fault point from the distribution side to stop the flow of power from the grid. The second is the one after the fault point to separate it from the load side so no power flows from this side due to the interconnected system. In case of a short circuit fault, the faulty section is separated from the system without any delay, so the fault cannot harm the rest of the network. In case of an overloading fault, an auto-recloser tries three times to reconnect to the network as if the fault is temporary. But if the fault is permanent, it is separated from the system after the third try of auto-recloser. The flow chart of the proposed methodology is shown in Fig.1

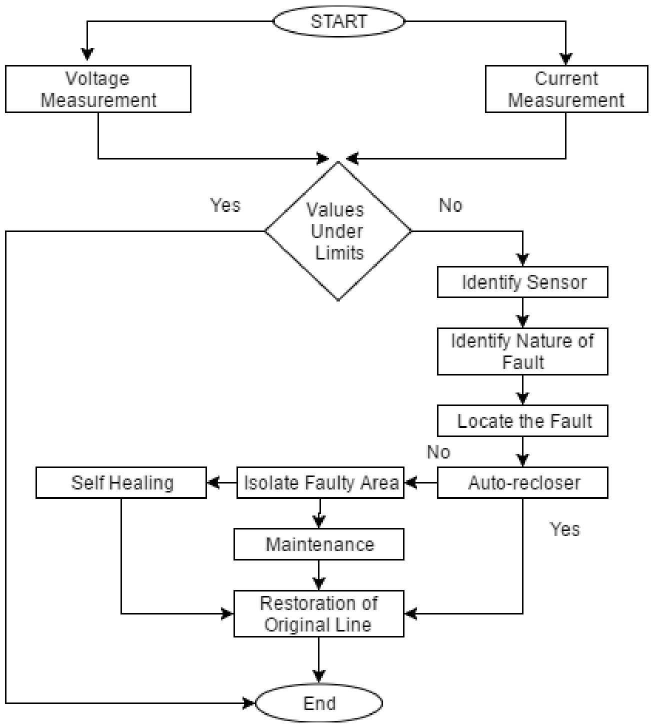

Fig. 1. Flowchart of the proposed methodology

IV. DESIGNED MODEL

Designed model of a distribution system consists of mainly three loads i.e. industrial, commercial and residential. Each load is supplied by a dedicated feeder. All the system is interconnected. Three Arduino Mega 2560 are used for the control of three loads. For measurement of current ACS712 current sensor is used and for the measurement of system voltages a three-phase voltmeter is designed compatible with Arduino. All three Arduinos are interconnected with each other. To simulate the behavior of circuit breakers, relays are used to make and break the circuit.

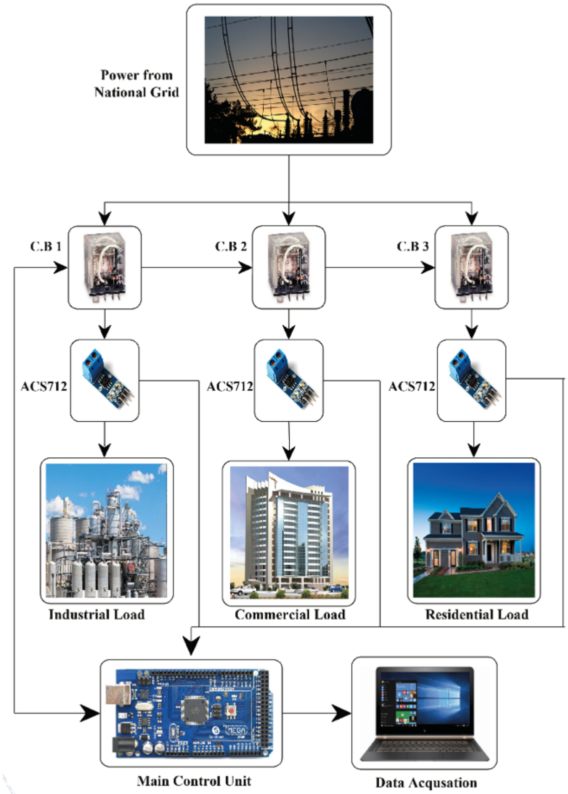

Fig. 2. Block diagram of complete system

V. WORKING

A. Short Circuit Fault

In case of short circuit fault at any point in the system between the load and distribution grid, the current sensor placed before the location of fault indicate the sudden increase the magnitude of the current. And the current sensor after the location of fault will indicate the magnitude of current not equal to the magnitude of current entering the system or the magnitude of current will be zero. On the basis of behavior of current, the nature fault is identified. After the identification of fault, the faulty area is isolated from the healthy area by operation of relays placed before and after the indicated sensors. Now on the basis of location of current sensors location of fault is identified. After the isolation of faulty area, the power to the load is supplied from an alternate path available in the interconnected network. After the maintenance of faulty area, original path of the system is restored.

In case of short circuit fault at load side, the load will be disconnected permanently from the system. And a message is generated for the user indicating the occurrence of fault. The power of the load is restored after the elimination of fault from the load by the user.

B. Overloading Fault

In case of overloading fault, the sensor connected before the connected load will indicate an increased magnitude of current from its nominal value. Relay of the faulty load operates and disconnects the load from the system. After a short interval of time relay operates and try to reconnect the load to the system. The control unit will try for three times after equal intervals to reconnect the load to the system. If the fault is temporary the load is connected to the system. But in case of permanent fault the load is disconnected form the system permanently. And a message is generated for the user indicating the occurrence of fault. The power of the load is restored after the elimination of fault from the load by the user.

C. Under Voltage Fault

In case of under voltage fault, the designed voltmeter will indicate a decrease in the magnitude of voltage at sending end. If the voltages are less than 3% of the nominal voltages, alarm is generated indicating premature under voltage fault. If the voltages are less than 5% of the nominal voltage, main relay will operate and disconnect the system from power supply. As soon as the voltages regain their nominal value, the system is connected to the power supply automatically.

D. Over Voltage Fault

In case of over voltage fault, the designed voltmeter will indicate an increase in the magnitude of voltage at sending end. If the voltages are greater than 3% of the nominal voltages, alarm is generated indicating premature over voltage fault. If the voltages are greater than 5% of the nominal voltage, main relay will operate and disconnect the system from power supply. As soon as the voltages regain their nominal value, the system is connected to the power supply automatically.

VI. FUTURE WORK

Following are the recommendation for the future work and improvement of this project for implementation for a larger network.

- Transmission system.
- Micro Grids and DG's
- Real-time monitoring

- Electrical theft control
- Prediction of power demand

A. Transmission System

The proposed scheme can be implemented on transmission system for its protection.

B. Micro Grids and DG's

Feature of micro grids can be added to proposed scheme. By addition of micro grids, in case of fault or complete blackout power to the system can be supplied from the micro grids and DG's. This will reduce the load on the feeder used as an alternative path for backup supply.

C. Real-time Monitoring

Using the real-time data from the sensors, power flows in the system can be monitored. The proper working of the system can be insured by comparing the real-time power flows to the nominal power flows.

D. Electrical Theft

Using the real-time data electrical theft can be controlled by monitoring and identifying the extra power flow in the system which is not allocated and consumed by registered users.

E. Prediction of Power Demand

Using the data gathered from real-time monitoring future power demand can be predicted, to take necessary measure to meet the future demand. Data can be used for scheduling and coordination of different generating stations.

VII. CONCLUSION

A working hardware of smart protection scheme for existing distribution system was successfully designed using microcontrollers. All the objectives of the project were achieved with an additional feature of live data acquisition. Fault was identified, located and isolated from the healthy system successfully within 5 to 8 seconds after the occurrence of fault. A backup path was also provided successfully to keep the consumer provided with power supply 24/7 with a minimal interruption due to the occurrence of fault. All types of faults were simulated and successfully tested on the designed hardware. With the help of live data acquisition 24/7 monitoring of the load is also done.

REFERENCES

[1] M. Vaiman, M. Vaiman, S. Maslennikov, E. Litvinov, and X. Luo, "Calculation and Visualization of Power System Stability Margin Based on PMU Measurements," in 2010 First IEEE International Conference on Smart Grid Communications, 2010, pp. 31–36.

[2] M. Chertkov, F. Pan, and M. G. Stepanov, "Predicting failures in power grids: The case of static overloads," IEEE Trans. Smart Grid, vol. 2, no. 1, pp. 150–160, 2011.

[3] V. Calderaro, C. N. Hadjicostis, A. Piccolo, and P. Siano, "Failure Identification in Smart Grids Based on Petri

Net Modeling," IEEE Trans. Ind. Electron., vol. 58, no. 10, pp. 4613–4623, Oct. 2011.

[4] M. Kezunovic, "Smart Fault Location for Smart Grids," IEEE Trans. Smart Grid, vol. 2, no. 1, pp. 11–22, Mar. 2011.

[5] K. Sun, Q. Chen, and Z. Gao, "An Automatic Faulted Line Section Location Method for Electric Power Distribution Systems Based on Multisource Information," IEEE Trans. Power Deliv., vol. 31, no. 4, pp. 1542–1551, Aug. 2016.

[6] [M. Aljahani, "An Enhanced Self-Healing Protection System in Smart Grid: Using Advanced and Intelligent Devices and Applying Hierarchical Routing in Sensor Network Technique," 2014.

Electromagnetic Analysis of Single Phase Transformer with Steel and Ferrite Core Material

Muhammad Ramiz Zakir, Neelam Qadeer, Salman Ali, Fabrizio Marignetti
Dept. of Electrical Engineering, University of Cassino and Southern Lazio, Cassino, Italy,
Email:
ramizzakir1@gmail.com
Neelam.qadeer@unicas.it

Abstract

Single phase transformers have great importance in daily life due to its wide range of usage in almost every sector. Two transformer design objectives are ameliorating the performance of transformer and mitigating overall cost. Using suitable materials for loss reduction can help to improve transformer efficiency. Materials with good magnetic properties can significantly enhance the performance of the transformer. This paper compares the performance analysis of single phase transformer with steel core material and ferrite core material. This analysis is made for step down 6600/440V and step up 440/6600V transformers at no load with 50Hz frequency. The single phase transformer is designed in solid-work and 3-D finite element analysis (FEA) is done in JMAG. This electromagnetic analysis helps to optimize the design of the transformer by implementing different techniques. In this paper, analysis is made for step down and step up transformer voltages, flux linkages, magnetic field strength, magnetic flux distribution, core losses and hysteresis losses. FEA shows that ferrite core has good magnetic properties and less losses as compared to steel core. In step up transformer operation, ferrite core shows magnetic saturation which exhibits fractionally more losses as compared to normal core operation.

Index Terms

Single phase transformer, Steel core; Ferrite core, 3-D Finite element analysis (FEA), Electromagnetic analysis, Transformer, Core Materials

I. Introduction

Single and three phase transformers have great importance in daily life. These transformers are being used every single day to provide us desired power supply. Traditional three phase distribution transformers use delta star configuration that creates harmonics in primary delta side. Ultimately it introduces the losses and mitigate the performance of transformer. By adopting star- star configuration, this harmonics power recovery can be retrieved [1].

Ferrite core transformers are a popular type of electrical transformers that employ ferrite cores. These cores are composed of a mixture of iron and other metal oxides. They possess exceptional magnetic properties and offer efficient performance, making them widely utilized in various electronic devices and power systems. The high permeability and low electrical conductivity of ferrite cores make them ideal for applications that require effective magnetic

coupling while minimizing energy losses. The core material consists of small magnetic domains that easily align with an applied magnetic field, allowing ferrite core transformers to efficiently transfer electrical energy between different circuits.
One notable advantage of ferrite core transformers is their capability to operate at high frequencies. Unlike traditional transformers that employ laminated iron cores, ferrite cores exhibit lower eddy current losses and reduced core losses. Consequently, they can handle higher frequencies without significant energy dissipation. This characteristic renders ferrite core transformers suitable for use in switch-mode power supplies, telecommunications equipment, computer peripherals, and other electronic devices operating at high frequencies.
In paper [2] authors designed a transformer with combination of high voltage 5kV, high frequency 5kHz with small size, cheap and least losses for high frequencies. It has high resistivity, high magnetic permeability, low eddy current loss and high frequency.
In paper [3] authors utilize Solid-works software to perform electromagnetic analysis, specifically using the Electro Magnetics Simulation (EMS) module. The analysis considers normal working conditions and a frequency of 50Hz. Various parameters, including current density, field intensity, and loss density, are examined. The simulation results demonstrate a close correspondence with the theoretical values. This analysis enables the achievement of an optimized transformer design.
In paper [4]-[5] authors aim to design and optimize a nanocrystalline core transformer capable of efficiently handling high power densities and operating at high frequencies. It focuses on the necessity of transformers that can handle high power and operate at high frequencies, specifically in resonant converters. These converters have become increasingly important in various power electronic applications, such as renewable energy systems and electric vehicles. It highlights the limitations of existing estimation methods and emphasizes the necessity for a new approach. The proposed evaluation method offers a promising solution by providing a more accurate and practical way to determine transformer volume, leading to potential improvements in design optimization and efficiency.
In paper [6]-[7] author aims to enhance the characteristics of Mn-Zn ferrites in order to improve the performance of transformer cores in forward mode switching power supplies. The authors undertake experiments and analysis to examine the magnetic properties, permeability, core loss, and other relevant parameters of the developed ferrites. It underscores the necessity for materials that can offer high permeability and low core loss to optimize the efficiency and reliability of these power supplies.

This paper investigates the performance analysis of single phase transformer with step up and step down voltage using ferrite core and steel core. This 3-D Finite element analysis (FEA) includes the magnetic field strength, magnetic flux distribution, step up and step down voltages graph, flux linkages of coils, core losses and hysteresis losses in single phase transformer. The transformer is designed in solidwork and FEA analysis is made in JMAG. This paper has following sections. The transformer design is explained in section II. Section III describes the Simulations results obtained from finite element analysis. Section IV concludes the conclusion.

VIII. DESIGN OF SINGLE PHASE TRANSFORMER

Single phase transformer design rating is 440/6600V for step up transformer and 6600/440 V for step down transformer. The performance analysis is made for both step up and step down transformer using steel core and ferrite core. Transformer core parameters are shown in table 1[3]. Coil specifications for step up and step down transformers are mentioned in table 2 and table 3 respectively. Table 2 is providing information for step down transformer. Number of turns for primary coils are 1790 and number of turns for secondary coils are 120. Voltage excitation for step down transformer is 440V on primary winding. Table 3 is providing information for step up transformer. Number of turns for primary coils are 120 and number of turns for secondary coils are 1790. Voltage excitation for step up transformer is 6600V on primary winding.

D. Modeling of transformer

Performance analysis is made for steel core 35JN201 and ferrite core material while copper material is selected for coils. Limb of transformer core is made rectangular and the coils space from core is 1mm. Primary and secondary windings are made rectangular as the limb of core. Transformer width and height are equals is dimension. Core dimensions are mentioned in Fig 1(a).

Transformer parts, core and coils are made using solidwork software and model is finalized after assembling each part in sloid work. Then model is imported to JMAG to analyze the performance of transformer using steel and ferrite core material. Performance analysis is done using 3D finite element analysis (FEA) with the help of JMAG. Induced EMF in Primary and secondary winding is following,

$$E1 = 4.44 f N_1 \varphi_m = 4.44 f N_1 B_m A \quad primary\ winding \tag{1}$$

$$E2 = 4.44 f N_2 \varphi_m = 4.44 f N_2 B_m A \quad secondary\ winding \tag{2}$$

Where $E1$ and $E2$ are denoting induced EMF in primary and secondary winding, N_1 and N_2 shows number of turns for primary and secondary winding, φ_m shows maximum flux in core, B_m denotes maximum flux density, f is frequency and A is area. Hysteresis loss is due to magnetization and demagnetization of transformer core is following

$$W_h = \eta B_{max}^{1.6} f V \tag{3}$$

Where W_h is denoting hysteresis loss, B_{max} shows maximum magnetic flux, η shows hysteresis coefficient, f shows frequency and V is denoting the volume of core.

TABLE 1: Design Parameters of Single Phase Transformer

Items	**Value**
Transformer Cores	Steel 35JN210 and Ferrite Mn-Zn PC90
Limb of core	Rectangular
Height of transformer (H)	560mm
Width of transformer (W)	560mm
Core upper and lower height (H_Y)	142.74mm
Core inner space width (W_W)	242.5mm
Core inner space height (H_W)	274.2mm
Core depth	100mm
Coil width	25mm
Coil height	272mm
Coil total length	152mm
Coil inner space from core	1mm

TABLE 2: Coil Specifications in step down Transformer

Items	Value
Primary coil turns	1790
Secondary coil turns	120
Frequency	50Hz
Primary coil excitation	6600v

TABLE 3: Coil Specifications in step up Transformer

Items	Value
Primary coil turns	120
Secondary coil turns	1790
Frequency	50Hz
Primary coil excitation	440v

Fig. 1(b) shows the single phase transformer that is designed in solid-work. Core upper and lower yoke and two limbs have same dimensions so total volume is 4. Overall volume is 8 because primary and secondary windings are also distributed on core limbs. Air medium is kept between the core and primary winding, and between the core and secondary winding.

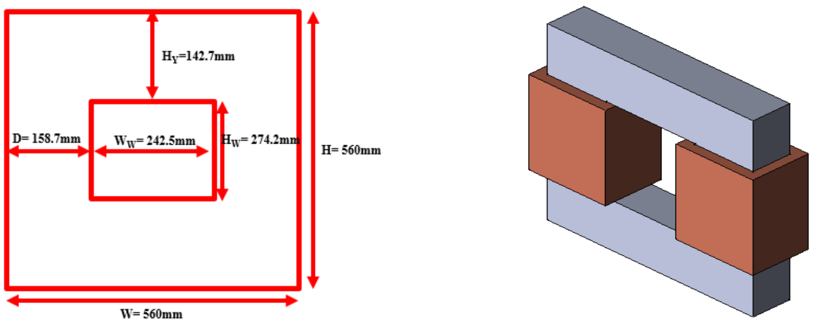

(a) (b)

Fig. 1: (a) Core dimensions for Transformer, (b) Design of Single Phase Transformer

Simulation is performed using solid-work that includes core and coils of transformer then model is imported to the JMAG software while materials are assigned to the each part using JMAG software. In order to evaluate the performance of transformer separately, two types of materials steel core and ferrite core materials are used separately. First transformer analysis is performed using steel core with step up and step down voltage. Second transformer analysis is performed using ferrite core with step up and step down voltage. These all analysis are no load analysis.

Fig. 2 shows the meshed design of single phase transformer. Meshed is performed in JMAG in order to get precise results. By parts mesh is applied on each part of the transformer keeping the constant size element of 10mm.

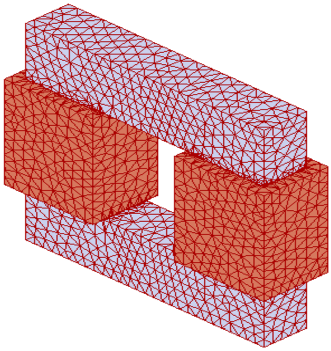

Fig. 2: Meshed design of Single Phase Transformer

IX. 3-D FEA ANALYSIS

Transformer performance is analyzed using 3-D finite element method with the help of JMAG software to obtain precise results. The comparative analysis is made between single phase transformer with steel core material and single phase transformer for ferrite core material. Both analysis are performed for step up and step down transformer at no load. This simulation is made for 6600/440V and 440/6600V transformer. This analysis of transformer is made at 50Hz frequency.

Fig. 3(a) shows the flux linkage for primary and secondary coils for step down transformer that is using steel core. Primary coil flux linkage is 41.03Wb while secondary coil flux linkage is 2.63Wb. Fig. 3(b) shows the secondary side desired voltage 440V. This voltage is stepped down from 6600V to 440V.

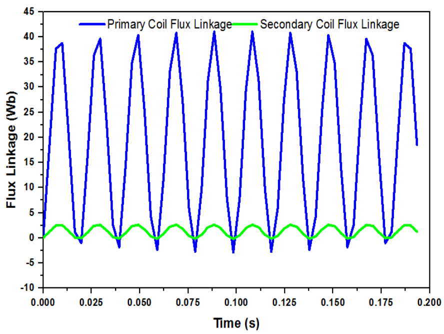

(a)

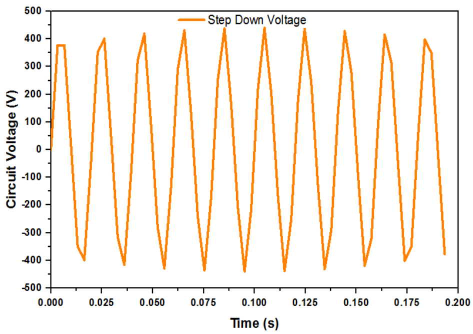

(b)

Fig. 3: (a) Flux linkage for step down transformer using steel core, (b) Step down voltage for single phase transformer using steel core

Fig. 4(a) shows the flux linkage for primary and secondary coils for step down transformer using ferrite core. Primary coil flux linkage is 38.3Wb while secondary coil flux linkage is 1.02Wb. Fig. 4(b) shows the secondary side desired voltage 440V. This voltage is stepped down from 6600V to 440V.

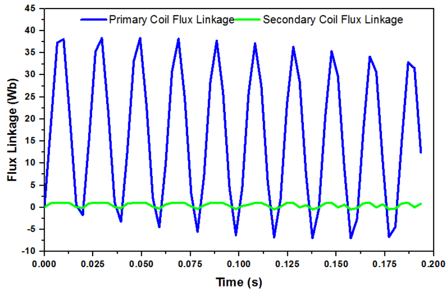

(a)

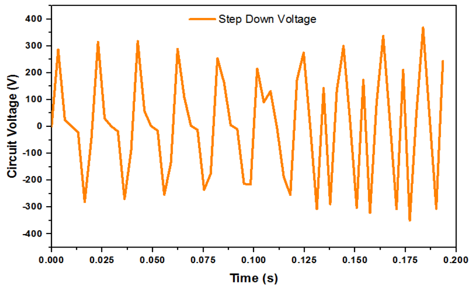

(b)

Fig. 4: (a) Flux linkage for step down transformer using ferrite core, (b) Step down voltage for single phase transformer using ferrite core

Fig. 5(a) shows the flux linkage for primary and secondary coils for step up transformer that is using steel core. Primary coil flux linkage is 2.59Wb while secondary coil flux linkage is 37.6Wb. Fig. 5(b) shows the secondary side desired voltage 6600V. This voltage is stepped up from 440V to 6600V.

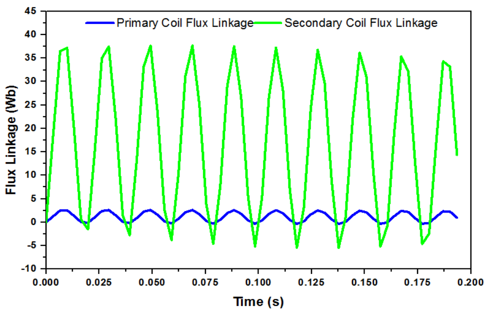

(a)

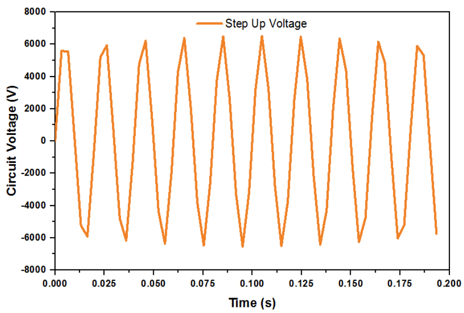

(b)

Fig. 5: (a) Flux linkage for step up transformer using steel core, (b) Step up voltage for single phase transformer using steel core

Fig. 6(a) shows the flux linkage for primary and secondary coils for step up transformer that is using ferrite core. Primary coil flux linkage is 1.33Wb while secondary coil flux linkage is 14.15Wb. Fig. 6(b) shows the secondary side desired voltage 6600V. This voltage is stepped up from 440V to 6600V.

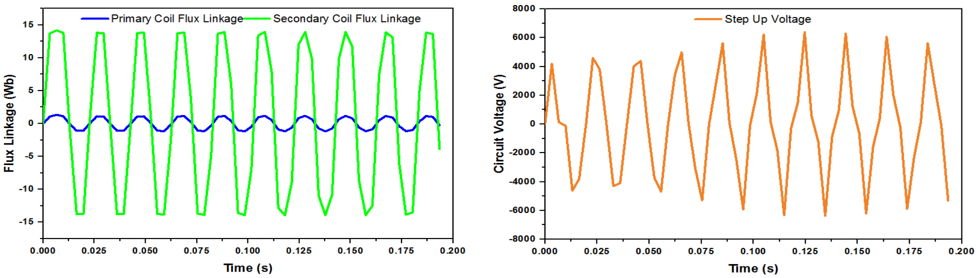

(a) (b)

Fig. 6: (a) Flux linkage for step up transformer using ferrite core, (b) Step up voltage for single phase transformer using ferrite core

Fig. 7(a) shows the magnetic field strength of the step down transformer with steel core. Its maximum values ranges from 0.0610 to 31032.2 A/m. Its minimum values ranges from 0.063 to 127.2 A/m. Contour plot of magnetic flux density using steel core is shown in Fig. 7(b). Its minimum values ranges from 8.6e^{-01} T to 5.6e^{-07} T. Its maximum values ranges from 5.8e^{-05} T to 1.943 T. Fig 7(c). Shows the vector plot of magnetic flux density using steel core material.

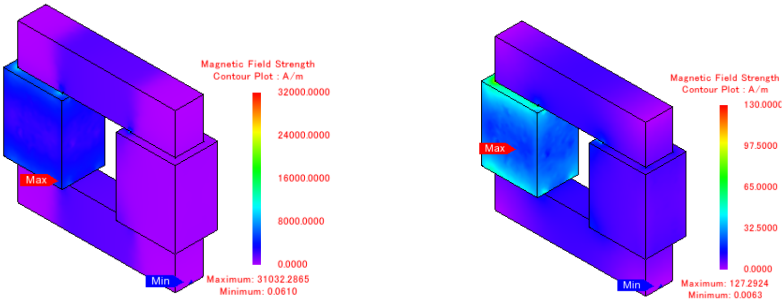

(a)

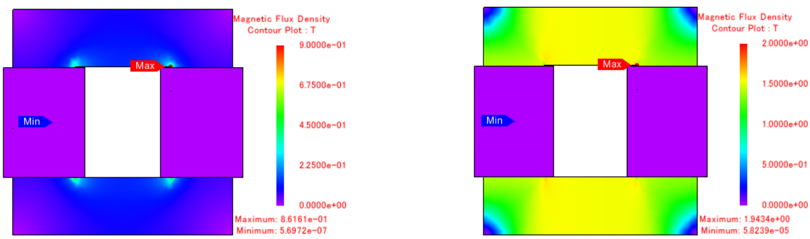

(b)

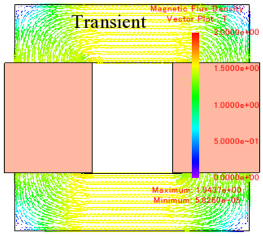

(c)

Fig. 7: (a) Magnetic Field strength using Steel Core with step down voltage, (b) Magnetic Flux density Contour plot using Steel Core with step down voltage, (c) Magnetic Flux density Vector plot using Steel Core with step down voltage

Fig. 8 (a) shows the magnetic field strength of the step up transformer with steel core. Its maximum values ranges from 0.0730 to 18585 A/m. Its minimum values ranges from 0.0042 to 83.3 A/m. Contour plot of magnetic flux density using steel core is shown in Fig. 8 (b). Its minimum values ranges from $9.3e^{-01}$ T to $5.9e^{-07}$ T. Its maximum values ranges from $2.78e^{-05}$ T to 1.8917 T. Fig. 8(c). Shows the vector plot of magnetic flux density using steel core material.

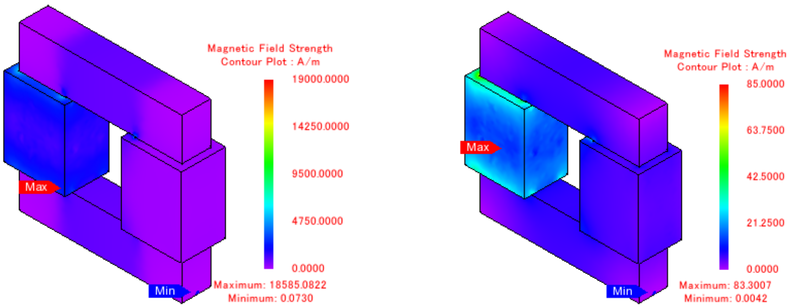

(a)

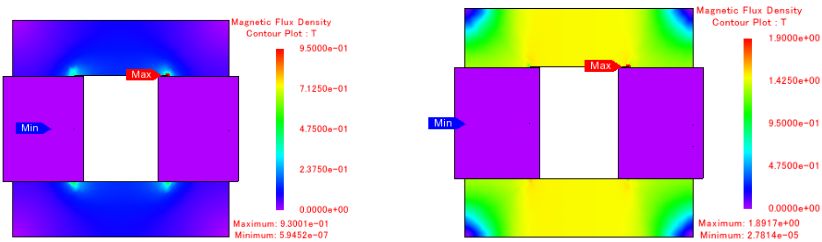

(b)

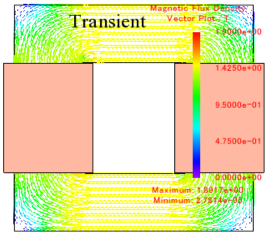

(c)

Fig. 8: (a) Magnetic Field strength using Steel Core with step up voltage, (b) Magnetic Flux density Contour plot using Steel Core with step up voltage, (c) Magnetic Flux density Vector plot using Steel Core with step up voltage

Fig. 9(a) shows the magnetic field strength of the step up transformer with ferrite core. Its maximum values ranges from 0.2570 to 260944 A/m. Its minimum values ranges from 0.0021 to 42.6 A/m. Contour plot of magnetic flux density using steel core is shown in Fig. 9(b). Its minimum values ranges from 2.23e^{-02} T to 7.26e^{-07} T. Its maximum values ranges from 0.0003 T to 0.8582 T. Fig. 9(c) shows the vector plot of magnetic flux density using ferrite core material.

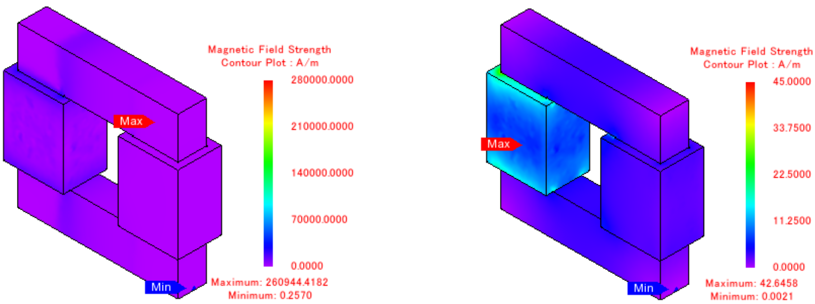

(a)

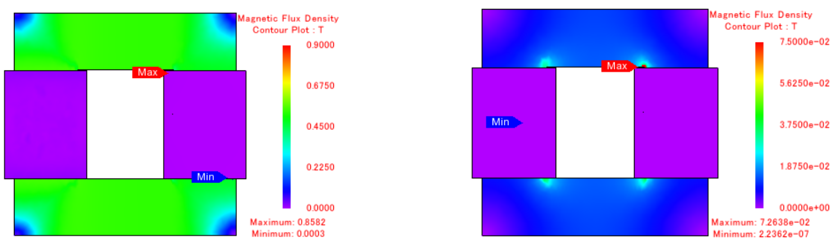

(b)

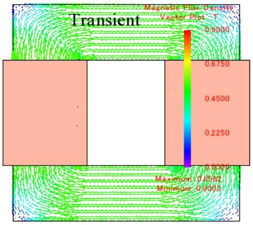

(c)

Fig. 9: (a) Magnetic Field strength using Ferrite Core with step up voltage, (b) Magnetic Flux density Contour plot using Ferrite Core with step up voltage, (c) Magnetic Flux density Vector plot using Ferrite Core with step up voltage

Fig. 10(a) shows the magnetic field strength of the step up transformer with ferrite core. Its maximum values ranges from 1.7979 to 675923 A/m. Its minimum values ranges from 0.0027 to 54.9 A/m. Contour plot of magnetic flux density using steel core is shown in Fig. 10(b). Its minimum values ranges from 9.95e^{-02} T to 1.74e^{-07} T. Its maximum values ranges from 0.0005 T to 5.9850 T. Fig 10(c). shows the vector plot of magnetic flux density using ferrite core material.

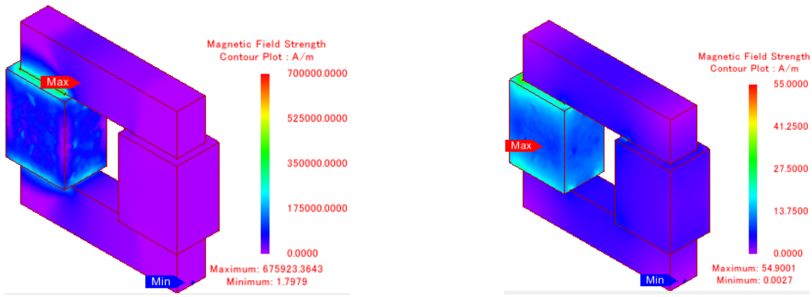

(a)

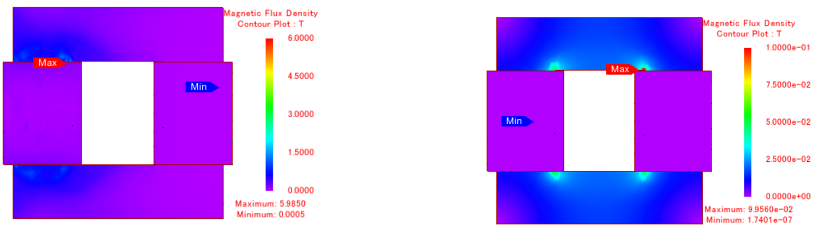

(b)

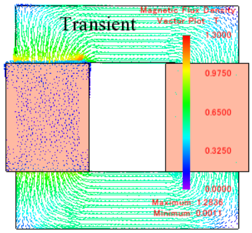

(c)

Fig. 10: (a) Magnetic Field strength using Ferrite Core with step down voltage, (b) Magnetic Flux density Contour plot using Ferrite Core with step down voltage, (c) Magnetic Flux density Vector plot using Ferrite Core with step down voltage

Transformer performance can be increased by mitigating the losses of transformer i.e core loss, and hysteresis loss. These losses can be mitigated by opting good materials for transformer that has good magnetic properties and less losses. Losses depends upon magnetic properties of materials. The loss analysis is made for steel core transformer and ferrite core transformer. Fig. 11(a) shows the core loss of transformer for step up voltage at 50Hz. This loss study of the transformer shows that the steel core has loss of 90.76W while ferrite core has loss of 40.63W. Fig. 11(b) shows the core loss of transformer for step down voltage at 50Hz. This loss study of the transformer shows that the steel core has loss of 91.7W while ferrite core has loss of 30.18W. The core loss is significantly mitigated with the help of ferrite core material. It means ferrite core material has less core losses as compared to steel core material. So transformer utilizing ferrite core can ameliorate the performance of transformer by mitigating core losses.

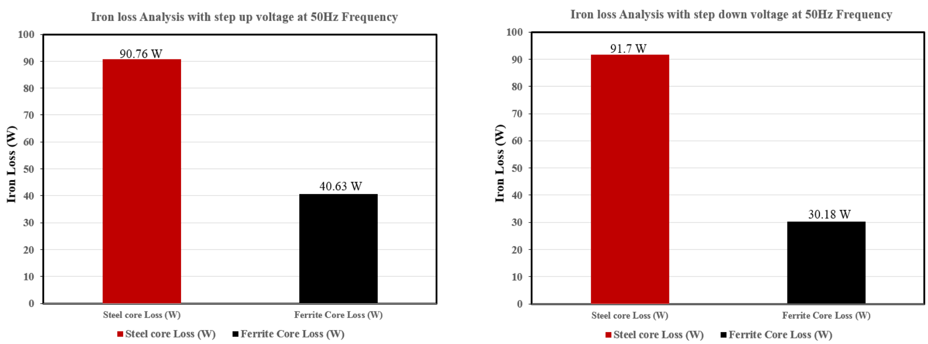

(a) (b)

Fig. 11: (a) Loss analysis using Steel and Ferrite core for step up Transformer, (b) Loss analysis using Steel and Ferrite core for step down Transformer

It is necessary to mitigate hysteresis loss in transformer as well in order to increase the performance of transformer. If the core of transformer gets easily magnetized and demagnetized then no extra energy is needed and transformer performance improves. When core material exhibits magnetic saturation it produces hysteresis losses because core has reached its maximum point. Fig. 12(a) shows the hysteresis loss of transformer for step down voltage at 50Hz. This loss study of the transformer shows that the steel core has loss of

40.99W while ferrite core has loss of 30.17W. Fig. 12(b) shows the hysteresis loss of transformer for step up voltage at 50Hz. This loss study of the transformer shows that the steel core has loss of 39.12W while ferrite core has loss of 40.62W. In step up transformer, hysteresis losses are almost equal because ferrite core has reached to its saturation level that produced a little more losses in ferrite core in step up transformer while hysteresis losses are less in step down transformer using ferrite core because transformer obtained its required voltage before reaching its saturation level.

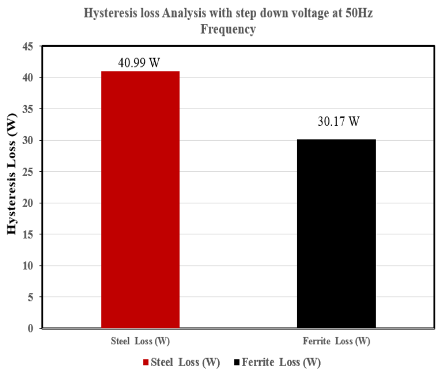

(a)

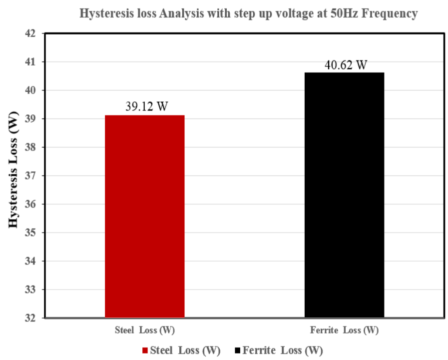

(b)

Fig. 12: (a) Hysteresis loss analysis using Steel and Ferrite core for step down Transformer, (b) Hysteresis loss analysis using Steel and Ferrite core for step up Transformer

Fig. 11(a) and Fig. 11(b) shows the losses for the step up and step down transformer using the ferrite and steel core. When we step down the voltage in limits of the flux density and magnetic field curve, then it attains the desired voltage level without heating up the core or without going into saturation zone as happened using steel core. The different flux density and magnetic field curves are utilized in the research paper for steel core and ferrite core that decides the some part of the losses in the transformer. The flux density and magnetic field curve for the ferrite core is small as compared to the steel core curve. Optimized results are obtained with this small flux density and magnetic field curve utilizing ferrite core as compared to the large flux density and magnetic field curve with steel core. When we step up the voltage then the ferrite core shows a little bit saturation because of the high output voltage inside the small flux density and magnetic field curve, but still this loss is small as compared to the steel core. Table 4 shows the comparative loss analysis of the single phase transformer with steel and ferrite core.

TABLE 4: Loss Analysis of the Single Phase Transformer with Steel and Ferrite Core

Items	Units	Single phase step up transformer	Single phase step down transformer
Steel Core Loss	W	90.76	91.7
Steel Core Hysteresis Loss	W	39.12	40.99
Ferrite Core Loss	W	40.63	30.18
Ferrite Core Hysteresis Loss	W	40.62	30.17

X. CONCLUSIONS

Single phase and three phase transformers have huge applications in electrical and electronics industry. In order to get precise design and manufacturing of the transformer, it is mandatory to get knowledgeable about working and performance of the transformer. In this paper, single phase transformer is designed with step down voltage 6600/440 V and step up voltage 440/6600 V using steel and ferrite core separately. The performance analysis of the single phase transformer is made between the steel core transformer and the ferrite core transformer. Magnetic field density, magnetic field strength, flux linkages, core losses and hysteresis losses are analysed. This analysis shows that the single phase transformer with the ferrite core has better flux density and less losses as compared to the steel core. The transformer core attains saturation level in step up transformer using ferrite core due to which core exhibits a little more losses as compared to the normal core operation. Ferrite core attains saturation level due to the small flux density and magnetic field curve. This analysis assists in designing optimal model of the transformer.

ACKNOWLEDGEMENT

This study was carried out within the MOST – Sustainable Mobility Center and received funding from the European Union Next-GenerationEU (PIANO NAZIONALE DI RIPRESA E RESILIENZA (PNRR) – MISSIONE 4 COMPONENTE 2, INVESTIMENTO 1.4 – D.D. 1033 17/06/2022, CN00000023). This manuscript reflects only the authors' views and opinions, neither the European Union nor the European Commission can be considered responsible for them.

REFERENCES

[1] Nair, PS Chandramohanan, and P. K. Preetha. "*A novel method for recovery of drainage power from distribution transformers.*" In 2011 2nd IEEE PES International Conference and Exhibition on Innovative Smart Grid Technologies, pp. 1-5. IEEE, 2011.

[2] Lakshminarayanan, Vaduganathan, B. Anand, and P. A. Balakrishnan. "*Analysis and design of ferrite core transformer for high voltage high frequency which is used in ozonators*." International Journal of Engineering and Applied Sciences 2, no. 1 (2012).

[3] Warrier, P.V. and Preetha, P.K., 2015, June. *Electromagnetic analysis of transformer using Solidworks.* In 2015 International Conference on Technological Advancements in Power and Energy (TAP Energy) (pp. 427-431). IEEE.

[4] Verma, A., Alam, M.I., Chatterjee, R., Goel, T.C. and Mendiratta, R.G., 2006. *Development of a new soft ferrite core for power applications. Journal of Magnetism and Magnetic Materials*, 300(2), pp.500-505.

[5] Shen, W., Wang, F., Boroyevich, D. and Tipton IV, C.W., 2008. *High-density nanocrystalline core transformer for high-power high-frequency resonant converter.* IEEE Transactions on Industry Applications, 44(1), pp.213-222.

[6] Hatakeyama, T. and Onda, K., 2011, December. *Novel evaluation method for the volume of transformers with various magnetic cores.* In 2011 IEEE Ninth International Conference on Power Electronics and Drive Systems (pp. 480-485). IEEE.

[7] Gotoh, S., Otake, T., Fukuda, Y. and Togawa, J., 2011. *High performance MnZn ferrites for transformer core used in forward mode switching power supply.* JFE Techn. Rep, 16.

[8] *Effects of Ferrite Material PC90 and Application Products,* Technical Report, TDK-EPC Corporation, Dempa Shimbun High-Technology November 4, 2004 Edition.

Centrifugal Force and Principal Stress Calculations on Synchronous Reluctance Machine Rotor using Finite Element Analysis

Neelam Qadeer, Salman Ali , Fabrizio Marignetti

Dept of Electrical Engineering, University of Cassino and Southern Lazio, Cassino, Italy

Email:neelamqadeer@gmail.com

Abstract

Synchronous Reluctance Machines (SynRM) are one of the popular choices among PM-free electric machines for traction applications. Centrifugal forces and stress acting on rotor of electric machine are crucial. This paper presents calculations of centrifugal forces and mechanical stress on SynRM rotor using Finite Element Analysis (FEA). Electric motors used for traction applications have different speed range for different application. So, 2D FEA is performed for a speed range of 5000 RPMs to 20000 RPMs using JMAG and results are compared to see the principal stress and displacement at different operating speeds of SynRM rotor.

Index Terms

Synchronous Reluctance Machine, Centrifugal Force, Principal Stress, PM free machine,

I. Introduction

Use of electric machines in traction application is becoming increasingly popular for several reasons including the combination of environmental concerns, cost savings, technological advancements, and consumer demand. These factors have contributed to the increasing popularity of electric vehicles in recent times.

Rare-Earth magnets are being used to develop high power density permanent magnet (PM) electric machines for traction. The growing adoption of electric and hybrid vehicles, as well as the increasing use of rail powertrains and wind generators, has brought to light the scarcity and price fluctuations of high-energy permanent magnets, figure 1 shows the trend of prices. The higher demand for these magnets is driven by their crucial role in powering these technologies, leading to supply challenges and significant price volatility. [1]

To cater these issues, R&D efforts are being made to develop PM free electric motors for traction. Synchronous Reluctance machines are among the best candidates for the purpose. Synchronous reluctance machines are electric motors that use the principal of reluctance torque to generate rotational motion. One advantage of SynRMs over PMSMs is their simplicity and lower cost. SynRMs do not require permanent magnets, which can be expensive and difficult to source, and can be made using simpler manufacturing processes. This makes SynRMs a more cost-effective option, particularly for high-volume applications.

Additionally, SynRMs do not suffer from demagnetization or magnetic saturation, which can limit the performance of PMSMs. SynRMs are also more tolerant of high temperatures and can operate at higher temperatures than PMSMs. Overall, the simplicity, efficiency, and cost-effectiveness of SynRMs make them a popular choice for a wide range of industrial and automotive applications.

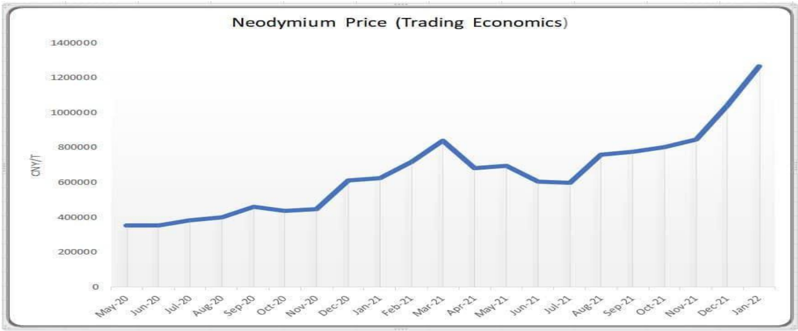

Fig. 1. Rare-Earth Magnet Price Trend 2020-2022 (Source: Magnosphere)

Unlike other types of synchronous machines, an SynRM does not have windings on the rotor. The rotor is made up of a stack of laminated iron cores with salient poles, but it does not have any windings or permanent magnets. The rotor is typically designed with a simple and robust structure to ensure efficient flux linkage with the stator magnetic field. The absence of windings on the rotor is one of the distinguishing features of an SynRM, which differentiates it from other synchronous machine designs. Based on rotor geometry topologies, SynRMs are mainly classified in three types, which are Salient pole rotor, Axially Laminated Anisotropic (ALA) rotor and Transversally Laminated Anisotropic (TLA) rotor (shown in figure 2).

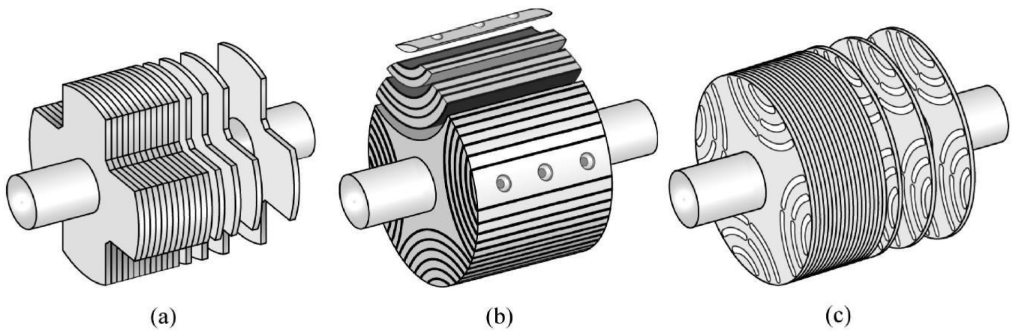

The salient pole rotor as the first possibility is made by removing some iron material from each rotor in the transversal region. In the axially laminated Anisotropic-ALA rotor, which is the second type of SynRM, the laminations (iron) are suitably shaped at each pole and insulated from each other using electrically and magnetically passive materials (insulation) and the resulting stacks are connected through pole holders to the central region to which the shaft is

connected. In the third type of rotor the laminations are punched in the traditional way. Thin ribs are left when punching, thus the various rotor segments are connected to each other by these ribs.
The TLA (Transverse Laminated Anisotropic) structure is more suitable for industrial manufacturing. This is because the rotor lamination can be punched as a single unit, just like in other conventional machines. On the other hand, the ALA rotor structure is theoretically attractive because it resembles an ideal "distributed anisotropic structure." However, it may be more challenging to manufacture compared to the TLA structure. However, ALA rotor SynRM has been developed and found one of competent option for power trains as they keep Ld/Lq ratio higher than 1/10 even at increasing speed [3]. Hence its very important to do a comprehensive electromagnetic and mechanical structure analysis of SynRMs. The paper [4] presents structural and electromagnetic study of synchronous reluctance machine. Comparative analysis shows that synchronous reluctance machine is cost effective solution as compared to induction motor and switched reluctance motor in PM free electric traction system. The authors also considered stress on motor because of inertial load. This study investigates the impact of stator yoke and tooth tip width on the average torque value and torque ripple in a machine. The findings suggest that increasing the yoke width enhances the torque values obtained in the machine, although it results in a less favourable torque/volume ratio. On the other hand, the influence of tooth tip width is found to be less significant, with larger slot openings leading to higher torque ripples. Additionally, the study examines the widths of the rotor ribs and bridge, revealing that very thin ribs and bridge yield the highest average torque values but come at the cost of increased torque ripple values. As compared to traditional air-filled flux barrier, authors introduced aluminium beam and resin filled barrier. The analysis shows that aluminium insert barrier can achieve high speed up to 12000rpm without increasing stress while resin and air-filled barrier can achieve speed only up to 8000rpm.
The paper [5] presents the electromechanical and electromagnetic analysis of synchronous reluctance rotor. The machine consists of four poles rotor and stator with single tooth coils. The analysis shows that electromagnetic performance will be disturbed by enhancing tangential and radial rib width. The tangential rib has huge impact on the performance of rotor design. The radial rib is primary portion of flux barrier. Under steady state operation, radial rib has huge impact on increasing minimum safety factor for mechanical integrity while tangential rib has less importance in structural integrity. This prototype machine can obtain 25% over speed mechanical integrity. Usually, synchronous reluctance machine has maximum four poles because beyond these poles, it can have negative impacts on machine performance.
In paper [6] authors suggest a synchronous reluctance rotor by automatic design of multi layers using objective GA optimization and FEA. This motor can be modelled in less width and have number of degrees of freedom for rotors. From all of these degrees, two number of rotor degrees are favourable. According to FEA, these two opted degrees have same potential. These degrees have comparable torque and less torque ripples.
The paper [7] suggests cogging torque and torque ripples mitigating technique for Permanent Magnet synchronous reluctance machine (PMSynRM). For this purpose, authors proposed stator auxiliary groove and combining magnet pole migration. The authors used Taguchi method to optimize the proposed structure by considering width, depth, position, number, and shape of auxiliary slot. This proposed model significantly mitigate the cogging torque and torque ripples without disturbing electromagnetic properties of the machine, so it proves the reliability of the machine.
In paper [8] authors present high speed synchronous reluctance motor for traction applications.

Traditional synchronous reluctance motors use radial ribs to enhance the mechanical robustness, but it also degrades the performance of the motor as shown in fig. 1. The authors suggest multiple positions for structural ribs by optimizing position, sizing, and amount. For this purpose, the topology optimization is used for proper information to optimize the rotor he structures. The suggested technique provides the high speed with strong mechanical robustness and no extra cost is required for this purpose except geometry.

The paper [9] presents synchronous reluctance motors for hybrid electric vehicles. The authors improved the rotor design by presenting angle of flux barrier to mitigate the torque ripples. The torque is maximized by using current vector control
method. Multiple rotor configurations with good electromagnetic performance optimize the overall system.

In paper [10] authors suggest synchronous reluctance motor for high-speed applications. The authors analysed the results of the rotor without ribs and analysis show that motor have good electromagnetic properties without ribs. But motor cannot be used for high-speed applications due to stress caused by centrifugal force. Presence of ribs in rotor improve the mechanical robustness in motor. So, it can be used for high speed applications.

The paper [11] presents analytical model of synchronous reluctance machine with Zhukovski barrier based on pattern of flux lines in rotor. The authors analyzed the accuracy of motor output torque and air gap flux density distribution using linear analytical technique and linear FEA model. Both techniques results have accordance. The authors suggested that by using linear analytical technique, average output torque and air gap flux distribution results can be obtained faster than the expensive numerical computation technique.

In paper [12] authors suggest ferrite permanent magnet synchronous reluctance machine due to high cost and unavailability of rare earth magnets, however machine has good performance with rare earth magnet. The authors analyzed the results considering mechanical strength and irreversible demagnetization. The results obtained using ferrite magnet in synchronous reluctance machine are favorable.

The paper [13] presents high cold rolled grain oriented electrical steel due to high quality magnetic property for transverse laminated rotor. It is used for high compactness, high torque density and high efficiency in synchronous reluctance motor. This segmented rotor exhibits lower induction in q axis and high induction in d axis. It ameliorates the saliency ratio of synchronous reluctance machine. Furthermore, torque ripples are minimized proposing rotor geometry design by rotor and stator slot pitch angles.

In paper [14] authors present synchronous reluctance motor with 4 pole 6 slot fractional slot non- overlapping concentrated winding. Due to coils bobbin winding, coils high fill factor with short end windings and segmented stator, motor has high efficiency and high torque density. The empirical data matches with accuracy for magnetization curve of d-q axis flux linkages and d-q axis inductance. The paper [15] presents ultra-high speed synchronous reluctance rotor that uses soft magnetic flux guides with two pole rotor. Authors built two prototype motor with output rating of 1.8kw and 100kw. Both motors results are verified using 2D and 3D analysis. These designs were able to produce required torque and mechanical stability against centrifugal force.

As there is different speed range of SynRM for different applications, the calculations of centrifugal forces and consequent stress on the SynRM rotor is crucial. This paper presents calculations centrifugal forces and consequent stresses on the SynRM rotor from 5000 RPM to 20000 RPM speed, which is the typical speed range of electric motors in modern day traction applications.

II. DESIGN DETAILS

Basic design details of the motor are given in following sections.

A. Basic dimensions and Parameters

4 pole 24 slots three phase SynRM is used for this research. Basic dimensions and parameters are given in Table 1

TABLE I: Table Example

Items	**Value**
Stator Outer Diameter	150 mm
Stator Inner Diameter	80 mm
Rotor Outer Diameter	78 mm
Rotor Inner Diameter	25 mm
Airgap	1 mm
No. of Pole Pairs	2
No. of Stator Slots	24
No. of Slots per pole per Phase	2

B. Back EMF and Torque

The torque equation used for calculating torque in a synchronous reluctance machine (SynRM) depends on the specific design and configuration of the machine. However, the most used torque equation for an SynRM is based on the principle of reluctance torque. The reluctance torque equation for an SynRM is given by equation (1):

$$Tr = (Ld - Lq)\ Iq \qquad (1)$$

Where:
Tr is the reluctance torque, Nm.
Ld is the d-axis inductance,
Lq is the q-axis inductance,
Id is the d-axis current,
Iq is the q-axis current,
Pn is pole logarithm,

In a reluctance torque, the average value is larger when the difference between the d-axis inductance and q-axis inductance is large, and the ripple decreases as the change in difference is small. When there is increase in the difference between the d-axis and q-axis inductance, resulting in a higher average torque.

In a synchronous reluctance machine (SynRM), the other thing that is very important is to consider back electromotive force (EMF). EMF refers to the voltage generated in the stator windings due to the relative motion between the rotor and the stator magnetic field. The back EMF opposes the applied voltage and is responsible for limiting the current flowing through the machine.

The calculation of the back EMF in an SynRM involves considering the rate of change of the magnetic flux linkage in the stator windings. The back EMF can be determined using equation (2):

$$E_{back} = -\frac{d(\Psi s)}{dx} \tag{2}$$

Where:

E-back is the back EMF,

And $\frac{d(\Psi s)}{dx}$ represents the rate of change of stator flux linkage with respect to time,

The back EMF in an SynRM helps limit the current, regulates the torque-speed characteristics, improves motor efficiency, and provides valuable feedback for motor control.

III. MECHANICAL ASPECTS

Basic design details of the motor are given in following sections.

A. Centrifugal Force

Prime cause of mechanical stress on rotor is due to Centrifugal force (Fc). It is of great importance to calculate and manage centrifugal force of the rotor specially in heavy weight and high-speed machines because the Fc is directly proportional to the mass of the rotor as well as to the square of the rotating speed. Design equation for calculating Fc acting on rotor is given in Equation (3)

$$F_c = m.r.w^2 \tag{3}$$

Where:

m indicates the mass of the rotor (kg),

r is the radius of rotor,

ω is the angular velocity (rad/s).

B. Torque and Tangential stress on Rotor

Torque in terms of Maxwell's tension can be calculated by equation (4)[16]-[18]. Where B_n is the normal flux density and B_t is the tangential flux density. μo represents the air permeability.

$$T_t = \oint r B_n B_t \, dS \tag{4}$$

IV. Finite Element Analysis

Finite Element Analysis (FEA) for the calculations of mechanical stress is performed at different rpms of rotor from 5000 to 20000 rpm for every 5000-rpm difference.

Electrical steel is used as back iron and copper is used for winding. Material details and properties are given in table 2.

Table 2. Materials and properties

Description	Back-Iron	Copper
Density [g/cm^3]	5.132	8.96
Young's Modulus [MPa]	210000	130000
Poisson's Ratio	0.3	0.343

2D FEA of 4 pole 24 slots SynRM is performed. Outer diameter of machine is 150 mm. Thickness of the laminations is chosen to be 0.35mm. Dimensions and parameters of geometry are given in Table.1. Geometry of machine is shown in Figure 3a and Mesh is shown in Figure 3b.

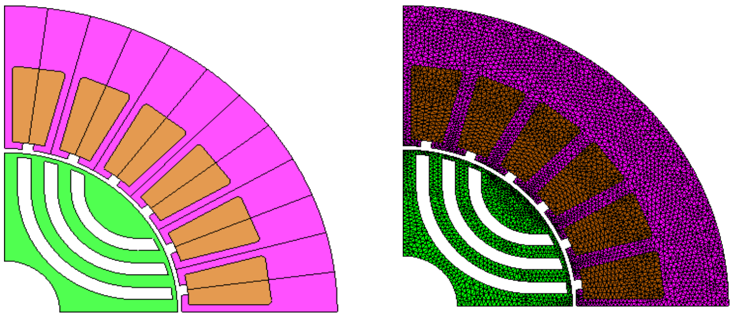

(a) (b)

Results of Principal stress on rotor structure are given in Figure 4. Fig. 4(a) shows the principal stress on the rotor at 5000 rpms. Its maximum value is 0.0654 MPa. Fig. 4(b). shows the principal stress on the rotor rotating at 10000 rpms with the maximum value of Principal stress 0.2616 MPa. Fig 4(c). shows the principal stress on the rotor rotating at 15000 rpms with the maximum value of Principal stress 0.5887 MPa. Fig 4(d). shows the principal stress on the rotor rotating at 15000 rpms with the maximum value of Principal stress 01.0466 MPa.

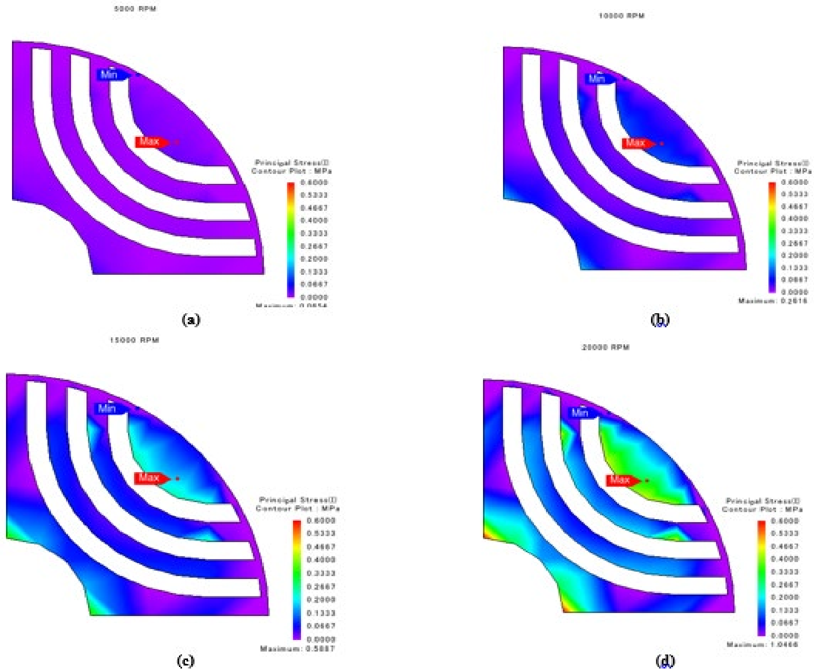

Fig. 4. (a) Principal stress on the rotor at 5000 rpms, (b) Principal stress on the rotor at 10000 rpms, (c) Principal stress on the rotor at 15000 rpms, (d) Principal stress on the rotor at 20000 rpms

Principal stress caused by centrifugal force is analysed using finite element analysis. FEA shows that with the increase in rotational speed, the principal stress increases exponentially. Maximum principal stress of rotor with 5000 rpm, 10000 rpm, 15000 rpm and 20000 rpm are 0.0654 MPa, 0.2616 MPa, 0.5887 MPa and 1.0466 MPa, respectively. Figure 5 shows the graph between peak principal stress and different rpm speeds. This graph verifies the exponential increase in peak principal stress with the increase in rotational speed.

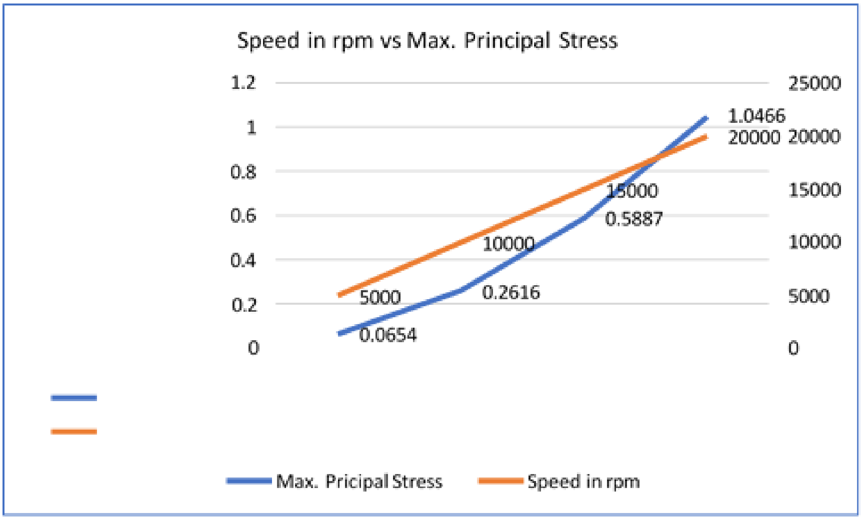

Fig.5: Graph of Speed in rpm and Max. Principal stress

ACKNOWLEDGEMENT

This study was carried out within the MOST – Sustainable Mobility Center and received funding from the European Union Next-GenerationEU (PIANO NAZIONALE DI RIPRESA E RESILIENZA (PNRR) – MISSIONE 4 COMPONENTE 2, INVESTIMENTO 1.4 – D.D. 1033 17/06/2022, CN00000023). This manuscript reflects only the authors' views and opinions, neither the European Union nor the European Commission can be considered responsible for them.

REFERENCES

[1] *I. Boldea, F. Marignetti, G. Graber, M. Porzio, L. Fratelli "PM-free electric motor powertrains in road and rail transport: an overview", ESARS 2023.*

[2] *I. Boldea, F. Fukar, T. A. Lipo, L. Malesani, T. J. E. Miller, A. Vagati, "Synchronous reluctance motor drives: a new alternative", IEEE Tutorial Course at IAS Annual Meeting 1994.*

[3] *I. Boldea, L.Tutelea, "Reluctance electric machines design and control", book, CRC Press, New York 2019.*

[4] *Oprea, Claudiu Alexandru, Claudia Steluta Martis, Petru Cristinel Irimia, Călin Husar, and Mihail Grovu. "Electromagnetic and structural analysis of a Synchronous Reluctance Machine." In 2015 Intl Aegean Conference on Electrical Machines & Power Electronics (ACEMP), 2015 Intl Conference on Optimization of Electrical & Electronic Equipment (OPTIM) & 2015 Intl Symposium on Advanced Electromechanical Motion Systems (ELECTROMOTION), pp. 564-569. IEEE, 2015.*

[5] *Donaghy-Spargo, Christopher M. "Electromagnetic–mechanical design of synchronous reluctance rotors with fine features." IEEE Transactions on Magnetics 53, no. 11 (2017): 1-8.*

[6] *Pellegrino, Gianmario, Francesco Cupertino, and Chris Gerada. "Automatic design of synchronous reluctance motors focusing on barrier shape optimization." IEEE Transactions on Industry Applications 51, no. 2 (2014): 1465-1474.*

[7] *Li, Xinmin, Zihan Sun, Wenbo Sun, Liyan Guo, and Huimin Wang. "Design of Permanent Magnet- Assisted Synchronous Reluctance Motor with Low Torque Ripple." World Electric Vehicle Journal 14, no. 4 (2023): 82.*

[8] *Credo, Andrea, Giuseppe Fabri, Marco Villani, and Mircea Popescu. "Adopting the topology optimization in the design of high-speed synchronous reluctance motors for electric vehicles." IEEE Transactions on Industry Applications 56, no. 5 (2020): 5429-5438.*

[9] *Ferrari, Marco, Nicola Bianchi, Alberto Doria, and Emanuele Fornasiero. "Design of synchronous reluctance motor for hybrid electric vehicles." IEEE Transactions on Industry Applications 51, no. 4 (2015): 3030-3040.*

[10] *Dziechciarz, Arkadiusz, Claudiu Oprea, and Claudia Martis. "Multi-physics design of synchronous reluctance machine for high speed applications." In IECON 2016-42nd Annual Conference of the IEEE Industrial Electronics Society, pp. 1704-1709. IEEE, 2016.*

[11] *Pohl, Matthias, and Dieter Gerling. "Analytical model of synchronous reluctance machines with Zhukovski barriers." In 2018 XIII International Conference on Electrical Machines (ICEM), pp. 91-96. IEEE, 2018.*

[12] *Liu, Xiping, Ya Li, Zhangqi Liu, Tao Ling, and Zhenhua Luo. "Analysis and design of a high power density permanent magnet-assisted synchronous reluctance machine with low-cost ferrite magnets for EVs/HEVs."COMPEL- The international journal for computation and mathematics in electrical and electronic engineering 35, no. 6 (2016): 1949-1964.*

[13] *Taghavi, Seyedmorteza, and Pragasen Pillay. "A novel grain-oriented lamination rotor core assembly for a synchronous reluctance traction motor with a reduced torque ripple algorithm." IEEE Transactions on Industry Applications 52, no. 5 (2016): 3729-3738.*

[14] *Spargo, Christopher M., Barrie C. Mecrow, James D. Widmer, Christopher Morton, and Nick J. Baker. "Design and validation of a synchronous reluctance motor with single tooth windings." IEEE transactions on energy conversion 30, no. 2 (2015): 795-805.*

[15] *Ikäheimo, Jouni, Jere Kolehmainen, Tero Känsäkangas, Ville Kivelä, and Reza R. Moghaddam. "Synchronous high-speed reluctance machine with novel rotor construction." IEEE Transactions on Industrial Electronics 61, no. 6 (2013): 2969-2975.*

[16] *H. Vu Xuan, D. Lahaye, H. Polinder and J. A. Ferreira, "Influence of Stator Slotting on the Performance of Permanent-Magnet Machines With Concentrated Windings," in IEEE Trans on Magnetics, vol. 49, no. 2, pp. 929-938, Feb. 2013, doi: 10.1109/TMAG.2012.2212025.*

[17] *H. V. Xuan, D. Lahaye, S. O. Ani, H. Polinder and J. A. Ferreira, "Electrical generators for maritime application," Int Conf on Electrical Machines and Systems, 2011, pp. 1-6, doi:*

[18] *H. VuXuan, D. Lahaye, S. O. Ani, H. Polinder and J. A. Ferreira, "Effect of design parameters on electromagnetic torque of PM machines with concentrated windings using nonlinear dynamic FEM," 2011 IEEE International Electric Machines & Drives Conference (IEMDC), 2011, pp. 383- 388, doi: 10.1109/IEMDC.2011.5994625.*

Day-ahead Quantile Regression Forecast of the Active Power Absorbed by a Public Building

Sara Perna, Anna Rita Di Fazio
Department of Electrical and Information Engineering
University of Cassino and Southern Lazio, Cassino, Italy Email: sara.perna@unicas.it

Abstract

Forecasting analysis is a very useful tool for improving the services of power systems. In the modern context of renewable energy communities, efficient forecasting algorithms are crucial for the maximization of the shared energy and financial incentives. This paper develops a univariate probabilistic forecasting method based on quantile regression model and applies it to the power absorbed by a public building, whose data are collected in a private database. After a brief overview of the basic steps of a forecasting analysis, the considered forecast method is described; then the results of day-ahead forecast applied on 200 kW rated power public building are reported. The accuracy of the method is evaluated through the pinball loss index which shows great accuracy: the maximum error index is equal to 4 kW and it is related to forecasted hours distant to the origin time of the forecast. This research activity was supported by Regione Lazio under the project ComER ("Methods and tools for managing renewable energy communities").

Index Terms

probabilistic forecast, quantile regression model, renewable energy communities.

I. Introduction

In the modern energy scenario, the distributed energy resources (e.g. distributed re- newable generators, battery energy storage systems, and controllable loads) are widely spread throughout the grid, especially on the low voltage distribution network. Although these resources provide economical and environmental benefits, they affect the network operation. To cope with these issues the European energy policies have introduced the renewable energy communities (RECs).

RECs are defined as user associations that aim to produce energy from renewable sources and consume and share it within the members belonging to the community. From a technical prespective, RECs enable to limit the inversion of the power flow toward the upstream network by promoting self-consumption and self-sustainability. From a economical point of view, RECs allow community members to increase their revenue by receiving: (i) the restitution of a part of the energy use tariff; (ii) the profit from the sale of the energy delivered to the grid by each renewable power plants installed within the community; and (iii) an incentive proportional to the shared energy [1].

Actually, the challenge lies in maximizing shared energy to promote the widespread adoption of RECs. However, this entails a critical aspect with it, which is the innovation of the management and control techniques. A strategic approach to achieve this goal is to equip with efficient power forecasting algorithms these techniques [2]. In literature, there are several studies regarding the forecasting analysis applied on the power absorbed by a user [3], [4], [5] and on the power generated from renewable sources [6], [7]. The recent scenario is focusing on probabilistic forecasting methods since they provide more information than deterministic approaches (e.g., uncertainty of the forecasts). The most- used probabilistic forecasting methods are based on quantile regression (QR) model, due to the fact that this approach is able (i) to represent the entire probability distribution of the forecasted variable and (ii) to reveal more information regarding outliers data.

The core of this paper is the development of a probabilistic forecast algorithm based on the QR model with the aim of perform a day-ahead forecast on the power absorbed by a public building of 200 kW rated power, whose data are collected in a private dataset. The day-ahead forecasts are performed for each hour of the day and considering both endogenous and exogenous predictors. In order to improve the accuracy, the forecasting method has been applied on working-days and on weekend-days separately.

This study gives a contribution to the Italian project ComER ("Methods and tools for managing renewable energy communities"), developed by the University of Cassino (Italy) and the Campus Bio-Medico University of Rome (Italy).

This paper is organized as it follows. The basic steps of the forecasting analysis are summarized in Section II, along with an overview of the adopted QR forecasting method. Numerical results are reported and discussed in Section III. The conclusion and future works are illustrated in Section IV.

II. The Forecast Analysis: Basic Steps and Quantile Regression Model

The forecast analysis is performed in five essential steps, that are: the problem definition, the gathering information, the preliminary analysis, the choosing and fitting of forecasting models and the evaluation of the forecasting accuracy.

A. Problem definition

The problem definition aims to identify the forecasted variable (also known as target variable), the time resolution and the time horizon of the forecast. The time resolution represents the interval time between two forecasts, whereas the time horizon describes the entire forecasted period. To efficiently manage and control RECs it is necessary forecast the power consumed/absorbed by the users belonging to the community. In this paper the target variable is the power consumption of a public building and the forecast is performed for each hour (time resolution) of the next day (time horizon).

B. Gathering information

The time series data are the most-used information gathered to perform and test a forecast. To improve the accuracy of the forecast, it is important to collect data of the target variable and of other variable that may affects the target variable value (e.g., meteorological data). Data are post-processed in order to detect and eliminate outliers, such as missing, duplicated, and erroneous data. Then, the available data are divided in training data (used to estimate the parameters of a forecasting model) and test data (used to evaluate the forecast accuracy).

C. Preliminary analysis

Th preliminary analysis is a crucial task of the forecasting studies since it is responsible for the selection of the predictor variables involved in the forecasting model. Basically, the preliminary analysis consists of the graphical representation of the dataset over the observation period and of the autocorrelation and correlation analysis. The first analysis aims at evaluating the components of time series, such as trend, seasonal and cyclic patterns [8]; the second and the third analysis aim at calculating the autocorrelation and the correlation coefficients, *r* and *p* respectively. The *r* coefficient describes the strength of the linear relationship of the target variable with respect to its lagged values; the *p* coefficient quantifies the strength of the linear relationship between the target variables and the exogenous variables. It is worth noting that lagged variables with a high value of *r* and exogenous variables with a high value of *p* are selected as candidate endogenous and exogenous predictors of the forecasting models. In this paper, the exogenous predictors are the temperature measured at the site where the building is located.

D. Choosing and fitting forecasting models

The forecasting method is choosen according to the available data and the problem definition. Moreover, based on the accuracy of the forecasting, it is possible to choose among simple and complex methods. The simple widely-use forecasting method is the persistance (naïve) method, which states that the forecast of the target variable is equal to the last observed value. This method is usually considered as benchmark due to its simplicity. The complex forecasting methods can be classified depending on the undelying model, such as auto-regression model, and neural networks.

Further classification depends on the used approach: the deterministic approach provides as output of the forecast only a single value of the variable of interest (point forecast), whereas the probabilistic approach provides as output analytical distributions (such as probabiliti density functions, cumulative density functions).

In this paper a probabilistic forecasting method based on QR model has been applied. The formulation of the understudying method for a given quantile α_q is described in (1):

$$\hat{y}_t^{\alpha_q} = \beta_0^{\alpha_q} + \beta_1^{\alpha_q} x_{1t} + \cdots + \beta_M^{\alpha_q} x_{Mt} \tag{1}$$

where $\hat{y}_t^{\alpha_q}$ is the forecasted α_q quantile of the target variable at the time *t*; $\beta_0^{\alpha_q}, \ldots, \beta_M^{\alpha_q}$ are the M+1 parameters of the model for quantile α_q; and $x_{1t}, \ldots, x_{Mt}$ are the M predictors variables involved into the model. Equation (1) states that the forecast of the target variable assumes a value less than or equal to $\hat{y}_t^{\alpha_q}$ with a probability equal to α_q. The strength of the QR method is the possibility of deriving the probability distribution of the forecasted value, which can be obtained by interpolating the 99 quantiles.

The choice of the model (i.e., the selection of the predictors) can be made after the preliminary analysis, whereas the fitting of the forecasting model consists on the estimation of its parameters. This last task is performed by minimizing the pinball loss function for a particular quantile and using the training data [9].

E. Evaluation of the forecasting accuracy

The final step is to test and evaluate the accuracy of the forecasting method. This task is performed through the use of indices, which are considered as error indices.

In the probabilistic framework, the most common indices are: the winkler score (WS), the pinball loss function (PLF), and the continuous ranked probability score (CRPS) [10]. In this study only the PLF has been considered, which gives a higher penalty when the observation is greater than the estimated quantile and viceversa; as a result a lower PLF value indicates a better estimate of the quantile. The formula of the PLF is reported in (2).

$$PLF_t^{\alpha_q} = \begin{cases} 2(1-\alpha_q)(\hat{y}_t^{\alpha_q} - y_t) & if\ y_t < \hat{y}_t^{\alpha_q} \\ 2\alpha_q(y_t - \hat{y}_t^{\alpha_q}) & if\ y_t \geq \hat{y}_t^{\alpha_q} \end{cases} \tag{2}$$

where $\hat{y}_t^{\alpha_q}$ is the forecasted α_q quantile of the target variable and y_t is the historical data. As described in (2), if the order α_q is equal to 0.5 the PLF can be interpreted as an absolute error.

III. Numerical Results

The day-ahead QR forecast is performed on the "center for the health of the elderly", which is a public building of 200 kW rated power located in Rome (Italy).

The target variable dataset is provided by the Campus Bio-Medico University of Rome and it collects the active power absorbed by the public building from 1 January 2017 to 31 December 2022. The temperature data are extracted from public dataset in [11]. It is worth of noting that the forecasting analysis has been conducted only considering the whole weeks (i.e., from Monday to Sunday); therefore only the period from 2 January 2017 to 5 December 2022 has been considered. The data are plotted in order to evaluate the presence of time series components and anomalies. In the dataset of the target variables some missing data are presented, which are replaced with the value of the same day-hour of the previous week. In Fig.1 the active power absorbed by the public building during the observed period is reported. As shown in the figure, the active power absorbed during the last two years are significant different from the first three years. This phenomenon is related to the covid period: the reduction in building occupancy led to a decrease in the consumption of electrical power.

In Fig.2 the overlapping target variable trend is reported in order to evaluate the time series components. It is clearly observed a weekly seasonality: the active power consumption during the working-day (Monday to Friday) and the weekend-days (Saturday and Sunday)

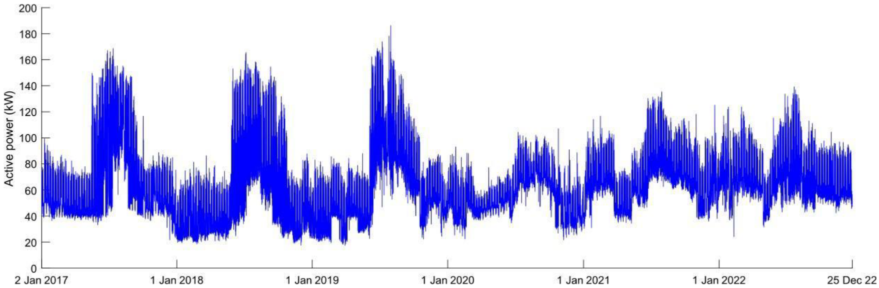

Fig. 1: Active power consumption during the observed period

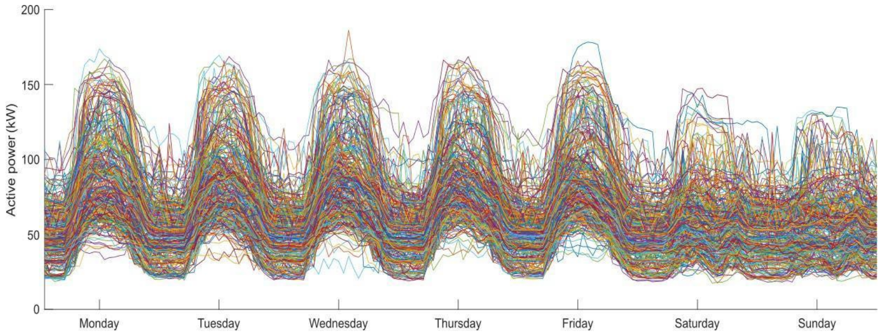

Fig. 2: Week overlapping trend

are significantly different. Consequently the dataset are divided in a working-days and a weekend-days datasets. Then, the two datasets are splitted into training and test data. The first subset consists of 80 % of the entire dataset, the second subset is built with the remainder 20 % of data.

The preliminary analysis ends with the autocorrelation and correlation analysis, which diagrams are reported in Fig.3 and Fig.4 respectively. As shown in Fig.3, the target variable has a marked correlation (higher r coefficient) with the three hours preceding the hour to be forecasted, and also with the 24^{th} and 168^{th} lagged values, respectively one day and one week before. The correlation diagram (Fig.3) shows a good linear relationship between the active power absorbed by the public building and the external temperature; the p coefficient is equal to 0.60.

For a given quantile, the day-ahead forecasts are estimated for each hour of the day and generated by 99 quantiles at level 0.01, 0.02, . . . , 0.99. Moreover, as previously defined, the QR forecasting method is performed separately for the working-day and the weekend-day substes.

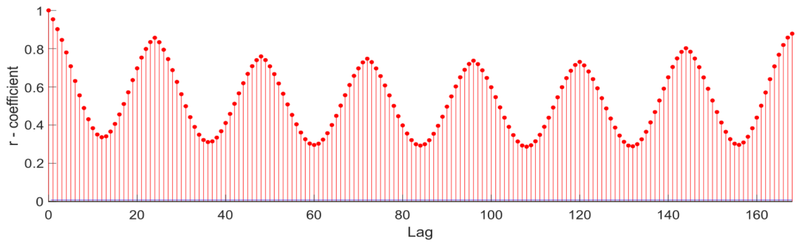

Fig. 3: Autocorrelation (a) and correlation (b) diagrams

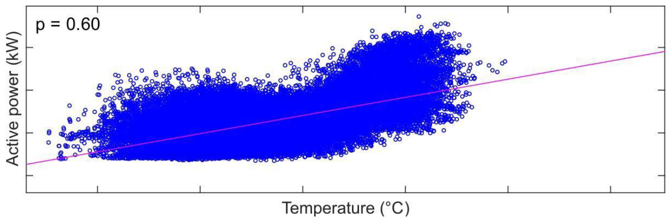

Fig. 4: Autocorrelation (a) and correlation (b) diagrams

According to the autocorrelation and correlation diagrams, different forecasting models have been developed. For the sake of brevity, in this paper only the numerical results of the most accurate forecasting model is reported (3).

$$\hat{P}_h^{a_q} = \beta_0^{a_q} + \beta_1^{a_q} P_{h-k} + \beta_2^{a_q} P_{h-24} + \beta_3^{a_q} P_{h-168} + \beta_4^{a_q} T_h \quad (3)$$

The forecasted a_q quantile of the target variable at the hour h is obtained considering the endogenous predictors referred to the active power consumed at the origin time of the forecast P_{h-k} (k is the lead time), the active power consumed one day P_{h-24} and one week P_{h-168} before the forecasted hour and the external temperature at the forecasted hour T_h. Since the forecasts are related to the last past year, in this study the external temperature measurements have been considered as known[1].

In other words, for each subsets the QR forecasting method has been applied 24 times for each hour of the day obtaining every time 99 forecasted quantile.

The numerical results consist in the day-ahead forecasts of the entire test data for both working-day and weekend-day dataset and considering each hour of the day as the origin time of the forecast. In Fig.5.a and Fig.5.b the results of day-ahead forecast of one working- day and one weekend-day at origin time equal to 00:00 are reported. In each figure, the red line represents the measured powers (historical values), the yellow line is the expected value of the day-ahead forecast and the blue area represents the region bounded by 0.1 and 0.9 quantiles where the forecasts lie. As shown in the figures, the expected values are close to the measured active power proving the great accuracy of the forecasting method.

[1]To forecast future time period, it will be required gathering information about forecasted temperature.

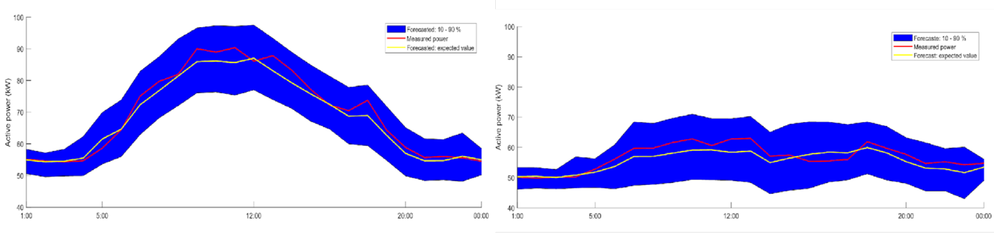

a) b)

Fig. 5: Day ahead forecasts of (a) working day and (b) weekend-day

TABLE I: Error index averaged on 99 quantiles for a working day and weekend-day

PLF (kW)		
Forecasted hour	Working day	Weekend day
01:00	0.223	0.243
02:00	0.237	0.284
03:00	0.277	0.198
04:00	0.400	0.308
05:00	0.861	0.489
06:00	0.727	0.920
07:00	1.235	1.361
08:00	1.274	1.414
09:00	0.873	1.504
10:00	1.464	1.608

11:00	1.258	1.097
12:00	1.714	1.709
13:00	0.801	1.647
14:00	1.720	1.135
15:00	1.472	0.979
16:00	0.924	0.940
17:00	0.726	1.091
18:00	0.990	0.869
19:00	1.655	0.908
20:00	0.854	0.846
21:00	0.885	1.027
22:00	0.644	0.783
23:00	0.713	0.924
00:00	0.543	1.041

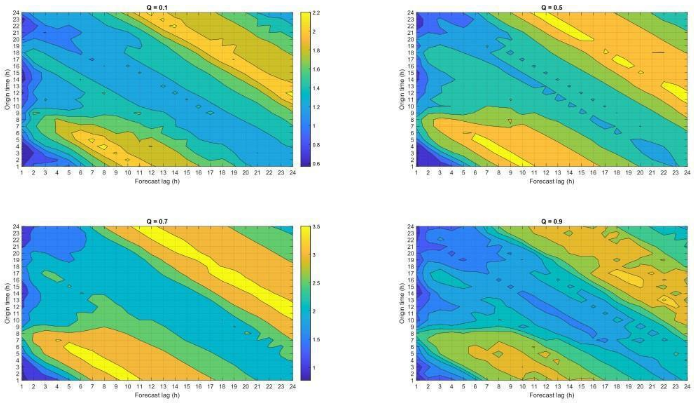

Fig. 6: Working day contour map: 0.1, 0.5, 0.7 and 0.9 quantiles

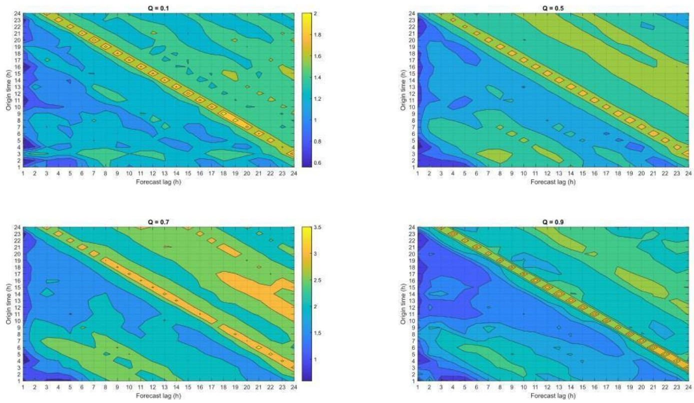

Fig. 7: Weekend day contour map: 0.1, 0.5, 0.7 and 0.9 quantiles

This results are also shown in Tab.I, where the PLF avareged on 99 quantiles for each forecasted hour and for each type of the weekly day are reported. The error index is measured in kW. As shown in table, the error index are very limited, with a maximum error equal to 1.72 kW at 14:00 for working-day and to 1.70 kW at 12:00 for weekend- day. In Fig.6 and Fig.7 the contour maps of the two weekly test dataset for the quantiles 0.1, 0.5, 0.7 and 0.9 are reported. The figures represent the PLF in kW of the 24 forecasted hours (y-axis) considering each hour of a day as origin time of forecast (x-axis) and averaged the results on the working-days (Fig.6) and weekend-days (Fig.7) of the test subset. In conclusion, the numerical results show great accuracy, with a low error index for forecasted hours close to the origin time and slightly higher errors for the remaining hours, with the maximum error amounting to 4 kW.

IV. CONCLUSIONS

This paper focuses on the development of a probabilistic forecast algorithm based on the QR model in order to perform a day-ahead forecast on the power absorbed by a public building of 200 kW rated power, whose data are collected in a private dataset. The preliminary analysis led to the the separation of the dataset into working-days and weeken- days and to the use of both endogenous and exogenous predictors, which are choosen on the basis of the value of autocorrelation and correlation coefficients. Several models have been developed to evaluate the accuracy of the forecasts based on the complexity of the forecasting model. For the sake of brevity, only the numerical results of the most accurate forecasting model have been reported. The numerical results consist in the day- ahead forecasts of the entire test data for both working-day and weekend-day considering as the origin time each hour of the day. The accuracy of the method is evaluated through the pinball loss index which shows great accuracy, with a low PLF index for forecasted hours close to the origin time and slightly higher errors for the remaining hours, with the maximum error amounting to 4 kW
Future works will compare the results with a na¨ıve benchmark forecasting method and then a real-time forecast will be implemented.

REFERENCES

[30] Anna Rita Di Fazio, Arturo Losi, Mario Russo, Filippo Cacace, Francesco Conte, Giulio Iannello, Gianluca Natrella, and Matteo Saviozzi. Methods and tools for the management of renewable energy communities: the comer project. In 2022 AEIT International Annual Conference (AEIT), pages 1–6, 2022.
[31] G.C. Reinsel G.E.P. Box, G.M. Jenkins and G.M. Ljung. Time series analysis: forecasting and control. 5th ed. Wiley, 2015.
[32] Sivakavi Naga Venkata Bramareswara Rao, Venkata Pavan Kumar Yellapragada, Kottala Padma, Darsy John Pradeep, Challa Pradeep Reddy, Mohammad Amir, and Shady S. Refaat. Day-ahead load demand forecasting in urban community cluster microgrids using machine learning methods. Energies, 15(17), 2022.
[33] Grzegorz Dudek, Paweł Piotrowski, and Dariusz Baczyn´ski. Intelligent forecasting and optimization in electrical power systems: Advances in models and applications. Energies, 16(7), 2023.
[34]
[35] M. Hadi Amini, Amin Kargarian, and Orkun Karabasoglu. Arima-based decoupled time series forecasting of electric vehicle charging demand for stochastic power system operation. Electric Power Systems Research, 140, 06 2016.
[36] Philippe Lauret, Mathieu David, and Hugo T. C. Pedro. Probabilistic solar forecasting using quantile regression models. Energies, 10(10), 2017.
[37] Ioannis K. Bazionis and Pavlos S. Georgilakis. Review of deterministic and probabilistic wind power forecasting: Models, methods, and future research. Electricity, 2(1):13–47, 2021.
[38] Grzegorz Dudek. Std: A seasonal-trend-dispersion decomposition of time series. IEEE Transactions on Knowledge and Data Engineering, 35(10):10339–10350, 2023.
[39] INGO STEINWART and ANDREAS CHRISTMANN. Estimating conditional quantiles with the help of the pinball loss. Bernoulli, 17(1):211–225, 2011.
[40] Tze Leung Lai, Shulamith T. Gross, and David Bo Shen. Evaluating probability forecasts. The Annals of Statistics, 39(5):2356–2382, 2011.
[41] Nasa power data access. https://power.larc.nasa.gov/.

Dimensional Analysis in NDT&E framework

Tamburrino[1], A. Sardellitti[1], M. Laracca[2], F. Milano[1] and L. Ferrigno[1]

[1] Dept. of Electrical and Information Engineering, University of Cassino and Southern Lazio, Cassino, Italy
Email: {tamburrino, alessandro.sardellitti, filippo.milano, ferrigno}unicas.it
[2] Dept. of Astronautics, Electrical and Energy Engineering, Sapienza University of Rome, Rome, Italy
Email: marco.laracca@uniroma1.it

Abstract

In this work an Eddy Current Testing (ECT) method is proposed for the simultaneous estimation of the thickness and the electrical conductivity of metallic plates. In-line and simultaneous estimation of these parameters is fundamental during industrial production, for quality controls. The proposed method uses dimensional analysis via Buckingham's π theorem. This is the first time that this approach has been applied in the framework of Nondestructive Testing. Experimental tests have demonstrated the effectiveness of the proposed approach, giving excellent accuracy over a wide range of thicknesses and electrical conductivities.

Index Terms

Non-destructive Testing, Eddy Current Testing, Thickness Estimation, Electrical conductivity Estimation, Dimensional Analysis.

V. Introduction

Non-Destructive Testing and Evaluation (NDT&E) issues often entail several different factors. As a matter of fact, the results of an NDT&E test depend on (i) the probe's parameters, (ii) the sample's physical and geometrical parameters, and (iii) the geometrical parameters describing the probe's position with respect to the sample. These issues are challenging to solve considering to the large number of variables involved and the complex nature of these variables.

To this end, a methodology that can reduce systematically the complexity of problems by decreasing the number of variables involved, plays an important role. Dimensional analysis is a mathematical technique for analyzing problems involving physical quantities. Through the application of dimensional analysis, complicated equations may be made simpler by emphasizing the key elements defining a situation.

Within this framework, the celebrated Buckingham's π theorem plays a key role in reducing the number of variables describing a physical problem to its essential by means of dimensionless numbers called π groups [1].

In this contribution we propose a new method for simultaneous estimating of thickness and electrical conductivity of metallic plates based on the Buckingham's π theorem. This contribution highlights how the proposed approach allows to reduce the complexity of the problem while ensuring high accuracy and real-time operations, for on-line simultaneous estimation of thickness and electrical conductivity in industrial applications.

VI. Proposed method and experimental results

The proposed method exploits the Buckingham's π and the related π groups to the simultaneous estimation of the electrical conductivity σ and the thickness Δh of a conducting plate. Specifically, it is possible to prove [2] that the measured impedance $\Delta\dot{Z}$ is related to σ and Δh as follows:

$$\frac{\Delta\dot{Z}(\omega)}{\omega\mu 0D} = F\left(D\sqrt{\frac{\omega\mu_0\sigma}{2}},\frac{\Delta h}{D}\right). \quad (1)$$

Where ω is the angular frequency, μ_0 is the free-space magnetic permeability, and D is a proper reference length. Dimensionless quantities $\Delta Z(\omega)/\omega\mu_0 D$, $D\sqrt{(\omega\mu_0\sigma/2)}$ and $\Delta h/D$ form the three groups π_1, π_2 and π_3, respectively. The estimate of σ and Δh is, then, carried out by plotting in the (π_2, π_3) plane the level curves corresponding to Real(π_1), Imag(π_1), |(π_1)| and φ(π_1). The use of different features is possible because π_1 is related to the mutual impedance (i.e., a complex number).

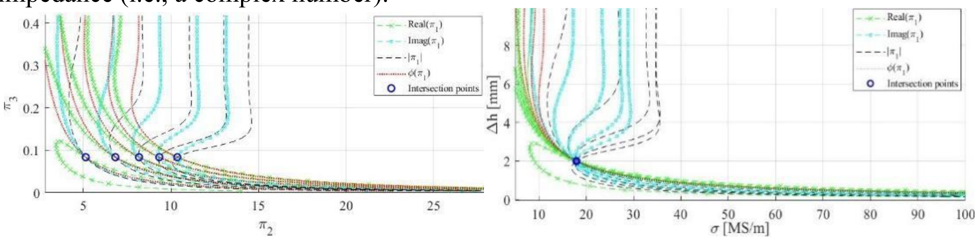

(a) (b)

Figure 1 - Representation of five different frequency measurements in the case of the plate with Δh=2 mm and σ=18 MS/m for the dimensionless curves Re(π1), Im(π1), |π1|, Φ(π1).

The intersection of the curves obtained from the impedance measured at a given ω provide both σ and Δh (Figure 1(a)). When different angular frequencies are analyzed, the point of intersection shift horizontally (see Figure 1(a)). In this case, the level curves are conveniently plotted in the ($\sigma, \Delta h$) plane (see Figure 1(b)) and their intersection directly give the unknown values.

The proposed experimental set-up and the measurement procedure described in [2] was repeated 20 time and the Mean Measured (MM), the Relative Error of the Mean Measured (RE_{MM}), the Standard Deviation (SD_{MM}) of the obtained MM values were evaluated for both thickness (Δh) and electrical conductivity(σ). Table 1 shown the obtained results confirmed the goodness of the proposed method as the relative errors obtained in the estimation of thickness and electrical conductivity estimation reach maximum values under the 3%.

Table 1 – Summary of the obtained results for the thickness and electrical conductivity estimation.

Reference values		MM		SD_{MM}		RE_{MM}	
Δh[mm]	σ [MS/m]	Δh[mm]	σ [MS/m]	Δh[mm]	σ [MS/m]	Δh[%]	σ [%]
0.985	58.50	0.981	58.44	0.087	6.76	0.40	0.10
1.973	28.23	1.983	28.26	0.17	4.82	0.51	0.11
1.030	35.27	1.021	35.77	0.14	4.21	0.91	1.44
3.981	35.91	3.870	36.76	0.19	2.30	2.77	2.38

REFERENCES

[1] E. Buckingham, ‘On physically similar systems; illustrations of the use of dimensional equations,’ Phys. Rev., Vol 4, pp 345–376, 4 1914. [Online]. Available: https://link.aps.org/doi/10.1103/PhysRev.4.345.

[2] A.Tamburrino, A.Sardellitti *et alii*, Old but not obsolete: Dimensional analysis in nondestructive testing and evaluation, NDT & E International, Vol. 141,2024, DOI: 10.1016/j.ndteint.2023.102977.

Effect of fibre orientation on the mechanical response of reinforced sand detected with x-ray tomography.

Michela Arciero[1], Erminio Salvatore[1], Alessandro Tengattini[2], Giuseppe Modoni[1] and Gioacchino Viggiani[2]

[1] University of Cassino and Southern Lazio, Department of Civil & Mechanical Engineering, via G. Di Biasio 43, 03043 Cassino, Italy

Email: michela.arciero@unicas.it

[2] Univ. Grenoble Alpes, Laboratoire 3SR, 1270 Rue de la Piscine, 38610 Gières, France

Abstract

The present laboratory study explores the mechanical behavior of fiber-reinforced sands (FRS), with a focus on the orientation of fibers in relation to principal stress directions. Direct shear and triaxial shear tests were conducted on samples of pure sand and samples with randomly and oriented fibers, all compacted to high relative density. The results indicates that reinforcing sand with oriented fibers increases its sand strength and ductility.

Additionally, a micro-scale analysis was conducted with X-ray tomography. This revealed the significance of fiber orientation within the shear band. When properly activated, fibers alter the strain distribution, preventing brittle failure along the shear plane and enhancing the overall response of the reinforced material to be more dilatant and ductile.

Index Terms

Fibre reinforced sands; strain localization; X-ray tomography; porosity; dilatancy.

I. INTRODUCTION

Numerous studies have explored fiber reinforced sands (FRS) to enhance properties like resistance, stiffness, and ductility in geotechnical structures, typically focusing on factors as soil type, fiber characteristics, and ground improvement optimization. This study combines element scale analysis observed with classical laboratory geotechnical testing – direct shear and triaxial tests – and micro scale analysis detected with X-ray tomography to understand the role of fibers in reinforced sands, especially considering fibers orientation concerning localized strains during shearing. To achieve this aim, several tests varying fibers orientation were conducted, always comparing the results with natural sand behavior response.

The reinforcement of sands by a diffuse inclusion of fibres is promoted by the idea that filaments of controlled mechanical characteristics intruded in the soil pores, somehow, inhibit the mobility of grains, provide additional properties to the assembly (e.g., resistance, stiffness, ductility or damping) and improve the performance of geotechnical structures [1],

[2], [3]. An investigation of the soil-fibres interaction would disclose the mechanisms that take place locally and affect the global behavior of the soil assembly, providing great benefits for the reinforcement's design and for performance predictions.

II. Experimental tests and results

A. Element scale response

Direct shear and triaxial tests were carried out on samples of natural sand (Hostun sand HN31) and reinforced sand with fluorocarbon fibres with concentration χf=0.50%, and length lf=30mm (for DS) and lf=10mm (for TX).

For Direct Shear test, square prismatic samples were formed with base and height respectively equal to 60 and 30 mm (as described in ASTM D3080-04). Three sets of samples were prepared, one with natural sand, another with randomly oriented fibres, and one with fibres oriented along 45° angle with respect to the shear plane, i.e., along a direction close to the minimum principal stress. For miniature triaxial test cylindrical specimens were prepared with diameter and height equal to respectively 11 and 22mm. The samples were packed with randomly oriented fibres and horizontal fibers (always correspondent to the minimum principal stress direction).

Fig. 1 shows the positive role of fibres reinforcement and, more specifically, of their orientation. The samples with oriented fibres show a higher strength, (almost double compared with the unreinforced soil), but a different global response. The response is a more ductile, the peak being reached at larger displacements, and dilatancy develops with lower rates compared with the randomly oriented fibres, but for a longer period throughout the test. The volume change of oriented fibers samples is globally higher than for the unreinforced soil and for the randomly oriented fibre reinforcement.

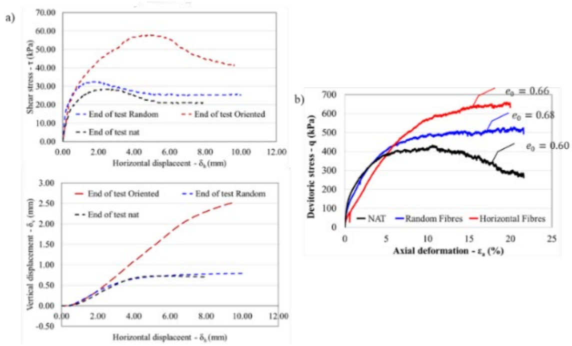

Fig. 1: (a) Direct Shear Test (DS) and (b) Triaxial test (TX) mechanical response.

B. Microscale analysis

Fig. 2 shows DS test micro analysis results. Porosity maps show that fibre-packed samples have a more heterogeneous initial porosity field due to the more open structure at the fibre-grain interface. The differences become progressively clearer with sample deformation. At peak and ultimate conditions, volumetric strain in the natural sand sample localizes in a narrow sub-horizontal band, imposed by the equipment, while the fibre-packed samples show a much more diffuse volumetric deformation with higher values at the interface between grains and fibres. This diffusion effect is considerably more pronounced for the sample with fibres oriented at 45°.The sample with random fibres, on the other hand, shows a response intermediate between the other two cases, showing a clear horizontal shear band as well as the formation of voids related to the local fibre orientation.

Fig. 3 shows TX tests microscale results. For natural and FRS samples, it is possible to identify a central region where there is an evident variation of porosity (samples in yellow), especially after 8% of axial strain. The region that changes in porosity tends to take the form of an oblique band, inclined at approximately 45°, indicating a dilatant shear band. In the case of FRS sample, a greater volume is involved in the deformation, which suggests that fibres can mobilize a greater number of grains. The fibres represent an element of interconnection between grains. The incremental field of the first and second invariant of the strain tensor, i.e., the volumetric and maximum shear strain, are also reported, for each loading step (Fig. 3). As deformation increases, a shear band develops. This indicates that homogeneity is lost from very low strain values and a dilatant shear band develops.

In summary, fibre orientation affects the pattern of displacement fields, and fibres hinder localized shear bands, extending them. Fibres can mobilize larger tensile forces, generating diffused strain localization.

Fig. 2

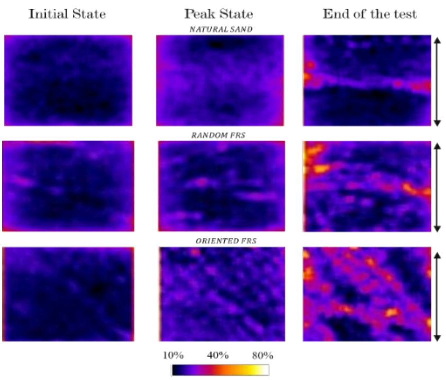

Fig. 3

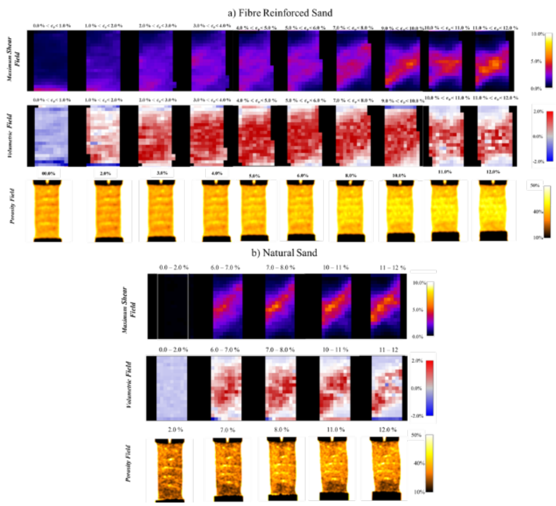

Fig. 2: Porosity fields determined by DS tests in the initial condition, at peak and ultimate state.

Fig. 3: a) Maximum shear strain, volumetric strain and porosity field for FRS sample subjected to TX test; b) Maximum shear strain, volumetric strain and porosity field for natural sand sample subjected to TX test.

III. Conclusion and perspectives

Fibre orientation plays a key role in fiber reinforcement. Fibres must undergo tensile stress to produce enhancement, therefore, they must be oriented to ensure maximum interaction with the shear bands, along the minimum principal stress direction.

Porosity and strain are more homogeneous and diffuse in the presence of fibres and the shear band thickness is larger.

References

[1] Gray, D. H., & Ohashi, H. 1983. Mechanics of fiber reinforcement in sand. Journal of geotechnical engineering, 109(3), 335-353.

[2] Maher, M. H., & Ho, Y. C. 1994. Mechanical properties of kaolinite/fiber soil composite. Journal of Geotechnical Engineering, 120(8), 1381-1393.

[3] Park, T., & Tan, S. A. 2005. Enhanced performance of reinforced soil walls by the inclusion of short fiber. Geotextiles and geomembranes, 23(4), 348-361.

Local seismic response in complex geological conditions

Vincenzo Colagiacomo[1], Michele Saroli[2], Matteo Albano[3], Matteo Fiorucci[4]
[1]Dept. of Civil and Mechanical Engineering, University of Cassino and Southern Lazio, Cassino (FR), Italy, Email: vincenzo.colagiacomo@unicas.it
[2]Dept. of Civil and Mechanical Engineering, University of Cassino and Southern Lazio, Cassino (FR), Italy
INGV-Istituto Nazionale di Geofisica e Vulcanologia, Rome, Italy
Email: michele.saroli@unicas.it
[3]INGV-Istituto Nazionale di Geofisica e Vulcanologia, Rome, Italy, Email: matteo.albano@ingv.it
[4]Dept. of Civil and Mechanical Engineering, University of Cassino and Southern Lazio, Cassino (FR), Italy, Email: matteo.fiorucci@unicas.it

Abstract

Local seismic response (LSR) analysis and microzonation studies represent fundamental tools for assessing and mitigating seismic risk in urban areas.

In particular, LSR studies and quantifies the modifications of the seismic motion, in terms of amplification or deamplification, caused by its passing through lithologies characterized by different rigidity, going from the earthquake source (hypocentre) to a specific point near, or on the surface. Effects of such modifications have an important impact on the structures.

Numerical analyses, although originating in the '70s, have fully entered Italian technical legislation starting from the D.M. 14/01/2008 (so-called NTC08) and, in particular, in Lazio Region they had a further impulse first from the D.G.R. n. 489/2012 and then from the following regional laws that integrate and/or modify it. Furthermore, Lazio Seismic Regional Regulation n. 26 (D.G.R. n. 724/2020) introduces for the first time as mandatory the two-dimensional LSR approach in some specific stratigraphic and morphologic conditions. On a territorial planning level, numerical analyses are strictly required to realize level 3 seismic microzonation studies [1].

This research project, through LSR analyses of 1D and 2D seismic modelling of the Cassino centre area [2], aims first of all to quantify the variability in the results deriving from the two approaches and in a second phase will estimate the impact of the so calculated seismic effects at ground on civil structures. From an operational point of view, the first step is to build a GIS project containing old geological, geotechnical and seismic investigations, together with new seismic noise measurements [3] specifically realized in the frame of this project. This latter will allow to parameterize lithologic units as requested from LSR modelling and to identify the depth of the seismic bedrock [4] under the surficial soft-soil deposits. Furthermore, seismic noise measurements on a sample of civil structures, chosen on the basis of parameters that can affect their vibration frequency (shape, age of construction, number of floors, construction materials), will allow the classification of those structures according to the impact that the ground motion, previously estimated with LSR methods, might have on them.

The results of this study and its approach could be crucial in influencing future project choices or in the field of Civil Protection where territorial emergency plans should provide accurate risk scenarios.

REFERENCES

[1] Floriana Pergalani, Dario Albarello, Marco Amanti, Vittorio Chiessi, Massimo Compagnoni, Roberto De Franco, Anna D'Onofrio, Sebastiano Foti, Iolanda Gaudiosi, Giuseppe Lanzo, Lucia Luzi, Claudia Madiai, Giuliano Milana, Guido Martini, Salvatore Martino, Alessandro Pagliaroli, Francesco Silvestri, Marco Tallini, Chiara Varone. *Modellazione della risposta sismica locale in configurazione 2D*. Centro per la Microzonazione Sismica e le sue applicazioni. Protocolli di acquisizione ed elaborazione dati relativi alle attività di Microzonazione Sismica di livello 3 in Italia Centrale, pp. 72-84, Roma: Cnr Edizioni, 2020.

[2] Michele Saroli, Michele Lancia, Matteo Albano, Giuseppe Modoni, Marco Moro, Gabriele Scarascia Mugnozza. *New geological data on the Cassino intermontane basin, central Apennines, Italy. Intermontane basins in central-southern Italy.* Rend. Fis. Acc. Lincei. Volume 25, Issue 2 Supplement, pp. 189-196, 2014.

[3] S. Molnar, A. Sirohey, J. Assaf, P.Y. Bard, Silvia castellaro, C. Cornou, B. Cox, B. Guillier, B. Hassani, H. Kawase, S. Matushima, F.J. Sanchez-Sesma, A. Yong. *A review of the microtremor horizontal-to-vertical spectral ratio (MHVSR) method.* J. Seismol 26, 653-685, 2022.

[4] Michele Saroli, Matteo Albano, Giuseppe Modoni, Marco Moro, Giuliano Milana, Rose-Line Spacagna, Emanuela Falcucci, Stefano Gori, Gabriele Scarascia Mugnozza. *Insights into bedrock paleomorphology and linear dynamic soil properties of the Cassino intermontane basin (Central Italy)*. Engineering Geology, Volume 264, 1-17, 2020.

Methods and procedure of analysis of minor historical centers for safeguard and enhancement.

Laura Lucarelli
[1]Laboratory of Documentation, Analysis, Survey of Architecture and Territory, Cassino, Italia
Email:
laura.lucarelli@unicas.it

Abstract

This contribution is focused on an area of southern Lazio which includes the territories of the so-called Land of Saint Benedict and Comino Valley. These territories have valuable characteristics from the environmental and historical construction point of view. Is part of a research path carried out within the Laboratory of Documentation Analysis Survey of Architecture and Territory (DART) at the University of Cassino and Southern Lazio which deals with analysis of the historical centers of the southern Lazio, from architectural to environmental emergencies.

Index Terms

minor historical centers, Atina, Comino Valley, cultural heritage, urban analysis

I. Introduction

The Italian territory is dotted with a continuous network of small historical centers which characteristics can vary within just a few kilometres. This work aims to create a catalog of these centers in order to deepen the knowledge of the built environment. A scientific exploration of the territory carried out in a systematic and objective way. Through the synergy between conservation and revitalization, which safeguards and prevents negative impacts, this research aims to experiment a methodology for an in-depth analysis of historic centers in order to enhance them. This approach will be initially applied to the territory of the land of Saint Benedict (Fig. 1) [2] [4] located in southern Lazio. In ancient time it was a strategic location for communications between the central and southern parts of Italy. The territory was donated in the mid-8th century by the Duke of Benevento to the Montecassino monastery and later named Terra Sancti Benedicti [6]. Its morphology consists of a flat area, formed by the valleys of the Rapido and Liri-Garigliano rivers, and a mountainous area composed of the Abruzzo Apennines to the north and the Aurunci Mountains to the south. The choice of this study area is due to several factors:

- the way in which the territory has formed and evolved over time
- its strategic location within the region
- the presence of historical centers with a high historical and cultural value.

Its territory includes many municipalities, some of which belong to the so-called "Valle dei Santi" and the nearby "Valle di Comino". This offers a potential sampling of minor historical centers, a significant aspect of the regional territory. The convergence of multiple concurrent factors like the mountainous nature of these settlements and their belonging to an "inland area", the absence of formerly catalogued data and the needs suggested by the regional administration, has also made this choice appropriate. The methodology identifies the steps to set up analyse and intervention hypotheses for minor historical centers. It can then be expanded and adapted to different regional contexts as well as other territorial realities.

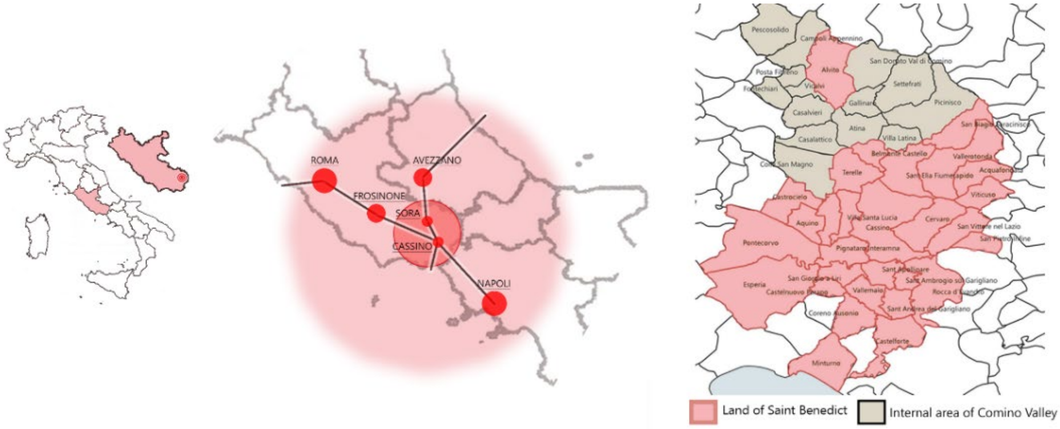

Fig. 1: Study area location.

II. METHODOLOGY

The logical order for the study of this territory is multi-scalar and multidisciplinary (Fig. 2), but the main focus is on urban centers, in their morphological and typological characteristics. The analysis of these characteristics, together with the ways in which they are represented, forms the specific approach of the study. [7]

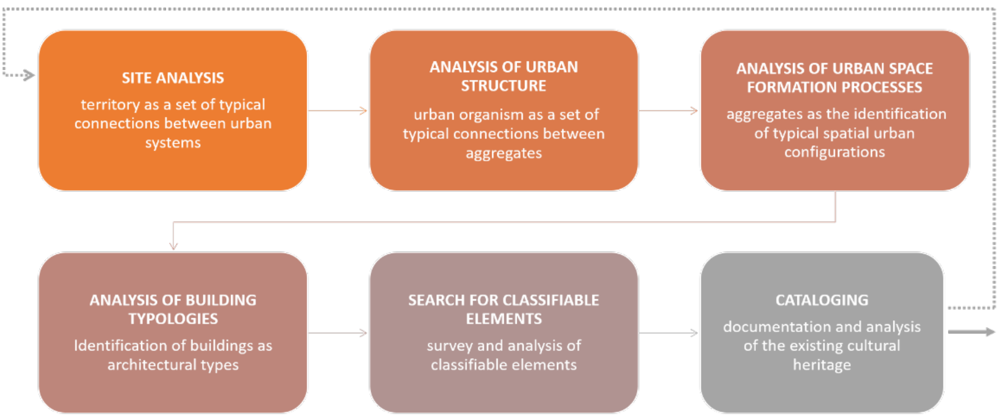

Fig. 2: Synthesis of the knowledge path.

The initial knowledge operations aim to study the location through territorial and historical analysis. Different layers and any events that have impacted the form of the territory and the built environment are examined. This step helps in understanding the urban structure of the area, along with its formative process. The next step involves scaling down from the territorial level to that of the historical center. Position, shape, and types of pathways of the historic center are investigated in relation to the natural features of the site. A particular type of analysis which helps to understand the structure and connectivity of historical centers is Space Syntax. This translates the urban spatial dimension into a network of relationships, breaking down spaces into components and representing them as maps or graphs describing the connectivity of these spaces (Fig. 3).

Fig. 3: Atina: filled and empty spaces of the historic center.

The methodological approach involves the development of the following steps:

A. Characteristics of settlement analysis in historical centers

The first step concerns the general framework of historical centers within their polycentric system. The close relationship that these centers have with the landscape in which they are located calls for specific and careful knowledge of the territory [5]. The analysis highlights a relation between the centers and the hydrographic characteristics of the site (Fig. 4), the initial layout and subsequent developments distinguished by recognizable typological-morphological phases (Fig. 5).

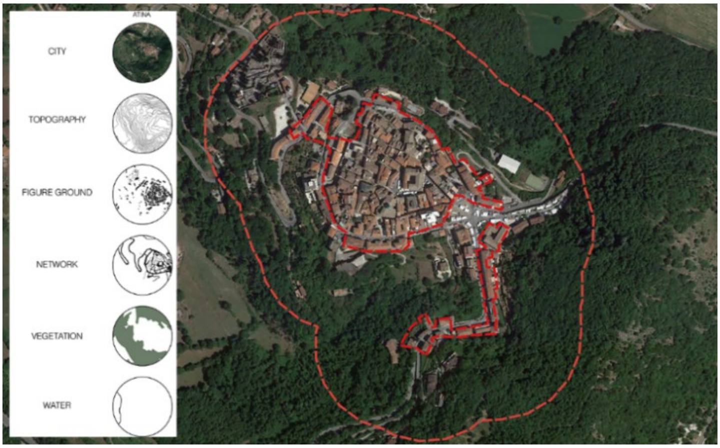

Fig. 4: Aerial photo with the perimeter of the historical center of Atina and its buffer zone.

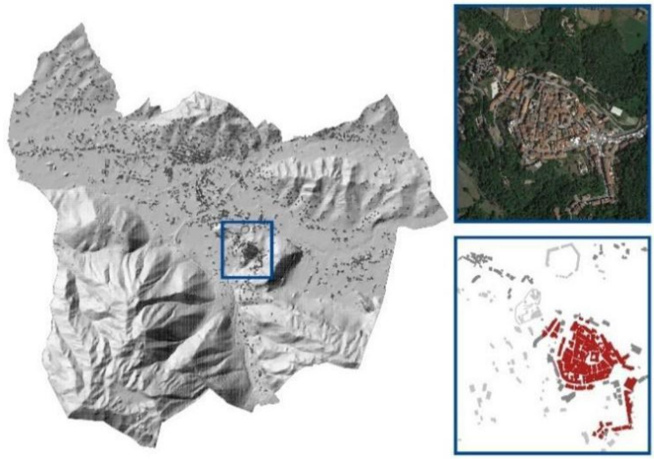

Fig. 5: Digital Elevation Model (DEM) of Atina territory. Urban morphology of Atina.

B. Analysis of the typological and construction characteristics of historic buildings

After a brief historical/geographical overview, the second step deepens the knowledge of the current state in order to identify specific architectural highlights (Fig. 6). The analysis leads to the classification of the existing architectural types and the identification of their distribution, both in their original forms and as altered types. It also highlights transformations that are consistent with the historically established built environment and those that are, on the contrary, inconsistent or detrimental.

Fig. 6: Identification of historical, religious, and monumental buildings in Atina.

Building aggregates on which to work are identified in order to recover their use and restore their formal and typological unity, defining the intervention units. These are portions of the urban layout characterized by their own architectural and functional features (Fig. 7).

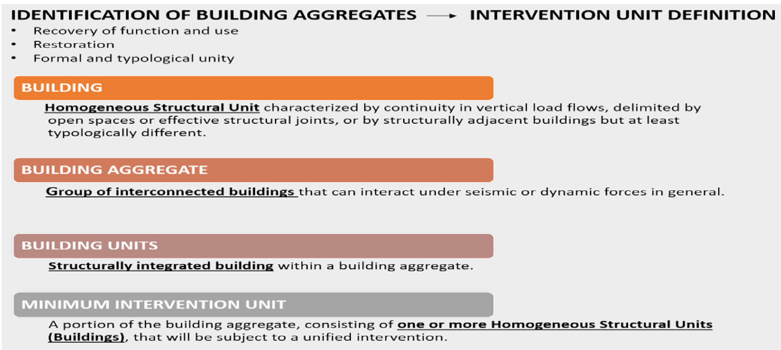

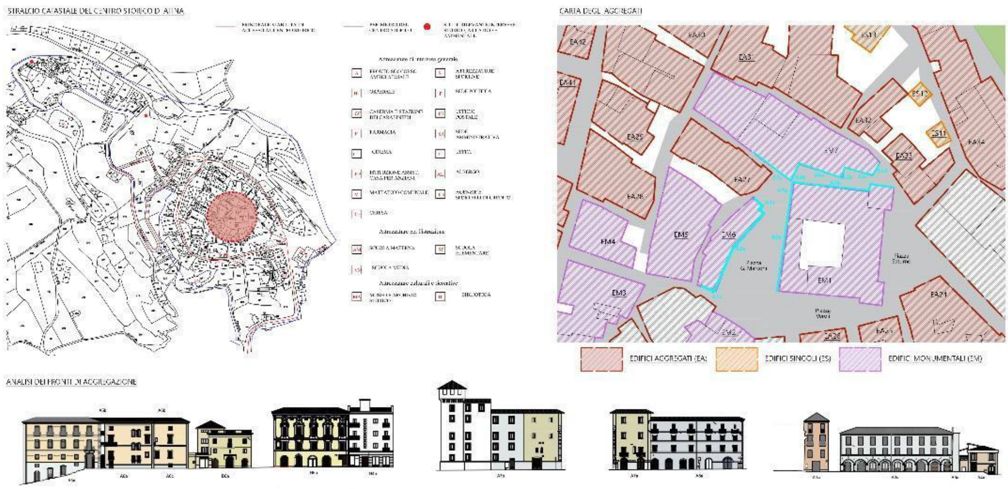

Fig. 7: Building aggregates of the historical center of Atina [3]. Reworking of "Progetto di recupero e risanamento di abitazioni nel centro storico di Atina" [1].

As Chapter 8 of the NTC 2018 (Fig. 8) reminds us, adequate and accurate knowledge of the structure is a fundamental prerequisite and an essential moment to understand individual critical issues and structural behaviour. Vulnerability, in consolidated areas, depends on numerous factors:

- the characteristics of settlement sites, often marked by geomorphological and seismic criticalities
- the use of specific construction techniques
- subsequent stratifications
- functional and structural modifications
- contiguity of buildings in complex aggregates, and the resulting structural interactions and dynamic effects
- the morphology of pathways and open spaces

For this reason, over time, there has been a true evolution of the concept of vulnerability from the analysis of individual Structural Units up to the aggregate and the entire urban center. So it is an extension both in terms of scale and in terms of concept.

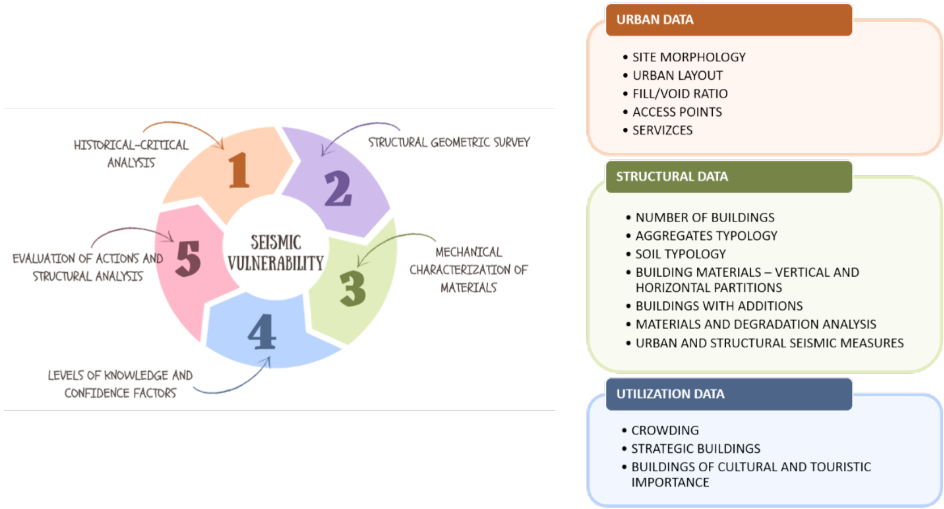

Fig. 8: Reconstructed framework based on the reference model for analyses of existing buildings from NTC 2018.

C. Urban Recovery Hypotheses

As a complement to this type of analysis, where necessary, a detailed representation of the architectural particulars that characterize the buildings is developed. Accurate technological and structural surveying is indispensable in interventions on historical structures because, if the goal is preservation, it can only be achieved with a full knowledge of what needs to be preserved. This survey, in detail, examines all the construction solutions concerning foundations, masonry, ceilings, roofs. This model allows the creation of a catalog of typical and traditional architectural elements that can be used as a basis for a restoration project as well as the replacement or reconstruction of individual elements (Fig. 9). The final step concerns the intervention parameters which aim to requalify and enhance the urban context. Taking into account the state of preservation and the greater or lesser architectural, environmental, and cultural value of each building, as well as their degree of adaptability, protection levels can be defined, for each structure, to identify possibilities and methods of intervention. Protection levels can be defined in accordance with the state of preservation, the value of each building, and their degree of adaptability.

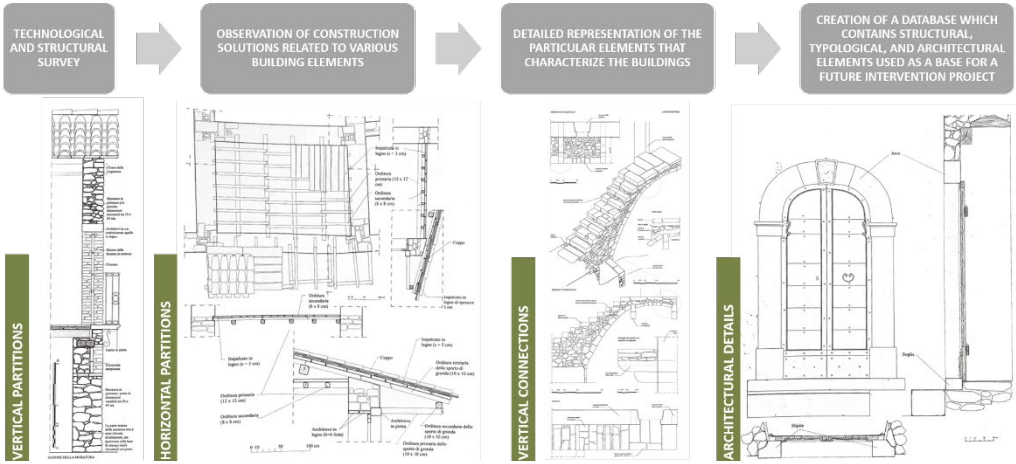

Fig. 9: Example of elements abacus, reworking of "Piano di ricostruzione comune di Castelli post terremoto del 6 aprile 2009"

Preservation and restoration elements of historic buildings that still retain their original characteristics will be identified, providing precise instructions, including the catalog of architectural and structural elements (Fig. 8) [13] [14]. Interventions should preferably be carried out through the development of a unified project which maintains the autonomy of the territorial portions and the buildings falling within. In any case, any type of intervention should aim to achieve the following fundamental objectives:

- preservation of physical integrity and enhancement of the cultural identity of historical centers.
- maintenance or restoration of the urban layout.
- protection, enhancement, and revitalization of the basic minor building heritage.
- integration of missing facilities and services, in accordance with the morphology of the urban layout as well as the typological and stylistic architectural characteristics of the historic building heritage.

III. Results

This study, besides providing a detailed and in-depth analysis of the historical evolution of the territory, it also aims at conducting a census of the main cultural heritage existing in the area. This approach recognizes that the relationship between architectural typology and urban morphology is the focal point where the identity of an urban reality is concentrated. An expansion of the concept of recovery, extended to the entirety of buildings, vacant spaces, and public areas. The concept of conservation extends from the individual building to all of the spaces that constitute the urban reality, in an ambivalent shift in scale, from the architectural to the urban planning level, and vice versa. By expanding the knowledge of the selected territory as a system of urban centers, it reveals the environmental characteristics and historical values that now represent an asset to be transformed into opportunities. The preservation of this heritage on one hand, and its enhancement through targeted interventions for better utilization on the other, aim to avoid polarization towards the more functionally important centers. This can be done with a territorial competition that take the form of a horizontal network which restores geographical, morphological, and cultural unity. PRODUCT: Hypothesis for recovery interventions to be carried out through a collection of guidelines related to technological and performance adaptation in relation to evolutionary characteristics, environmental compatibility, and the context. The enhancement of cultural heritage consists of all activities which seek to promote the knowledge of the national heritage and ensuring its best conditions of use and fruition [11]. Among the objectives aimed at enhancing the territory, also shared by the most recent development policies, we find:

- enhancing cultural heritage
- regenerating and revitalizing the small villages (fig. 10) in order to increase their attractiveness
- strengthening the identity of lesser-known destinations, also by directly involving local communities
- increasing social and economic development in more fragile territorial contexts
- promoting circular and sustainable reuse of spaces and buildings
- a 4.0 tourism

Fig. 10: Photomosaic of some of the historical centers of the study territory.

REFERENCES

[1] Marco Centofanti, Michela Cigola, Fabio Dalmi, Carlo Giannandrea, *Progetto di recupero e risanamento di abitazioni nel centro storico di Atina, 2011.*

[2] Michela Cigola e Arturo Gallozzi. *"L'abbazia di montecassino nei secoli X-XIII e l'incastellamento della Terra di S. Benedetto"*, in Atti del I Colloquio internazionale "Castelli e Città Fortificate" De' Castelli di pietra e di ... cristallo, Università di Trieste e Udine, Udine ottobre 1999, pp. 114-118.

[3] Michela Cigola, Arturo Gallozzi, Stefano Petrucci, Davide Sansovini, Luca Senatore, Rodolfo Maria Strollo. *Citizen science, gamification, fotogrammetria per il contrasto al rischio di oblio dei beni culturali minori.* Archeomatica 8(3), pp. 10-15, 2019.

[4] Luigi Fabiani. *La terra di S. Benedetto: studio storico giuridico sull'Abbazia di Montecassino dall'8. al 13. Secolo, (Miscellanea Cassinese, 42),* Montecassino: Badia di Montecassino, 1980.

[5] Luca Maria Franchina, *La nuova questione dei centri storici in Italia. Una ricognizione: nella letteratura, nelle politiche e urbanistiche, nei progetti,* Milano: 2010.

[6] Arturo Gallozzi (ed), *Territorio, città e architettura. Montecassino e Cassino*, Arte Stampa Editore, 2020.

[7] Laura Lucarelli, *Knowledge and exploitation of local resources: the historical centers of the Comino Valley*, Tafter Journal n. 122, Giugno-Luglio 2023.

[8] Laura Lucarelli, *Instrumentos de conocimiento para salvaguardar y valorar los centros históricos menores*, ReUSO XI, in pubblicazione, 2023.

[9] Paolo Marconi, *Il restauro e l'architetto*, Padova: Marsilio, 1993

[10] Regione Lazio, Assessorato all'urbanistica. (Ed.). *Oltre la tutela, 70 interventi al cuore dei comuni. Recupero dei centri storici del Lazio. Programma 2008*, Roma: Palombi Editore, 2009.

[11] Francesca Romana Stabile, *Cultura dei luoghi e recupero dell'edilizia storica in Centri storici minori. Progetti per il recupero della bellezza*, Roma: Gangemi editore, 2009.

[12] Rodolfo Maria Strollo, "*Disegno e restauro: conoscenza analisi intervento per il patrimonio architettonico e artistico*" in collana di Studi e Ricerche sul Disegno dell'Architettura e dell'Ambiente, Roma: Aracne Editrice.

[13] Luigi Zordan, *Lettura tipologica del costruito, metodologia critica e strumenti operativi*, in Centri antichi minori d'Abruzzo: recupero e valorizzazione, Roma: Gangemi Editore, 1996, pp. 316-364.

[14] Luigi Zordan, Alessandra Bellicoso, Pierluigi De Berardinis, Gianni Di Giovanni, Renato Morganti, *Le tradizioni del costruire della casa in pietra: materiali, tecniche, modelli e sperimentazioni*, L'Aquila: GTE, 2002.

APPLICATIONS OF COMPUTATIONAL MODELS IN GEODESY

V. Manzari [1]

[1] University of Cassino and Southern Lazio, Department of Civil and Mechanical Engineering - Via G. Di Biasio 43, 03043 Cassino. “Dottore di ricerca in Metodi, Modelli e Tecnologie per l’Ingegneria - XXXIV Ciclo”

Abstract

The calculation of the gravitational effects due to given mass distributions is a fundamental problem in the applications of geophysics and geodesy.

Potential Theory can only be partially used in geophysics: in gravity, magnetism, methods of calculating electromagnetic, electrical heat flux, and calculating the flux of fluids. Therefore, potential Theory, with the use of complex mathematical tools, constitutes the basis for the solution of various geophysical problems, managing in fact to be almost indispensable to better understand some geophysical data.

Potential Theory has for object the mathematics of equilibrium and, in particular, the study of harmonic functions, given their fundamental role in equilibrium problems in a homogeneous medium.

The advent of Inverse Theory has revolutionized the whole procedure for interpreting geophysical data. This was made possible thanks to the very rapid development of computer science, technology that has improved calculation software, and the numerous methods used in mathematical modelling.

In the thesis work I will present new expressions for the gravitational potential that involve alternative and less expensive computational capabilities than those reported in the specialized literature.

I will show that the singularities that can influence the computation of the effects of gravity (potential, gravity, and tensor gradient fields) can be systematically addressed by invoking the theory of distribution with suitable differential calculus formulas.

The general approach will be led with reference to the case of models of polyhedral bodies, regular or not, having either a constant or a depth-relative mass density.

The validated analytical formulas have been fully confirmed by applications with Matlab® programs, coded and carefully tested by calculating the effects of gravity induced by attractive bodies positioned in arbitrary observation points. The formulae illustrated in the thesis have been numerically checked with the alternative ones derived on the basis of different approaches, already established in scientific literature, intensively and repeatedly testing the effects of gravity induced by real attractive bodies with arbitrarily assigned density variations.

The efficiency of the proposed formulae lies in the ability to correctly evaluate the singularities that arise in cases where the attracted points occupy different positions of the

attractive mass.

The research activity was further implemented with the introduction of analytical formulations based on the approximation of the ground masses with shapes of vertical prisms considered as prisms with polynomial density.

The gravitational anomaly associated with a polyhedral body of arbitrary geometric shape and with different values of polynomial density in both horizontal and vertical directions is analytically evaluated. The gravity anomaly is evaluated at an arbitrary point that does not necessarily coincide with the origin of the reference system in which the assigned density function is located.

It has been established that the density contrast is comparable to exponential polynomial functions of higher order than the third. By invoking the recent results of Potential Theory, the solutions have proved to be devoid of singularities and are expressed as the sums of algebraic quantities that depend only on the vertices of the polyhedron and on the density function of the polynomial. The accuracy, robustness and effectiveness of the approach can be demonstrated with numerical calculations on the basis of examples derived from the existing literature.

Index Terms

Potential Theory, geophysical data, gravitational potential, polyhedral bodies, density contrast, tensor calculus, polynomial functions.

I. NEW ANALYTICAL EXPRESSIONS OF THE GRAVITATIONAL POTENTIAL

The research was focused on the elaboration and implementation of new analytical expressions for calculating the gravitational potential and its first and second order derivatives, as a consequence of the gravity pull of the distribution of masses represented by a Digital Terrain Model (DTM).

II. NEW EXPRESSIONS OF THE GRAVITATIONAL POTENTIAL AND OF ITS DERIVATIVES FOR PRISMATIC SOURCES SECTION

The modelization of the sources of gravity in the form of prismatic bodies for determining the gravitational effects due to a determined mass distribution has always had a very important role, especially in cases where the so-called "flat-Earth" approximation is sufficiently applicable. However, the analytic expressions previously used by diverse authors generate singularities what the calculation of the potential is determined correspondingly to the vertices of the prism. A similar situation arises whenever a polyhedral body is concerned.

Recent formulations have been elaborated for calculating the potential and its gradients in the case when the observation point P coincides with a vertex of the prismatic polyhedron. The formulae resulting, thanks to Gauss's law, show how the relevant singularities can be appraised without recurring to artificial adjustments.

The result has been reached by transforming volume integrals, the well-known Newton integral [1]:

$$U(P) = G\delta \int_{\Omega} \frac{1}{(r \cdot r)^{1/2}} dV \qquad (1)$$

As the sum of surface integrals extended to each of the faces of the prism, therefore expressing each of the surface integrals as the sum of linear integrals extended to the vertices of each of the generic faces of the prism.

The approach is based on the so-called “theory of distributions” that enable an identification and eventually a resolution of the singularities thanks to a double application of Gauss’s theorem.

III. New expressions of the Gravitational Potential for polyhedral sources

The hypothesis on which the applications are based is the one according to which the generic ridge of the polyhedral body does not contain the origin of the local frame of reference of the generic face of the polyhedron. In this hypothesis the integrals will give results devoid of singularities.

The numerical applications implemented in Matlab® have confirmed the hypotheses.

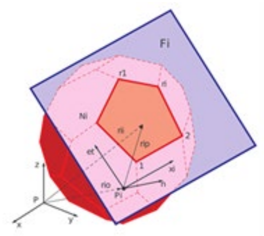

Fig. 1: Bidimensional reference framework of a polyhedral body.

IV. The gravitational effects of linearly variable density polyhedral bodies

The approach taken for calculating the gravitational effects of constant density polyhedral bodies can be extended to the case of linearly variable density bodies, while attentively assessing the relative singularities. The constant density polyhedron has been repeatedly analyzed. However, the constant density hypothesis is hardly realistic. [2]

Let us consider, for example, that a sedimentary basin, in the course of its geological evolution, has undergone a compacting, as a result of which the density generally increases with depth. This consideration has led various authors to study the gravitational effects produced on bodies that have a linearly variable density in two or three dimensions.

The degree of complexity of the analyses has gone so far as to examine modelizations of exponentially varying densities as well. Moreover, from vertical, depth-oriented variations of density, various authors have begun to consider more complex distributions of density, both vertical and horizontal. The modelization of bodies has become a problem of primary importance, so that the modelization of prismatic bodies has led to the modelization of polyhedral bodies. Therefore, the study of gravitational effects has been extended to the case of linearly variable density polyhedral bodies, while taking into account the relevant singularities that are occasionally emerging.

In particular, analytical formulae for the gravitational potential and for the related first and second order derivatives have been reached [3] as the sums of values represented by unidimensional integrals extended to the generic edge of the polyhedron. Besides, thanks to the theory of distributions [4], the singularities in calculating the gravitational effects have been calculated exactly, independently of the position of the point of observation.

The same approach has been applied, in D'Urso and Marmo [15], to problems of geomechanics and one problem of geophysics.

In [5], the analytical formulae for calculating the gravitational effects of polyhedral bodies of linearly variable density have been expressed as explicit functions of the coordinates of the vertices of the relative faces, or with the basic geometrical data used to define the polyhedral body. The author has demonstrated that, with this method, only the second order derivative of the potential can present singularities, and this happens if and only if the point of observation is aligned on one of the edges of the polyhedron.

Take for instance an arbitrary limited domain, of which the continual mass distribution has a density δ(s) linearly variable according to position vector s applied arbitrarily in one or the other of its points. Therefore: δ(s) = δo + g · s; where δo is a constant reference density assessed at the origin O of a tridimensional Cartesian coordinate system (O, x, y, z), in which the coordinates of s are given; in addition, vector g represents the gradient of the linear law (s).

The gravitational potential, if p indicates the position vector of an arbitrary point P, can be expressed as:

$$U(P) = U_{(p)} = G \int_{\Omega} \frac{\delta_{(s)}}{[(p-s)\cdot(p-s)]^{1/2}} dV_{(s)} \tag{2}$$

where G is the gravitational constant.

The first order derivative of the gravitational potential is expressed as:

$$d_p\, U(P) = G \left\{ -(\delta_0 + \boldsymbol{g}\cdot\boldsymbol{p}) \sum_{i=1}^{N_F} \left(l_{F_i} - |d_i|\alpha_i \right)\boldsymbol{n}_i + \frac{1}{2}\sum_{i=1}^{N_F} d_i\, F_{F_i} g \right\} \tag{3}$$

The particularity of this expression consists in the fact that it depends only on the tridimensional coordinates of the vertices of the polyhedron, and it is demonstrated that it does not generate singularities, thus avoiding the introduction of the small corrective coefficients admitted by some authors in other expressions so as to avoid indefinite operations.

The gravitational tensor, i. e. the second order gradient of the potential in P is obtained by differentiating the expression of the first order derivative mentioned above, to obtain, by means of apposite substitutions, the expression:

$$\mathrm{d_p}\,(\mathrm{Ag}) = -\sum_{\mathrm{i=1}}^{\mathrm{N_F}}\left[\mathrm{F_{F_i}}(\mathrm{g}\otimes n_i)\right] \tag{4}$$

The integral appearing in the expression of FFi is indefinite when the point of observation P is aligned with any one of the edges of face Fi. The second order derivative of the potential of a linearly variable density polyhedral body shows the same type of singularity that characterizes constant density.

However, contrarily to this latter case in which the singular terms were confined to the non-diagonal entries, the singularity can now influence all the entries of the matrix associated to the second order derivative.

V. GRAVITATIONAL ANOMALIES

VI. GRAVITATIONAL ANOMALY OF A 2D BODY

It is extremely advantageous to dispose of analytical solutions of the gravitational anomaly associated to a body characterized by complex distributions of gravity. However, given the mathematical complexity of the problem, the gravitational anomaly of an irregular body, of which the density is spatially variable, has first been calculated by approximating the body as an ensemble of vertical rectangular parallelepipeds (prisms) in which the density is presumed to be constant.

Consequently, the gravitational anomaly of the entire body is calculated as the algebraic sum resulting of all the vertical prisms of appropriate depth and of the distances from the observation point. The calculations and the numerical verifications were accomplished for the first time by Talwani et al. (1959) and Bott (1960). The closed expressions of the gravitational anomaly were successively derived by Nagy (1966), Banerjee and DasGupta (1977), Cady (1980), Nagy et al. (2000), Tsoulis (2000), Jiancheng and Wenbin (2010), D'Urso (2012), Plouff (1975, 1976), Won and Bevis (1987), Montana et al. (1992) for the computer codes.

An analytical expression of the gravitational anomaly for polygonal bodies of which the density variation is expresses as a polynomial function with an arbitrary coefficient in both the horizontal and the vertical directions has recently been obtained by reducing the integral of the original domain to an edge integral according to Gauss's theorem generalized and successively applied to various problems of geodesy, geomechanics, geophysics, and heat transfer. The gravitational pull exerted by a tridimensional body $\widehat{\Omega}$ on a mass unit in O is given by:

$$\boldsymbol{g}(O) = G\int_{\widehat{\Omega}} \frac{\Delta\rho(\boldsymbol{r})\boldsymbol{r}}{(\boldsymbol{r}\cdot\boldsymbol{r})^{3/2}}\,dV \tag{5}$$

Where G is the gravitational constant, r is the position vector that starts in O and ends in a generic point of $\widehat{\Omega}$, and $\Delta\rho$ (r) is the density contrast in r. The product of $\Delta\rho$ (r) dV (r) represents the infinitesimal difference between the mass in r and the remain-ing part of the volumetric mass density. The interest resides in the bidimensional problem, as indicated in figure 15, where Ω indi-cates the section of $\widehat{\Omega}$.

The vertical component g_z (O) is given by the formula:

$$\boldsymbol{g_z}(O) = G \int_{\widehat{\Omega}} \frac{\Delta\rho(\boldsymbol{r})\boldsymbol{r}\cdot\boldsymbol{k}}{(\boldsymbol{r}\cdot\boldsymbol{r})^{3/2}} dV \tag{6}$$

in which k is the unitary vector pointing down.

Considering that $\widehat{\Omega}$ is infinite in the direction of y, the integration can be achieved through due ordinates $\pm d_y$, with $d_y \to \infty$, to obtain:

$$\boldsymbol{g_z}(O,O) = G \int_{\Omega} \frac{\Delta\rho(x,y)z}{x^2+z^2} dA \tag{7}$$

This is the general formula of the 2D integral for calculating the gravitational anomaly in *O* produced by a distribution of 2D masses with a $\Delta\rho$ density contrast relatively to the rest. Actually, the gravitational anomaly is defined as the line integral of the components of the 2D vectorial gravitation along the edge of the mass of a body.

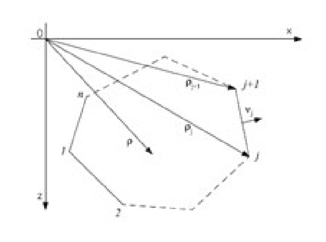

Fig. 2: Polygonal domain and geometrical entity of the ith edge.

The integration of the latter equation is rather complex, for the reason that the distribution of the density contrast in Ω can be arbitrary, and this is due to the geological and geochemical processes.

For this reason, a rather generic expression for Δρ, likely to encompass a large variety of geological formations, is given by a double polynomial in x and z [8][9][7][6][10]:

$$\boldsymbol{\Delta}\rho(x,y) = \theta(x,z) = \sum_{i=0}^{N_x}\sum_{j=0}^{N_z} c_{ij}\ x^i z^j \tag{8}$$

where Nx and Nz represent the maximal force of the polynomial density variation along x and z respectively.

The cij scalars represent the coefficients of the polynomial law. They can be estimated from the given and known points by means of a least squares approach (Johannes e Smilde 2009) [16]. In [11] the treatment is generalized to the case of Nx+Nz=3, that can easily be generalizable case Nx+Nz>3. To simplify the successive developments, we have introduced the bidimensional vector ρ = (x, z) and Kz (0,1). So that equation (7) has been rewritten as:

$$\boldsymbol{g_z}(\boldsymbol{o}) = 2G \int_{\Omega} \frac{\boldsymbol{\theta}(\rho)(\rho \cdot K_z)}{\rho \cdot \rho} dA \tag{9}$$

which demonstrates that the previous integral can be expressed as a line integral extended to the ∂Ω edge of Ω. As a consequence, equation (8) has been rewritten, that is to say the general expression of the density of contrast, using second and third order tensors:

$$\theta(\rho) = \theta_0 + \boldsymbol{c} \cdot \boldsymbol{\rho} + \boldsymbol{C} \cdot \boldsymbol{D_{\rho\rho}} + \mathbb{C} \cdot \mathbb{D}_{\rho\rho\rho} \tag{10}$$

which leads to the expression:

$$\boldsymbol{g_z}(\boldsymbol{o}) = 2G\left[\theta_0 d_\rho^{\Omega} + \boldsymbol{c} \cdot \boldsymbol{d_\rho^{\Omega}} + \boldsymbol{C} \cdot \boldsymbol{D_{\rho\rho}^{\Omega}} + \mathbb{C} \cdot \mathbb{D}_{\rho\rho\rho}^{\Omega}\right] \tag{11}$$

The analytical expression of the gravitational anomaly obtained in an arbitrary point P in terms of contour integral; the algebraic expression of the gravitational anomaly in an arbitrary point P; the assessment of the third order tensor, can be obtained by introducing the $\boldsymbol{\rho} = \boldsymbol{\sigma} - \boldsymbol{\omega}$ vector, to define the relative position of the generic point σ = (x, z) of Ω relatively to P.

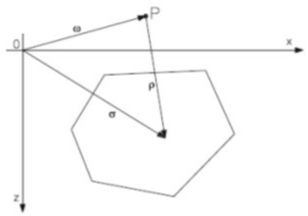

Fig. 3: Representation of the symbols used to assign the contrast density σ and to define the position of Ω relatively to an arbitrary point P.

One obtains: the analytical expression of the gravitational anomaly obtained in an arbitrary point P in terms of the contour integral; the algebraic expression of the gravitational anomaly in an arbitrary point P; the assessment of third order tensors. One has demonstrated that the analytical expression is rigorously conserved whatever the position of point O relatively to X. The same property applies in the case when vector $\boldsymbol{\rho}$ is introduced, and in the case of algebraic expressions of the gravitational anomaly [11]

The formulae illustrated in this paragraph and in the thesis have been codified by the authors in a Matlab® programme to control their correctness and robustness. “Model tests” of case studies derived from the specialized literature have been applied. In particular, the density contrast has been hypothesized to vary separately along the horizontal and vertical axes, or along both. In all the examples, the density contrast has been expressed in grams per cubic centimeter, while the distances have been expressed in kilometers; the value of the gravitational constant G has been assumed to be equivalent to 6,67259x10^{-11} m^3 kg^{-1} s^{-2}.

VII. THE GRAVITATIONAL ANOMALY OF POLYHEDRAL BODIES WITH VARIATION OF POLYNOMIAL DENSITY

This paragraph further explores the question of the gravitational anomaly associated to a polyhedral body having an arbitrary geometrical form and a polynomial density contrast, whether horizontally or vertically. The gravitational anomaly is assessed at an arbitrary point that does not necessarily coincide with the origin of the frame of reference to which the density function is assigned.

The density contrast is supposed to be at the utmost a third order polynomial, but the approach can easily be extended to polynomial functions of superior orders. Gravity is an economical instrument to explore and discover natural resources. In this respect, density is one of the most diagnosed physical properties of an ore deposit and is also fundamental for the prospection of oil and gas. To this day, density has been one of the most difficult properties to measure and deduce.

It is of fundamental importance to efficiently assess the gravitational anomaly associated to a body characterized by a complex density distribution, since this represents an important task of modelization.

Because of the mathematical complexity of the problem, the gravitational anomaly of an irregular body of which the density contrast is spatially variable has been first calculated by approximating the body to a congeries of vertical rectangular parallelepipeds (prisms) in which the density is supposed to be constant.

In alternative to the use of prisms, characterized by complex functions describing the density contrast, polyhedra with a simple description of the density contrast have been introduced.

Then progresses were made, but regarding only the linear variation of density. The introduction and treatment of more complex density functions in combination with polyhedral models have considerably augmented the difficulties of treatment, most of all in the search for an analytical solution.

For 2D bodies with only depth-relative density contrast, Zhou [12] has converted the integral of the original domain for the gravitational anomaly into a line integral (LI), by using Stokes’s theorem. In particular, he has derived two types of LI for the calculation of the gravitational anomaly of bodies. In an ulterior article, Zhou [13] has extended his method to account for the functions of density contrast that depended not only on depth, but also on the horizontal variation, or that were both horizontal and vertical.

The gravitational anomaly in the points of observation different from the origin has been subsequently assessed by Zhou [10], since historically the gravitational anomaly was calculated only from the origin of the frame of reference. In the same article, Zhou tackled the singularity of the gravitational anomaly that occurs when the observation point coincides with the vertex of the domain of integration, a problem already discussed by other authors.

A first approach to assessing the gravitational anomaly of bodies characterized by a complicated density contrast, also in presence of bidimensional domains, was numerical and semi-analytical, based on the use of prisms or 2D geometrical forms.

Actually, this latter geometrical hypothesis, that can be used to modelize domains extending towards the infinite in a single direction, remarkably simplify the mathematical treatment of the problem.

Other authors have transformed the original domain integrals into integrals of inferior orders to simplify the adoption of rules of numerical quadrature to assess the gravitational anomaly.

The derivation of analytical expressions to calculate the gravitational anomaly of polygonal bodies was recently achieved by D'Urso [15], using first the generalization of Gauss's theorem presented in [3], and then applying it to various problems of geodesy [5] [7] [8].

The methodology outlined in [11] has been generalized so as to receive an analytical expression of the gravitational anomaly for polyhedral bodies with a contrast density expressed as a polynomial function of arbitrary coefficient whether in a horizontal or in a vertical direction, a problem recently tackled by Ren et al. [14]. The result is obtained by first reducing the integral of the original domain to a 2D contour integral, by virtue of Gauss's theorem generalized. Surprisingly, this also allows to demonstrate that the expression of the edge integral of the gravitational anomaly is exempt of any singularity whatever the position of the observation point relatively to the body.

In the case of a polyhedral body, the 2D expression of the gravitational anomaly is written out as the finite sum of 2D integrals extended to the faces of the same.

By a further application of Gauss's theorem generalized, every face integral is reduced to the sum of the 1D integrals extended to the vertices of every face. Such 1D integrals are valued analytically as products of the positions of the vectors of the vertices at the end of every edge and of the scalar coefficients that provide the analysis of the value of the real variable integrals.

Although these latter integrals can exhibit a singularity when the projection of the point of observation on one face belongs to an edge, it is demonstrated that such singularities produce a contribution of the i^{th} arc to the general expression of the gravitational anomaly equal to zero. It follows that the derived expression is deprived of singularity.

Thanks to an apposite change of variable, it is also possible to deduce from this an advanced algebraic formula expressing the gravitational anomaly in an arbitrary point P, which conforms itself to the ordinary situation when P = O.

It is a noteworthy and interesting fact that the improved expression of the gravitational anomaly has been derived without any modification of the density contrast function. The enhanced formula has been implemented in a Matlab® code and its accuracy and robustness have been assessed by means of numerical comparisons with examples drawn from the literature.

D'Urso illustrates a general approach to express the 3D integrals as 2D integrals extended to the faces that constitute the border of Ω. The generality resides in the fact that, because of the symmetry of the integrals, the application of Gauss's theorem can be based on a unique formula. Thus is in fact demonstrated the obtention of the result:

$$\int_{\Omega} \frac{k_r[\otimes \boldsymbol{r}, m]}{(\boldsymbol{r}\cdot\boldsymbol{r})^{3/2}} dV = \frac{1}{m+1}\int_{\Omega} \frac{k_r[\otimes \boldsymbol{r}, m](\boldsymbol{r}\cdot\boldsymbol{n})}{(\boldsymbol{r}\cdot\boldsymbol{r})^{3/2}} dA \qquad m = 0,1,\dots\dots \tag{12}$$

where kr = r · k, n is the 3D unit toward the normal outside at the border of the polyhedral body, and [⊗r, m] denotes an appositely defined m rank tensor.

In conclusion, the application of (12) enables us to rewrite (13) in the following format:

$$\Delta \boldsymbol{g_z}(\boldsymbol{o}) = G\left[\theta_0 d_r^{\partial\Omega} + \frac{\boldsymbol{c}\cdot\boldsymbol{d}_r^{\partial\Omega}}{2} + \frac{\boldsymbol{C}\cdot\boldsymbol{D}_{rr}^{\partial\Omega}}{3} + \frac{\mathbb{C}\cdot\mathbb{D}_{rrr}^{\Omega}}{4}\right] \tag{13}$$

This formula is useful to transform the 2D integrals into 1D integrals.

With a view to obtaining an expression adapted to the programming in Matlab®, formula (13) has been perfected for polyhedral domains, since this is by far the most general case treated in the problems of inverted gravity. The integral relative to the ith face, obtained through diverse integrations, is assessed by the author as the tensorial product of 2D vectors:

$$\int_{\mathrm{F}_i} \frac{[\otimes \boldsymbol{\rho}_i, m]}{(\boldsymbol{\rho_i}\cdot\boldsymbol{\rho_i} + d_i^2)^{3/2}} dA_i \qquad m \in [0,4] \tag{14}$$

When the gravity measures are carried out in several points and/or when multiple bodies are taken into consideration, it is far more convenient to establish an arbitrary frame of reference in which the coordinates of each observation point, as well as the density of all the bodies, are assigned at the same time.

Alternately, it is possible to follow the approach outlined by D'Urso [11] and to define the position vector r as entering in the definition of the gravitational anomaly as follows: r = s – p, where p is the position vector of the point of observation and s is the position vector of an arbitrary point belonging to Ω. See for example the following figure.

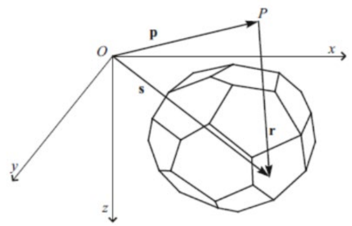

Fig. 4: Representation of the geometrical entities used to assign the density contrast (**s**) and to define the position of Ω relatively to an arbitrary point P.

With the introduction of vector r into the form just indicated here above, recalling formula (5.2) into the form with (s) in place of (r), one gets:

$$\Delta \boldsymbol{g_z}(P) = G \int_{\Omega} \frac{\Delta\rho(\boldsymbol{s})\boldsymbol{r}\cdot\boldsymbol{k}}{(\boldsymbol{r}\cdot\boldsymbol{r})^{3/2}} dV \tag{15}$$

which in the case of multiple observation points can be written as:

$$\Delta \boldsymbol{g_z}(P_i) = G \sum_{j=1}^{N_B} \int_{\Omega_i} \frac{\Delta\rho(\boldsymbol{s_j})\boldsymbol{r_j}\cdot\boldsymbol{k}}{(\boldsymbol{r_j}\cdot\boldsymbol{r_j})^{3/2}} dV \tag{16}$$

in which Ω_j is the domain of the j^{th} body, N_B is the number of bodies to analyze and the j^{th} position vectors individuate each time the position vector of points P_i relatively to the assigned frame of reference with its origin in an arbitrary point O.

VIII. NUMERICAL SOLUTIONS FOR DETERMINING THE EFFECTS OF GRAVITY FOR DIGITAL MODELS OF THE DTM TERRAIN

IX. ASSESSING THE EFFECTS OF GRAVITY FOR DIGITAL MODELS OF CONSTANT DENSITY DTM TERRAIN.

To calculate the gravitational potential, a Matlab® code has been implemented, in which the gravitational constant, the terrestrial density, the dimensions of the side-graduation grid, and the coordinates of the point attracted by the mass of the DTM, which vary on a case-by-case basis in the test numerals. The tests have been conducted on the DTM of an area in the southern zone of the Comune of Cassino. The gravitational constant is equal to G = $6.67259\cdot10^{-11}m^3kg^{-1}sec^{-2}$, the terrestrial density, by hypothesis considered initially constant is equal to 2.670 kg/m^3.

The points that constitute the grid are defined from cartographic coordinates (E, N, H) expressed in meters. The calculation of the gravitational effects has been carried out on 20 attracted points. Successively, the coordinates of the points of the DTM under study are uploaded from ASCII format files, and all the possible faces of the element chosen for the modelization from text files.

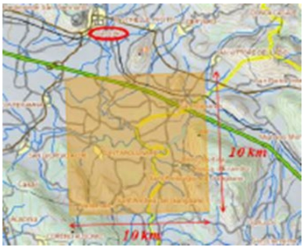

Fig. 5: DTM Cassino south

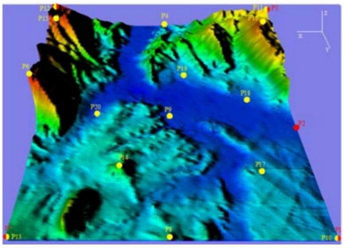

Fig. 6: Position of the attracted points on the Cassino south DTM

In Figure 6 the red circles characterize the zero-elevation attracted points, the yellow circles the points whose vertical datum coincides with that of the DTM, and the bicolor yellow/red circles coincide planimetrically with the coordinates of the DTM but with a different elevation.

The DTM that covers and area of 10 km x 10 km, given a spacing of 20 meters along both axis x and axis y (i. e. E and N), has been discretized into 250,000 prisms and polyhedra. For the various attracted points, defined in Table 1, relatively to the attracting masses represented by all the prisms and polyhedra that form themselves on the 250,000 point that constitute the DTM, every test calculates the potential and its vertical gradient.

TABLE I: Coordinates of the 20 attracted points

Punto	X	y	z
P1	400000	4589980	0
P2	400000	4584980	0
P3	400000	4580000	0
P4	400000	4580000	32
P5	409980	4580000	0
P6	409980	4584980	450
P7	409980	4589980	0
P8	405000	4589980	83
P9	405000	4584980	39
P10	400000	4589980	45
P11	400000	4580000	345
P12	409980	4580000	433
P13	409980	4589980	100
P14	406700	4587680	129
P15	409240	4581200	517
P16	400720	4581000	408
P17	402280	4587852	40
P18	402307	4584780	8
P19	404420	4581550	60
P20	406675	4584360	17

Following the approach for the two different modelizations, the prismatic and the polyhedral (Figure 7), the values of the potential are given in the following table (Table 2).

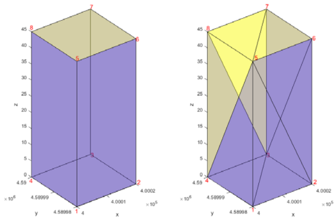

a) Prismatica a 6 facce   b) Poliedrica a 12 facce

a) 6 faces prismatic   b) 12 faces polyhedral

Fig. 7: Modelization tipology

The results demonstrate that the difference between the two modelizations has been quasi null, i. e. of the order of $10^{-12} - 10^{-14}$; besides, it appears that, also for the values of the first derivative of the potential given in the table (Table 3), the results present certain differences between the two null modelizations, of the order of $10^{-14} - 10^{-17}$.

Concerning the values of the potential calculated for the whole DTM, the highest values have been obtained in precise correspondence with the points of highest quote. The calculating duration for the modelization of the prismatic DTM elements are about 1.5 times lower than those required for the polyhedral modelization.

TABLE II: Values of the constant density potential and difference between the prismatic and polyhedral modelizations

Punto	Uprismi (A) $[m^2/s^2]$	Upoliedri (B) $[m^2/s^2]$	A - B $[m^2/s^2]$
P1	0,2249656023052	0,2249656023029	2,27301511E-12
P2	0,3452817352857	0,3452817352841	1,59000590E-12
P3	0,4112902659790	0,4112902659781	9,60009849E-13
P4	0.3957940693468	0.3957940693464	4,19997370E-13
P5	0,4375471123664	0,4375471123659	4,98046049E-13
P6	0,5435182037856	0,5435182037924	-6,79800660E-12
P7	0,2707507871322	0,2707507871332	-1,01002540E-12
P8	0,3092953423160	0,3092953423161	-2,79776202E-14
P9	0,4299239526042	0,4299239526037	4,55024907E-13
P1O	0,2249666989167	0,2249666989145	2,17501017E-12
P11	0,4092758486353	0,4092758486346	7,86981591E-13
P12	0,4349287352645	0,4349287352647	-1,82964754E-13
P13	0,2706858110161	0,2706858110175	-1,39499523E-12
P14	0,4342518592824	0,4342518592823	7,89923682E-14
P15	0,6513545355220	0,6513545355218	1,91957561E-13
P16	0,6261579199526	0,6261579199532	-5,42010881E-13
P17	0,3475921275315	0,3475921275306	8,66029470E-13
P18	0,4115009108499	0,4115009108487	1,24000810E-12
P19	0,5333225842480	0,5333225842467	1,35202960E-12
P2O	0,4626401008262	0,4626401008252	9,75997061E-13

The example just illustrated and documented is relative to the application of the analytic method to a real case, with a view to calculating the effects of gravity in determined points of the terrestrial surface. More particularly, both the prismatic and the polyhedral modelizations have been studied as the elements of a digital model of the terrain, by applying the formulae of the potential, of the acceleration of gravity (first derivative of the potential), and of its variation (second derivative of the potential). The applied formulae, implemented in a Matlab® code, have proved efficient to the point of resolving the singularities that, by contrast, frequently appear in the literature on analogous cases.

TABLE III: Values of the first derivative of the constant density potential and difference between the prismatic and polyhedral modelizations.

	Modellazione Prismatica (A) [m/s²]			Modellazione Poliedrica (B) [m/s²]			Differenza (A-B) [m/s²]		
Punto	UX	Uy	Uz	UX	Uy	Uz	UX	Uy	Uz
P1	6,2564096882E-05	-4,9545985357E-05	1,9101975275E-05	6,2564096883E-05	-4,9545985357E-05	1,9101975275E-05	-8,5029910630E-16	5,3905176763E-17	-9,0998443589E-17
P2	1,1033171260E-04	-5,5294651562E-05	3,2273531419E-05	1,1033171260E-04	-5,5294651562E-05	3,2273531461E-05	1,0600786741E-16	9,4305260216E-17	-4,2387100774E-14
P3	1,7873372261E-04	1,7991440031E-04	8,3973492327E-05	1,7873372261E-04	1,7991440031E-04	8,3973492327E-05	2,0599841277E-16	6,2992146221E-17	5,0779964001E-16
P4	1,9709372587E-04	1,9835515553E-04	6,7022501003E-05	1,9709372587E-04	1,9835515553E-04	6,7022501001E-05	-1,8298622166E-16	3,3800002727E-16	1,2081942434E-15
P5	-1,6953960395E-04	2,2227081490E-04	1,1691440513E-04	-1,6953960395E-04	2,2227081490E-04	1,1691440513E-04	1,5100225757E-16	3,0300740216E-16	1,0599431489E-16
P6	-3,0515471692E-04	-1,2552718082E-04	-2,1347181198E-04	-3,0515471692E-04	-1,2552718082E-04	-2,1347181194E-04	-1,2002118049E-16	4,4501078170E-16	-3,8199017517E-14
P7	-8,1703164350E-05	-8,7792716448E-05	5,0309072283E-05	-8,1703164350E-05	-8,7792716448E-05	5,0309072285E-05	-6,8520222048E-16	4,2759578430E-16	-2,0076984780E-15
P8	1,9902622220E-05	-1,0888244877E-04	-5,9155811047E-05	1,9902622220E-05	-1,0888244877E-04	-5,9155811089E-05	-6,7110081598E-16	-1,3999760552E-16	4,1809898642E-14
P9	1,8632113170E-05	-1,0499665110E-05	-2,4662623913E-05	1,8632113170E-05	-1,0499665110E-05	-2,4662623912E-05	4,4699622693E-17	5,1801146922E-17	-8,1709880290E-16
P1O	6,2452225074E-05	-4,9425631849E-05	-1,8994712481E-05	6,2452225074E-05	-4,9425631849E-05	-1,8994712481E-05	-6,1639604011E-16	9,9096078565E-17	7,4599885731E-17
P11	1,6996113497E-04	1,7224825884E-04	-9,0971907634E-05	1,6996113497E-04	1,7224825884E-04	-9,0971907635E-05	4,9005938196E-17	1,7699600466E-16	1,0330007249E-15
P12	-1,5191909003E-04	2,1541839415E-04	-1,2118873244E-04	-1,5191909003E-04	2,1541839415E-04	-1,2118873244E-04	1,2601139750E-16	4,9401671989E-16	8,5001450323E-17
P13	-7,9946298031E-05	-8,6073821243E-05	-5,1015856702E-05	-7,9946298030E-05	-8,6073821243E-05	-5,1015856701E-05	-5,2570252838E-16	-8,7007224342E-17	-9,3959670773E-16
P14	3,3380332953E-06	-2,0802803912E-06	-1,2714217526E-04	3,3380332957E-06	-2,0802803912E-06	-1,2714217528E-04	-3,4229999003E-16	-1,1669996431E-17	1,8062997929E-14
P15	6,0859224196E-05	7,2928855601E-05	-4,1461642925E-04	6,0859224196E-05	7,2928855601E-05	-4,1461642924E-04	3,2610090843E-16	2,2400972136E-16	-2,9150401711E-15
P16	9,9078564749E-05	1,0570395699E-04	-3,6166670311E-04	9,9078564749E-05	1,0570395699E-04	-3,6166670311E-04	-4,4070107806E-16	3,7200331791E-16	-9,1580389106E-15
P17	6,7811673308E-06	-1,0765943090E-05	-2,8210084468E-05	6,7811673315E-06	-1,0765943089E-05	-2,8210084469E-05	-6,9889027291E-16	-3,8720078305E-16	7,0970180145E-16
P18	8,7137760697E-06	-4,2172258125E-05	1,2191718771E-05	8,7137760697E-06	-4,2172258125E-05	1,2191718793E-05	1,4580825154E-17	-9,0896799636E-17	-2,1938000868E-14
P19	-4,5312391432E-05	3,0250342137E-05	-4,0269084160E-07	-4,5312391432E-05	3,0250342137E-05	-4,0269087301E-07	1,5380085443E-16	5,7022258009E-18	3,1410335006E-14
P2O	2,2210004130E-05	-9,2465482621E-06	-1,0375289133E-05	2,2210004130E-05	-9,2465482622E-06	-1,0375289126E-05	-9,1398243141E-17	1,2229122879E-16	-6,6678010091E-15

X. Assessment of the gravitational potential and graphic representation for polynomial density DTM

The formulae proposed in chapter 6 of the thesis, obtained by considering variable density as the 4th degree polynomial law, have been codified in the Matlab® environment and applied to the case study of the Cassino DTM, calculating the gravitational effects, with the relative graphic representations. The coefficients of the polynomial have been drawn from references in the literature [17] (Karcol) and adapted to the Z component of our concern.

The reference DTM of the comune of Cassino, provided by the IGM (Istituto Geografico Militare), is characterized by a 20 m x 20 m grid pattern covering an area of 10 km x10 km.

The grid is constituted of 500 x 500 points distributed along the x and y axes, defined by cartographic coordinates (E, N, H), expressed in meters in the geodetic frame of reference ED50 in the UTM representation (contained in an ASCII format text file).

The modelization adopted for the discretization of the DTM is polyhedral. Given a frame of reference OXYZ, with the X coordinate corresponding to the East, the Y coordinate to the North, and the Z coordinate to the altitude, the generic polyhedron, composed of 8 nodes (see Figure 8), is subdivided into 7 faces, each face being characterized by an outgoing unit vector ni perpendicular to the surface:

- F5 base face, nodes [1 4 3 2] at elevation z=0,00 m, perpendicular -z (Figure 8a);
- F1, F2, F3 and F4 lateral faces (Figure 8b and Figure 8c);
- top face subdivided into two triangular faces F6 and F7 with perpendicular +z.

The top faces are adapted to the elevation of the DTM nodes, so as to improve the accuracy of the discretization, thus rendering the model more realistic.

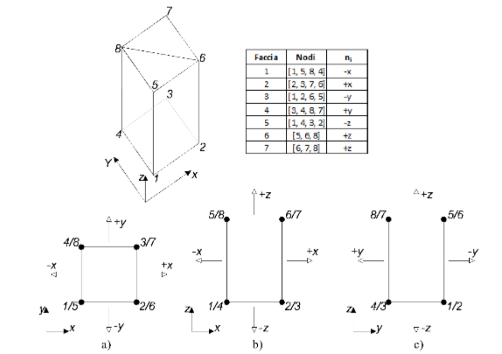

Fig. 8: Modelization tipology

So, the distribution of the masses of attracting terrain are subdivided into “finite elements” and the variable density is considered on a case-by-case basis as follows:

1. constant density:

$\delta(z) = 1743.957$ [kgm^{-3}]

2. variable density with variable function:

$\delta(z) = 1743.957 - 0.768z$

3. variable density with square function:

$\delta(z) = 1743.957 - 0.768z - 0.722 \cdot 10^{-3}z^2$

4. variable density with cubic function:

$\delta(z) = 1743.957 - 0.768z - 0.722 \cdot 10^{-3}z^2 - 5.097 \cdot 10^{-7}z^3$

5. variable density with fourth degree polynomial:

$\delta(z) = 1743.957 - 0.768z - 0.722 \cdot 10^{-3}z^2 - 5.097 \cdot 10^{-7}z^3 - 1.685 \cdot 10^{-10}z^4$

To guarantee a good representation of the gravitational effects of the 10 km x 10 km DTM area, the calculation should be carried out for a high number of attraction or observation points, which would prove burdensome from the computational point of view, so this phase of the analysis has been focused on an advanced study of a limited portion of the Cassino DTM (Figure 9).

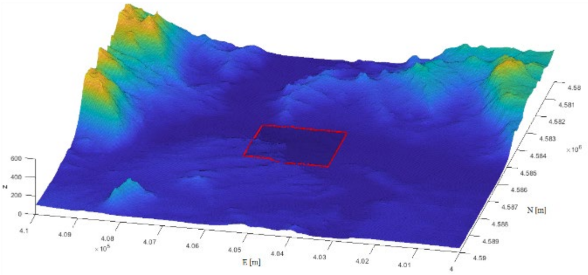

Fig. 9: 2 km x 2 km DTM portion extrapolated from 10 km x 10 km DTM

The object of study is a central portion of the DTM covering a 2 km x 2 km area, composed of a grid of 101 x 101 points, corresponding to the vertices of the top face of the polyhedra.

As can be observed from Figure 10, the spacing of the nodes in the grid, provided by the IGM, amounts to 20 meters, while for the observation points along axes x (E) and y (N), localized on the surface of the DTM, the spacing is of 60 meters.

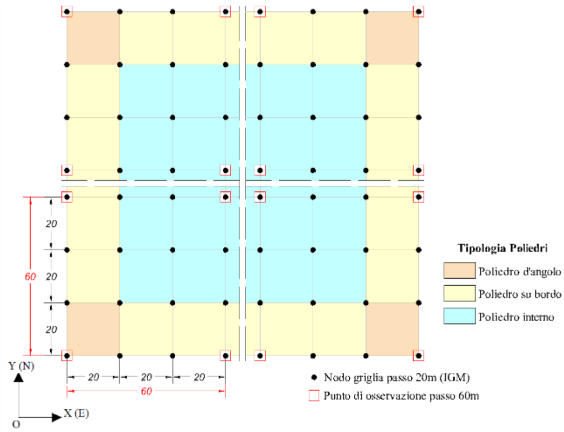

Fig. 10: Polyhedra typology
Angle polyhedron
Edge polyhedron
Internal polyhedron
2 km x 2 km DTM portion extrapolated from 10 km x 10 km DTM2 km x 2 km DTM portion extrapolated from 10 km x 10 km DTM

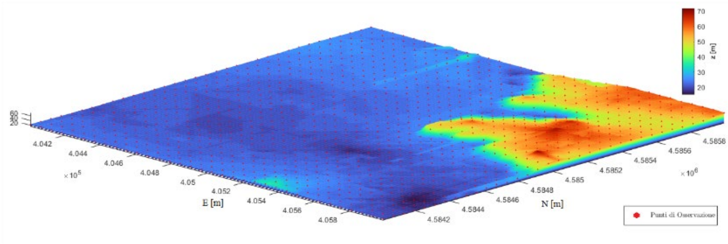

Fig. 11: 2 km x 2 km DTM portion and observation points grid

Thus, a grid of 34x34=1156 observation points is obtained, and at these points the variable density gravitational potential is calculated with a 4th degree polynomial function.

The potential is obtained by the following volumetric integral:

$$U(P) = G \int_{\Omega} \frac{\delta(s)}{[(p-s)\cdot(p-s)]^{\frac{1}{2}}} dV(s)$$

(17)

which is reconducible to various surface integrals, and each of these to linear integrals, through the application of Gauss's theorem. This allows to obtain formulations that can be used to assess in analytical form the gravitational effects, relatively to the coordinates of the vertices of the border of the attractive mass.

As a result, the DTM is subdivided into $(n-1)^2 = (101-1)^2 = 10000$ polyhedra. For each polyhedron with a top face subdivided into two triangular faces, 70,000 2D surface integrals should calculated, so, on the whole, for a grid of 34x34=1156 observation points, a total of 1156x70000= 80920000 surface integrals, which is a very burdensome calculation from the computational point of view. According to the position of the polyhedra in the discretized DTM (Figure 10 – Polyhedra typology), it is possible to bypass the calculation of the 2D integrals in the polyhedra that present joint vertical faces with other polyhedra. In fact, the faces are characterized by perpendicular unit vectors of opposite sign, that give a null overall result in calculation. The calculation of the integrals is bypassed for 2 faces of the angle polyhedra, for 3 faces of the edge polyhedra, and for the 4 vertical faces of the internal polyhedra.

This allows to reduce the number of integral calculations by 30,400 for each observation point, and therefore the time of elaboration. For the 34x34 observation points assessed, the values of the gravitational potential of the DTM portion are assessed, according to the variation of density, as shown in the following table with the related graphic representations and two sections along axes x and y, corresponding to the value of maximum potential, localized in the point of the DTM terrestrial surface, at the highest elevation.

For constant density, $\delta(z) = 1743{,}957$ [kgm^{-3}]:

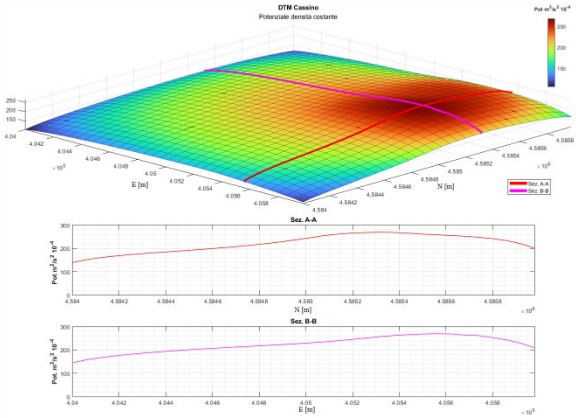

Fig. 12: Graphic representation of the constant density Potential

For linearly variable density, $\delta(z) = 1743.957-0.768z$:

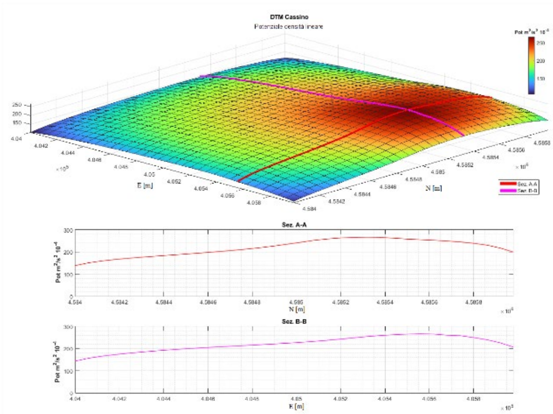

Fig. 13: Graphic representation of the linearly variable density potential

For density varying with square function, $\delta(z) = 1743.957-0.768z-0.722\cdot10^{-3}z^2$:

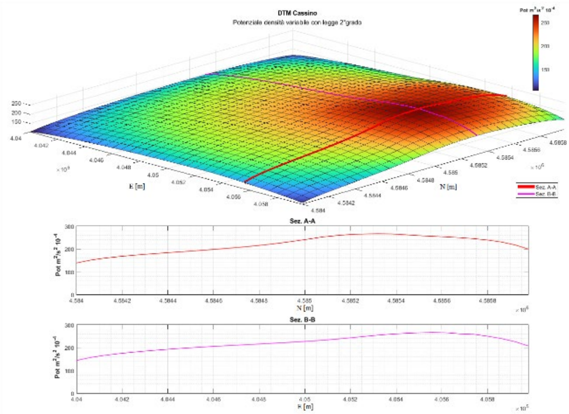

Fig. 14: Graphic representation of the density potential with square function variation

For density varying with cubic function, $\delta(z) = 1743.957 - 0.768z - 0.722 \cdot 10^{-3}z^2 - 5.097 \cdot 10^{-7}z^3$:

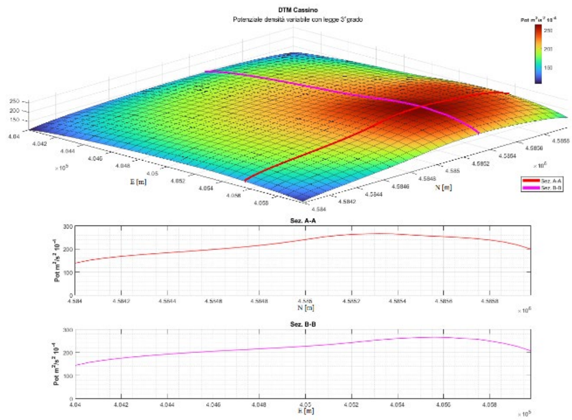

Fig. 15: Graphic representation of the density potential with cubic function variation

For density varying with 4th degree polynomial,

$\delta(z) = 1743.957 - 0.768z - 0.722 \cdot 10^{-3}z^2 - 5.097 \cdot 10^{-7}z^3 - 1.685 \cdot 10^{-10}z^4$:

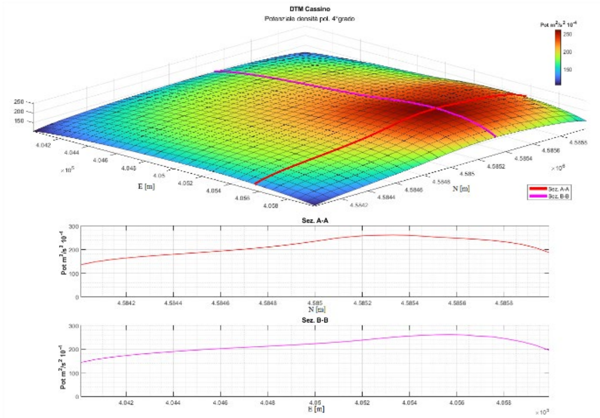

Fig. 15: Graphic representation of the density Potential with 4th degree polynomial variation

XI. CONCLUSIONS

The thesis addresses and develops the theme of the applications of computational methods in geodesy aiming at the analytic calculation of the effects of gravity, of the gravitational potential and its first and second derivatives, due to the determined distributions of masses in discretizable bodies with prismatic and polyhedral models, and a density either constant or variable according to a polynomial function of determined degree.

Potential Theory mathematically describes not only the gravitational attraction, but also a vast series of phenomena, including magnetostatic and electrostatic fields, fields generated by uniform electric currents, constant heat transfer through a homogenous conductor, the constant flux of ideal fluids, the behavior of elastic solids, the unstable movement of the water wave, and the theory of complex functions.

Gravitational attraction is what is at stake in the scope of this study. It constitutes a vectorial field, but geophysical instruments generally measure only one component of the vector, and this single component constitutes a scalar field.

The principal component of gravity measured by gravimeters and used in most gravity analyses is the intensity Fz of the force per mass unit on the vertical axis, which in the literature is often indicated by the special symbol g. Recent advancements in the measurement of gravity and in the realization of instruments and processes have renewed the interest in the usefulness of utilizing vectorial components and the gradients of their tensors. The components of the tensor gradient are useful to improve the identification and the resolution of abnormal sources.

The effects of gravity in tridimensional and bidimensional idealized bodies can be determined by means of the calculation of tridimensional integrals imposing determined conditions to the contour.

A profuse literature provides the values of the effects of gravity for bodies diversely modelized by means of equations that are affected with errors due to limited basic assumptions. Generally, the effects of gravity on an extended and variably articulated body are determined by subdividing the body into slices and by summing up the effects of all the slice sections relatively to the observation point. Thus, the tridimensional problem becomes bidimensional. The linear integration method has been adopted since the 1960's. However, numerical integration proves easier with the Gaussian quadrature method.

From the interactive relationship between gravitational field and gravitational potential, by using the Divergence theorem, one obtains Poisson's equation, which allows to determine the gravitational potential from the density of mass distribution. The resolution of Poisson's equation cannot forgo the correct use of boundary conditions, i. e. that the potential becomes null when the distance from the mass becomes infinite. In fact, from Poisson's equation, integrating side to side on an arbitrary volume containing a mass M, and applying the Divergence theorem, one obtains Gauss's theorem, which allows to determine the flux of the gravitational field through a closed surface S containing a determined mass M. However, Gauss's theorem univocally relates the integral of the source to the mass but says nothing of the characteristics or of the distribution of the mass itself.

The difficulty consists in seeking to approximate complicated geological formations through geometrical forms, these forms themselves being sufficiently simple to make it possible for the volume integral, obtained by the elaboration of the integral of Gauss's theorem, to be calculated automatically. The point is essentially to simplify the apprehension of gravitational sources and the hypothetical source divided into N parts.

A sequence of rectangular prisms provides a simple way to approximate the volume of a determined mass. If each prism is small enough, it can be presumed that each one of these has a constant density. Then, by the principle of superimposition, the body's gravitational anomaly in any point could be approximated by summing up the effects of all the prisms.

Although it is conceptually simple, the approach just mentioned would not be feasible. In fact, the geological formations are often difficult to modelize with rectangular blocks. Besides, the calculation is not facilitated, because if the densities of the neighboring prisms are identical, it is useless to include their interface in the calculation.

A more practical method has successively been described by Talwani and Ewing. Their technique is close to the modelization of a body consisting of a stack of infinitely subtle slices. The form of each slice is approximated to a polygon and the polygonal confines of the individual slices can be taken from topographic contour maps. A more useful way of approximating geological situations is to substitute simplified polygons for the forms of the transversal sections of bidimensional bodies.

The effects of the gravity of idealized tridimensional and bidimensional bodies can be determined by means of the calculation of integrals imposing determined conditions to the contour. Generally, the effects of gravity on an extended and variably articulated body are determined by subdividing the body into slice sections and by summing up the effects of all the sections relatively to the observation point.

The 2D and 3D sources have been widely modelized, respectively by using vertical slices and vertical stacks of horizontal slices cutting through a body of irregular form. In both cases, the slice is approximated to a polygon with linear edges, of which the gravitational effect completely involves the geometrical elements described by the coordinates of the final point of the linear element.

The stretched source of finite length is widely used for the interactive modelization of the gravitational vector and of the components of the vectorial tensors. Gauss's law and Laplaces's and Poisson's equations are useful to understand the nature of the fields.

However, the analytical expressions formulated in the past by various authors generate singularities when the calculation of the potential is determined correspondingly to the vertices of the prism. A similar situation is verified whenever the object of study is a polyhedral body. Recent formulations have been elaborated for the calculation of the potential and of its gradient in the case when observation point P coincides with a vertex on the prismatic body. The formulae obtained, thanks to the application of Gauss's theorem, show how to consider these singularities in the most relevant way.

The formulae given in chapter 4 have been the object of computational application for the calculation of the gravitational effects for a prismatic or polyhedral body; the results did not contain any singularities.

The approach taken to calculate the gravitational effects of polyhedral bodies with uniform density can be extended to the case of bodies with linearly variable density, by attentively assessing the relative singularities. The constant density polyhedron has been repeatedly analyzed. However, the constant mass hypothesis is hardly realistic. For example, it is invalided by the fact that a sedimentary basin, in the course of its geological history, has undergone a compacting, by reason of which the density generally increases with depth. This consideration has led various authors to study the gravitational effects produced on bodies with a linearly variable density in two or three dimensions.

Furthermore, from vertical depth-relative density variations, various authors have begun to address more complex distributions of density, whether vertical or horizontal. The problem of the modelization of bodies has acquire fundamental importance, so much so that the modelization of prismatic bodies has been followed by the modelization of polyhedral bodies.

The documented approaches address whatever sources of singularities independently from the position of observation point P relatively to the prismatic or polyhedral body. The documented applications of computational methods prove more efficient in terms of calculation and running time, comparatively to the analogues found in scientific literature.

Computational approaches relative to polyhedral bodies for the determination and assessment of gravitational effects are based on repeated applications of Gauss's theorem. The effects of the singularities that occur in the development of the calculations can be tackled without any a posteriori necessity to introduce corrective coefficients in the final formulae, as often happens in so many approaches that can be found in the literature.

More particularly, it is demonstrated that, except for calculation of the second derivative of the potential, the singularities can be eliminated, both for the gravitational potential and for its first derivative.

The studied analytical formulae have allowed to determine the effects of the gravity of polyhedral bodies as the sum of unidimensional integrals extended to their sides.

The formulae indicated for the calculation of the potential and of its first and second derivatives are always well defined, unless the observation point belongs to line containing an edge of the polyhedron; in fact, in this case the second derivative of the potential shows a singularity.

The examined analytical formulae have been implemented in Matlab® codes. The codes have been initially validated by means of the execution of basic tests, successively used in the calculation of the effects of gravity induced from polyhedral models, in growing order of complexity.

The approaches identified in the sections of the thesis, based on distribution theory and differential calculus, have also been used to address and resolve the singularities concerning the integrals necessary to calculate the gravitational effects of variable density polyhedral bodies.

As far as it is examined and improved in the section relative to numerical solutions for the determination and calculation of the effects of gravity for Digital Terrain Models (DTM), the procedure is based on the repeated application of Gauss's theorem, applied to domains represented in polyhedral form, as it has been extensively indicated in chapter 8.

The code of calculation implemented in Matlab® has been tested and specifically applied to the case of the DTM of a geographical area in the southern zone of the territory of the comune of Cassino.

In particular, both the prismatic and the polyhedral modelizations of the terrain have been examined, for the available elements of the digital model of the terrain, for which the values of the potential and of its first derivative have been obtained.

The results obtained by means of the algorithm in the Matlab® environment have demonstrated that the implemented formulae are particularly efficient, to the point of resolving the singularities that, on the contrary, frequently appear in the literature on similar cases.

The results have been obtained both in the hypothesis of a constant density of the terrain, and in the hypothesis of a density varying according to a polynomial function up to the 4th degree.

The polyhedra used for the discretization of the terrain have been subdivided into seven faces, so as to obtain a better accuracy of the calculations.

The potential calculated for the 1,156 observation points, by means of applying Gauss's theorem, is reconducible to the calculation of numerous surface integrals, and, successively, to the calculation of numerous linear integrals.

All in all, 30,400 integrals have been calculated, taking advantage of the possibility to forgo the calculation of those integrals that concerning faces in common with other polyhedra, characterized by outgoing perpendicular unit vectors of opposite sign.

The values of the potential and of the first order derivative (gravity; g) have been calculated for the points of a 10 km x 10 km wide DTM, on the basis of a constant density prismatic and polyhedral modelization.

Moreover, for a reduced, 2 km x 2 km wide DTM, on the basis of a prismatic modelization, the values of the potential and of the first derivative have been calculated for 1,156 observation points (attraction points) characterized by variable density values.

Finally, corresponding to the value of the maximum potential, localized in the highest point, the graphic representations and 2 sections, along axes x and y, have been elaborated for all the cases under study and characterized by density values either constant or variable according to a polynomial function up to the 4th degree.

The first derivative of the potential has been represented for values of constant and linear density.

REFERENCES

[1] R. J. Blakely, Potential Theory in Gravity and Magnetic Applications. 1995.
[2] M. Okabe, "ANALYTICAL EXPRESSIONS FOR GRAVITY ANOMALIES DUE TO HOMOGENEOUS POLYHEDRAL BODIES AND TRANSLATIONS INTO MAGNETIC ANOMALIES.," Geophysics, vol. 44, no. 4, pp. 730–741, 1979, doi: 10.1190/1.1440973.
[3] M. G. D'Urso, "On the evaluation of the gravity effects of polyhedral bodies and a consistent treatment of related singularities," J. Geod., vol. 87, no. 3, pp. 239–252, 2012, doi: 10.1007/s00190-012-0592-1.
[4] K.-T. Tang, Mathematical Methods for Engineers and Scientists 3. 2007.
[5] M. G. D'Urso, "Analytical computation of gravity effects for polyhedral bodies," J. Geod., vol. 88, no. 1, pp. 13–29, 2013, doi: 10.1007/s00190-013-0664-x.
[6] X. Zhou, "2D vector gravity potential and line integrals for the gravity anomaly caused by a 2D mass of depth-dependent density contrast," Geophysics, vol. 73, no. 6, 2008, doi: 10.1190/1.2976116.
[7] X. Zhou, "General line integrals for gravity anomalies of irregular 2D masses with horizontally and vertically dependent density contrast," Geophysics, vol. 74, no. 2, 2009, doi: 10.1190/1.3073761.
[8] X. Zhou, "Analytic solution of the gravity anomaly of irregular 2D masses with density contrast varying as a 2D polynomial function," Geophysics, vol. 75, no. 2, 2010, doi: 10.1190/1.3294699.
[9] X. Zhou, "3D vector gravity potential and line integrals for the gravity anomaly of a rectangular prism with 3D variable density contrast," Geophysics, vol. 74, no. 6, 2009, doi: 10.1190/1.3239518.
[10]X. Zhou, "On 'Gravity anomalies of 2D bodies with variable density contrast' (Jianzhong Zhang, Benshan Zhong, Xixiang Zhou, and Yun Dai, 2001, GEOPHYSICS, 66, 809-813)," Geophysics, vol. 74, no. 4. 2009, doi: 10.1190/1.3119482.
[11]M. G. D'Urso, "The Gravity Anomaly of a 2D Polygonal Body Having Density Contrast Given by Polynomial Functions," Surv. Geophys., vol. 36, no. 3, pp. 391–425, 2015, doi: 10.1007/s10712-015-9317-3.
[12]X. Zhou, "Analytical solution of gravity anomaly of irregular 2D masses with density contrast varying as a 2D polynomial function.," Geophysics 75:I11–I19, 2010.
[13]Z. Ren, C. Chen, K. Pan, T. Kalscheuer, H. Maurer, and J. Tang, "Gravity Anomalies of Arbitrary 3D Polyhedral Bodies with Horizontal and Vertical Mass Contrasts," Surveys in Geophysics, vol. 38, no. 2. 2017, doi: 10.1007/s10712-016-9395-x.
[14]M. G. D'Urso and S. Trotta, "Gravity Anomaly of Polyhedral Bodies Having a Polynomial Density Contrast," Surv. Geophys., vol. 38, no. 4, pp. 781–832, Apr. 2017, doi: 10.1007/s10712-017-9411-9.
[15]M. G. D'Urso and F. Marmo, "Vertical stress distribution in isotropic half-spaces due to surface vertical loadings acting over polygonal domains," ZAMM Zeitschrift fur Angew. Math. und Mech., vol. 95, no. 1, 2015, doi: 10.1002/zamm.201300034.
[16]W. J. Johannes and P. L. Smilde, Gravity interpretation: Fundamentals and application of gravity inversion and geological interpretation. 2009.
[17]R. Karcol and R. Pašteka, "Density function evaluation from borehole gravity meter data – regularized spectral domain deconvolution approach," Geophys. Prospect., vol. 65, no. 1, 2017, doi: 10.1111/1365-2478.12427.

From sewage sludge to microbial protein: the role of H2S- and CO-tolerant hydrogen-oxidizing bacteria in syngas aerobic fermentation

Vincenzo Pelagalli[1], Silvio Matassa[2], Marco Race[1], Michela Langone[3], Stefano Papirio[2], Piet N. L. Lens[4], Marco Lazzazzara[5], Alessandro Frugis[5], Luigi Petta[6], Giovanni Esposito[2]

[1]Department of Civil and Mechanical Engineering, University of Cassino and Southern Lazio, Cassino, Italy
Email: vincenzo.pelagalli@unicas.it; marco.race@unicas.it

[2]Department of Civil, Architectural and Environmental Engineering, University of Napoli Federico II, Napoli, Italy
Email: silvio.matassa@unina.it; stefano.papirio@unina.it; gioespos@unina.it

[3]Laboratory Technologies for the Efficient Use and Management of Water and Wastewater, Italian National Agency for New Technologies, Energy and Sustainable Economic Development (ENEA), Rome, Italy
Email: michela.langone@enea.it

[4]National University of Ireland Galway, Galway, Ireland
Email: piet.lens@universityofgalway.ie

[5]Acea Elabori Spa, Rome, Italy
Email: marco.lazzazzara@aceaspa.it; alessandro.frugis@aceaspa.it

[6]Laboratory Technologies for the Efficient Use and Management of Water and Wastewater, Italian National Agency for New Technologies, Energy and Sustainable Economic Development (ENEA), Bologna, Italy
Email: luigi.petta@enea.it

Abstract

The aerobic fermentation of syngas, generated through the pyrolysis of municipal sewage sludge, for the purpose of producing value-added products like microbial protein (MP), holds the potential to open new horizons in biorefinery approaches for wastewater treatment plants. In this regard, this study aimed to investigate the capability of a mixed community of hydrogen-oxidizing bacteria (HOB) to convert a synthetic syngas with varying H_2/CO_2 ratios, along with increasing concentrations of H_2S and CO, into MP.

Remarkably, no inhibition of the enriched HOB culture within H_2/CO_2 ratios ranging from 2 to 10, H_2S concentrations up to 0.4%, and CO concentrations up to 40%, was observed. Moreover, this process exhibited consistent performance over an extended period of 30 days and resulted in the production of MP containing as much as 65% protein content in biomass.

Index Terms

Aerobic syngas fermentation; biorefinery; hydrogen-oxidizing bacteria; resource recovery; sewage sludge pyrolysis; single cell protein

I. INTRODUCTION

Large quantities of municipal sewage sludge (MSS) are generated globally each year, resulting in significant operational expenses for wastewater treatment plants (WWTPs) and environmental concerns [1]. Pyrolysis allows not only MSS treatment and reduction, but also transforms it into syngas, a gas mixture primarily composed of H_2, CO, and CO_2. This syngas can be further utilized to produce valuable products like microbial protein (MP) [2], a protein-rich material (up to 80% protein content by weight) obtained from microbial biomass. MP serves as an alternative protein source for both feed and food, as well as for the production of biopolymers and slow-release fertilizers [3]. Hydrogen-oxidizing bacteria (HOB) can grow on gas mixtures of H_2, O_2 and CO_2, accumulating proteins in concentrations of up to 75% by weight. This makes HOB crucial in developing a syngas-to-MP process [4]. However, MSS-derived syngas exhibits variable compositions, with H_2/CO_2 ratios ranging from 0.1 to 10.0, and may contain inhibitory gases like H_2S and CO in concentrations as high as 2000 parts per million by volume (ppmv) and 40% by volume (v/v), respectively [5–8]. The ability of HOB to ferment gases with high H_2S concentrations remains unexplored, while only a few studies have examined pure HOB cultures exposed to CO concentrations as high as 30% v/v [9]. In this study, a mixed culture of HOB was enriched, and its performance during aerobic fermentation of simulated MSS-derived syngas, with realistic H_2, CO_2, CO, and H_2S concentrations and ratios, was evaluated. During the experiments, gas consumption, biomass concentration (as volatile suspended solids (VSS)), biomass yield on chemical oxygen demand (COD) H_2 equivalents (H_2-COD), biomass productivity, and protein content in biomass, were monitored. Additionally, the microbial community evolution in the enriched HOB culture was assessed.

II. MATERIALS AND METHODS

Active compost was employed as inoculum source for the enrichment of HOB. The enrichment was conducted in 306 mL serum bottles partially filled with 40 mL of mineral medium prepared according to [10]. A mixture of $H_2/O_2/CO_2$ in a 65/20/15 volumetric ratio was injected in the headspace of each bottle [11] up to an initial pressure of 1.5 bar. The enrichment was agitated at 600 rotations per minute (rpm) at a temperature of 30 °C. During the enrichment phase, the culture and gas substrate were periodically diluted and refreshed, achieving a stable growth after 5 weeks. The enriched HOB culture was then employed in two different series of batch aerobic fermentation tests, aimed to the evaluation of the effect of specific syngas compositions. In the first series of batch tests, the effects of different syngas mixtures characterized by H_2/CO_2 ratios of 2.0, 4.3, and 10.0, H_2S concentrations from 2000 to 8000 ppmv, and CO concentrations from 10 to 40 % v/v, were evaluated in short-term applications (48 h). In the second series of batch tests, a 30 days-long observation of the effects of CO concentrations of 10 and 40 % v/v, and those of a mixed condition with CO at 10% v/v and H_2S at 2000 ppmv, was conducted by refreshing the gas and liquid phase of each bottle on a 48-96 h basis.

III. Results and discussion

A. Short-term batch tests

The short-term batch tests helped in screening the performances of the enriched HOB culture in the presence of variable syngas compositions. H_2/CO_2 ratios variable between 2 and 10 caused no differences in terms of biomass yield and final concentration (0.14-0.16 g VSS/g H2-COD and 0.53-0.57 g VSS/L, respectively), as well as for protein content of biomass (62-66 %VSS) and H2 consumption (83-87%). A significatively higher CO_2 consumption (90%) was observed for H_2/CO_2 = 10, enlightening a more efficient CO_2 recovery as MP from syngas with high H_2/CO_2 ratios. The addition of H_2S and CO in concentrations up to 4000 ppmv and 40 % v/v, respectively, had no significant impact on the HOB culture, revealing its remarkable resistance towards these inhibitors. No negative effect came from H2S and CO on biomass protein content as well, with values varying in the ranges of 39-56 %VSS and 53-59 %VSS in the H_2S and CO concentration tests, respectively.

B. Long-term batch tests

During the long-term batch test, CO concentrations as high as 10 and 40 % v/v (conditions CO10 and CO40, respectively), and the simultaneous exposure to CO and H_2S in concentrations of 10 % v/v and 2000 ppmv, respectively (condition CO10+H_2S) (Fig. 1), had no negative influence on the process. Biomass yield on H_2 for CO40 was significatively higher with respect to the other conditions, due to H_2-limiting conditions occurring with a lower H_2 supply. The microbiological analysis of the HOB culture before and after the long-term test revealed the determinant role played by its mixed composition. CO-tolerant HOB, such as *Advenella kashmirensis, Hydrogenophaga, and Xanthobacter autotrophicus*, sustained the fermentation process even at CO concentration of 40% v/v, when the genus *Paracoccus* (the most abundant for lower CO concentrations) was inhibited. The HOB mixed culture showed a high degree of resistance to H_2S and CO as never reported before in literature for pure/axenic HOB cultures.

The results of this study suggest that mixed HOB cultures could drive aerobic syngas fermentation even by directly employing raw syngas, with stable process performances and the production of MP with remarkable protein content up to 65 %VSS. These outcomes could positively influence the costs and technical feasibility of the syngas-to-MP route applied to MSS management.

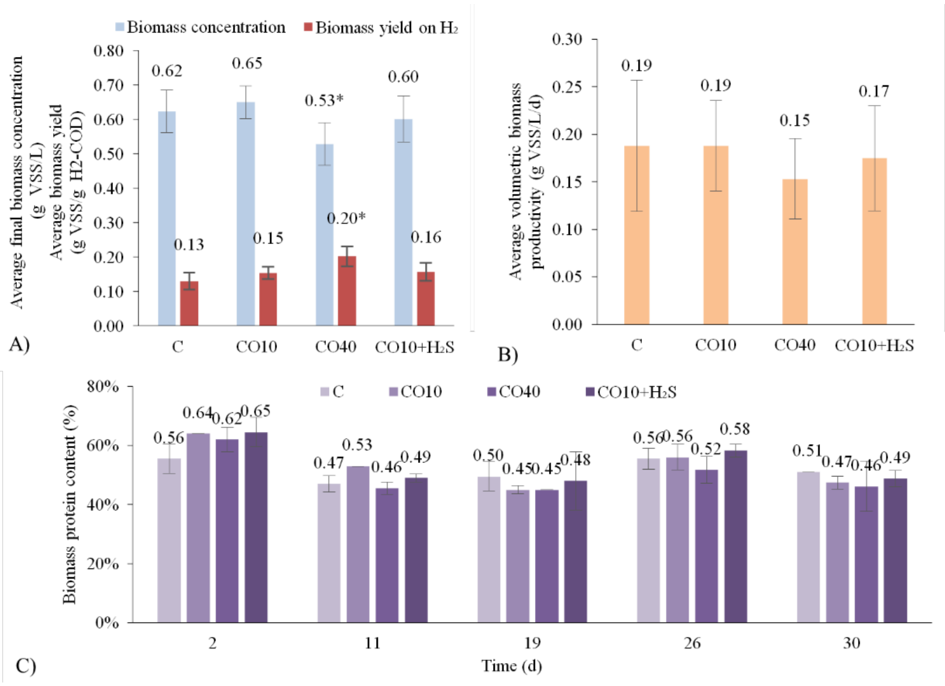

Fig. 1: Results of the long-term batch test in terms of **A)** average final biomass concentration and biomass yield, **B)** average volumetric productivity, and **C)** biomass protein content. *: statistically different value (*p value* < 0.05).

References

[1] N. Gao, K. Kamran, C. Quan, P.T. Williams, Thermochemical conversion of sewage sludge: A critical review, Prog Energy Combust Sci. 79 (2020) 100843.

[2] X. Sun, H.K. Atiyeh, R.L. Huhnke, R.S. Tanner, Syngas fermentation process development for production of biofuels and chemicals: A review, Bioresour Technol Rep. 7 (2019) 100279.

[3] M. Areniello, S. Matassa, G. Esposito, P.N.L. Lens, Biowaste upcycling into second-generation microbial protein through mixed-culture fermentation, Trends Biotechnol. (2022).

[4] S. Matassa, S. Papirio, I. Pikaar, T. Hülsen, E. Leijenhorst, G. Esposito, F. Pirozzi, W. Verstraete, Upcycling of biowaste carbon and nutrients in line with consumer confidence: the "full gas" route to single cell protein, Green Chemistry. 22 (2020) 4912–4929.

[5] N. Gao, J. Li, B. Qi, A. Li, Y. Duan, Z. Wang, Thermal analysis and products distribution of dried sewage sludge pyrolysis, J Anal Appl Pyrolysis. 105 (2014) 43–48.

[6] R. Han, C. Zhao, J. Liu, A. Chen, H. Wang, Thermal characterization and syngas production from the pyrolysis of biophysical dried and traditional thermal dried sewage sludge, Bioresour Technol. 198 (2015) 276–282.

[7] A. Jaramillo-Arango, I. Fonts, F. Chejne, J. Arauzo, Product compositions from sewage sludge pyrolysis in a fluidized bed and correlations with temperature, J Anal Appl Pyrolysis. 121 (2016) 287–296.

[8] S. Xiong, J. Zhuo, B. Zhang, Q. Yao, Effect of moisture content on the characterization of products from the pyrolysis of sewage sludge, J Anal Appl Pyrolysis. 104 (2013) 632–639.

[9] Y. Jiang, X. Yang, D. Zeng, Y. Su, Y. Zhang, Microbial conversion of syngas to single cell protein: The role of carbon monoxide, Chemical Engineering Journal. 450 (2022) 138041.

[10] J. Yu, A. Dow, S. Pingali, The energy efficiency of carbon dioxide fixation by a hydrogen-oxidizing bacterium, Int J Hydrogen Energy. 38 (2013) 8683–8690.

[11] S. Matassa, W. Verstraete, I. Pikaar, N. Boon, Autotrophic nitrogen assimilation and carbon capture for microbial protein production by a novel enrichment of hydrogen-oxidizing bacteria, Water Res. 101 (2016) 137–146.

The effect of settlements on the seismic vulnerability of masonry panels

Marina Serpe[1], Maura Imbimbo[1], Valentina Tomei[1], Ernesto Grande[2]
[1] University of Cassino and Southern Lazio,
Italy, Cassino,
[2] University of Guglielmo Marconi,
Rome, Italy.

Abstract

Foundation settlements in masonry buildings often produce widespread and/or concentrated damage to the structures that can result in a significant reduction in their capacity with respect to both vertical loads and seismic actions. There are many simplified methods in the literature for assessing the effects of subsidence on masonry structures, however, these approaches do not explicitly take into account the complex geometries, materials and masonry typology that characterize historic buildings. Based on these premises, this paper focuses on the in-plain seismic response of masonry buildings subjected to settlements, with specific reference to two-dimensional homogenized continuum masonry panels using a model based on damage mechanics. For this purpose, nonlinear static FEM analyses were carried out in Abaqus CAE. The validation of the model has been performed on literature experimental tests of masonry panels. Then, parametric pushover and push-down analyses were carried out to evaluate the influence of different parameters in the in-plane capacity of the buildings: i.e. geometry (such as height and length) and settlement profiles. Two types of analysis were carried out: pushover analysis on masonry walls subjected only to horizontal load; push-down and pushover analysis on the same panels previously damaged by settlements subjected to the equal seismic action. The reduction of the seismic resistance due to settlements has been evaluated by comparing the force-displacement curves obtained from the push-over analyses of the walls with and without settlement applications. Finally, push-down curves are defined to evaluate the damage of masonry structures in the case of settlements, capacity curves which relate the vertical reaction and the displacement at a control point are used to quantify the values of settlement corresponding to different damage states.

Index Terms

Masonry, settlements, seismic vulnerability, pushover analysis, FEM analysis.

I. INTRODUCTION

Unreinforced masonry buildings, particularly widespread in historic centers of Italian and European small and medium towns, are often characterized by a high vulnerability toward seismic actions shown by damages and collapses due to the activation of in-plane and/or out-of-plane failure mechanisms. Moreover, historic masonry structures are often damaged by soil settlements and ground movements, often caused by the current increase in urban tunneling and underground excavation. The occurrence of free-field settlements can lead to damages to the buildings [1], which could particularly affect their vulnerability toward seismic actions [2]. From this discussion, it is clear the importance of considering the influence of soil settlements on the seismic response of masonry buildings.

In literature, different simplified methods are proposed for the assessment of the effects of settlements on masonry structures [3-6], which model masonry walls as equivalent beams and correlate the damage with the maximum tensile deformations. These approaches do not take into account the wide variety of geometric and mechanical characteristics, nor the construction techniques that significantly influence the behavior of the panels. Given the complexity and the uncertainties that affect the structural properties of historical masonry buildings, it is important to adopt a modeling strategy that can accurately describe the response while being simple and based on few mechanical parameters.

II. VALIDATION OF THE PROPOSED NUMERICAL MODEL

In this work, a 2D finite-element approach, which takes into account the non-linear behavior of the material, is implemented in the Abaqus CAE environment. Masonry panels are modeled as homogenized continuum shell elements and their mechanical behavior is described with the analytical material model called Concrete Damaged Plasticity (CDP) [7]. This model is based on damage mechanics: it was created to describe the plastic properties of concrete [8] but can be used to model quasi-brittle materials like masonry [8–10]. The parameters required to define the yield surface employed by the CDP model are the dilation angle (10°); the flow potential eccentricity (0.1); the ratio between the initial biaxial compressive yield stress and the initial uniaxial compressive yield stress (1.16); the ratio of the second stress invariant on the tensile meridian to that on the compressive meridian (0.666); the viscosity parameter (0.002) [11]. Two different constitutive laws in compression and tension can be defined. In both cases, the constitutive behavior follows a linear elastic response with a slope equal to Young modulus until the yielding stress and the ultimate tensile strength respectively; then a softening behavior is implemented once crushing is attained in compression and the ultimate deformation is reached in traction. The parameters are summarized in Table 1.

TABLE I: Mechanical parameter for the numerical simulation

E	ν	fc	εc	ft	εt
3900	0.2	9	0.01	0.3	0.008

At first, the model is validated on tests on masonry shear walls carried out by Raijmakers and Vermeltfoort in 1992 [12]. The specimen was a full panel with a width of 990 mm and a height of 1000 mm. It presented 18 courses of Josteen solid clay bricks (204 x 98 x 50 mm^3) and 10 mm thick mortar. The wall was subjected to an initial vertical uniformed distributed load of different intensities (0.30, 1.21, 2.12 N/mm^2) and then to a horizontal load monotonically increased under displacement control until failure, applied at the top of the panel. The comparison between the experimental and numerical results (Fig. 1) indicates that the model successfully captures the masonry behavior, both in terms of failure load and damage pattern. Initially, horizontal tension cracks appear at the top and bottom of the wall. As the applied deformation increases, a diagonal shear crack develops, ultimately leading to collapse [13]. In terms of pushover curve, the model accurately predicts the base shear capacity and both pre-peak and post-peak behaviors.

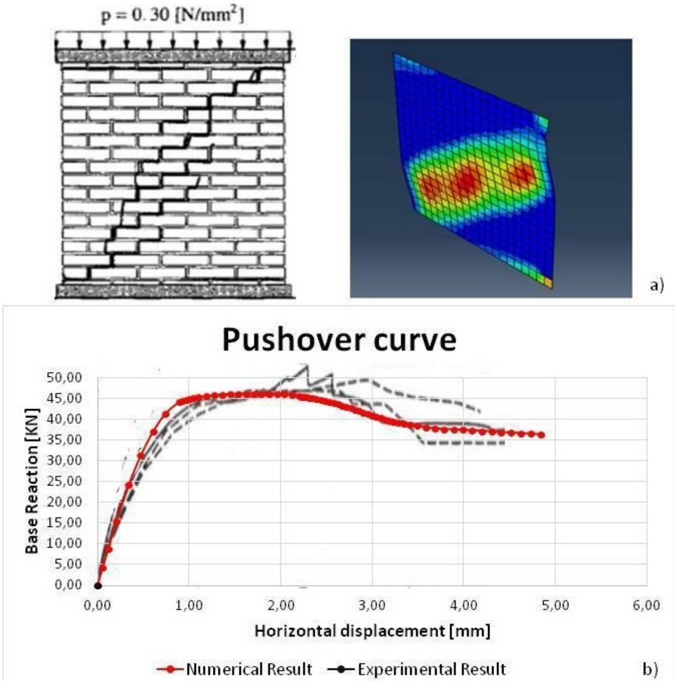

Fig. 1: a) Comparison of damage status, b) Experimental and numerical capacity curves [13]

III. PARAMETRIC ANALYSIS

In order to investigate the influence of soil settlements on the response of masonry walls to seismic events, this work explores the possibility of employing force-displacement-based assessment methods to evaluate the seismic performance of existing structures under differential settlements. To this aim, pushover analyses on masonry panels are developed by considering different settlement profiles (diffused along the base and concentrated in a part of the base) and different geometries by varying height *H* and thickness *t*.

D. The effect of diffused settlements

A widespread parabolic differential settlement was applied across the entire base of the wall, with a maximum value at the midpoint of 10 mm. A monotonically increasing horizontal load was applied to the damaged wall and the pushover curves were obtained. The results were compared with the pushover curves evaluated for the undamaged masonry walls with the same geometrical configurations (Fig. 2). The pushover curves indicate that the variation in thickness does not significantly affect the percentage reduction in maximum seismic resistance due to settlements, with respect the case without settlements; it remains approximately at 10% in all cases (Fig. 2.a). Walls with a ratio between the base *B* and the height *H* (*B/H*) ratios less than 1 show results consistent with those obtained by varying the wall thickness, with a reduction slightly below 10%. (Fig. 2.b). On the contrary, the walls with a *B/H* ratio greater than 1 are more vulnerable to sagging settlements, showing a reduction of strength ranging from 20% to 50% (Fig. 2.b). In all cases, the presence of settlements strongly reduces the pre-peak slope of the curves.

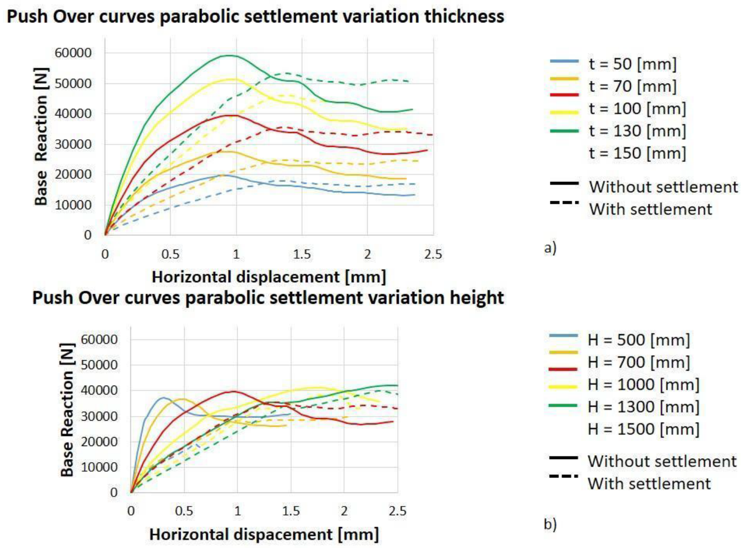

Fig. 2: Push Over curves for parabolic settlement a) Results with variation of the thickness b) Results with the variation of the height

E. The effect of lateral settlements

Considering the same geometrical configurations as before, a lateral settlement was applied, affecting only a portion of the foundation of 200 mm. The entity of the applied settlements have been selected on push-down curves, obtained by a static non-linear analysis at displacement control. The push-down curves plot the vertical reaction of the part of the base involved in the settlement versus the vertical displacement of the control point. From these curves, two values of settlements are selected, which correspond to: maximum elastic vertical displacement (DL2); vertical displacement corresponding to the minimum reaction in the capacity curve (DL3)[15]. At title of example, a push-down curve is shown in Figure 3, and the two intensities of settlements are highlighted.

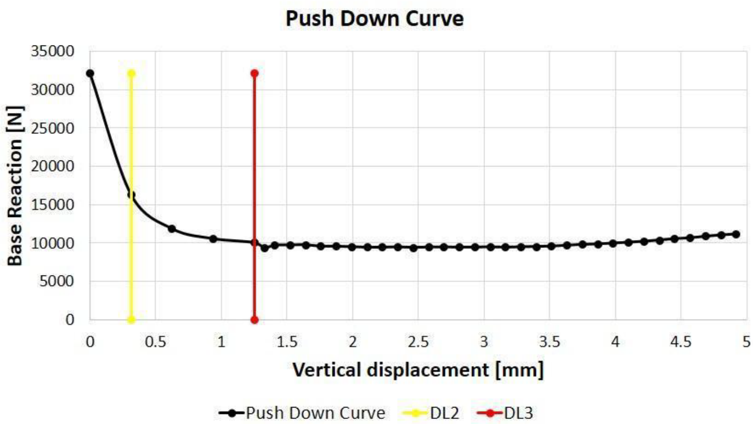

Fig. 3: Example of push-down curve

These curves indicate that the vertical reaction at the base, prior to the application of the settlement, is equal to the self-weight of the panel involved in the settlement. Indeed, it starts from the weight of the part of the panel above the portion of the base to which the settlements are applied and decreases until the self-weight of the portion of the wall that detaches. Similar to the case of parabolic settlement, pushover analyses were conducted on masonry panels by applying these settlement values and comparing them to those evaluated on the undamaged ones. For sake of brevity, Figure 4 shows the pushover curves for a damage level DL3 due to settlements. In this case, the capacity curves demonstrate a reduction in stiffness and maximum strength as the height *H* of the wall increases. Specifically, walls with a *B/H* ratio greater than 1 show a seismic capacity reduction of less than 15/20%. Conversely, walls with *B/H* ratio lower than 1 exhibit a reduction in resistance to horizontal actions ranging from 50% to 70%. (Fig. 4.b). The variation in thickness *t* indicates a strong reduction of strength for thicker walls, with a reduction in maximum strength ranging from 10% to 30% and from 40% to 50%, respectively (Fig. 4.a).

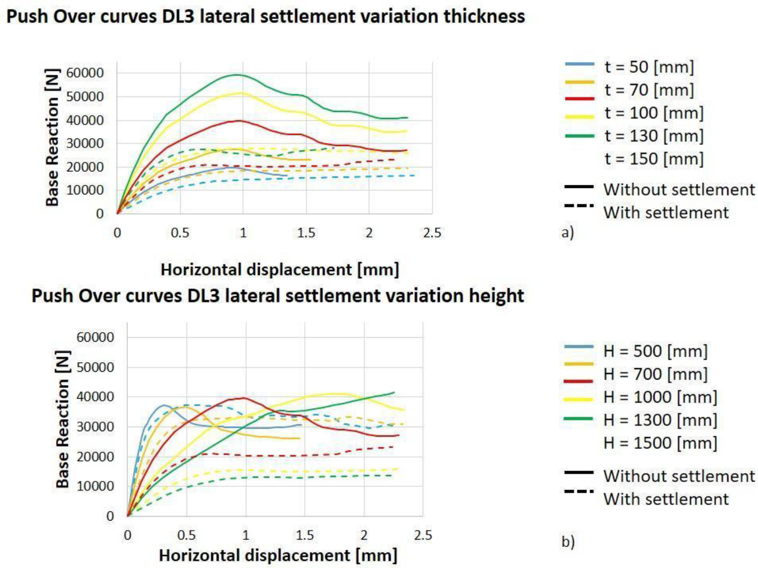

Fig. 4: Pushover curves for DL3 settlement a) Results with variation of the thickness b) Results with the variation of the height

The parametric analyses conducted have demonstrated that unreinforced masonry walls are more susceptible to localized settlements compared to distributed differential ones. This is evident in all the different geometric configurations considered, where the maximum percentage reduction in strength, as evaluated by the push-over curves, is more pronounced for walls subjected to lateral vertical displacement, or at the most, comparable to what is observed in the case of parabolic settlement. It's worth noting that, furthermore, in the configuration of a distributed parabolic profile, the maximum vertical displacement is approximately ten times greater than that in the case of localized one. This data confirms that masonry walls are more sensitive to damage caused by lateral configuration of settlements.

IV. CONCLUSIONS AND FUTURE DEVELOPMENTS

The paper addresses the issue of foundation settlements in masonry constructions and the impact these settlements can have on the structures' ability to withstand vertical and seismic actions. Existing simplified methodologies in the literature for assessing the effects of settlements on masonry structures often overlook the complexity of geometries, materials, and masonry types found in historic buildings. This work proposes a methodology for assessing damage due to foundation settlements to historical masonry buildings and its impact on their seismic capacity through non-linear static analysis.

The study focused on the in-plane seismic response of masonry buildings subjected to settlements, with specific reference to two-dimensional homogenized continuum masonry panels using a damage mechanics-based model through nonlinear static FEM analyses in Abaqus CAE.

Parametric pushover and push-down analyses were performed to evaluate the influence of geometry and settlement profiles on the in-plane capacity of the buildings. Two types of analyses were conducted: pushover analyses on undamaged masonry walls and push-down and pushover analyses on panels with the same geometrical configuration to obtain the response of walls subjected to seismic action but previously damaged by settlements.

From the comparison of the pushover curves, it became evident that the reduction in seismic resistance due to settlements is significant, with a decrease that can vary depending on the cases, in fact, the application of different settlement profiles induces a different behavior of the wall with the same geometric characteristics. Overall, the parametric analyses highlighted that unreinforced masonry walls are more vulnerable to localized differential settlements compared to distributed differential ones, with a difference of over ten times in the maximum vertical displacement applied. Finally, it's important to consider that even small vertical displacements, when applied, can lead to a significant percentage reduction in terms of capacity, which can reach up to 50/70%.

These conclusions emphasize the importance of considering the effects of foundation settlements in assessments of the seismic capacity of masonry structures, especially in historic buildings, and underscore the importance of adopting accurate models that account for the complexity of factors influencing masonry behavior.

In addition, future endeavors should encompass a broader range of parameter variations and a more comprehensive set of parametric analyses. Furthermore, it is imperative to consider the influence of additional parameters that may impact the seismic response, including the presence of openings and mechanical characteristics.

REFERENCES

[1] Nghiem L., Al Heib M., Emeriault F., Understanding subsidence consequences on masonry structures using large small-scale physical modeling. 8th International Conference on Physical Modelling in Geotechnics (ICPMG 2014), Jan 2014, Perth, Australia. pp.1195-1202.

[2] Drougkas A., Licciardello L., Rots Jan G., Esposito R., "In-plane seismic behaviour of retrofitted masonry walls subjected to subsidence-induced damage" 10.1016/j.engstruct.2020.111192, Engineering Structures, vol. 223, 2020.

[3] Burland J.B., Wroth C.P. (1974) – Settlement of buildings and associated damage. Proc. Conf. Settlement of Structures, Cambridge, UK, pp. 611-654.

[4] Boscardin M.D., Cordinge E.J. (1989) – Buildings response to excavation-induced settlement. Journal of

Geotechnical Engineering, ASCE, 115, n.1, pp. 1-21.

[5] Burland J.B. (1995) – Assessment of risk of damage to buildings due to tunneling and excavation. 1st Int. Conf. on Earthquake Geotechnical Engineering, Tokyo, pp. 1189-1201.

[6] Pickhacer J.A., Burd H.J., Houlsby G.T. (2010) – An equivalent beam method to model mansory buildings in 3D finite element analysis. Computers and Structures,88, nn. 19-20, pp. 1049-1063.

[7] Abaqus Version 2022 User Manual. Dassault Systèmes.

[8] S. Tiberti, M. Acito, G. Milani, Comprehensive FE numerical insight into Finale Emilia Castle behavior under 2012 Emilia Romagna seismic sequence: Damage causes and seismic vulnerability mitigation hypothesis, Eng. Struct. 117 (2016) 397–421.

[9] M. Valente, G. Milani, Non-linear dynamic and static analyses on eight historical masonry towers in the North-East of Italy, Eng. Struct. 114 (2016) 241–270.

[10] G. Castellazzi, A.M.D. Altri, S. De Miranda, F. Ubertini, An innovative numerical modeling strategy for the structural analysis of historical monumental buildings, Eng. Struct. 132 (2017) 229–248.

[11] S. Degli Abbati, et al., Seismic assessment of interacting structural units in complex historic masonry constructions by nonlinear static analyses, Comput. Struct. 213 (2019) 51–71, https://doi.org/10.1016/j.compstruc.2018.12.001.

[12] Vermeltfoort, A.Th., Raijmakers, T.M.J., 1993. Deformation Controlled Tests in Masonry Shear Walls. Part 2 (in dutch). Report UE/BKO/93.08. Eindhoven University of Technology, Eindhoven, The Netherlands.

[13] Lourenço PB, Rots JG. Multisurface interface model for analysis of masonry structures. J Eng Mech 1997;123(7):660–8.

[14] De Felice G., Malena M., 2019- Failure pattern prediction in masonry - dx.doi.org/10.2140/jomms.2019.14.663/ JOURNAL OF MECHANICS OF MATERIALS AND STRUCTURES Vol. 14, No. 5.

[15] Gagliardo R., Portioli F., Cascini L., Landolfo R., Lourenco P., 2021/02/01 - 111609 - A rigid block model with no-tension elastic contacts for displacement-based assessment of historic masonry structures subjected to settlements - 229 - 10.1016/j.engstruct.2020.111609- Engineering Structures

The hydrogeological response of the Sibillini hydrostructure to the M_W 6.5 Norcia earthquake: conceptual model and numerical analysis

Enrica Zullo[1], Matteo Albano[2], Michele Saroli[1,2], Marco Moro[2], Gabriel Testa[1], Nicola Bonora[1], Marco Petitta[3], Thomas Reimann[4] and Carlo Doglioni[2,3]

[1] Department of Civil and Mechanical Engineering, University of Cassino and Southern Lazio, Cassino 03043, Italy
Email: enrica.zullo@unicas.it
[2] National Institute of Geophysics and Volcanology (INGV), Rome 00143, Italy
[3] Department of Earth Sciences, University of Rome "La Sapienza" 00185, Italy
[4]Institute for Groundwater Management, Technische Universität Dresden 01062, Germany

Abstract

Keywords: earthquake, Groundwater, numerical modeling

The Sibillini Mts. hydrostructure is characterized by the coexistence of a shallow and a basal regional aquifer [1] whose spatial distribution, recharge area and groundwater dynamics are strongly controlled by a complex regional tectonic framework.
The 2016 Central Italy seismic sequence, which resulted from the rupture of the Vettore-Bove normal fault system, drastically changed the hydrodynamics of the carbonate aquifers of the Sibillini Mts., causing sustained variations in groundwater flow and resulting in several issues for the local water supply system. Significant hydrogeological changes occurred especially after the Mw 6.5, 30 October main shock (the Norcia earthquake), the most important of which include: i) a surplus of groundwater discharge at springs bordering the western side of the Sibillini Mts. and along the main drainage system of the Nera River basin; ii) the reappearance of Torbidone spring in the Norcia plain, dry since 1979 [2, 3] and iii) a strong discharge reduction and water-table decrease at the Adriatic springs located at high altitude, on the eastern side of the Sibillini Mts.
Considering previous recent studies [4] and according to Mastrorillo *et al*. [5], the “aquifer fault rupture” mechanism better explain the observed permanent hydrogeological variations, coupled with the general increase in bulk crustal permeability, related to the dynamic stress induced by the seismic waves’ propagation [6].

In this work, we aim at assessing the hydrodynamic response of the fractured carbonate Basal Aquifer of the Sibillini Mts. to the coseismic dislocation of the Vettore fault by using a multidisciplinary approach and numerical analysis as a main tool.
To this purpose, we collected geological and hydrogeological data to first define a hydrogeological conceptual model, which represents the supporting structure of numerical analysis. We created a simplified 3D geometric model at surface scale (up to 2 km depth) to reconstruct the Basal Aquifer bottom surface and to define the spatial relations with the main tectonic structures.
Then we performed a numerical analysis to create a regional scale hydrogeological model to simulate the groundwater flow, in steady-state conditions, in two different scenarios:

i) at the pre-rupture stage, by considering faults as hydraulic barriers with a lower permeability than that of the carbonate aquifer;
ii) at the post-rupture stage, by assuming an increased permeability for the Vettore normal fault.

The computed distributions of the hydraulic head and the directions of groundwater flow are qualitatively consistent with the water-levels observations and discharge values measured before and after the earthquake.
Future work will be devoted to the calibration of the models. We are going to perform an automatic calibration of the hydrogeological models in order to estimate the hydraulic parameters, by using the available discharge values and water table measurement as calibration targets. In addition, a full 3D geomechanical model for the simulation of the Norcia earthquake will be developed, calibrated using a fem numerical inversion of interferometric SAR data available for the 30 October earthquake, to estimate the crustal stress and strain variations. The coseismic volumetric strain changes obtained by the simulation of the seismogenic fault dislocation will be exploited to assess the permeability changes in the crust. This latter will be compared with the results obtained from the calibrated hydrogeological model.

REFERENCES

[1] Viaroli S., Mirabella F., Mastrorillo L., Angelini S. & Valigi D., 2021. *Fractured carbonate aquifers of Sibillini Mts. (Central Italy).* Journal of Maps, 17:2, 140-149.

[2] Valigi D., Mastrorillo L. Cardellini C., Checcucci R., Di Matteo L., Frondini F., Mirabella F., Viaroli S., Vispi I., 2019. *Springs discharge variations induced by strong earthquakes: The Mw 6.5 Norcia event (Italy, 30 October 2016)*. Rend. Online Soc. Geol. Ital., 47, 141–146. https://doi.org/10.3301/ROL.2019.25.

[3] Petitta M., Mastrorillo L., Preziosi E., Banzato F., Barberio M.D., Billi A., Cambi C., De Luca G., Di Carlo G., Di Curzio D., Di Salvo C., Nanni T., Palpacelli S., Rusi S., Saroli M., Tallini M., Tazioli A., Valigi D., Vivalda P., Doglioni C., 2018. *Water-table and discharge changes associated with the 2016–2017 seismic sequence in central Italy: hydrogeological data and a conceptual model for fractured carbonate aquifers.* Hydrogeol J 26, 1009–1026. https://doi.org/10.1007/s10040-017-1717-7.

[4] Saroli M., Albano M., Moro M., Falcucci E., Gori S., Galadini F., Petitta M.; 2022. *Looking into the Entanglement between Karst Landforms and Fault Activity in Carbonate Ridges: The Fibreno Fault System (Central Italy).* Front. Earth Sci., 10:891319. Doi:10.3389/feart.2022.891319.

[5] Mastrorillo L., Saroli M., Viaroli S., Banzato F., Valigi D. & Petitta M., 2020. *Sustained post-seismic effects on groundwater flow in fractured carbonate aquifers in Central Italy.* Hydrological Processes, 34(5),1167–1181.

[6] Manga M., Beresnev I., Brodsky E.E., Elkhoury J.E., Elsworth D., Ingebritsen S.E., Mays D.C., Wang C.Y., 2012. *Changes in permeability by transient stresses: Field observations, experiments and mechanisms*. Reviews of Geophysics 50: RG2004. http://dx.doi.org/10.1029/2011RG000382.

Generalization Challenges in Network Intrusion Detection: A Study on CIC-IDS2017 and CSE-CIC-IDS2018 Datasets

Marco Cantone1, Claudio Marocco1, Alessandro Bria1

[1]Department of Electrical and Information Engineering, University of Cassino and Southern Latium, Cassino, FR 03043 Italy
Email: marco.cantone@unicas.it, c.marrocco@unicas.it, a.bria@unicas.it

Abstract

In the ever-evolving landscape of cybersecurity, Network Intrusion Detection Systems (NIDS) are indispensable safeguards against network breaches and malicious activities. The effectiveness of Network Intrusion Detection Systems (NIDS) in safeguarding computer networks against unauthorized access and malicious activities largely depends on their ability to generalize from training data to real-world scenarios. In this study, we investigate the generalization capability of NIDS models based on machine learning when trained on one dataset and evaluated on another, utilizing the widely recognized CIC-IDS2017 and CSE-CIC-IDS2018 datasets.

To execute this study, we adopted a supervised machine learning approach. We trained both LDA and Random Forest models on the CIC-IDS2017 dataset, a comprehensive repository of network traffic data, encompassing various intrusion scenarios and traffic patterns. This dataset served as the foundation for the training phase, enabling the models to learn and discern normal network behaviors from intrusive ones.

Subsequently, we subjected these models to rigorous evaluations using the CSE-CIC-IDS2018 dataset, a dataset featuring a similar set of attack classes but characterized by differences in data distribution and other dataset-specific factors. Our analysis encompassed a comprehensive set of performance metrics, including mainly Matthews Correlation Co-efficient (MCC) but also accuracy, precision, recall and F1-score. Additionally, in certain cases, we conducted a thorough inspection of specific subsets of the feature space to gain insights into the models' behavior and better understand their performance. The findings of our study were both surprising and significant. Both the LDA and Random Forest models exhibited near-perfect performance when tested on the dataset they were initially trained on (CIC-IDS2017). This result was anticipated, as the models had effectively learned to detect intrusions within a familiar environment.

However, a noteworthy and somewhat unexpected trend emerged when the models were evaluated on the CSE-CIC-IDS2018 dataset. Their performance experienced a sharp and substantial drop, revealing the challenge of NIDS model generalization across datasets with varying characteristics. This stark contrast underscores the significance of dataset- specific factors, including differences in data distribution, feature relevance, and the pres- ence of dataset-specific anomalies In light of these findings, our study underscores the critical

importance of thoroughly assessing the generalization capability of NIDS models. Network security practitioners and developers must be cognizant of the limitations in adaptability that arise when models trained on one dataset are confronted with diverse datasets. As a way forward, we propose that future research should explore transfer learning techniques and domain adaptation methods tailored to the unique characteristics of network intrusion detection. These ap- proaches have the potential to enhance NIDS generalization and improve their effectiveness in real-world network security applications.

Index Terms

Network Intrusion Detection System, Dataset Generalization, CIC-IDS2017, CSE-CIC-IDS2018.

References

[1] Laurens D'hooge, Tim Wauters, Bruno Volckaert, and Filip De Turck. Inter-dataset generalization strength of supervised machine learning methods for intrusion detection. *Journal of Information Security and Applications*, 54:102564, 2020.

[2] Ansam Khraisat, Iqbal Gondal, Peter Vamplew, and Joarder Kamruzzaman. Survey of intrusion detection systems: techniques, datasets and challenges. *Cybersecurity*, 2(1):1–22, 2019.

[3] Mohanad Sarhan, Siamak Layeghy, Nour Moustafa, and Marius Portmann. Cyber threat intelligence sharing scheme based on federated learning for network intrusion detection. *Journal of Network and Systems Management*, 31(1):3, 2023.

[4] Mohanad Sarhan, Siamak Layeghy, and Marius Portmann. Towards a standard feature set for network intrusion detection system datasets. *Mobile networks and applications*, pages 1–14, 2022.

[5] Iman Sharafaldin, Arash Habibi Lashkari, and Ali A Ghorbani. Toward generating a new intrusion detection dataset and intrusion traffic characterization. *ICISSp*, 1:108–116, 2018.

[6] Deris Stiawan, Mohd Yazid Bin Idris, Alwi M Bamhdi, Rahmat Budiarto, et al. Cicids-2017 dataset feature analysis with information gain for anomaly detection. *IEEE Access*, 8:132911–132921, 2020

OneBitPitchTracking (OPBT): a Novel pitch tracking algorithm based on OPB and soft-decision

Davide Coccoluto, V. Cesarini

Dept. of Electronic Engineering, University of Rome Tor Vergata, Rome, Italy

davide.coccoluto@gmail.com

Abstract

This paper presents a novel, high-speed and low latency implementation of a pitch tracking algorithm. The pitch is a characteristic parameter of a periodic signal and it's defined as the fundamental frequency [1] (the inverse of the minimum repetition period of the signal).
The real-time knowledge of the fundamental frequency is extremely useful in various scenarios like radio frequency tracking, doppler effect estimation, mechanical faults detection [2] and audio/vocal processing.
This paper presents a new implementation of a pitch tracking algorithm, focused on high speed and low latency performances for fast real-time applications.
The base ground algorithm used is the OneBitPitch (OPB)[3] because of its fast execution time and the proven high quality results. Moreover the intrinsic low-level bit operation of OPB makes it is perfectly suitable for a Field Programmable Gate Array (FPGA) implementation achieving high parallelization and low area consumption.
Being based on estimations, every pitch detection algorithm is susceptible to false detection and errors. In particular the correlation based algorithms (like OPB) are prone to octave errors [4] occasionally estimating the half or the double of the real frequency.
In a pitch tracking scenario the previous estimations can be exploited to model a statistical behavior of the system and a maximum-likelihood decision can be made to confirm if the current estimation is correct or if it's affected by errors.
The most effective maximum-likelihood estimators are based on neural networks [5] or on minimum-path search like Viterbi algorithm [6]. The performances of these approaches are extremely reliable obtaining a low error rate and high accuracy but at the cost of high computational complexity and high latency [7].
On the other hand this research is aiming to the complete opposite: exploiting a simple soft-decision algorithm that can lead to a fast result while keeping the error rate in an acceptably low bracket.

The fundamental idea of this soft decision is based on the mathematical fact that, starting from a perfect periodic signal, the autocorrelation of the signal itself is equal to the autocorrelation of the signal reversed in time (mirrored on the y-axis).
A soft-decision algorithm is estimating these differences between these two autocorrelations to minimize the errors.
An extensive dataset has been used to test this algorithm and it’s based on both real audio signals and synthetical digital signals.
The data dataset is based on an incremental difficulty and a gradually more challenging input signals.
The first cluster is based on synthetic waveforms with perfectly defined pitch, without noise and impurity. Different patterns have been tested like frequencies increasing in a linear shape, parabolic, sinusoidal, exponential ecc.
The second cluster is based on real audio signals recorded from an electric guitar. The sound is intrinsically noisey and the pitch is not perfectly constant in time but the waveform periodicity is still understandable even by visual inspection.
The last cluster is based on The Pitch Tracking Database from Graz University of Technology (PTDB-TUG). It’s a well established dataset and it contains hundreds of vocal recordings each of them is paired with the corresponding theoretical pitch that has been measured during the recording with laryngoscopic techniques. This vocal dataset is the more challenging being the one with more noise, differences of intonations and without a clear pitch in a huge amount of English un-vocal sounds.
The OPBT shows to be robust to harsh environment and noise also with the most challenging voice dataset obtaining an error of less than 2% on voiced signals and 95% of the estimation without octave errors. The comparison with well-established algorithms like SWIPE and YIN shows how, in certain conditions, they show a higher accuracy and less errors but for both complexity and execution time they perform around 100 times worse than OPBT.
These results show how a simple and highly optimized at low-level implementation can be extremely fast and reliable for audio applications and can be exploited in all the scenarios where low latency and high speed is more important than extreme accuracy.

References:

[1] Ruslan, N.; Mamat, M.; Porle, R.; Parimon, N. A Comparative Study of Pitch Detection Algorithms for Microcontroller Based Voice Pitch Detector. Adv. Sci. Lett. **2017**, 23, 11521–11524

[2] Qurthobi, A.; Maskeliūnas, R.; Damaševičius, R. Detection of Mechanical Failures in Industrial Machines Using Overlapping Acoustic Anomalies: A Systematic Literature Review. Sensors **2022**, 22, 10

[3] Coccoluto, D.; Cesarini, V.; Costantini, G. OneBitPitch (OBP): Ultra-High-Speed Pitch Detection Algorithm Based on One-Bit Quantization and Modified Autocorrelation. *Appl. Sci.* **2023**, *13*, 8191. https://doi.org/10.3390/app13148191

[4] Bharathi, V.; Abraham, A.; Ramya, R. Vocal pitch detection for musical transcription. In Proceedings of the 2011 International Conference on Signal Processing, Communication, Computing and Networking Technologies, Thuckalay, India, 21–22 July 2011

[5] Costantini, G.; Cesarini, V.; Robotti, C.; Benazzo, M.; Pietrantonio, F.; Di Girolamo, S.; Pisani, A.; Canzi, P.; Mauramati, S.; Bertino, G.; et al. Deep learning and machine learning-based voice analysis for the detection of COVID-19: A proposal and comparison of architectures. Knowl. Based Syst. **2022**, 253, 109539

[6] Staudacher, M.; Steixner, V.; Griessner, A.; Zierhofer, C. Fast fundamental frequency determination via adaptive autocorrelation. EURASIP J. Audio Speech Music. Process. **2016**, 2016, 17

[7] Wang, D.; Wei, Y.; Wang, Y.; Wang, J. A Robust and Low Computational Cost Pitch Estimation Method. Sensors **2022**, 22, 1

Deep Learning Techniques to Support Alzheimer's Disease Detection

Tiziana D'Alessandro[1], Francesco Fontanella[1], Claudio De Stefano[1]
[1]Department of Electrical and Information Engineering, University of Cassino and Southern Lazio, Cassino, Italy
Email: tiziana.dalessandro@unicas.it

Index Terms

Alzheimer's disease, Handwriting, Deep Learning.

Abstract

Neurodegenerative diseases (NDs) are characterized by the progressive degeneration or deterioration of the structure and function of the nervous system, particularly the neurons in the brain and spinal cord. These diseases can significantly impact a person's quality of life and may eventually lead to disability or even death. Alzheimer's Disease (AD) is the most common, typically resulting in a gradual decline in cognitive, motor, and sometimes psychiatric functions. AD remains without a cure, although various therapies can slow disease progression and enhance the quality of life for patients. An imperative requirement in managing these conditions is early detection to initiate treatments promptly. Indeed, irreversible damage may have already occurred when disease symptoms become evident. In this context, it is widely accepted that handwriting is one of the initial skills affected by the onset of cognitive disorders, as it results from a complex network of cognitive and motor skills. To address this issue, we conducted a study using a database of handwriting and drawing samples. The proposed approach involved generating and collecting different kinds of images for each handwriting sample, leveraging the capabilities of Convolutional Neural Networks (CNNs) to extract features from these raw images automatically. This study's primary objective is to assess which is the most important information between morphological shape and dynamic characteristics of handwriting, to increase the performance of a decision support system in diagnosing Alzheimer's Disease.

Multivariate Cryptography: An improvement of Oil and Vinegar scheme

Antonio Corbo Esposito[1], Rosa Fera[1] and Francesco Romeo[1]
[1]Department of Electrical and Information Engineering, University of Cassino and Southern Lazio, Cassino, Italy 03043
Email: corbo@unicas.it
rosa.fera@unicas.it
romeofra95@gmail.com

Abstract

Current encryption standards (both military and commercial) could not ensure communications' safety. It is indeed known that quantum computers can run Shor's algorithm, which is capable to "break" main current encryption algorithms (e.g. problems based over elliptic curves or RSA). NIST (National Institute of Standards and Technologies, USA) has already completed a first international call of "quantum resistant" algorithms, choosing the best ones them in the summer 2022, and this selection is still proceeding. Among other topics, NIST focused the attention on the digital signature algorithms. Some of these algorithms are based on the mathematical problem of solving Multivariate Quadratic Polynomials' System over Finite Field, for example, UOV or Rainbow. Indeed, Multivariate Quadratic System are "Quantum Resistant", so we propose an innovative algorithm, suitable not only for digital signatures, based on them.

Index Terms

Cryptography, Commutative Algebra, Multivariate Cryptography, Post-Quantum Cryptography, Finite Fields, Multivariate Quadratic Polynomials, Rainbow, Oil and Vinegar scheme, Hilbert Series

I. Introduction

In the last years there is a lot of interest in quantum computers' development since they could solve many mathematical problems that are difficult for conventional computers. In particular quantum computers are able to break the most widely used public-key cryptosystems; for example, the ECDSA protocol used for authentication in cryptocurrencies schemes is very well-known to be vulnerable to Shor's Algorithm (see [10], [17]): such algorithm can be efficiently implemented on a quantum computer. These issues led the National Institute of Standards and Technology (NIST) to open a call in 2016 for "Post-Quantum" encryption algorithms. The goal to reach is to create new cryptographic protocols that are secure against both quantum and classical computers.

All mathematical problems that are known to be NP-complete are natural candidates for building algorithms that satisfy such requirements. One of these problems is the resolution of Systems of Multivariate Polynomials over Finite Fields, that is NP-complete even for systems of quadratic equations on $\mathbb{F}_2$. This feature inspired many researchers to build cryptosystems based on Multivariate Quadratic systems (MQ for brevity), i.e. algebraic systems of multivariate polynomials of degree 2.

The first MQ-scheme has been introduced by Matsumoto and Imai in 1988 (see [13]). Although their C^* scheme was broken by Jacques Patarin in 1995 (see [14]), such a scheme was generalised by Patarin himself: in 1996, in [15] he presented the *Hidden Field Equations* (HFE) scheme that can be used in the context of asymmetric cryptography, for digital signatures or encryption of very short messages.

However, there have been many attacks that broke HFE scheme: the first attack was presented by Kipnis and Shamir in 1999 (see [12]) by an innovative technique called relinearization; other attacks are the XL algorithm (see [7]), based on the linearization of the system or the one due to Faugere and Joux (see [9]), which is based on the computation of Gröbner basis of the multivariate quadratic system.
However in 1997, Patarin proposed a new scheme, suitable for digital signatures, called *Oil and Vinegar scheme* (for more details, see II) [16]. Such a scheme is based on an under-determined MQ-system and the goal is to find one of the many preimages of the original message.

It must be highlighted that in the case in which the number of oil variables is equal to the number of the vinegar variables, the scheme was already broken by Kipnis and Shamir (see [11]), therefore it was modified to the so-called "Unbalanced Oil and Vinegar scheme" (UOV), where the number of vinegar variables is greater than the number of oil ones (see [1]). Among the various algorithms based on the UOV scheme, there is one that succeeded to be selected to the third round of NIST competition, that is Rainbow. It is a digital signature scheme designed by Ding and Schmidt in 2004 (see [8]).

In our opinion, the initial failure of HFE and the challenges of solving an OV system with numerous vinegar variables led many researchers to disregard the potential use of the OV scheme for over-determined systems.

On the other hand, the early success of UOV and Rainbow multiplied interest and research into building attacks on this type of systems; these studies culminated very recently into very important breakthroughs: Bardet et al. introduced a very efficient attack, Support Minors Modeling, to solve the so-called MinRank problem, i. e. how, given a finite set of matrices, to find their existing linear combinations having a prescribed small rank (see [2]). Such improvement, gave an important contribution to more targeted attacks to UOV and Rainbow, whose security was significantly weakened by Beullens (see [3], [4]). Ultimately, this led to the defeat of Rainbow in the final round of NIST competition for signature protocols.

Another weak point of all of the systems cited above are their restricted application only to digital signatures schemes, given their under-determined structure. The purpose of the present paper is to announce that it is possible to build an over-determined MQ-system with trapdoor (therefore suitable not only for signature protocols but also for encryption ones), based on a suitable mixing of OV-type equations and fully quadratic ones. Moreover, up to the current knowledge, there is no known attack running in a time bounded by polynomial function of the decryption time that solves this type of system. In particular, we analyzed the Hilbert series of both OV systems and the mixed ones (see III). Finally, we want to apply some algebraic techniques to speed up the complexity of the solving algorithm of the system.

II. Oil and Vinegar scheme

We now introduce the MQ system of our interest: an over-determined mixed system of quadratic polynomials in $\mathbb{F}_2[x_1,\ldots,x_n]$, that is, a system composed by fully quadratic polynomials and the Oil and Vinegar ones. For this reason, we recap that a fully quadratic polynomial in $\mathbb{F}_2[x_1,\ldots,x_n]$ is a polynomial of the form:

A. *Fully Quadratic polynomial*

$$p(x_1,\ldots,x_n) = \sum_{1\le i\le j\le n} \alpha_{ij}x_ix_j + \sum_{i=1}^{n}\beta_i x_i + \gamma \tag{1}$$

To describe an Oil and Vinegar polynomial in n variables over $\mathbb{F}_2$, let $v,n \in \mathbb{N}$ be positive integers with $v < n$. A quadratic polynomial of the form

B. *OV polynomial*

$$f(x_1,\ldots,x_n) = \sum_{i=1}^{n}\sum_{j=1}^{v}\alpha_{i,j}x_ix_j + \sum_{i=1}^{n}\beta_i x_i + \gamma, \tag{2}$$

namely with no monomial x_ix_j for $i,j \in \{v+1,\ldots,n\}$, is called an Oil and Vinegar (OV) polynomial. The variables $x_1,\ldots,x_v$ are called *vinegar* variables, while the variables $x_{v+1},\ldots,x_n$ are called *oil* variables.

Now, we assume that $v << n$ and $o = n - v > v$. Let $\varepsilon, u \in \mathbb{N}$ be positive integers such that $1 \le \varepsilon \le n$, and set $m = n + \varepsilon + u$. A mixed multivariate quadratic system, that represents our public key, is an over-determined system, given by

C. *mixed multivariate quadratic system*

$$P(x_1\ldots,x_n) = (p_1(x_1,\ldots,x_n),\ldots,p_m(x_1,\ldots,x_n)), \tag{3}$$

where for $i \in \{1,\ldots,n+\varepsilon\}$ we have

$$p_i(x_1,\ldots,x_n) = g_i(x_1,\ldots,x_n) + \sum_{j=1}^{u}\lambda_{ij}q_j(x_1,\ldots,x_n), \tag{4}$$

with $\lambda_{ij} \in \mathbb{F}_2$, and for $i \in \{n+\varepsilon+1, \dots, m\}$

$$p_i(x_1, \dots, x_n) = q_{i-(n+\varepsilon)}(x_1, \dots, x_n). \tag{5}$$

In particular, the polynomials $g_i(x_1, \dots, x_n)$ are obtained as

$$g_i(x_1, \dots, x_n) = f_i(S(x_1, \dots, x_n)), \tag{6}$$

for $i \in \{1, \dots, n+\varepsilon\}$, where $f_1(x_1, \dots, x_n), \dots, f_{n+\varepsilon}(x_1, \dots, x_n) \in \mathbb{F}_2[x_1, \dots, x_n]$ are OV polynomials and $S \in GL_{\mathbb{F}_2}(n)$, and $q_1(x_1, \dots, x_n), \dots, q_u(x_1, \dots, x_n) \in \mathbb{F}_2[x_1, \dots, x_n]$ are fully quadratic polynomials, for any $i \in \{1, \dots, u\}$.

III. Hilbert Series and main results

In this section, we recall the definition of the Hilbert series that allows to estimate the solving degree of the system and so, its complexity.
Given $I \subseteq R = \mathbb{K}[x_1, \dots, x_n]$ homogeneous ideal, the Hilbert-Poincaré series of R/I is

A. *Hilbert-Poincaré series*

$$HS_{R/I}(t) := \sum_{d \in \mathbb{N}} H_{R/I}(d) t^d, \tag{7}$$

where $H_{R/I} : \mathbb{N} \to \mathbb{N}$, defined as

B. *Hilbert function*

$$H_{R/I}(d) := \dim_{\mathbb{K}} (R/I)_d, \tag{8}$$

is the so-called Hilbert function and $(R/I)_d$ is the d-degree component of the gradation of R/I (see [6], [5]).

By the Hilbert-Serre theorem, the Hilbert-Poincaré series of R/I is a rational function. In particular, by reducing this rational function we get

$$HS_{R/I}(t) = \frac{h(t)}{(1-t)^d}. \tag{9}$$

that is called *reduced Hilbert series*. It is well-known that for large d the Hilbert function $H_{R/I}(d)$ is a polynomial, called *Hilbert polynomial*, denoted by $HP_{R/I}(t)$. The least d for which $H_{R/I}(d) = HP_{R/I}(d)$, is called *index of regularity*. Observe that, since $H_{R/I}(d) = \dim_{\mathbb{K}} R_d - \dim_{\mathbb{K}} I_d$, the index of regularity can be seen as the smallest d for which I_d generates all the space R_d. We define the *degree of regularity* of a system of polynomial equations as the index of regularity of $R/(f_1, \dots, f_m)$. It can be seen as the least degree d such that we obtain relations on the equations, that is the number of equations is greater than the number of monomials. Moreover, one can completely solve the system at a given

degree D if the sum of the coefficients up to degree D is negative.
Among the results announced in this work, there is the following theorem in which we give an exact expression for the Hilbert series of a OV-system.

Theorem 1: Let F be a homogeneous system of m quadratic OV-equations with v vinegar variables. Then for any $d \in \mathbb{N}$

$$H_{R/F}(d) = \binom{n-v+d-1}{d} + H_{\mathcal{V}/F}(d), \tag{10}$$

where $\mathcal{V} = (x_1, \ldots, x_v)$ is the ideal generated by the vinegar variables.

References

[1] Jacques Patarin Aviad Kipnis and Louis Goubin. *Unbalanced Oil and Vinegar Signature Schemes*. Advances in Cryptology — EUROCRYPT '99. Springer, 1999.

[2] Magali Bardet, Maxime Bros, Daniel Cabarcas, Philippe Gaborit, Ray Perlner, Daniel Smith-Tone, Jean-Pierre Tillich, and Javier Verbel. *Improvements of algebraic attacks for solving the rank decoding and MinRank problems*. International Conference on the Theory and Application of Cryptology and Information Security, ASIACRYPT 2020. Springer Cham, 2020.

[3] Ward Beullens. Improved cryptanalysis of uov and rainbow. Cryptology ePrint Archive, Paper 2020/1343, 2020. https://eprint.iacr.org/2020/1343.

[4] Ward Beullens. Breaking rainbow takes a weekend on a laptop. Cryptology ePrint Archive, Paper 2022/214, 2022. https://eprint.iacr.org/2022/214.

[5] Alessio Caminata and Elisa Gorla. Solving multivariate polynomial systems and an invariant from commutative algebra. *Lecture Notes in Computer Science, 2021, 12542 LNCS, pp. 3-36*, 2021.

[6] Alessio Caminata and Elisa Gorla. Solving degree, last fall degree, and related invariants. *Journal of Symbolic Computation*, 2022.

[7] Nicolas Courtois, Alexander Klimov, Jacques Patarin, and Adi Shamir. *Efficient Algorithms for Solving Overdefined Systems of Multivariate Polynomial Equations*. International Conference on the Theory and Applications of Cryptographic Techniques, EUROCRYPT 2000. Springer, 2000.

[8] Jintai Ding and Dieter Schmidt. *Rainbow, a New Multivariable Polynomial Signature Scheme*. International Conference on Applied Cryptography and Network Security. Springer, 2005.

[9] Jean-Charles Faugère and Antoine Joux. *Algebraic cryptanalysis of hidden field equation (HFE) cryptosystems using Gröbner bases*. Annual International Cryptology Conference, CRYPTO 2003. Springer, 2003.

[10] Stephen Holmes and Liqun Chen. Assessment of quantum threat to bitcoin and derived cryptocurrencies. Cryptology ePrint Archive, Paper 2021/967, 2021. https://eprint.iacr.org/2021/967.

[11] Aviad Kipnis and Adi Shamir. *Cryptanalysis of the oil and vinegar signature scheme*. Annual International Cryptology Conference, CRYPTO '98. Springer, 1998.

[12] Aviad Kipnis and Adi Shamir. *Cryptanalysis of the HFE Public Key Cryptosystem by Relinearization*. Annual International Cryptology Conference, CRYPTO '99'. Springer, 1999.

[13] Tsutomu Matsumoto and Hideki Imai. *Public Quadratic Polynomial-Tuples for Efficient Signature-Verification and Message-Encryption*. Workshop on the Theory and Application of of Cryptographic Techniques, EUROCRYPTO '88'. Springer, 1988.

[14] Jacques Patarin. Cryptanalysis of the matsumoto and imai public key scheme of eurocrypt'88. *CRYPTO'95, pp. 248-261*, 1995.

[15] Jacques Patarin. Hidden field equations (hfe) and isomorphisms of polynomials (ip): Two new families of asymmetric algorithms. *Advances in Cryptology—EUROCRYPT 96 (Ueli Maurer, ed.), Lecture Notes in Computer Science, vol. 1070, Springer-Verlag*, 1996.

[16] Jacques Patarin. The oil and vinegar algorithm for signatures. *Dagstuhl Workshop on Cryptography*, 1997.

[17] P. W. Shor. Polynomial–time algorithms for prime factorization and discrete logarithms on a quantum computer. *SIAM J. on Computing, pp. 1484–1509*, 1997.

Energy Efficiency Maximization in RIS-Assisted Networks: Exploring the Benefits of Global Reflection Constraints

Robert Kuku Fotock[1], Alessio Zappone[2], Marco Di Renzo[3]
[1]CNIT & University of Cassino and Southern Lazio, Cassino, Italy.
Email: robertkuku.fotock@unicas.it
[2]University of Cassino and Southern Lazio, Cassino, Italy.
Email: alessio.zappone@unicas.it
[3]CentraleSupelec-University Paris, France.
Email: marco.di-renzo@universite-paris-saclay.fr

Abstract

This study investigates energy efficiency in RIS-assisted wireless networks, focusing on active and nearly-passive RISs with a novel approach of applying a global reflection constraint. This constraint significantly improves network performance in single-user settings, offering better energy efficiency than local constraints. The research derives analytical formulas for SNR gains under global constraints and contrasts these gains with local constraint models, highlighting the impact of channel coefficients on performance. Further, it explores the role of path-loss exponents in determining the optimal placement of RISs and compares the efficiency of nearly-passive RISs under both constraint types in varying Rician factor scenarios. The findings provide valuable insights for optimizing RIS deployment in different wireless environments, demonstrating the advantages of global reflection constraints for enhanced network efficiency.

Index Terms

Reconfigurable Intelligent Surfaces, Signal-to-Noise Ratio (SNR), energy efficiency, global reflection constraints, local reflection constraints, single-user scenario, path loss exponent, Rician fading, optimal positioning.

I. Introduction

As we transition towards 6G technology in wireless networks, Reconfigurable Intelligent Surfaces (RISs) have emerged as a key technology, lauded for their ability to offer substantial signal flexibility with minimal power consumption [1], [2]. The quest for energy efficiency (EE) is particularly crucial, considering the modest fourfold improvement in EE achieved in 5G, far from the expected 2000x enhancement [3].

RISs, predominantly passive in nature, have been a focus of studies aiming to enhance spectral efficiency [4] and reduce power consumption [5]. However, the critical aspect of optimizing EE in terms of bits per Joule has often been overlooked.

In this research, we explore energy efficiency (EE) maximization in wireless networks using RISs with global reflection capabilities [6]. Our novel approach applies a unified reflection constraint across the entire RIS, broadening the scope of feasible reflection matrices and enhancing network performance. We focus on the advantages in EE, especially in single-user scenarios, and establish equations for quantifying SNR gains due to global constraints, validated through comparative analyses [7]. Additionally, our study investigates the effects of path loss exponents on RIS placement and compares the efficiency of nearly-passive RISs under both local and global constraints in different Rician factor scenarios, thus providing valuable insights for the deployment of energy-efficient RISs in wireless networks.

II. System Model and Problem Formulation

The system consists of K single-antenna mobile terminals that communicate over a shared resource block. The communication is facilitated by a Base Station (BS) equipped with N_R antennas. Additionally, an RIS with N reflecting elements is employed in the system, as shown in Figure 1. The channel from user k to the reconfigurable intelligent surface (RIS) is denoted by $\boldsymbol{h}_k$, which has dimensions $N \times 1$. On the other hand, $\mathbf{G}$ represents the channel from the RIS to the base station (BS), with dimensions $N_R \times N$. The matrix $\boldsymbol{\Gamma}$ is defined as a diagonal matrix, denoted as $\text{diag}(\gamma_1, \ldots, \gamma_N)$, where $\gamma_1, \ldots, \gamma_N$ represent the reflection coefficients of N RIS elements. The user's transmit power and information symbol are represented by p_k and s_k, respectively.

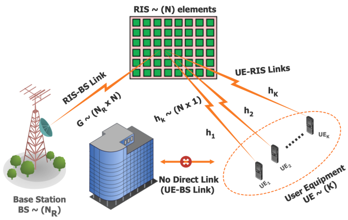

Fig. 1: RIS-aided wireless network scenario

Differing from traditional passive RISs with individual reflection constraints, we delve into an active RIS with collective constraints. This exploration leads to two significant insights:

1) Active RISs apply a collective constraint $P_{out} - P_{in} \leq 0$, in contrast to passive RISs' individual element constraints $|\gamma_n|^2 \leq 1$ (see Section III for details).
2) They use reflection-type amplifiers, allowing P_{out} to exceed P_{in}, with the power constraint being $P_{out} - P_{in} \leq P_{R,max}$, where $P_{R,max}$ is the RIS's maximum amplification power.

The subsequent discussion will differentiate between active and nearly-passive RIS scenarios.

A. *Active RIS*

The signal received at the BS is $\boldsymbol{y} = \sum_{k=1}^{K} \sqrt{p_k}\boldsymbol{G}\boldsymbol{H}_k\boldsymbol{\gamma}s_k + \boldsymbol{G}\boldsymbol{\Gamma}\boldsymbol{n} + \boldsymbol{\omega}$, with $\boldsymbol{n}$ as the thermal noise introduce by the RIS[1] and $\boldsymbol{\omega}$ as the receiver's thermal noise and are both modeled as $\boldsymbol{n} \sim \mathcal{CN}(0, \sigma^2_{\text{RIS}}\boldsymbol{I}_N)$ and $\boldsymbol{\omega} \sim \mathcal{CN}(0, \sigma^2\boldsymbol{I}_{N_R})$ respectively. The SINR for user k after applying the linear receive filter $\boldsymbol{c}_k$ is:

$$\text{SINR}_k = \frac{p_k|\boldsymbol{c}_k^H\boldsymbol{A}_k\boldsymbol{\gamma}|^2}{\boldsymbol{c}_k^H\boldsymbol{W}\boldsymbol{c}_k + \sum_{m\neq k} p_m|\boldsymbol{c}_k^H\boldsymbol{A}_m\boldsymbol{\gamma}|^2}\ , \tag{1}$$

where $\boldsymbol{A}_k = \boldsymbol{G}\boldsymbol{H}_k$ and $\boldsymbol{W}$ is the covariance matrix of the total noise at the receiver.

In the presence of power amplification, the RIS radio-frequency power [8] required for amplification purposes is given by $P_{out} - P_{in} = \text{tr}\left(\left(\boldsymbol{\gamma}\boldsymbol{\gamma}^H - \boldsymbol{I}_N\right)\boldsymbol{R}\right)$, where $\boldsymbol{R}$ is a positive definite, diagonal matrix defined as: $\boldsymbol{R} = \sum_{k=1}^{K} p_k\boldsymbol{H}_k^H\boldsymbol{H}_k + \sigma^2_{\text{RIS}}\boldsymbol{I}_N$.

The problem is to maximize the GEE, considering the RIS power constraints, transmit power, and linear receive filters:

$$\max_{\boldsymbol{\gamma},\boldsymbol{p},\boldsymbol{C}}\ \text{GEE} = \frac{B\sum_{k=1}^{K}\log\left(1 + \text{SINR}_k\right)}{\text{tr}((\boldsymbol{\gamma}\boldsymbol{\gamma}^H - \boldsymbol{I}_N)\boldsymbol{R}) + \sum_{k=1}^{K}\mu_k p_k + P_c} \tag{2a}$$

$$\text{s.t. } \text{tr}\left(\boldsymbol{R}\right) \leq \text{tr}(\boldsymbol{R}\boldsymbol{\gamma}\boldsymbol{\gamma}^H) \leq P_{R,max} + \text{tr}\left(\boldsymbol{R}\right) \tag{2b}$$

$$0 \leq p_k \leq P_{max,k}\ \forall\ k = 1, \ldots, K\ , \tag{2c}$$

With $P_{R,max} > 0$, the RIS operates actively without exceeding its power budget. The matrix $\boldsymbol{C}$ is defined as $\boldsymbol{C} = [\boldsymbol{c}_1, \ldots, \boldsymbol{c}_K]$. Given the diagonal nature of $\boldsymbol{R}$, (2b) is always feasible by choosing $|\gamma_n| = 1$ for all n.

Remark 1: *Previous works, e.g., [9], [10], equate the RIS amplification power only to P_{out}. Contrarily, we consider $P_{out} - P_{in}$ stated above, which ensure a more accurate estimation of RIS power consumption. [7]*

B. *Nearly-passive RIS*

From a mathematical perspective, the nearly-passive RIS scenario can be represented as a specific instance of the active case. Specifically, for a nearly-passive RIS, it is imperative that $P_{R,max} = 0$ and $\sigma^2_{RIS} = 0$ [11] since there is no noise amplification occurring at the RIS. Furthermore, the static power consumption parameters for the RIS in this scenario are expected to be lower than those in the active case due to the deployment of simpler hardware at the RIS. Moreover, as previously highlighted, for nearly-passive RISs, the condition $P_{out} \leq P_{in}$ must be satisfied. This indicates that the RIS does not utilize any power beyond the static power consumption required for the reconfiguration of its reflecting elements.

[1]Note that due to the presence of power amplifiers, an active RIS introduces a noise amplification effect, as opposed to its nearly-passive counterpart that needs no amplification power.

III. Analysis of RISs with Global Reflection Constraints

This section examines RISs operating under global reflection constraints, comparing them to traditional local reflection models. Our analysis primarily focuses on nearly-passive RIS scenarios, chosen for their simplicity and representation of worst-case power reception scenarios. This global constraint, crucial for maximizing energy efficiency, is formally represented as a mathematical constraint in the system model.

$$P_{out} - P_{in} \leq 0 \iff \sum_{k=1}^{K} p_k \sum_{n=1}^{N} |h_{n,k}|^2 (|\gamma_n|^2 - 1) \leq 0 \tag{3}$$

In the global reflection model, $h_{n,k}$ represents the n-th component of vector $\mathbf{h}_k$, assuming $\sigma_{RIS}^2 = 0$. This model inherently meets the local constraint $|\gamma_n| \leq 1$ for $n = 1, \ldots, N$. However, the global constraint, as defined in (3), allows for more diverse configurations of $\boldsymbol{\gamma}$, where some elements may exceed one in magnitude but still comply with the overall power constraint $P_{out} \leq P_{in}$.

The metasurface's ability to act as a singular reflector, as opposed to an array of multiple elements, imparts a unique characteristic to globally reflective RISs. This capability allows for the redistribution of energy among elements, enhancing performance [12]. Specifically, in scenarios like a single-user, single-antenna system assisted by a nearly-passive RIS, the primary objective is to optimize the RIS reflection vector $\boldsymbol{\gamma}$. This optimization (4), aiming at GEE maximization, is significantly simplified in the global reflection constraint model outlined in (3). Such global constraints expand the feasible vector space for $\boldsymbol{\gamma}$, offering potential for improved performance.

$$\max_{\boldsymbol{\gamma}} |\boldsymbol{g}^H \boldsymbol{\Gamma} \boldsymbol{h}|^2 \tag{4a}$$

$$\text{s.t. } \operatorname{tr}\left(\left(\boldsymbol{\gamma}\boldsymbol{\gamma}^H - \boldsymbol{I}_N\right) \boldsymbol{R}\right) \leq 0 \,, \tag{4b}$$

where $\mathbf{g}$ represents the channel from the RIS to the single-antenna receiver, and $\boldsymbol{H} = \operatorname{diag}(\boldsymbol{h})$, with $\boldsymbol{h}$ being the channel from the user under consideration to the RIS. Subsequently, by applying the variable change $x = \boldsymbol{R}^{1/2}\boldsymbol{\gamma}$, and defining the vector $\boldsymbol{z}^H = \boldsymbol{g}^H \boldsymbol{H} \boldsymbol{R}^{-1/2}$, whose n-th component is denoted by z_n, we derive:

$$\max_{\boldsymbol{\rho}, \boldsymbol{\Phi}} \left| \sum_{n=1}^{N} \rho_n e^{j\phi_n} z_n \right|^2 \tag{5a}$$

$$\text{s.t. } \sum_{n=1}^{N} \rho_n^2 \leq \operatorname{tr}(\boldsymbol{R}) \,, \tag{5b}$$

where ρ_n and ϕ_n represent the modulus and phase of the n-th component of $\boldsymbol{x}$ respectively.

Proposition 1: *The optimal solution to problem* (5) *is achieved by setting, for all* $n = 1, \ldots, N$

$$\rho_n = |z_n| \sqrt{\frac{\operatorname{tr}(\boldsymbol{R})}{\sum_{m=1}^{N} |z_m|^2}} \;, \; \phi_n = -\angle z_n \;. \tag{6}$$

Proof: The optimal ϕ_n is the one which compensates the phases of the product channel z_n, leading to the phases in (6). Substituting these phases into (5a), Problem (5) transforms to

$$\max_{\boldsymbol{\rho}} \left(\sum_{n=1}^{N} \rho_n |z_n| \right)^2 \tag{7a}$$

$$\text{s.t. } \sum_{n=1}^{N} \rho_n^2 \leq \operatorname{tr}(\boldsymbol{R}) \,, \rho_n \geq 0 \,, \forall\, n = 1, \ldots, N \tag{7b}$$

Next, as (7b) bounds the squared norm $\boldsymbol{\rho} = [\rho_1 \ldots \rho_N]$, from the Cauchy-Schwarz inequality, it follows that (7a) is maximized when $\boldsymbol{\rho}$ and $\mathbf{z} = [|z_1| \ldots |z_N|]$ are parallel. Hence, for all $n = 1, \ldots, N$, the optimal ρ_n is $\rho_n = \alpha |z_n|$. To compute α, we note that at the optimum, the first constraint in (7b) must be satisfied with equality, as the objective (7a) is increasing in each ρ_n. Thus, enforcing the equality $\sum_{n=1}^{N} \rho_n^2 = \operatorname{tr}(\boldsymbol{R})$ leads to (6). ■

Defining the vector $\boldsymbol{d} = \boldsymbol{H}^H \boldsymbol{g}$, the SNR achieved by optimal allocation derived above is computed as

$$\text{SNR}_{\text{opt}} = \frac{p}{\sigma^2} \operatorname{tr}(\boldsymbol{R}) \|\boldsymbol{z}\|^2 = \frac{p}{\sigma^2} \operatorname{tr}(\boldsymbol{R}) \boldsymbol{d}^H \boldsymbol{R}^{-1} \boldsymbol{d} = \frac{p}{\sigma^2} \|\boldsymbol{h}\|^2 \sum_{n=1}^{N} \frac{|\boldsymbol{d}_n|^2}{|\boldsymbol{h}_n|^2} \tag{8}$$

where in the last step, we have denoted by $d_n = h_n^* g_n$ the n-th component of $\boldsymbol{d}$ and utilized that, in the considered single-user scenario with nearly-passive RIS, $\boldsymbol{R} = p\boldsymbol{H}^H \boldsymbol{H}$ with $\boldsymbol{H}^H \boldsymbol{H} = \operatorname{diag}\left(|h_1|^2, \ldots, |h_N|^2 \right)$, implying that $\operatorname{tr}(\boldsymbol{R}) = p\|\boldsymbol{h}\|^2$.

Let's also introduce $\delta_n = \frac{\|\boldsymbol{h}\|^2}{|h_n|^2} \geq 1, \; \forall\, n = 1, \ldots, N$, enabling us to rewrite (8) as:

$$\text{SNR}_{\text{opt}} = \frac{p}{\sigma^2} \sum_{n=1}^{N} \delta_n |d_n|^2 \tag{9}$$

If we replace the global constraint in (4b) with its local counterpart, i.e., $|\gamma_n|^2 \leq 1$ for all $n = 1, \ldots, N$, the optimal solution would be to set the n-th RIS phase to compensate the phase of the product channel $g_n^* h_n$, for all $n = 1, \ldots, N$, while $|\gamma_n| = 1$ for all $n = 1, \ldots, N$. This allocation is referred to as the unit modulus RIS allocation, resulting in the SNR:

$$\text{SNR}_{\text{uni}} = \frac{p}{\sigma^2} \left(\sum_{n=1}^{N} |h_n g_n^*| \right)^2 = \frac{p}{\sigma^2} \left(\sum_{n=1}^{N} |d_n| \right)^2 \tag{10}$$

since $|h_n g_n^*| = |h_n^* g_n|$.

Lemma 1: *We always have* $SNR_{opt} \geq SNR_{uni} \implies \eta = \frac{SNR_{opt}}{SNR_{uni}} \geq 1$.

Proof: The proof is straightforward when noting that the *unit modulus RIS allocation* is a feasible solution for Problem (4). Any $\phi_n \in [0, 2\pi]$ is feasible for (4), and by setting $|\gamma_n| = 1$ for all $n = 1, \ldots, N$, we achieve $\mathrm{tr}\left(\left(\boldsymbol{\gamma}\boldsymbol{\gamma}^H - \mathbf{I}_N\right)\mathbf{R}\right) = 0$, satisfying (4b). ■

To further quantify the gain offered by the RIS with global reflection capabilities, we use the relation: $\left(\sum_{n=1}^{N} |d_n|\right)^2 = \sum_{n=1}^{N} |d_n|^2 + 2\sum_{n=1}^{N}\sum_{m=n+1}^{N} |d_n|\,|d_m|$

From which η can be expressed differently, as stated below;

$$\eta = \left[\beta - 2\frac{\sum_{n=1}^{N}\sum_{m=n+1}^{N} |d_n|\,|d_m|}{\sum_{n=1}^{N} |d_n|^2 + 2\sum_{n=1}^{N}\sum_{m=n+1}^{N} |d_n|\,|d_m|}\right] \tag{11}$$

where:

$$\beta = \left[\frac{\sum_{n=1}^{N} \delta_n |d_n|^2 + 2\sum_{n=1}^{N}\sum_{m=n+1}^{N} |d_n|\,|d_m|}{\sum_{n=1}^{N} |d_n|^2 + 2\sum_{n=1}^{N}\sum_{m=n+1}^{N} |d_n|\,|d_m|}\right] \geq 1 \tag{12}$$

Given that $\delta_n \geq 1$ for all $n = 1, \ldots, N$.

Intuitively, η should be at its minimum value, i.e., $\eta = 1$, when all channels have equal magnitude. In this scenario, the distribution of the reflected signal power across different channels becomes irrelevant.

However, if the product channels differ in magnitude, a gain strictly greater than one is anticipated. For instance, modifying the previous scenario by assuming $|g|_n = 0$ for all $n \neq k$ and $|g|_k > 0$, we find that $|d_n| = 0$ for all $n \neq k$ and $|d_k| = |d| > 0$. In this case, it's evident that $\eta = \beta$ since the cross product $|d_n|\,|d_m| = 0$ for all n and m. Thus:

$$\eta = \beta = \delta_k = \frac{\sum_{n=1}^{N} |h_n|^2}{|h_k|^2} > 1 \tag{13}$$

This result shows that the gain scales with N. If we assume $|h_n| = |h|$ for all $n = 1, \ldots, N$, (13) gives $\eta = N$.

In this section, we explored the nearly-passive RIS setup, emphasizing the benefits of global reflection capabilities for energy efficiency. Our analysis revealed that RISs with global reflection constraints outperform locally constrained ones in SNR enhancement. We also clarified how the channel coefficient magnitudes influence the performance difference between these two RIS models.

IV. Numerical Analysis

In our numerical analysis, we consider a single-user wireless network setup with $K = 1$, $N_R = 1$, $N = 100$, and other specified parameters as in Section III. The study primarily focuses on the potential of RISs with global reflection constraints in enhancing energy efficiency. Key parameters include a noise spectral density of $-174\,$dBm/Hz and a noise figure of 5 dB. The user distribution, RIS and BS positioning, power decay factors, and Rician fading parameters ($K_t = 4$ for RIS to BS and $K_r = 2$ from users to RIS) are all configured to reflect realistic communication scenarios.

The benefits of global reflection capabilities over traditional local reflection models are evident from Figs. 2a and 2b, which demonstrate notable gains in energy efficiency (EE) and rate. These gains are particularly pronounced under lower Rician factors, as indicated by diversified channel realizations, as further supported by Fig. 3a.

Additionally, Fig. 3b investigates the impact of RIS positioning on GEE. The results show that the optimal location of the RIS varies based on the channel decay factors between RIS-BS and UE-RIS. If the decay from RIS to users is more significant, positioning the RIS closer to users is advantageous, while a dominant RIS-BS decay suggests a nearer placement to the BS.

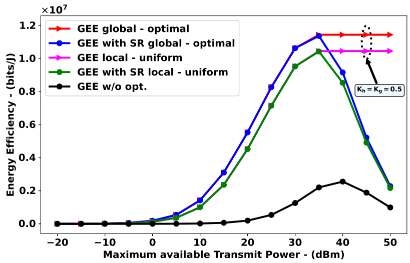

(a) Achieved GEE versus $P_{t,max}$. $K = 1$, $N_R = 1$, $N = 100$, $n_h = 4, n_g = 2$.

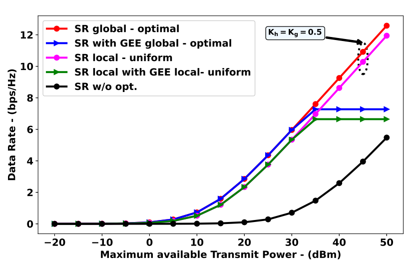

(b) Achieved Spectral Efficiency versus $P_{t,max}$. $K = 1$, $N_R = 1$, $N = 100$, $n_h = 4, n_g = 2$.

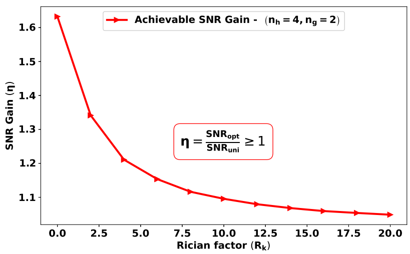

(a) Achieved SNR Gain ($\boldsymbol{\eta}$) versus Rician factor ($\boldsymbol{R_k}$). $K = 1$, $N_R = 1$, $N = 100$, $P_{t,max} = 40$ dBm.

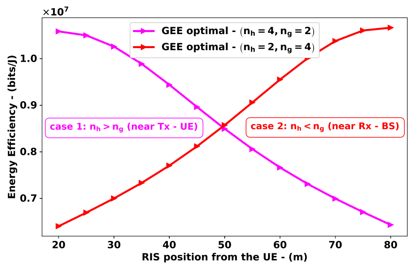

(b) Achieved GEE versus RIS placement ($\boldsymbol{x}_{\text{ris}}$). $K = 1$, $N_R = 1$, $N = 100$, $P_{t,max} = 40$ dBm.

V. Conclusion

This research delved into the potential of reconfigurable intelligent surfaces (RISs) in enhancing energy efficiency within wireless networks, emphasizing the advantages of global reflection constraints. Our findings underscored the superiority of RISs with global reflection constraints, especially in single-user settings. The exploration of various path-loss exponents provided insights into the optimal positioning of RISs, emphasizing energy-efficient deployment. The distinction between globally reflective and locally constrained RISs was highlighted, revealing the metasurface's ability to function as a singular reflector, offering enhanced performance.

ACKNOWLEDGMENT

The research conducted by R. K. Fotock and A. Zappone received support from the European Commission, specifically through the H2020-MSCA-ITN-METAWIRELESS project under grant agreement number 956256. Additionally, M. Di Renzo's work was partially funded by the European Commission through the H2020 ARIADNE project (grant agreement 871464) and the H2020 RISE-6G project (grant agreement 101017011).

REFERENCES

[1] M. Di Renzo, A. Zappone, M. Debbah, M.-S. Alouini, C. Yuen, J. de Rosny, and S. Tretyakov, "Smart radio environments empowered by reconfigurable intelligent surfaces: How it works, state of research, and the road ahead," *IEEE Journal on Selected Areas in Communications*, vol. 38, no. 11, pp. 2450–2525, 2020.

[2] Q. Wu, S. Zhang, B. Zheng, C. You, and R. Zhang, "Intelligent reflecting surface-aided wireless communications: A tutorial," *IEEE Transactions on Communications*, vol. 69, no. 5, pp. 3313–3351, 2021.

[3] D. David Lopez-Perez, A. De Domenico, N. Piovesan, G. Xinli, H. Bao, S. Qitao, and M. Debbah, "A survey on 5g radio access network energy efficiency: Massive mimo, lean carrier design, sleep modes, and machine learning," *IEEE Communications Surveys and Tutorials*, vol. 24, no. 1, pp. 653–697, 2022.

[4] P. Zeng, D. Qiao, Q. Wu, and Y. Wu, "Throughput maximization for active intelligent reflecting surface-aided wireless powered communications," *IEEE Wireless Communications Letters*, vol. 11, no. 5, pp. 992–996, 2022.

[5] Q. Wu and R. Zhang, "Intelligent reflecting surface enhanced wireless network: Joint active and passive beamforming design," in *2018 IEEE Global Communications Conference (GLOBECOM)*, 2018, pp. 1–6.

[6] M. Di Renzo, F. H. Danufane, and S. Tretyakov, "Communication models for reconfigurable intelligent surfaces: From surface electromagnetics to wireless networks optimization," *Proceedings of the IEEE*, vol. 110, no. 9, pp. 1164–1209, 2022.

[7] R. K. Fotock, A. Zappone, and M. Di Renzo, "Energy efficiency optimization in ris-aided wireless networks: Active versus nearly-passive ris with global reflection constraints," *IEEE Transactions on Communications*, pp. 1–1, 2023.

[8] ——, "Energy efficiency in ris-aided wireless networks: Active or passive ris?" in *ICC 2023 - IEEE International Conference on Communications*, 2023, pp. 2704–2709.

[9] R. Long, Y.-C. Liang, Y. Pei, and E. G. Larsson, "Active reconfigurable intelligent surface-aided wireless communications," *IEEE Transactions on Wireless Communications*, vol. 20, no. 8, pp. 4962–4975, 2021.

[10] C. You and R. Zhang, "Wireless communication aided by intelligent reflecting surface: Active or passive?" *IEEE Wireless Communications Letters*, vol. 10, no. 12, pp. 2659–2663, 2021.

[11] R. K. Fotock, A. Zappone, and M. D. Renzo, "Energy efficiency maximization in ris-aided networks with global reflection constraints," in *ICASSP 2023 - 2023 IEEE International Conference on Acoustics, Speech and Signal Processing (ICASSP)*, 2023, pp. 1–5.

[12] M. Di Renzo, F. H. Danufane, and S. Tretyakov, "Communication models for reconfigurable intelligent surfaces: From surface electromagnetics to wireless networks optimization," *Proceedings of the IEEE*, vol. 110, no. 9, pp. 1164–1209, 2022.

Classifying Physical Activity Level from Kinematic Gait Data: a Machine Learning approach

Svonko Galasso[1,2,3], Renato Baptista[1,3], Mario Molinara[2], Serena Pizzocaro[1,4], Rocco Salvatore Calabrò[5] and Alessandro Marco De Nunzio[1,3]

[1]Department of Research and Development, LUNEX International University of Health, Exercise and Sports, 4671 Differdange, Luxembourg

[2]Department of Electrical and Information Engineering, University of Cassino and Southern Lazio, 03043 Cassino, Italy

[3]Luxembourg Health & Sport Sciences Research Institute ASBL, 4671 Differdange, Luxembourg

[4]Department of Electrical, Computer and Biomedical Engineering, University of Pavia, 27100 Pavia, Italy

[5]Istituto di Ricerca e Cura a Carattere Scientifico Centro Neurolesi "Bonino Pulejo", 98123 Messina, Italy

Abstract

The aim of the proposed study is to correctly classify subjects' Physical Activity Level (PAL), through Machine Learning (ML) techniques driven by kinematic gait data (Gait Analysis, GAn). GAn represents a valuable tool to assess gait disorders, impairment levels, and gait parameters, and is based on wireless wearable motion sensor systems. Such technologies generate extensive sets of data that are difficult to manage, analyse, and interpret. ML techniques can provide a viable solution to make GAn more manageable in clinic.

Kinematic gait data were collected from 37 healthy subjects (24 male, 23 y.o. ± standard deviation (std_dev) of 3 years) while walking on a treadmill at natural speed. Motion data were acquired from Inertial Measurement Unit (IMU) sensors using as ground-truth a self-reported questionnaire (International Physical Activity Questionnaire). For each subject, consecutive windows of 6 gait cycles were considered for data augmentation. Statistical feature extraction was performed and reduced to the most significant ones via the Neighborhood Component Analysis (NCA).

Systematic feature selection resulted in 20 retained features from lower limbs and leads to increased classification performance for the considered models. K-Nearest Neighbors (KNN), Random Forest (RF), Gradient Boosting (GBoost) and Support Vector Machine (SVM) models, have been trained and tested to validate the effectiveness of the approach. A 4-Fold Cross Validation evaluated the models' classification ability on unseen data, reporting the following performance (mean ± std_dev): KNN = 0.82±0.06, RF = 0.86±0.08, GBoost = 0.82±0.03, and SVM = 0.87±0.05.

As of today, no one has highlighted the prediction of a clinically validated questionnaire via ML algorithm based GAn data. This study shows that four IMUs are sufficient to predict PAL with good accuracy, as the NCA recognised only features derived from pelvis, right thigh, shank, and foot IMUs as relevant. The presented work served as a preliminary test on using ML techniques to extract clinically relevant information from kinematic data for future approaches to discriminate across levels of impairment.

Index Terms

kinematic gait data, gait analysis, inertial measurement unit, machine learning

Water Quality Classification Using Deep Learning

Hamza Mustafa[1], Mario Molinara[1], Luigi Ferrigno[1]
[1]Department of Electrical and Information Engineering University of Cassino and Southern Lazio, Cassino, Italy
Email: hamza.mustafa, mario.molinara, luigi.ferrigno @unicas.it

Abstract

Water quality assessment is a critical component of environmental stewardship. This paper presents an innovative approach to the classification of water quality, employing deep learning techniques in conjunction with advanced data preprocessing. Leveraging the Sensichips Smart Water Cable Sensor, we collect high-resolution data on water quality parameters, setting the foundation for precise analysis. Our research employs both Con- volutional Neural Networks (CNNs) and Long Short-Term Memory (LSTM) networks, catering to the temporal nuances of the data. As part of our data preprocessing pipeline, we apply the Exponential Moving Average (EMA) to enhance the quality of sensor readings. Furthermore, we introduce a subtraction step, subtracting EMA values from the original data to highlight deviations. Data is fed into the deep networks using the sliding-window approach, enabling the model to capture temporal dependencies. By combining advanced sensor technology and deep learning, this research contributes significantly to proactive water quality monitoring, providing information for environmental protection and public health initiatives, and directly supporting the UN Clean Water and Sanitation (SDG 6) goals for a sustainable and healthier world.

Index Terms

Deep Learning, EMA, Smart Cable Water

I. INTRODUCTION

Water is an essential component for the survival of living creatures, as it comprises a significant amount of cellular biomass in both plant and animal species. Indeed, the quantity of water on the Earth's surface remains constant. It is imperative to underscore that the issue about water is not primarily one of quantity but rather of flow. The Earth's surface is predominantly covered by water, accounting for about 70% of its total area. However, the proportion of usable freshwater is significantly limited, constituting a mere 1% [1]. Notwithstanding the limited quantity of freshwater available, it is subject to numerous environmental hazards, including agricultural runoff, home waste, and industrial pollution, among others [14]. The prevailing concern is in the fact that a substantial proportion of the global population, exceeding 800 million individuals, face inadequate availability of clean water [10]. Furthermore, an alarming annual mortality rate of around 2 million, primarily comprising infants, can be attributed to the absence of safe drinking water [16]. Currently, the deterioration of freshwater quality stands as a significant environmental concern [9]. This issue not only poses adverse consequences for human well-being and water resource sustain- ability but also contributes to the prevalence of water-borne diseases, which rank among the top 10 causes of global mortality [14]. Notably, diarrhea, malaria, trypanosomiasis, intestinal worm infections, dengue, and bilharzia emerge as the most fatal among these diseases. The monitoring of water quality serves a crucial function in the realm of environmental management and the safeguarding of water resources. In numerous developing nations, conventional approaches persist in the monitoring of water quality within the majority of drinking water production facilities, despite the presence of contemporary and sophisticated technology. The conventional approaches rely on the assessment of several parameters of the untreated water using laboratory-based chemical analyses. This information is then utilized to determine the water's condition and identify suitable techniques for rendering it potable. One drawback associated with these technologies is the necessity for human expertise and a significant time investment. In addition to the drawback of a comparatively lengthy delay period, these systems do not afford the ability to monitor the progression of raw water quality closely. In the context of monitoring stations for drinking water quality that rely on sensors, particularly those utilizing remote sensing (RS) and Internet of Things (IoT) technologies, there is a growing generation of large volumes of data at rapid and irregular intervals. This influx of data has resulted in the complexity of water quality data [7]. The advent of large data has resulted in the appearance of certain limitations in standard machine learning methods. Advanced deep learning algorithms have proven to be highly beneficial for large data applications in various industries, including Energy, Intelligent Transportation Systems (ITS), Agriculture, and more [11]. In recent years, the utilization of Long Short Term Memory Recurrent Neural Networks (LSTM RNNs) in time series prediction has become increasingly prevalent within the field of Artificial Intelligence (AI) and this technique has demonstrated notable efficacy in handling large datasets [8].

This paper presents an innovative approach to water quality classification that integrates cutting-edge technology and advanced data analysis methods. Leveraging the Sensichips Smart Water Cable Sensor, we collect data of unprecedented quality and detail, setting the foundation for a more accurate understanding of water quality dynamics. Our study combines environmental science and artificial intelligence to understand water quality over time using deep learning.

II. Related Work

In the past few years, there has been a growing application of machine learning ap- proaches in the assessment and classification of water quality [15]. Nida et al. [13] used different machine learning classifiers like SVM, Random Forest etc, for water quality classification. Victor et al. [3] classified and predicted the water quality utilizing the Random Forest classifier. Samil et al. [2] employed the LSTM RNNs and SVM, their approach is able to classify the quality of water into three classes based on independent variables, primarily physicochemical parameters. In their study, Liu et al. [6] introduced a model that utilizes a

Bi-directional Stacked Simple Recurrent Unit learning network (Bi-S-SRU) to predict water quality (WQ) parameters such as pH, water temperature, and dissolved oxygen in the context of smart mariculture. Jaloree et al. [5] introduced a decision tree model for the purpose of predicting six distinct quality indicators, namely ammonia-nitrogen (NH3-N), nitrate- nitrogen (NO3-N), pH, temperature, biochemical oxygen demand (BOD), and chemical oxygen demand (COD). The objective of this model was to assess the water quality (WQ) of the Narmada River located in India. Haghiabi et al. presented a comparative analysis of the performance of three different machine learning techniques, namely the group method of data handling (GMDH), artificial neural networks (ANN), and support vector machines (SVM), in the context of predicting the water quality of Tireh River in southwest Iran [4]. Using machine learning methods, Salisu et al. [12] proposed an effective classification model. Wang Xuan et al. proposed a methodology to address the challenges of non-linearity and insufficient data in classification and prediction tasks, using Support Vector Machines (SVM) [17].

III. Methodology

Our proposed approach consists of data collection, preprocessing, and the application of deep learning techniques, with a focus on the classification of water quality based on Exponential Moving Average (EMA) differences. We utilize a sliding window approach to prepare the input data for classification, and our model is designed to classify 15 different substances in water.

A. Data Collection

The data collection process is facilitated by the Sensichips Smart Water Cable Sen- sor(SCW), which continuously records high-resolution data on various water quality pa- rameters. It uses multi-sensor microsystem to measure the different substances in the water using an Electrochemical Impedance Spectrometer. The substances which are currently classified with SCW are :

- Acetic Acid
- Acetone
- Ammonia
- Calcium Nitrate
- Ethanol
- Formic Acid
- Hydrogen Peroxide
- Hydrochloric Acid
- Nelsen
- Potassium Nitrate
- Phosphoric Acid
- Potable Water
- Sodium Chloride

- Sodium Hydroxide
- Sodium Hypochlorite

B. Data Preprocessing

The EMA approach is used for the analysis of the raw data. The process of Exponential Moving Average (EMA) involves the reduction of noise and the emphasis on patterns within the data. This methodology provides a reliable approach to improving the accuracy and precision of sensor measurements. The calculation of EMA is performed for every parameter, leading to a dataset that is characterized by increased stability and reduced noise. The next step is calculating the disparities between successive exponential moving average (EMA) values for every parameter. These disparities are used to accentuate departures from the anticipated patterns, a critical aspect in the process of classification. In order to preprocess the data for classification we removed the transient part of the data and the sliding window methodology is used. The proposed approach includes partitioning the time series data into overlapping windows, wherein each window encompasses a series of Exponential Moving Average (EMA) differences. The sliding window is set up to have a size of 32- time steps, which allows the model to include temporal context and effectively capture relationships within the data as shown in Figure2. The data is traversed incrementally, with the sliding window being shifted by a one-time step at each iteration. This process generates a succession of input sequences that are used by the model. Every individual window is used for the purpose of extracting a consecutive series of EMA (Exponential Moving Average) differences. This approach guarantees that the model can capture temporal patterns and dependencies in the data. Figure 1 represents the graphical representation of the data for Acetic Acid measurements, with one of the sensors on the SCW.

C. Deep Learning

In order to do the classification, we employed Convolutional Neural Networks (CNNs) as well as Long Short-Term Memory (LSTM) networks. The EMA difference sequences are considered as distinct inputs, and both the CNN and LSTM models are trained in- dependently on these sequences. The CNN architecture has been specifically designed to efficiently classify water substances into one of the 15 separate classes. On the other hand, LSTM networks, known for their ability to capture temporal relationships within sequential data, are used. In addition, in order to thoroughly evaluate the performance of the model, we use a 10-fold cross-validation technique. The dataset is partitioned into 10 distinct subsets, and the models are subjected to ten iterations of training and evaluation. During each cycle, a single subset is designated as the validation set, while the other nine subsets are used for training purposes. The aforementioned procedure is iterated for each of the 10 folds, guaranteeing the inclusion of every data point in the validation set at least once. During each iteration of the cross-validation process, CNN and LSTM models are trained using the training data.

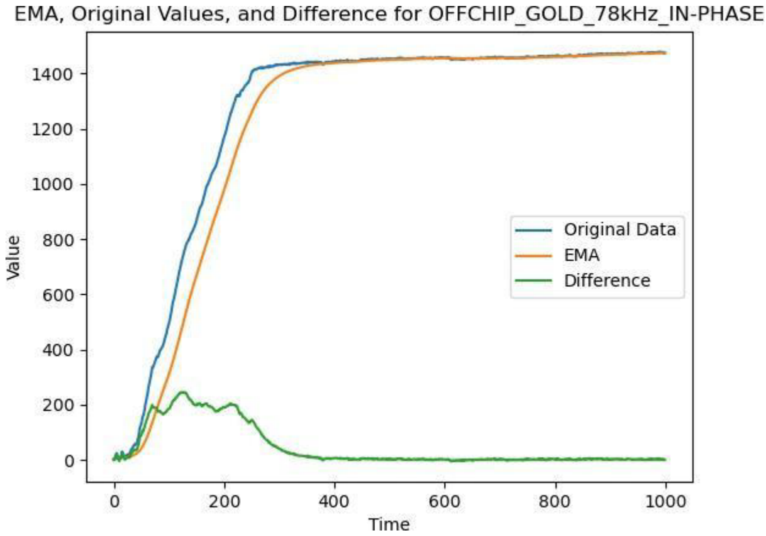

Fig. 1: Original Values , EMA and Differences Values Graphical Representation

IV. Results

The classification performance of CNN and LSTM networks throughout ten-fold cross-validation is shown in Table 1. The classification accuracy for each fold is presented, as well as the mean accuracy.

TABLE I: Classification Performance

Classifier	Fold-1	Fold-2	Fold-3	Fold-4	Fold-5	Fold-6	Fold-7	Fold-8	Fold-9	Fold-10	Mean
CNN	86.91%	87.02%	93.19%	95.92%	89.04%	89.29%	82.12%	88.45%	88.79%	78.80%	87.953%
LSTM	82.74%	82.81%	89.15%	90.18%	85.83%	82.16%	83.74%	80.63%	74.70%	69.77%	82.171%

The CNN model achieved a notable mean classification accuracy of 87.95%. The model consistently demonstrated a high level of accuracy throughout multiple folds, reaching a peak accuracy of 95.92% in Fold-4. The LSTM model achieved a mean accuracy of 82.171% while displaying competitive performance. Over the 10 folds, it kept accuracy levels mostly constant. Notably, in Fold-4, LSTM had a high accuracy of 90.18%. The results of this study indicate that the CNN model has potential as a reliable method for real-time monitoring of water quality classification of substances based on EMA differences. Furthermore, the mean accuracy of the

CNN model surpasses that of the LSTM model. CNN's ability to consistently attain high levels of accuracy over several instances highlights its promise as a dependable and accurate method of assessing water quality.

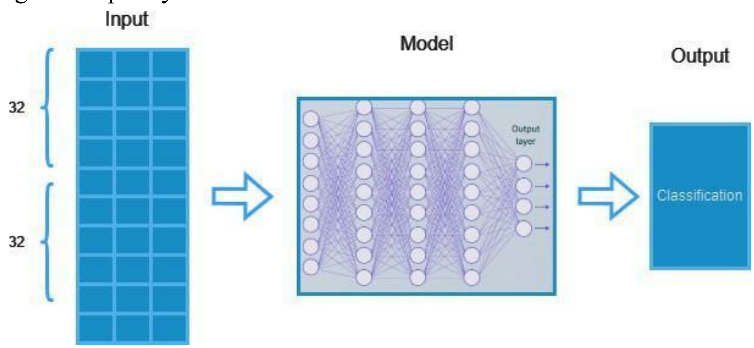

Fig. 2: Proposed Approach

V. Conclusion

In conclusion, this study is closely associated with and represents a substantial advance- ment towards the achievement of United Nations Sustainable Development Goal 6 (SDG 6), which pertains to the provision of clean water and sanitation. The approach we proposed for water quality classification is directly aligned with the goal of ensuring clean and readily available water for everyone. This contributes to the overall aim of safeguarding the welfare of communities and ecosystems on a global scale. Significantly, our research has resulted in a significant classification accuracy rate of 87% by using CNN. The accuracy achieved by our technique highlights its potential to significantly contribute to the area of water quality monitoring by providing improved precision in the classification of substances in water. One of the primary advantages of our approach is in its ability to efficiently capture temporal relationships, which is helped by the use of the sliding window technique. This methodology enables our model to comprehend and adjust to the ever-changing characteristics of water quality data, thereby enhancing its overall reliability and efficiency. It is crucial to acknowledge that the quest to achieve accurate water quality categorization is a continuing goal. It is essential to engage in continuous refinement and enhancement in order to effectively address the escalating requirements of water quality evaluation. Future research directions include the investigation of different deep learning models, such as Convolutional Long Short-Term Memory (ConvLSTM), and the use of ensemble techniques to leverage the combined predictive capabilities of numerous models.

References

[1] UNESCO International Water Conference. Leveraging inter sectorality for sustainable water security and peace, June 2019(last accessed October 24, 2023).

[2] Smail Dilmi and Mohamed Ladjal. A novel approach for water quality classification based on the integration

of deep learning and feature extraction techniques. Chemometrics and Intelligent Laboratory Systems, 214:104329, 2021.
[3] V´ıctor Flores, Ingrid Bravo, and Marcelo Saavedra. Water quality classification and machine learning model for predicting water quality statusmdash;a study on loa river located in an extremely arid environment: Atacama desert. Water, 15(16), 2023.
[4] Amir Hamzeh Haghiabi, Ali Heidar Nasrolahi, and Abbas Parsaie. Water quality prediction using machine learning methods. Water Quality Research Journal, 53(1):3–13, 2018.
[5] Shailesh Jaloree, Anil Rajput, and Sanjeev Gour. Decision tree approach to build a model for water quality.
[6] Binary Journal of Data Mining & Networking, 4(1):25–28, 2014.
[7] Juntao Liu, Chuang Yu, Zhuhua Hu, Yaochi Zhao, Yong Bai, Mingshan Xie, and Jian Luo. Accurate prediction scheme of water quality in smart mariculture with deep bi-s-sru learning network. IEEE Access, 8:24784–24798, 2020.
[8] Ping Liu, Jin Wang, Arun Kumar Sangaiah, Yang Xie, and Xinchun Yin. Analysis and prediction of water quality using lstm deep neural networks in iot environment. Sustainability, 11(7):2058, 2019.
[9] Yang Liu. Novel volatility forecasting using deep learning–long short term memory recurrent neural networks. Expert Systems with Applications, 132:99–109, 2019.
[10] Ting Ma, Na Zhao, Yong Ni, Jiawei Yi, John P Wilson, Lihuan He, Yunyan Du, Tao Pei, Chenghu Zhou, Ci Song, et al. China’s improving inland surface water quality since 2003. Science advances, 6(1):eaau3798, 2020.
[11] Alexandros K Makarigakis and Blanca Elena Jimenez-Cisneros. Unesco’s contribution to face global water challenges. Water, 11(2):388, 2019.
[12] Mehdi Mohammadi, Ala Al-Fuqaha, Sameh Sorour, and Mohsen Guizani. Deep learning for iot big data and streaming analytics: A survey. IEEE Communications Surveys & Tutorials, 20(4):2923–2960, 2018.
[13] Salisu Yusuf Muhammad, Mokhairi Makhtar, Azilawati Rozaimee, Azwa Abdul Aziz, and Azrul Amri Jamal. Classification model for water quality using machine learning techniques. International Journal of software engineering and its applications, 9(6):45–52, 2015.
[14] Nida Nasir, Afreen Kansal, Omar Alshaltone, Feras Barneih, Mustafa Sameer, Abdallah Shanableh, and Ahmed Al-Shamma’a. Water quality classification using machine learning algorithms. Journal of Water Process Engineering, 48:102920, 2022.
[15] Mansi Tripathi and Sunil Kumar Singal. Use of principal component analysis for parameter selection for development of a novel water quality index: a case study of river ganga india. Ecological indicators, 96:430–436, 2019.
[16] Tran Minh Tung, Zaher Mundher Yaseen, et al. A survey on river water quality modelling using artificial intelligence models: 2000–2020. Journal of Hydrology, 585:124670, 2020.
[17] Peter J Vikesland. Nanosensors for water quality monitoring. Nature nanotechnology, 13(8):651–660, 2018.
[18] Wang Xuan, Lv Jiake, and Xie Deti. A hybrid approach of support vector machine with particle swarm optimization for water quality prediction. In 2010 5th International Conference on Computer Science & Education, pages 1158–1163. IEEE, 2010.

RIS-aided Joint Communication and Sensing via Track-before-Detect

Georgios Mylonopoulos[1,2], Luca Venturino[1], Stefano Buzzi[1,2] and Emanuelle Grossi[1]
[1]University of Cassino and Southern Lazio, Cassino, Italy
[2]Consorzio Nazionale Interuniversitario per le Telecomunicazioni, Parma, Italy

Abstract

Reconfigurable intelligent surfaces (RISs) have attracted the interest of both academia and industry, due to their ability to create an adjustable propagation environment and providing additional sensing capabilities to wireless networks. Here, we consider the joint communication and detection problem of non-cooperative targets exploiting an RIS, which provides an alternative inspection point. Communicating users restrict beamforming as we need to minimize the interference of the sensing application. The energy of the received echoes drastically depends on the RIS's beampattern, the target's size and position. Track-before-detect (TBD) is an iterative procedure that increases the probability of detection as more inspections are jointly considered. The passive nature of the RIS and its low implementation cost allow for large RISs to be considered. Numerical results show that the large size of the RIS enables us to properly inspect the desired region, despite the constraints and that a TBD procedure is vital in low SNR sensing scenarios.

Index Terms

Reconfigurable intelligent surface, Joint communication and sensing, OFDM, Dual functioning RADAR and communication, track-before-detect

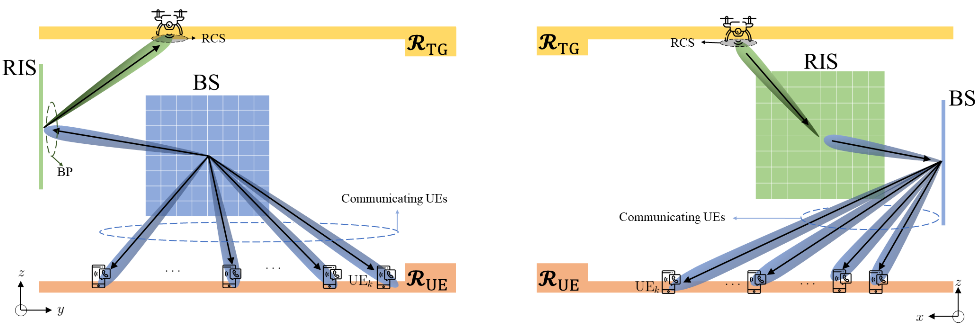

Figure 1: Considered JCAS scenario. The BS simultaneously communicates with users on the ground and scans the sky for potential airborne targets with the aid of an RIS.

I. Introduction

The role of reconfigurable intelligent surfaces (RISs) in future wireless networks is thoroughly discussed in both academia and industry, as they introduce various challenges and opportunities to enhance the system's performance [1]. As communication networks evolve, joint communication and sensing (JCAS) applications are considered, where the RISs' ability to provide a favorable propagation environment and additional inspection points is highly desirable [2]. Introducing RISs in RADAR-like applications can improve the probability of detection and provides additional degrees of freedom in the system's design [3]. Moreover, there are techniques such as track-before-detect (TBD), that aid the detection and tracking of non-cooperative targets as multiple sensing intervals are jointly considered [4]. Here we explore the introduction of an RIS in a JCAS scenario with a TBD scanning policy, as we highlight the restrictions and challenges of minimizing the communication interference and the designing the optimal RIS response.

II. System description

Consider a full-duplex base station (BS) equipped with two planar arrays; one array is used by the dual-function transmitter, while the other one is used by the radar receiver. The BS adopts an orthogonal frequency division multiplexing (OFDM) transmission format to serve K single-antenna downlink users (UEs) located in the region $\mathcal{R}_{\mathrm{UE}}$ and search for airborne targets located in the region $\mathcal{R}_{\mathrm{TG}}$. The radar function is assisted by a passive reconfigurable intelligent surface (RIS) which is employed here to extend the radar field of view, thus allowing scanning directions that would be otherwise not observable [3]. The RIS-assisted radar monitors a portion of the sky which is only in the RIS field of view. The inspected volume is divided into subvolumes which are sequentially scanned by the RIS. The RIS-assisted radar illuminates each subvolume for a time that contains a batch of OFDM symbols of equal duration. The radar transmitter (but not the communication transmitter) remains silent for a number of OFDM symbols between the illumination of consecutive subvolumes; this idle time is employed to elaborate the echoes received in the previous illumination and reconfigure the RIS and the dual-function transmitter before starting the next illumination.

III. Two-way beampattern & Detection

The radar application requires that more radiated power is focused on the desired subvolume and that the target's echo is well received, though appropriate RIS response design and beamforming. We define the two-way beampattern of the RIS-assisted radar, $\mathrm{BP}(\boldsymbol{\theta}) = \mathrm{BP}_{\mathrm{tx}}(\boldsymbol{\theta}) \times \mathrm{BP}_{\mathrm{rx}}(\boldsymbol{\theta})$, as the product between the transmit beampattern, which describes (up to an irrelevant scaling factor) the power radiated in each direction and the receive beampattern, which describes (up to an irrelevant scaling factor) the power received from a source as a function of angle of arrival. The two-way beampattern is controlled via the RIS response $\boldsymbol{\omega}$ and the sensing beamformer. The idea is to design the RIS response and sensing beamformer to obtain a desired two-way beampattern on each subcarrier. The

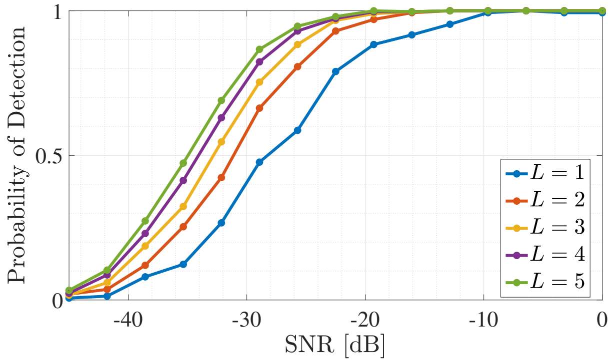

Figure 2: Probability of Detection with multiple Area Scans ($L = 1 - 5$).

design problem is far from trivial, as multiple parameters should be taken into account, including the overall gain, directivity and side lobes of the RIS response. The RIS needs to focus as much energy on the inspected area as possible and restrain from constructively redirecting undesired echoes. A sub optimal approach for the design process is an alternating maximization of each RIS element and based on the derived $\boldsymbol{\omega}$, maximising the transmission beampattern, $\mathrm{BP}_{\mathrm{tx}}(\boldsymbol{\theta})$.

The measurements collected during a coherent processing interval are processed through a bank of correlators matched to the direction under inspection and a pair of delay and Doppler shift; each correlator is followed by an energy detector and a noise variance normalization. During the ℓ-th scan, the correlator outputs of all CPIs that exceed η_1 are considered potential targets and a *plot* is saved, encapsulating position, velocity and received power information. To adapt a TBD procedure, a trajectory is defined as a collection of plots among successive scans [4]. Assuming that L scans are jointly processed to form possible target trajectories, each plot of the ℓ^{th} scan is added to a unique trajectory and then removed. Each plot is added to the best matched trajectory and each trajectory may have only a single plot from each scan. A Viterbi-like algorithm may be used to form the possible trajectories. Trajectories with a likelihood above a thresehold, η_2 are declared as true targets. Numerical results highlight that he probability of detection improves as more scans are jointly processed and the TBD procedure is essential in low SNR scenarios.

References

[1] Y. Liu, X. Liu, X. Mu, T. Hou, J. Xu, M. Di Renzo, and N. Al-Dhahir, “Reconfigurable intelligent surfaces: Principles and opportunities,” *IEEE communications surveys & tutorials*, vol. 23, no. 3, pp. 1546–1577, 2021.

[2] C. K. Sheemar, G. C. Alexandropoulos, D. Slock, J. Querol, and S. Chatzinotas, “Full-duplex-enabled joint communications and sensing with reconfigurable intelligent surfaces,” *arXiv preprint arXiv:2306.10865*, 2023.

[3] S. Buzzi, E. Grossi, M. Lops, and L. Venturino, “Foundations of MIMO radar detection aided by reconfigurable intelligent surfaces,” *IEEE Transactions on Signal Processing*, vol. 70, pp. 1749–1763, 2022.

[4] E. Grossi, M. Lops, and L. Venturino, “A track-before-detect algorithm with thresholded observations and closely-spaced targets,” *IEEE Signal Processing Letters*, vol. 20, no. 12, pp. 1171–1174, 2013.

Machine Learning for early diagnosis of neurodegenerative diseases through handwriting analysis

Emanuele Nardone1, Francesco Fontanella2, and Claudio De Stefano3

Universita` degli Studi di Cassino e del Lazio Meridionale, Cassino, Italy
[1]emanuele.nardone@unicas.it
[2]fontanella@unicas.it [3]destefano@unicas.it

Abstract

Artificial Intelligence has transformed various domains, including healthcare, where it has revolutionized diagnostic and therapeutic practices. This paper explores the potential of handwriting analysis as a biomarker for assessing neurodegenerative diseases. The complexity of handwriting, incorporating motor and cognitive components, makes it an attractive candidate for disease assessment. By leveraging machine learning techniques, we propose two approaches to extract features from online handwriting data to implement a machine learning system to support the diagnosis of Alzheimer's.

Index Terms

Artificial Intelligence, Machine Learning, Handwriting, Strokes

I. INTRODUCTION

Artificial Intelligence (AI) has emerged as a transformative force in various domains, revolutionizing medicine by enabling novel diagnostic and therapeutic strategies. Within the healthcare sector, the availability of digital medical data has facilitated the develop- ment of AI applications, particularly in the field of machine learning. These applications have demonstrated great potential in enhancing the discovery of therapeutic tools, aiding diagnostic decisions, and supporting rehabilitation processes. The collaboration between researchers and expert clinicians has played a critical role in translating complex medical data, such as genomic information and medical imagery, into actionable knowledge to improve patient care.

Over the past few decades, there has been a rapid proliferation of AI-enabled healthcare applications, driven by advancements in computing power, the expansion of genomic sequencing databases, improvements in Natural Language Processing and Computer Vision, advancements in deep learning techniques, and the development of Computer-Aided Diagnosis (CAD) systems. As the average life expectancy continues to rise, the prevalence of neurodegenerative diseases (ND), including Parkinson's (PD) and Alzheimer's (AD), has also increased, necessitating early diagnosis to mitigate symptom progression and enhance patients' quality of life.

While general neurologists typically handle the diagnosis of these diseases, consulting with a movement disorder specialist (MDS) is often recommended to avoid misdiagnosis. Neuroimaging techniques, such as magnetic resonance imaging (MRI) and DaTscan, serve as valuable tools in cases where diagnosis is uncertain or when distinguishing these syndromes from other conditions. However, these imaging methods can be invasive, expensive, and may not be widely accessible. Therefore, there is a pressing need for non-invasive alternative systems to aid in early disease detection.

Handwriting analysis has emerged as a promising biomarker for assessing neurodegenerative diseases. The intricate nature of handwriting, involving both motor and cognitive components, makes it an attractive candidate for disease assessment. Research has indicated a close correlation between changes in handwriting and disease severity, as well as cognitive impairment. Specifically, abnormalities such as micrographia and agraphia have been identified as characteristic symptoms associated with neurodegenerative diseases [1]. To develop an effective handwriting analysis system, a substantial dataset comprising brain and graphomotor ability assessments is required. However, such datasets are not readily available, necessitating the development of specific protocols for data collection. Recently, machine learning-based approaches have been developed to automatically analyze handwriting and support early diagnosis of AD. In this context, features are extracted from the coordinates of the handwriting traits, which are recorded using digital devices. Typically, these features consider the entirety of the handwriting task. However, in this paper, we present a comparison between a statistics-based and a stroke-based approach [2] that aims to predict AD. Specifically, the former analyzes the whole handwriting whilst the latter analyzes the individual elementary traits that comprise handwriting, known as strokes.

As mentioned before, in order to develop a machine learning system able to distinguish subjects affected by AD, it is necessary to build a significant dataset with handwriting collections. With the support of specialized medical figures, a protocol [3] composed of 25 tasks has been built. The goal of the protocol is to highlight the cognitive, kinesthetic, and perceptual-motor abilities, areas typically affected by NDs. As previously stated, handwriting is an activity that involves all the abilities mentioned before. The protocol thus requires patients to perform different tasks:

1) *Graphic tasks*, test the patient's ability to write elementary traits to join some points, or draw simple or complex figures;
2) *Copy and Reverse Copy tasks*, test the patient's abilities to repeat complex graphic gestures with semantic meaning such as letters, words, or numbers;
3) *Memory tasks*, test the variation of the graphic section, keeping in memory a word, a letter, a graphic gesture, or motor planning;
4) *Dictation Tasks*, investigate the writing changes along the tasks' variation in which the use of the working memory is necessary.

We acquired the data using a Wacom's Bamboo tablet equipped with a pen. This setup enabled participants to write on A4 white paper sheets positioned on the tablet. The tablet recorded the pen tip movements' x-y coordinates at a frequency of 200Hz. These coordinates were classified as either "on-paper" or "in-air" movements. "On-paper" refers to when the pen tip touches the paper, while "in-air" corresponds to movements when the pen tip is lifted from the paper within a maximum distance of 3 cm. For on-paper movements, we also captured the pressure exerted by the pen tip on the paper.

We then extracted features from the raw data, calculated on the strokes that make up the handwritten traits. A stroke represents the individual component of a handwritten trait and consists of points between consecutive segmentation points, such as pen-up, pen-down, and zero-crossing velocity along the y-axis.

II. Experiments

After extracting the features, we structured them into a dataset, assigning each feature to its corresponding task. To identify the most pertinent features for each task and stroke type, we conducted a feature selection procedure. Next, we employed Bayesian search to optimize the hyperparameters. Utilizing the optimized hyperparameters, we conducted a series of experiments for both approaches, employing XGBoost classifier and various machine learning techniques.

A. Majority Vote

In the first experiment, we performed a subject-wise train/test split on the complete dataset. The subjects were divided into two groups, with 70% allocated for training and 30% for testing. This division ensured balanced data representation at the subject level.

For each classifier and task, subject labels were predicted by majority voting among the strokes. Robust predictions were achieved using 5-fold Cross Validation. Thirty runs were conducted, with each run having an independent train/test subject split to ensure statistically reliable outcomes. The Accuracy Score metric was employed to measure model performance.

B. Ranking

To improve the performance of the Single Task classification method, we introduced a Ranking method for the tasks. To reduce noise and focus on task-specific information, feature selection is initially performed individually for each task, then each task is classified using the features that were chosen. Following classification, the tasks are ranked according to their accuracy scores. This ranking provides useful information about the classification models' performance for each task. A subset of tasks is chosen for majority voting based on the accuracy scores. The top n tasks are chosen from a predetermined range, where n represents the number of top tasks. This approach harnesses the collective knowledge of the selected tasks, resulting in enhanced classification performance.

C. Stacking

The Stacking approach represents a two-stage method for classification. It capitalizes on the distinctive information provided by each task, enabling more precise predictions by amalgamating the task responses. To enhance overall system performance, we train a second classifier using the combined dataset.

Initially, we divide the subject IDs of each task into two equal halves. Subsequently, we conduct feature selection for each task, aiming to identify the most relevant attributes while reducing dimensionality. Moving on to the classification process, we employ a highly parameterized classifier to initiate the first phase of classification. This classifier undergoes training on the preprocessed data specific to each task. Its objective is to generate preliminary responses based on the selected features, utilizing the first block of IDs for training and the second block for testing.

Following the initial classification phase, we aggregate the obtained responses, creating a comprehensive database that contains predicted labels from each task for every subject in the test set.

In the subsequent phase, we proceed with training a secondary classifier. We perform another Train/Test split on the combined dataset derived from the previous step. Then, we train the Second Classifier and make predictions, ultimately obtaining the final prediction from the system.

III. RESULTS

In the following tables, TABLE I and TABLE II are shown the mean accuracy obtained for 30 run along all the tasks forming the two distinct datasets and with the three ML techniques described in the section II.

TABLE I
ACCURACY STATISTICS-BASED APPROACH

	Majority Vote Accuracy			Ranking Accuracy			Stacking Accuracy		
	All	OnPaper	OnAir	All	OnPaper	OnAir	All	OnPaper	OnAir
MEAN 30 RUN	0.772	0.744	0.765	0.855	0.878	0.833	0.729	0.734	0.704

TABLE II
ACCURACY STROKE-BASED APPROACH

	Majority Vote Accuracy			Ranking Accuracy			Stacking Accuracy		
	All	OnPaper	OnAir	All	OnPaper	OnAir	All	OnPaper	OnAir
MEAN 30 RUN	0.71	0.679	0.671	0.884	0.884	0.817	0.735	0.714	0.69

IV. Conclusions

Results indicated that the stroke-based approach represent a valid alternative to explore further in next studies, using other Machine Learning Classifiers and Deep Learning technique, exploiting the larger amount of informative data given from the strokes.

References

[1] M. JE, N. K, T. HR, and S. RS., *Micrographia in Parkinson's disease.* J Neurol Sci., 1972 Feb.

[2] K. Yu, J. Epps, and F. Chen, "Cognitive load evaluation of handwriting using stroke-level features," *Association for Computing Machinery*, 2011. [Online]. Available: https://doi.org/10.1145/1943403.1943481

[3] N. D. Cilia, C. D. Stefano, F. Fontanella, and A. S. Di Freca, "An experimental protocol to support cognitive impairment diagnosis by using handwriting analysis," *Procedia Computer Science*, vol. 141, pp. 466–471, 2018, the 9th International Conference on Emerging Ubiquitous Systems and Pervasive Networks (EUSPN-2018) / The 8th International Conference on Current and Future Trends of Information and Communication Technologies in Healthcare (ICTH-2018) / Affiliated Workshops. [Online]. Available: https://www.sciencedirect.com/science/article/pii/S1877050918317903

Markerless Vision-Based Gait Analysis: A New Frontier in Early Parkinson's Disease Detection

Cesare Davide Pace[1], Alessandro De Nunzio[2], Claudio De Stefano[1], Francesco Fontanella[1], Mario Molinara[1]
[1]University of Cassino and Southern Latium, Italy
Email: cesaredavide.pace, claudio.destefano, francesco.fontanella, mario.molinara @unicas.it
[2]LUNEX International University of Health, Exercise and Sports, Luxembourg
Email: {alessandro.denunzio}@lunex-university.net

Index Terms

Parkinson's Disease, Markerless vision-based system, Gait Analysis, Machine Learning

Abstract

Parkinson's Disease(PD) is a progressive neurodegenerative disorder that primarily impacts movement. Early diagnosis is crucial, as timely interventions can potentially slow disease progression and significantly improve a patient's quality of life. While imaging examinations such as MRI play a role, they may not always provide definitive answers in the disease's nascent stages. The impending rise in PD prevalence due to global population aging underscores the need for efficient, non-invasive diagnostic tools.

Gait abnormalities, including impairments and irregular patterns, frequently indicate early PD. Analyzing and quantifying gait can offer critical insights into the potential presence and progression of the disease. With technological advancements, vision-based gait analysis systems have emerged as prospective non-invasive diagnostic tools.

Traditional marker-based systems, like Multi-camera motion capture, are considered the gold standard for motion analysis. However, these systems come with inherent chal- lenges. Firstly, they are cost-intensive, making them inaccessible to many research groups or clinics. Moreover, their setup is cumbersome, often requiring patients to wear specialized suits or markers on their bodies, which can alter natural movement patterns due to the consciousness of being observed. Furthermore, their utility is typically confined to clinical or laboratory settings. This confinement restricts their ability to monitor daily life scenarios, where some of the most genuine gait patterns emerge. Such limitations have paved the way for exploring more versatile alternatives like markerless systems. As the name suggests, these systems require no markers, ensuring the capture of natural gait patterns. Their flexibility makes them ideal for continuous monitoring in real-life scenarios, offering a broader perspective on the disease's impact on daily living.Leveraging this potential, our study aims to develop a markerless vision-based system for gait analysis using computer vision techniques to infer 2D/3D human poses directly from videos or images without needing pre-defined human models or physical markers. These methods offer a non-invasive, affordable, and adaptable solution, particularly relevant in areas with constrained resources. Furthermore, the potential for deployment in home environments can facilitate continuous monitoring, giving a comprehensive overview of disease progression.

A safety planner based on trajectory scaling and path deviation for human-robot interaction

Jozsef Palmieri, Paolo Di Lillo, Alessandro Marino
University of Cassino and Southern Lazio, Cassino, Italy
Email: {jozsef.palmieri,pa.dilillo,al.marino}@unicas.it

I. Introduction

Technological progress, especially in the last decades, has allowed disciplines such as robotics to considerably influence (and in some cases even change) our lives, jobs and habits. In particular, this progress has allowed figures like robots to become more and more present in our daily lives.

From factories [2] to operating rooms [1], from agricultural fields [7] to homes [3], robots are becoming increasingly used to perform several tasks, especially those classified as dangerous or tedious for humans. This has allowed human workers to focus their energies on more complex and less dangerous tasks, and companies, especially those which make extensive use of collaborative robots, to reach an increase in efficiency, productivity and cost savings. However, in a society in which robots are becoming more and more present and integrated, there is an important question to consider: how can humans and robots coexist in the same workspace in a way that could be classified as safe and "low-invasive" for both of them?

Regarding the safety aspects, current collaborative robots have numerous integrated safety features, e.g., a lightweight structure and emergency stop procedures. However, additional safety strategies must still be designed. In particular, strategies that, in any operational condition, make it possible to estimate the human safety level and intervene if the latter is compromised.

Although ensuring safety is of great importance, we also recognize the value of allowing the robot to successfully carry out the assigned tasks while adhering to its constraints. This means that a balance should be found between preserving the robot's activity and implementing a human safety strategy, i.e., the human safety strategy cannot be overly conservative; otherwise, it may prove unnecessarily invasive and detrimental to the robot's mission. One of the most commonly adopted methods to ensure a safe coexistence between humans and robots is the one based on implementing reactive and evasive strategies capable of increasing the human safety level, such as moving the robot away when the human is close to it. In this regard, the study in [4] defines a danger index based on distance, velocity and inertia measures and outlines a virtual force with which moving the robot away from the human with an intensity proportional to the above index. The concept of repulsive and attractive forces has also been exploited in [6], where the architecture in charge of generating the trajectory which will drive the robot towards the desired poses is an Explicit Reference Governor. A framework capable of generating the robot trajectory taking into account both the provided reference and the input and state constraints related to the non-linearity of robot dynamics.

Motivated by the above considerations, in this abstract, we propose a comprehensive architecture for a safe human-robot coexistence which modifies the robotic task by taking into account human safety features as well as constraints or secondary objectives of the robotic platform. Specifically, we design a safety planner that, based on an optimal formulation, allows modulating the velocity and deviating from the planned nominal path in order to ensure human safety. The proposed solution relies on Control Barrier Functions (CBFs) and is integrated within a Hierarchical Quadratic Programming (HQP) framework to take into account possible additional constraints or general objectives of the robotic platform. In order to prove its effectiveness, the proposed solution has been validated first within an indoor environment and then within a real agricultural setting inspired by the typical use case scenarios addressed within the H2020 European-funded project CANOPIES.

II. Human Safety Field

In [5], a safety field to account for the human-robot relative position is defined. The field takes into consideration the overall robotic structure as well as an arbitrary number of significant human points, e.g., the endpoints of the links composing the human skeleton.

The case of single point P of the robot structure and single point P_o of the human operator is first considered, and in order to account for the above features, the following local scalar safety index is defined:

$$f(\boldsymbol{p}, \boldsymbol{p}_o) = \alpha(d) \tag{1}$$

where $\boldsymbol{p} \in \mathbb{R}^3$ is the position vector of the robot point P, $\boldsymbol{p}_o \in \mathbb{R}^3$ is the position vector of the human point P_o, $d = \|\boldsymbol{p} - \boldsymbol{p}_o\|$ is the distance between P and P_o and α is any non-negative continuous monotonically increasing Lipschitz function.

The cumulative safety index associated with the mobile manipulator is obtained by integrating the function in Eq. (1) along the robot links and by then evaluating it for each human point. To make the computation affordable in practical applications, each link l has been approximated to a segment starting at $\boldsymbol{p}_l^0$ and ending at $\boldsymbol{p}_l^1$:

$$\begin{cases} F_l = \displaystyle\int_0^1 f\left(\boldsymbol{p}_l^s, \boldsymbol{p}_o\right) ds \\ \boldsymbol{p}_l^s = \boldsymbol{p}_l^0 + \left(\boldsymbol{p}_l^1 - \boldsymbol{p}_l^0\right) s \end{cases} \tag{2}$$

with $s \in [0,\, 1]$. By denoting with n_o the total number of human points and with $\boldsymbol{p}_{o,j}$ the position of the j-th one, the safety index associated with the j-th human point with respect to the robot and consequently the cumulative safety index can be easily obtained from Eq.(2) as:

$$F_j = \sum_{l=1}^{n} F_l \left(\boldsymbol{p}_l^0, \boldsymbol{p}_l^1, \boldsymbol{p}_{o,j}\right), \quad F = \frac{1}{n_o} \sum_{j=1}^{n_o} F_j \left(\boldsymbol{q}, \boldsymbol{p}_{o,j}\right). \tag{3}$$

III. Problem Formulation

Problem 1: Let us consider a dual-arm robotic system performing a cooperative task encoded by a task function $\boldsymbol{\sigma}$, for which a nominal desired trajectory $\boldsymbol{\sigma}^d(t)$ is assigned by a Trajectory Generation module. Let us also consider a human operator that shares the same workspace as the robots, that is monitored through a Perception System and whose level of safety is assessed by the index $F(t)$ in Eq. (3), for which a time-varying minimum value $\underline{F}(t)$ is assigned. The objective is to design a Safety Planner capable of:

- scaling down the nominal trajectory $\boldsymbol{\sigma}^d(t)$,
- modifying the nominal path of $\boldsymbol{\sigma}^d(t)$,
- finding a null space motion $\boldsymbol{u}_n$;

so as to generate a safe trajectory $\boldsymbol{\sigma}^s(t)$ and an input signal $\boldsymbol{u}_n$ capable of guarantee the fulfilment of the safety condition

$$F(t) \geq \underline{F}(t) \tag{4}$$

and at the same time, the meeting of any robot's position, velocity and acceleration constraints.

Figure 1 shows the proposed architecture that summarizes the interconnection between the Trajectory Generation module, the Safety Planner, the Low-level Controller and the Robot with its Perception System. The idea is to design a Safety Planner for online scaling and modifying the nominal trajectory computed by a Trajectory Generation module depending on the output of a Perception System in order to obtain a safe trajectory to be sent as a reference to the Low-level Controller module that computes the joint velocities to the Robot.

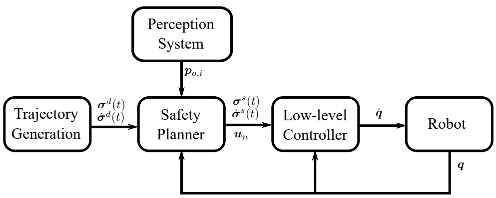

Fig. 1: Overall control architecture.

IV. Proposed Solution

The idea is to parameterize the nominal trajectory $\boldsymbol{\sigma}^s(t)$ with respect to two parameters: c, which allows to scale down the trajectory, and $\Delta\boldsymbol{\sigma}$ that allows modifying the path. Then, by defining proper virtual inputs u_c, $\boldsymbol{u}_\alpha$ that allows modulating the amount of scaling and path deviation, respectively, and $\boldsymbol{u}_n$ that generates internal motions in case of a redundant structure, the objective is to find the optimal values of these inputs in order to modify the nominal trajectory so as to keep the safety field value above the minimum threshold. This can be accomplished by adopting the Safety Planner scheme shown in Figure 2 based on the HQP framework. The entire approach has been validated on a mobile bimanual robot.

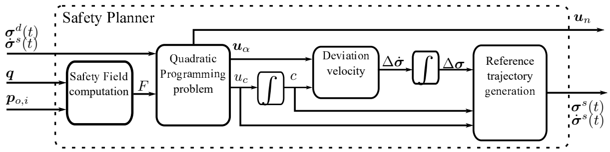

Fig. 2: Safety Planner functional architecture.

References

[1] Alaa Eldin Abdelaal, Prateek Mathur, and Septimiu E Salcudean. Robotics in vivo: A perspective on human–robot interaction in surgical robotics. *Annual Review of Control, Robotics, and Autonomous Systems*, 3:221–242, 2020.

[2] Abdelfetah Hentout, Mustapha Aouache, Abderraouf Maoudj, and Isma Akli. Human–robot interaction in industrial collaborative robotics: a literature review of the decade 2008–2017. *Advanced Robotics*, 33(15-16):764–799, 2019.

[3] Keith S Jones and Elizabeth A Schmidlin. Human-robot interaction: toward usable personal service robots. *Reviews of Human Factors and Ergonomics*, 7(1):100–148, 2011.

[4] D. Kulić and E. A. Croft. Real-time safety for human–robot interaction. *Rob. Auton. Syst.*, 54(1):1 – 12, 2006.

[5] M. Lippi and A. Marino. Human multi-robot safe interaction: A trajectory scaling approach based on safety assessment. *IEEE Trans. Control Syst. Technol.*, pages 1–16, 2020.

[6] Hongyan Liu, Daokui Qu, Fang Xu, Zhenjun Du, Kai Jia, Jilai Song, and Mingmin Liu. Real-time and efficient collision avoidance planning approach for safe human-robot interaction. *Journal of Intelligent & Robotic Systems*, 105(4):93, 2022.

[7] Juan P Vasconez, George A Kantor, and Fernando A Auat Cheein. Human–robot interaction in agriculture: A survey and current challenges. *Biosystems engineering*, 179:35–48, 2019.

Null-Space Shared Control of a mobile robot using motor imagery based brain-computer interface

Francesca Patriarca, Giuseppe Gillini, Paolo Di Lillo, Filippo Arrichiello
University of Cassino and Southern Lazio, Cassino, Italy
Email: {francesca.patriarca1, giuseppe.gillini, pa.dilillo, f.arrichiello}@unicas.it

IX. Introduction

Assistive robotics applications involving Human-Machine Interfaces (HMIs) aim to help people with motor disabilities to carry out daily-life activities [1]. In this context, two distinct control modes have been identified: shared and supervisory control. In a shared control mode, the user is included in the control loop as an active part and he generates high-frequency motion commands, that are then converted into low-level references for the robot, ensuring human safety constraints [2], [3]. On the other hand, supervisory control relies on low-frequency commands provided by the user to issue high-level directives to the robotic system, enabling it to execute tasks autonomously [4], [5]. In the assistive robotics field non-invasive brain-computer interfaces (BCIs) [6], that use electroencephalography (EEG) based techniques, including P300 component of the Event Related Potentials (ERPs) and motor imagery, to facilitate control commands [7], [8], have received considerable attention. Motor imagery is a cognitive process in which users can imagine movements without actually performing them [9]. Furthermore, hybrid BCI architectures, that combines motor imagery and P300 potential for the asynchronous operation of a brain-controlled wheelchair, has been developed [10].

The aim of this work is to teleoperate a non-holonomic mobile robot within a scaled house-like scenario, a shared control architecture based on motor imagery-based BCIs has been proposed to allow the user to control the robot with a maximum of two motor imagery commands [13]. To ensure safety during teleoperation, a task-priority inverse kinematic control algorithm is employed [11], [12]. Experimental validation of the proposed architecture was conducted using a healthy user operating a Turtlebot robot within a house-like scenario, confirming its efficacy and practicality [13].

X. SHARED CONTROL ARCHITECTURE

In the envisioned shared control strategy (shown in Figure 1), the motion is controlled in a cooperative manner by both the robot and the user.

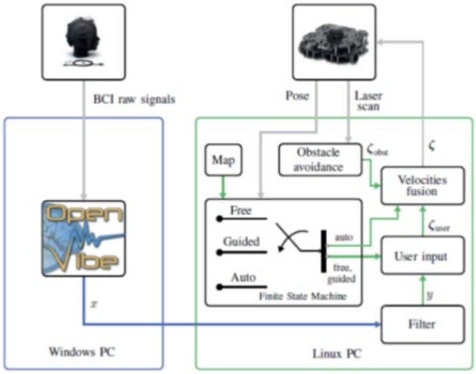

Figure 1: Implemented functional architecture

The architecture includes three control modes: free, guided and autonomous mode. In free mode, the robot autonomously moves forward at a constant velocity while the user controls the direction of motion using motor imagery based BCI. The robot embeds an autonomous obstacle avoidance behavior to assist the user in moving the robot without undesirable impacts. The user's intended motion is combined with the obstacle avoidance using null-space-based inverse kinematics technique to ensure safety constraints are satisfied. Autonomous mode allows the robot to move completely autonomously without user input; instead, in guided mode the user controls the forward/backward velocity. The transition among the control modes is managed by a finite state-machine algorithm.

BCI-based motor imagery allows users to control a robot's movement through motor imagery commands, classified using the OpenVibe framework. The user imagines right or left hand movements to control the robot's angular acceleration, in free mode, or the robot's linear velocity, in guided mode. However the classified commands from the BCI are affected by misclassifications, which can cause discontinuities in the robot's motion. To mitigate this effect, we introduce a filtering layer before the translation into motion commands, which has been first proposed in [13] for two class motor-imagery, and then extended also for 4-class in [9].

The filter output increment (Δy_t^{right}) is determined by combining two forces: the free force (F_{free}), a sinusoidal function that depends on the filter output, and the BCI force (F_{BCI}), that depends on BCI output. It is given by the following expression:

$$\Delta y_t^{right} = \chi \cdot [\phi \cdot F_{free}(y_{t-1}^{right}) + (1-\phi) \cdot F_{BCI}(x_t^{right})], \quad (1)$$

where x_t^{right} is the probability of the right class coming from the classifier output at time t, y_t^{right} is the filter output at time t and ϕ is the parameter used to weight the two forces. However, the original formulation of the filter has a drawback in managing the relaxed state, in which the user does not send any command to the system. To overcome this issue, a modification is proposed by adding a new restore force ($F_{restore}(x_t^{right})$), that help the user to push the filter output towards a "no command" state. The new filter output increment is given by the following expression:

$$\Delta y_t^{right,new} = \Delta y_t^{right} + F_{restore}(x_t^{right}). \quad (2)$$

This modification improves the usability of the system by allowing the user to stop the robot conveniently and naturally by using the relaxed state signal.

XI. NULL-SPACE-BASED SHARED CONTROL STRATEGY

The kinematics of a differential-drive robot are described. A low-level controller generates velocity commands using a 2D velocity vector in the robot's frame. The output of the shared control architecture is translated into this vector by fusing two behaviors: user input and obstacle avoidance. User input allows control of robot's linear velocity or angular acceleration, while the obstacle avoidance behavior maintains a minimum distance from obstacles along the user-commanded path. Velocities from these behaviors are fused using a null-space-based inverse kinematics framework [14], prioritizing obstacle avoidance while maximizing user control. The overall velocity command is computed by adding obstacle avoidance velocity to user input velocity in the null space of the obstacle avoidance task. This strategy is adaptable to robots with different kinematics and can handle multiple tasks.

XII. EXPERIMENTS

The proposed architecture was implemented and tested using a g.tec Unicorn BCI and a Turtlebot. The experiments involved an able-bodied subject navigating the Turtlebot through a simulated house-like scenario, as shown in Figure 2a, and utilized Lab Streaming Layer (LSL) and TCP/IP protocols for communication between workstations. The experiments demonstrated the successful completion of the task without any collisions, as shown in the path in Figure 2b.

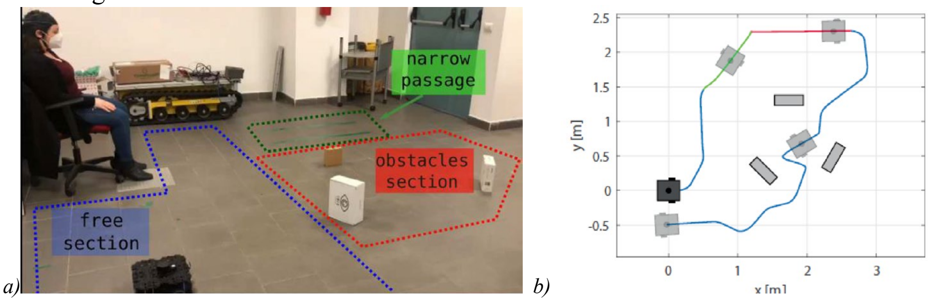

Figure 2: a) Snapshot of the built scenario for the experimental validation; b) Executed path during one of the runs of the experiment.

The shared control architecture assisted the user to teleoperate the robot through three different sections: an obstacle-free section, a narrow passage, and an obstacles area. The control modes and velocity fusion techniques ensured safe and efficient robot navigation. Linear and angular velocities were controlled based on the active control mode, and the user's commands were integrated with autonomous computations to achieve the desired location while avoiding collisions.

XIII. CONCLUSIONS

We proposed a shared control architecture aimed at assisting people to teleoperate a non-holonomic mobile robot in a scaled house-like scenario through motor imagery based BCI and we performed several experiments to demonstrate the effectiveness of both architecture and the proposed filter modification.

In the future, we would like to extend the experimental campaign by involving more users and collaborating with healthcare organizations to evaluate the effective usability of this architecture and to include different scenarios.

REFERENCES

[9] N. C. M. Nickelsen, "Imagining and tinkering with assistive robotics in care for the disabled," Paladyn, Journal of Behavioral Robotics, vol. 10, no. 1, pp. 128 – 139, 2019.

[10] H. Wang and X. P. Liu, "Adaptive shared control for a novel mobile assistive robot," IEEE/ASME Transactions on Mechatronics, vol. 19, no. 6, pp. 1725–1736, 2014.

[11] G. Quere, A. Hagengruber, M. Iskandar, S. Bustamante, D. Leidner, F. Stulp, and J. Vogel, "Shared control templates for assistive robotics," in 2020 IEEE International Conference on Robotics and Automation (ICRA). IEEE, 2020, pp. 1956–1962.

[12] A. De Luca and F. Flacco, "Integrated control for phri: Collision avoidance, detection, reaction and collaboration," in 4th IEEE RAS & EMBS International Conference on Biomedical Robotics and Biomechatronics (BioRob), 2012, pp. 288–295.

[13] D. Achanccaray, J. M. Chau, J. Pirca, F. Sepulveda, and M. Hayashibe, "Assistive robot arm controlled by a p300-based brain machine interface for daily activities," in 2019 9th International IEEE/EMBS Conference on Neural Engineering (NER). IEEE, 2019, pp. 1171–1174.

[14] S. Liyanage and C. Bhatt, "Wearable electroencephalography technologies for brain–computer interfacing," in Wearable and Implantable Medical Devices. Elsevier, 2020, pp. 55–78.

[15] G. Gillini, P. Di Lillo, F. Arrichiello, D. Di Vito, A. Marino, G. Antonelli, and S. Chiaverini, "A dual-arm mobile robot system performing assistive tasks operated via p300-based brain computer interface," Industrial Robot, 2020.

[16] P. Di Lillo, F. Arrichiello, D. Di Vito, and G. Antonelli, "BCI-controlled assistive manipulator: developed architecture and experimental results," IEEE Transactions on Cognitive and Developmental Systems, 2020.

[17] G. Gillini, P. D. Lillo, and F. Arrichiello, "An assistive shared control architecture for a robotic arm using eeg-based bci with motor imagery," pp. 4132–4137, 2021.

[18] Y. Yu, Z. Zhou, Y. Liu, J. Jiang, E. Yin, N. Zhang, Z. Wang, Y. Liu, X. Wu, and D. Hu, "Self-paced operation of a wheelchair based on a hybrid brain-computer interface combining motor imagery and p300 potential," IEEE Transactions on Neural Systems and Rehabilitation Engineering, vol. 25, no. 12, pp. 2516–2526, 2017.

[19] S. Moe, G. Antonelli, A. Teel, K. Pettersen, and J. Schrimpf, "Setbased tasks within the singularity-robust multiple task-priority inverse kinematics framework: General formulation, stability analysis and experimental results," Frontiers in Robotics and AI, vol. 3, p. 16, 2016.

[20] P. Di Lillo, S. Chiaverini, and G. Antonelli, "Handling robot constraints within a set-based multi-task priority inverse kinematics framework," in 2019 International Conference on Robotics and Automation (ICRA). IEEE, 2019, pp. 7477–7483.

[21] L. Tonin, F. C. Bauer, and J. d. R. Mill´an, "The role of the control framework for continuous teleoperation of a brain–machine interface-driven mobile robot," IEEE Transactions on Robotics, vol. 36, no. 1, pp. 78–91, 2019.

[22] B. Siciliano and J.-J. Slotine, "A general framework for managing multiple tasks in highly redundant robotic systems," in Proceedings 5th International Conference on Advanced Robotics, Pisa, I, 1991, pp. 1211–1216.

A novel approach for small object detection in medical images

Ciro Russo[1], Alessandro Bria[1], Claudio Marrocco[1],
[1]Department of Electrical and Information Engineering, University of Cassino and L.M., Via G. Di Biasio 43, 03043 Cassino (FR), Italy
Email: ciro.russo@unicas.it, a.bria@unicas.it, c.marrocco@unicas.it

Index Terms

Small object detections, Medical image analysis.

Abstract

In recent years, deep learning has received wide research interest in the field of medical image analysis. Exploiting advanced neural network architectures, it has revolutionized the ability to extract meaningful information from complex medical images, offering promising prospects for more accurate diagnostics and customized healthcare. Although current object detection models have achieved remarkable success, the increasingly high resolution of medical images poses a unique challenge, as it requires more attention to image details and the identification of tiny objects within the images. To address this problem, we propose a deep learning model that improves small object detection by using a novel anchoring techniques. The overall architecture consists of a backbone and two subnets of regression and classification. Our proposal significantly increases the accuracy of detection, contributing to early diagnosis and improved patient outcomes. The results demonstrate the relevance of our novel approach, with implications for a wide range of clinical applications as for instance: calcifications in digital mammograms and large-vessel- occlusion in computed-tomography-angiography.

The Value of Experience in Relation to the Degrees of Difficulty in the 3m and 10m Diving

Cecilia BRATTA[1] Sabrina DEMARIE [2], Cristina CORTIS [1]

[1]Department of Human Sciences, Society and Health, University of Cassino and Lazio Meridionale, 03043 Cassino, Italy

[2]Department of Movement, Human and Health Sciences, University of Rome "Foro Italico", Piazza de Bosis 15, 00135 Roma, Italy.

I. PURPOSE

Athletic performance increases from birth to youth reaching a peak level in early adulthood and declines thereafter, furthermore, the competitive performance may change between athletes in different sports and events [3]. As a general trend for both sexes, the disciplines concerning very specific technical skills involve the youngest athletes, such as for the gymnastics and aquatic disciplines [2]. Thus, the aim of the study was to investigate the value of experiences in terms of ages and the influence of this on both sexes' competitive performance in 3m and 10m diving.

II. METHODS

Diving competition results from Sydney 2000 to Tokyo 2020 were collected from the FINA official website [4]. For the female (F) and male (M) medalists (Olympic (OL): F=18, M=18; Word Championship (WCH): F=30, M=30; Word Diving Cup (WDC): F=33, M=33) of each event the sum of the Degrees of Difficulty (DDs), age (OG: F= 25,1 yrs, M= 23,8 yrs; WDC: F= 22,8 yrs, M= 23,2 yrs; WCH: F= 23,3 yrs, M= 23,5 yrs), and first years of competitions (1°yrs – OG: F= 15,1 yrs, M= 15,1 yrs; WDC: F= 14,9 yrs, M= 15,3 yrs; WCH: F= 14,7, M= 15,4 yrs) for both sexes were collected.

III. RESULTS

Observing the trend over time of the first year of competition, it seems that in the 3m men are older than women especially in bronze medalist (M: y=-0,1959; F: y=0,0573). Instead, silver medalist women seem to be older than men (F: y=0,157; M: y=0,0254). In 10m all medalists' women are younger than men (F: 1°y=0,0266; 2°y=0,0469; 3°y=0,0147; M: 1°y=- 0,1144; 2°y=-0,0084; 3°y=-0,0829). From the analysis of DDs: in 3m women DDs continuously increased in all medalists (1°y=0,0107; 2°y=0,0478; 3°y=0,0368), the same trend is observed in men's DDs especially for gold medalists (y=0,0316), while in silver and bronze there aren't a significant increase (Silver y=0,0017; Bronze y=0,0046). In 10m women's DDs values decrease with the increasing of the years for all medalists (1°y=-0,1879; 2°y=-0,1727; 3°y=-

0,0497); in men especially for gold and silver medalist DDs values increase (1°y=0,4599; 2°y=0,6401) while in bronze DDs decrease over the time (y=-0,225).

IV. CONCLUSION

The results suggest that age is a fundamental parameter that may influence performance results in both competitions. Furthermore, the experience, due to years of competitions, seems to have a great influence on DD and consequently affects the preparation phase for the competitions. A good knowledge of athletes' career and abilities could provide coaches a guidance on choosing athletes' routine and progression towards their performance goals [1].

REFERENCE:

[1] Allen et al. *Sport Med*, 2015, 45: 1431-1441
[2] Apollaro et al. *J Sport Med and Physical Fit,* 2021, 62(6): 838-845
[3] Elmenshawy et al. *AGE*, 2015, 37 (3): 1-8
[4] FINA Official Website - www.fina.org

Balancing Asymmetries with Mini-Trampoline Workouts

Francesca Di Rocco[1], Olga Papale[1], Emanuel Festino[1], Cristina Cortis [1], Andrea Fusco[1]

[1]Department of Human Science, Society and Health, University of Cassino and Lazio Meridionale, Cassino, Italy

Email: francesca.dirocco1@unicas.it

Abstract

Inter-limb asymmetry is defined as the performance imbalance of a limb with respect to the other one. Studies demonstrated how plyometric training could minimize inter-limb imbalance by reducing asymmetries and the relative risk of musculoskeletal injuries. Among the different plyometric training modalities, SuperJump® represented a reliable method. This study aimed to evaluate the acute effects of SuperJump® training on dynamic balance Unilateral Asymmetry and Bilateral Asymmetry Indexes. Thirty-seven subjects were randomly allocated in two groups: SuperJump® (N = 20) and Control (N = 17). The SuperJump® group participated in the SuperJump® session, whereas the Control group did not receive any workout session. Before (PRE) and after (POST) the SuperJump® session, both groups performed the Wobble Board balance test. A significant difference ($p < 0.003$) between the SuperJump® in POST and Control groups in PRE intervention for dominant leg was found. No significant differences ($p > 0.05$) emerged between groups in testing time on Bilateral Asymmetry Index. Significant differences ($p = 0.005$) between PRE and POST in the SuperJump® group and an 18.9% Unilateral Asymmetry Index threshold reduction for the subjects were found. A strong relationship ($R^2 = 0.79$) between delta (Δ) change Unilateral Asymmetry Index and Unilateral Asymmetry Index baseline parameters was tested. Lastly, no significant differences ($p > 0.05$) in Unilateral Asymmetry Indexes between the Bilateral Asymmetry equal and change categories in the SuperJump® group was found. In conclusion, SuperJump® training played a key role in reducing Unilateral Asymmetry Index.

Index Terms

plyometrics; musculoskeletal equilibrium; postural control; motor skills; college students

I. Introduction

The inter-limb asymmetry or inter-limb imbalance describes the concept of comparing the function (i.e., strength, balance) of a limb respect to the other [1]. Recently, the inter-limb asymmetry concept has been fully investigated, with inconsistent findings, particularly related to physical health and sporting performances [1]. Asymmetries between legs are influenced by several factors such as lateral dominance (left vs. right), injuries and sport specificity [2]–[4]. In particular, leg dominance is an important factor both in sports and in everyday tasks[5]. It leads to an increase in asymmetry magnitude and can contribute to the development of injuries, thus influencing sport and everyday tasks [6]. The type of activity in which the athlete is engaged and the training volume of sport exposure influence the magnitude of asymmetry [3], [7]. In fact, team-sport athletes exhibit significantly greater inter-limb asymmetries values with respect to non-athlete, due to the large number of unilateral actions such as jumping and changes in direction [2], [7]. In this context, training programs should be structured aiming to eliminate or limit the asymmetries in order to avoid negative effects on health and performances of athletes and non-athletes on the long-term. Previous research demonstrated how training strategies, such as balance training, resistance training and warm-up programs, could minimize inter- limb asymmetries and the relative risk of injuries [4], [8], [9]. Furthermore, studies show that plyometric training could contribute to improve several sports/physical domains as vertical jump performance, acceleration, leg strength, muscular power and postural control [10], [11]. Among the different plyometric training modalities, an effective method is represented by mini-trampoline training as it has been shown to increase lower body strength, bipodalic static and dynamic balance, and coordination in young subjects [12]–[14]. Among the mini-trampoline activities, in 2009, the American fitness teacher Jill Cooper developed the SuperJump® training (SJ) comprising aerobic and anaerobic exercises alternating upper and lower limbs performed to the rhythm of music. SJ training facilitates the reduction in body mass (−5%) and fat mass (−7%), the improvement of the lipid profile with the reduction in low-density lipoprotein (−28%), and the reduction in bone resorption (+34%) and parathyroid hormone (−23%) [15], [16]. Despite the beneficial acute and chronic effects of SJ on several physical outcomes, no study has yet investigated its acute effects on dynamic balance performances and balance inter-limb asymmetries in young subjects. Therefore, this study aimed to evaluate the acute effects of SJ training on dynamic balance performance and Bilateral Asymmetry (BA) and Unilateral Asymmetry (UA) Indexes in healthy young adults. Based on the positive effects of SJ on health-related domains, it could be hypothesized that SJ training might represent a good strategy in reducing dynamic BA and UA Indexes, providing an enjoyable and alternative training modality for both subjects and health specialists and/or coaches.

II. Materials and Methods

C. Study Design

Following the Declaration of Helsinki, the study was approved on 4 December 2019 from the Institutional Review Board of the Department of Human Sciences, Society, and Health of the University of Cassino and Lazio Meridionale (approval Number 26898) to examine the effects of the SJ training on subjects' balance performance, BA and UA. All participants were asked to read and sign the consent form. Subjects were able to withdraw from the study at any time for any reason, without any consequences. BA and UA Index are commonly used in strength and conditioning investigations, particularly when performing countermovement, vertical, repetitive and unilateral jumps. These methodologies are the most used in laboratory and field settings, due to their being easily exposed to several populations, effectiveness and low costs. Since they only focused on strength, a new methodological approach, represented by the SJ training, was preferred in this study to fill the lack of scientific evidence in evaluating dynamic BA and UA Indexes. Considering that mini-trampoline training includes both the characteristics of the stretching– shortening cycle and the displacements of the center of gravity due the elastic material of the surface, which characterize any type of plyometric training, it could provide more information with respect to countermovement, vertical, repetitive or unilateral jumps. Thus, to establish whether dynamic BA and UA Indexes could be modified by SJ training, the assessment of dynamic balance was performed before (PRE) and after (POST) SJ training.

D. Participants and Procedures

A total of sixty apparently healthy college students voluntarily participated in this study and received all information about the procedures and the aim of the study. Subjects were excluded if they reported pre-existing condition such as neurological condition, cardiovascular, respiratory, and/or metabolic diseases, hypertension previously diagnosed, osteoporosis, musculoskeletal injury of the back or lower extremities occurred during the past year, visual and vestibular disorders that could influence their balance ability, left- handed subjects and previous experience in SJ. Subjects were included if reporting to be minimally active according to International Physical Activity Questionnaire (IPAQ). Before starting the testing session, subjects' anthropometric characteristics were collected. Height and body mass were measured to the nearest 0.1 cm and 0.1 kg, respectively, by using a scale with an integrated stadiometer (Seca 709, Vogel & Halke, Hamburg, Germany). Body mass index (BMI) was subsequently calculated and reported as weight (kg)/height (m^2). Subjectively preferred dominant leg was also defined as the leg preferred when stepping on a platform [17]. The Italian version (7 items) of the IPAQ was also administered to determine the individual level of physical activity (PA) [18]. In the present study, physically active subjects were included. As proposed by the IPAQ Scoring Protocol, subjects had to meet at least one of the following criteria to be classified as minimally active: 3 or more days of vigorous activity of at least 20 min per day; 5 or more days of moderate-intensity activity or walking of at least 30 min per day; or 5 or more days of any combination of walking, moderate-intensity or vigorous intensity activities achieving a minimum of at least 600 metabolic equivalent task (MET) min/week. From a total of sixty subjects, twenty were excluded due to not meeting the inclusion criteria. Subsequently, the forty subjects were randomly allocated in two groups: twenty in SJ group (SJG) and twenty in the Control group (CON). Three subjects in CON discontinued the study without any specific reason. Twenty subjects in the SJG and seventeen subjects in the CON were finally analyzed (Figure 1). SJG participated in the SJ training session, whereas CON did not receive any training session. Before (PRE) and after (POST) SJ training session (intervention), both groups performed balance test (described in Section 2.4).

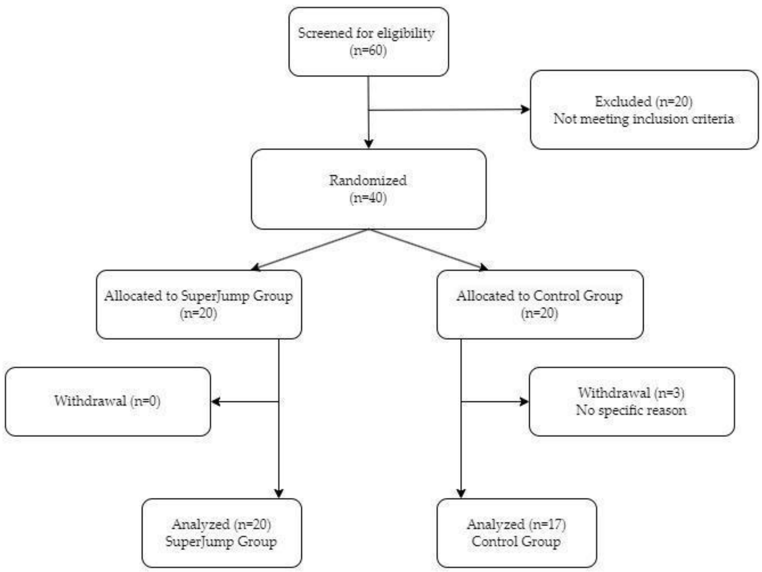

Fig. 1. Flow chart of the recruitment and selection process of the subjects included in the study.

During testing and training sessions, to ensure the safety of each individual, physical exercise experts took care of the subjects' due precautions, such as soft surfaces and various aids (i.e., mats).

E. SuperJump® Training

SJ was performed on a mini-trampoline (CoalSport, Rome, Italy) with the diameter of the elastic surface of 122 cm. The SJ training session included a session of free practice on the mini-trampoline and 30 min of workout. During the warm-up (5 min) and cool down (5 min) phases, subjects were required to continuously jump on the mini-trampoline while performing breathing and mobility exercises. During the central phase (20 min), consisting of jumping exercises and movements of the upper body, they performed the following exercises: double leg hops, single leg hops, alternated double leg hops on sagittal and frontal plan; single leg and double leg lateral hops, jumping jack, double leg hops with wide and close stance; wide to close-stance double leg hops. Subjects also performed hops alternating upper limb movements, such as hops with shoulder front and lateral raises, straight-arm push down, lateral elbow extension and flexion and alternating arms swing. The video workout was displayed on a computer screen, placed in front of the mini-trampoline, and the subjects had to follow the instructions. To monitor exercise intensity, rating of perceived exertion (RPE) was assessed by means of the Category-Ratio 10 (CR-10) scale 30 min after the end of the training session, in line with similar studies [19], [20].

F. Wobble Board Balance Test

A Computerized Wobble Board (WB) (Well Sport Project, G.S.J. Services S.r.l., Rome, Italy) was used in the present study to collect WB balance performance data. WB consists of a circular wooden surface with a diameter of 40 cm placed on a plastic semispherical support with a diameter of 12 cm and a height of 6 cm, containing a tri-axis accelerometer (Phidget Spatial 0/0/3 Basic 1041, Phidgets Inc. 2016, Calgary, AB, Canada) to measure tilt angles (maximal tilt angle = 20°). A USB cable connected to a computer facilitated data collection (sampling frequency: 200 Hz) and real-time display of the WB tilt angle. Real-time performance was displayed on a monitor (resolution = 1920 × 1080) and was represented by a yellow motion marker (MM). The WB software (W.S.P. version 1.0.0.1; G.S.J. Service S.r.l., Rome, Italy) user interface also displayed a target zone (TZ) representing the stability area (tilt angle = 0°), and a countdown. The balance performance counter becomes active when the MM is into the TZ for at least one second (integer is the only number recorded, not second fractions). The software allows the user to calibrate the platform on 5 different levels: easy, medium, sportive, agonist and elite agonist. For the testing procedures, software level was set on easy mode (diameter = 6.5 cm), following the validated protocols [21]–[24].

The WB test included 3 min of free familiarization with the platform and 1 min of rest in sitting position followed by one attempt of thirty seconds per lower limb with 1 min of rest in seated position in-between. Subjects were required to stay barefoot on the unstable platform, in a single leg stance, by adopting a comfortable and central position of foot, knee slightly bent and hands on their hips. The subjects were asked to focus on the MM and try to minimize its displacement with the aim of keeping it inside the TZ as long as they could. Starting limb chosen was completely random.

The test trial was interrupted and repeated if the subjects: (1) touched the floor with the raised leg; (2) used the arms as support; (3) braced the raised leg against the contralateral leg; and (4) dropped off the WB. WB balance performance was defined as the time (s) the MM was maintained into the TZ over the recording period.

G. Bilateral Asymmetry Index and Unilateral Asymmetry Index

To evaluate the magnitude of balance BA between dominant and non-dominant leg, the BA Index was calculated as follows [1]:

$$(\mathrm{dl} - \mathrm{ndl})/(\mathrm{dl} + \mathrm{ndl}) \cdot 100 \qquad [1]$$

where dl represents the dominant leg, and ndl indicates the non-dominant leg. The outcome extrapolated from the formula is represented as a vectorized percentage with positive values indicating that the dominant limb is preferred, whereas negative values favor the non-dominant limb.

Furthermore, to analyze the UA Index the following formula was used [1]:

$$[(100/\mathrm{high} \cdot \mathrm{low}) \cdot -1] + 100 \qquad [2]$$

where high and low correspond to the greater and lower values of the WB balance performance, respectively.

H. Statistical Analysis

Normal distribution was verified by Shapiro–Francia test, showing normal distribution. Means, standard deviations (SD) and 95% confidence intervals (95% CI) were calculated for all variables. Statistical analyses were performed using STATA (Version 14.2; StataCorp LLC, College Station, Texas, USA). Linear repeated-measures mixed model analyses were performed to examine the effects of the SJ training on subject's WB performance, BA and UA Indexes. In the model, subjects were considered as random effect, whereas the intervention (SJG vs. CON) and testing time (PRE vs. POST) were treated as fixed effect. The models were fitted using the residual maximum likelihood to account for the small sample. The repeated-measures Analysis of Variance (ANOVA) was used for computing the degrees of freedom of a*t* distribution, as the subjects were tested PRE and POST intervention. Subsequently, the contrast method was used to test whether the dependent variable means of SJ, CON and testing time (PRE and POST) were identical. When significant main effects and interactions were found, post hoc analysis was applied using Bonferroni correction. In order to avoid type 1 error, after Bonferroni correction, for the linear repeated-measures mixed model, significance was set at $p < 0.05$ for the main effects and at $p < 0.008$ for post hoc pairwise comparisons.
The magnitude of the difference was also determined using Cohen's d effect sizes (ES). In line with similar research, an ES value less than <0.20 = trivial; 0.20–0.60 = small; 0.61–1.20 =

moderate; 1.21–2.0 = large and >2.0 = very large [25].
Subsequently, only for the SJG, linear regression analysis was used to test the relationship between PRE UA Index values and UA delta (Δ) change to determine if UA asymmetry changes were related to baseline parameters. The Δ change were calculated as the difference between PRE exercise and POST exercise UA index values. Lastly, for analyzing a possible influence of the SJ training on the BA index, the relative changes in the BA index between PRE and POST were classified into two categories: (1) no change from PRE to POST (equal); (2) change from PRE to POST (change). Subsequently, one-way ANOVA was used to assess difference in the UA index Δ change between the two BA categories. For these analyses the level of significance was set at $p < 0.05$.

III.RESULTS

Anthropometric characteristics of subjects are presented in Table 1.

	SJG			**CON**		
	Female	***Male***	***Total***	***Female***	***Male***	***Total***
N	*10*	*10*	*20*	*6*	*11*	*17*
Age (years)	*24.1 ± 0.9*	*27.1 ± 2.8*	*25.6 ± 2.6*	*23.2 ± 1.6*	*23.5 ± 1.8*	*23.4 ± 1.7*
Body height (m)	*1.6 ± 0.1*	*1.7 ± 0.1*	*1.7 ± 0.1*	*1.6 ± 0.1*	*1.8 ± 0.1*	*1.7 ± 0.1*
Body weight (kg)	*57.2 ± 6.9*	*72.4 ± 11.4*	*64.8 ± 12.0*	*53.5 ± 7.8*	*72.7 ± 8.3*	*65.9 ± 12.3*
BMI ($kg \cdot m^{-2}$)	*22.5 ± 2.3*	*24.3 ± 2.7*	*23.5 ± 2.6*	*20.9 ± 2.8*	*23.6 ± 2.7*	*22.6 ± 2.9*

SJG = SuperJump® group; CON = Control group; N = number; BMI = body mass index.

Subject rated the SJ session as ‘somewhat hard’ (mean RPE = 3.5) to the (CR-10) scale, corresponding to 12–13 on the 6–20 RPE scale [26], indicating a moderate intensity exercise [27].
The linear repeated-measures mixed model analysis showed a significant main effect ($F_{(3,35)}$ = 3.50; $p < 0.044$; 95% CI = 0.11–7.28) between PRE and POST intervention for the WB balance performance on the dominant leg (Table 2), independently from the group (ES = 0.34). After Bonferroni correction, significant differences ($p < 0.003$; 95% CI = 2.30–11.04) were found

between the SJG in POST and CON in PRE intervention. No significant differences ($F_{(3,35)}$ = 2.35; $p > 0.05$) between groups during PRE and POST evaluation for the WB balance performance on the non-dominant leg were found.
No significant differences ($F_{(3,35)}$ = 1.07; $p > 0.05$) were found between SJG (ES = 0.09) and CON (ES = 0.22) groups in testing time (PRE and POST) on BA Indexes (Table 2).

Table 2. Means and standard deviations of Wobble Board performances for dominant and non-dominant leg and SuperJump® training on the Bilateral Asymmetry Index between testing time by group.

	SJG (N = 20)		***CON (N = 17)***	
	PRE	**POST**	**PRE**	**POST**
Dominant leg (s)	18.5 ± 6.4	22.2 ± 6.8 *	15.5 ± 7.1	16.3 ± 6.8
Non-Dominant leg (s)	18.0 ± 8.3	20.5 ± 5.9	15.5 ± 5.3	18.7 ± 6.1
BA Index (%)	6.11 ± 36.43	3.39 ± 13.57	−2.50 ± 26.47	−7.93 ± 21.18

SJG = SuperJump® group; CON = Control group; N = number; s = second; BA = Bilateral Asymmetry; % = percentage. * significantly different from PRE values of the CON group.

The linear repeated-measures mixed model analysis also showed significant differences ($F_{(3,35)}$ = 3.29; $p = 0.005$; ES = 0.87) for UA Index between PRE and POST in the SJG (Figure 2). Furthermore, the model identified an 18.9% UA threshold reduction for the subjects.

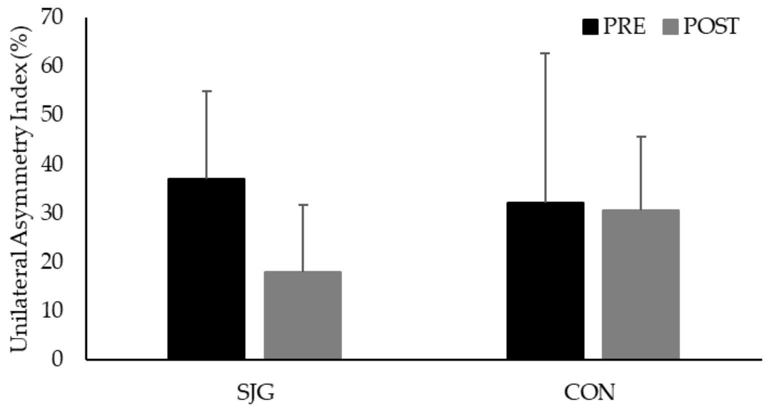

Fig. 2. Means and standard deviations of Unilateral Asymmetry Index between SuperJump® (SJG) and Control (CON) groups before (PRE) and after (POST) the training session. * significantly differences for SuperJump® group between testing time.

Linear regression analysis ($R^2 = 0.79$, $p < 0.0001$) was performed to test the relationship between Δ change UA Index and UA Index baseline parameters (Figure 3). Findings indicated that subjects with higher baseline values of lower-limb asymmetry had higher Δ change for UA Index after the SJ training.

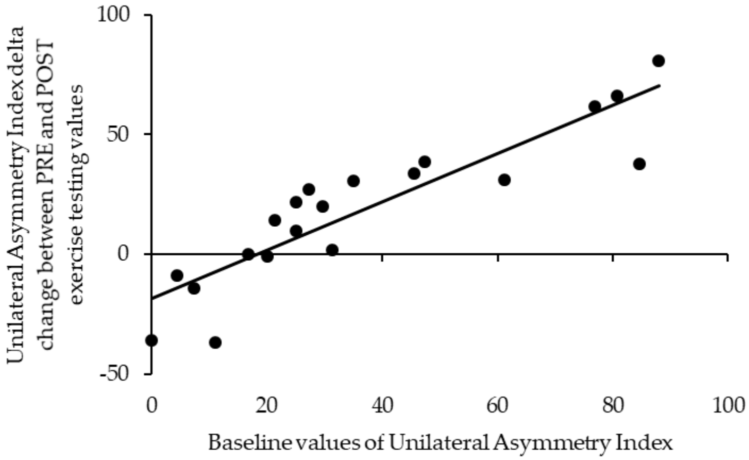

Fig. 3. Delta change between before (PRE) and after (POST) the exercise testing values for Unilateral Asymmetry Index ($R^2 = 0.79$, $p < 0.0001$).

One-way ANOVA analysis showed no significant differences ($p > 0.05$; ES = 0.22) in UA Indexes between the BA equal category and the BA change category in the SJG (Figure 4).

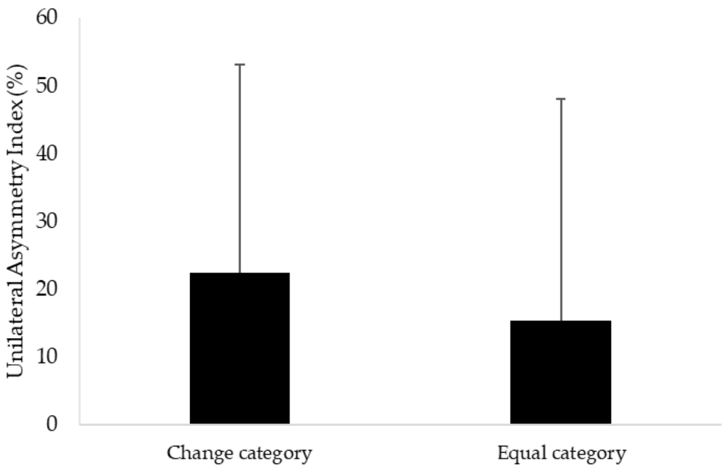

Fig. 4. Means and standard deviations of Unilateral Asymmetry Index between the Bilateral Asymmetry equal and change categories.

IV. DISCUSSION

This study aimed to investigate the effects of the SJ training on subject's dynamic balance performance and to observe BA and UA Indexes acute changes after the SJ training intervention in healthy young adults. The relevant findings of the present study suggested that SJ training positively affected the UA Index for the SJG, by significantly reducing the lower limb balance asymmetry. Furthermore, considering the relationship between the UA Index Δ change and UA Index baseline values, results showed that subjects with higher UA Index baseline values had higher UA Index Δ change after the SJ intervention. On the other hand, a marginal and not significant effect of the SJ on BA Index was found. Plyometric training, such as repetitive jumps, represents a dynamic form of resistance training that involves displacements of the center of gravity resulting in improved dynamic postural control [28], [29]. Thus, SJ training preserves both the characteristics of the stretching–shortening cycle and the displacements of the center of gravity, which characterize any type of plyometric training. It has been shown that plyometric training had chronic effects on the dynamic balance of young athletes in basketball [30], [31] soccer [32], and rhythmic gymnastics [33]. Alongside this, few studies have investigated the acute effects of plyometric training on the balance performance of young athletes in weightlifting [34], volleyball [35] and football [36] or in recreationally trained individuals [37]. Although dynamic balance is considered a physical ability that requires long-term intervention training protocols in order to be improved, different studies have indicated that a single plyometric intervention has the potential to improve balance performance [34]. In line with these previous studies, findings from the present study confirmed that SJ training acutely improved WB performances. In fact, the main difference was observed between the SJG in POST (22.2 ± 6.8 s) and CON in PRE (15.5 ± 7.1 s) intervention for the WB balance performance on the dominant limb with respect to the non-dominant one. Recently, Fusco and colleagues [21] have fully investigated the minimal detectable change values to determine significant changes in dynamic performance on the WB. Accordingly, the emerged mean difference of 6.7 s between the POST intervention of the SJG and PRE intervention of the CON might be considered a real change in WB dynamic balance performance. Therefore, these results suggested that SJ training could be considered in training programs to acutely enhance dynamic balance. However, further research to evaluate the acute effect of SJ on the dynamic performance assessed by WB in several populations is needed. Repeated jumps training may also cause fatigue and joint instability by negatively affecting postural control and increasing the BA Index [38]. In line with this assumption, a previous study showed that excessive jumps training cause muscle fatigue, decrease the concentric peak power and the stretching reflex and increase the magnitude of the BA Index in young athletes [39]. On the contrary, despite the 30 min of SJ workout performed in our study, no significant differences in BA Index between SJG and CON groups in PRE and POST evaluation were found. These results might be due to the selected workout. In fact, although the selected workout was standardized in terms of execution, performing repetitive jumps on a mini-trampoline may not have influenced the magnitude of BA Index. Thus, accurately selecting the type of plyometric training and type of surface where the jumps are executed might decrease the effects of fatigue on BA and consequently reduce the performance loss during balance dynamic performances. The literature identified that a UA threshold of >15% is considered as the real UA [1], [40]. Previous research has also highlighted that both athlete and non-athlete populations who exhibit values in the asymmetry threshold >15% have been associated with increased musculoskeletal injury risk for lower limbs when comparing to subjects who scored below this threshold [3]. However, due the variability in asymmetry, it seems premature for specialists providing the standardized threshold above which the rate of musculoskeletal injuries increases. Indeed, this threshold could differ depending on the morphological demands of the sport/physical performance itself, given the individual demands of each subject [41]. Among these physical activities, jumping, kicking and cycling have been indicated as detrimental to performances by increasing the inter-limb's difference [3]. Although in the present study, the SJG had beneficial effects on UA Index by showing a reduction in UA of 18.9% between PRE and POST intervention, only a few participants had an asymmetry threshold lower than 15%. Therefore, considering that the effect of repetitive jumps on the elastic mini-trampoline played a key role in decreasing UA, and in light of the beneficial effects of SJ, health specialists may consider incorporating repetitive jumps on elastic platforms into their training to acutely reduce lower limb UA and the associated injury risks. Furthermore, when testing the relationship between the difference in PRE exercise and POST exercise UA Index values with UA Index baseline parameters for the SJG, subjects with low baseline values had a minimal or detrimental effect on the UA Index Δ change. Thus, they tended to slightly improve or did not improve their UA Index after SJ training. However, subjects with higher UA Index baseline values tended to decrease their UA Index Δ change POST exercise with significant improvements. When considering the results of the present study, health specialists could consider encouraging mini-trampoline training for athletes or untrained subjects who present higher baseline UA values, in order to decrease the UA and the risk of injury with respect to subjects who present lower baseline values. Research has highlighted the importance of monitoring not only the magnitude of the asymmetries but also their directions [42]. The direction of asymmetry is commonly referred to the stronger-performing limb (dominant vs. non-dominant and left vs. right) during a task, such as the leg jumping higher during a unilateral jump task [43]. This asymmetry variability has also been observed in squats, countermovement jumps and drop jumps in youth soccer athletes, concluding that the dominant limb is stronger than the non-dominant one [44]. In the present study, only for the SJG, two BA categories (equal and change) were created, in order to determine if subjects displaying a change in BA index needed a higher or lower reduction in UA Index. The equal category represents subjects with no difference in BA Index from PRE to POST, whereas the change category represents those having difference in BA Index from PRE to POST. Findings from the present study did not highlight a significant difference between the two BA categories (equal and change). This could mean that the total reduction in UA was similar between subjects that maintained the same direction of asymmetry (equal category) and the subjects that change the direction of asymmetry (change category). These findings could indicate that structured training programs aiming at eliminating or limiting the asymmetries of athletes and non-athletes, should not focus on the execution of exercises for the weaker-performing limb only. Rather, not well-tailored training programs, such as monopodalic-only training, could lead to a change in the direction of asymmetry, and then move from the dominant limb to the non-dominant one or conversely, by not achieving improvements in UA. Therefore, exercises that focus on the execution of both limbs, such as SJ training, could represent an important method in improving UA in healthy young and athlete populations, independently from the direction of asymmetry. Although this study provided some insights, some limitations need to be acknowledged. Only young adults who declared themselves to be minimally active were included. Therefore, populations with different PA levels and ages, such as sedentary and athletes, children and older, should be evaluated. Moreover, healthy individuals were enrolled. Therefore, future studies should also involve subjects with lower limb injuries or patients with dysfunctions such as Parkinson's and Alzheimer's, by ensuring the due precautions (i.e., safety) and modifications (i.e., shorter training duration, lighter exercise intensity, etc.). Finally, the present study only focused on the acute effects of SJ, and therefore, future studies should examine the chronic effects of mini-trampoline SJ training on balance UA and BA Indexes.

V. PRACTICAL APPLICATIONS

The findings showed how SJ training had different effects on balance UA and BA Indexes. SJ reduced UA percentage, by giving to health specialists an alternative method to train their subjects, based on the settled individualized aims. Based on the abovementioned results, practitioners and health coaches might choose the SJ training to reduce UA Index in subjects at risk of lower limb injuries or adopt the SJ method during the warm-up of specific sport disciplines in order to increase specific dynamic balance performances that require a high involvement of the dominant limb.

VI. CONCLUSIONS

Studies widely demonstrated how plyometric training could minimize inter-limb imbalance by reducing asymmetries and the relative risk of sport or physical-related injuries. However, to date, this is the first study aiming at evaluating the effect of SJ on dynamic balance UA and BA Indexes, and it could have a high impact on training and evaluations protocols both in field and laboratory settings. In particular, the findings from the present study suggested that SJ training has the potential to reduce the UA Index in healthy subjects. In addition, the results indicated that subjects with higher baseline values of lower-limb asymmetry had a higher Δ change for the UA Index after the SJ training, suggesting that coaches and health specialists could consider encouraging the use of mini-trampoline training for athletes or untrained subjects at highest risk of musculoskeletal lower-limb injuries.

REFERENCES

[1] C. Bishop, P. Read, J. Lake, S. Chavda, and A. Turner, "Interlimb Asymmetries: Understanding How to Calculate Differences From Bilateral and Unilateral Tests," *Strength & Conditioning Journal*, vol. 40, no. 4, pp. 1–6, Aug. 2018, doi: 10.1519/SSC.0000000000000371.

[2] A. Fort-Vanmeerhaeghe, C. Bishop, B. Buscà, J. Aguilera-Castells, J. Vicens-Bordas, and O. Gonzalo-Skok, "Inter-limb asymmetries are associated with decrements in physical performance in youth elite team sports athletes," *PLoS ONE*, vol. 15, no. 3, p. e0229440, Mar. 2020, doi: 10.1371/journal.pone.0229440.

[3] C. Bishop, A. Turner, and P. Read, "Effects of inter-limb asymmetries on physical and sports performance: a systematic review," *Journal of Sports Sciences*, vol. 36, no. 10, pp. 1135–1144, May 2018, doi: 10.1080/02640414.2017.1361894.

[4] F. Noé, K. Baige, and T. Paillard, "Can Compression Garments Reduce Inter-Limb Balance Asymmetries?," *Front. Hum. Neurosci.*, vol. 16, p. 835784, Feb. 2022, doi: 10.3389/fnhum.2022.835784.

[5] A. Promsri, T. Haid, and P. Federolf, "How does lower limb dominance influence postural control movements during single leg stance?," *Human Movement Science*, vol. 58, pp. 165–174, Apr. 2018, doi: 10.1016/j.humov.2018.02.003.

[6] Y. Morishige *et al.*, "Difference in leg asymmetry between female collegiate athletes and recreational athletes during drop vertical jump," *J Orthop Surg Res*, vol. 14, no. 1, p. 424, Dec. 2019, doi: 10.1186/s13018-019-1490-5.

[7] S. J. Maloney, "The Relationship Between Asymmetry and Athletic Performance: A Critical Review," *Journal of Strength and Conditioning Research*, vol. 33, no. 9, pp. 2579–2593, Sep. 2019, doi: 10.1519/JSC.0000000000002608.

[8] C. Bishop, A. Turner, and P. Read, "Training Methods and Considerations for Practitioners to Reduce Interlimb Asymmetries," *Strength & Conditioning Journal*, vol. 40, no. 2, pp. 40–46, Apr. 2018, doi: 10.1519/SSC.0000000000000354.

[9] P. X. Fuchs, A. Fusco, C. Cortis, and H. Wagner, "Effects of Differential Jump Training on Balance Performance in Female Volleyball Players," *Applied Sciences*, vol. 10, no. 17, p. 5921, Aug. 2020, doi: 10.3390/app10175921.

[10] R. Hammami, M. J. Duncan, A. Nebigh, H. Werfelli, and H. Rebai, "The Effects of 6 Weeks Eccentric Training on Speed, Dynamic Balance, Muscle Strength, Power, and Lower Limb Asymmetry in Prepubescent Weightlifters," *Journal of Strength and Conditioning Research*, vol. 36, no. 4, pp. 955–962, Apr. 2022, doi: 10.1519/JSC.0000000000003598.
[11] P. X. Fuchs, A. Fusco, J. W. Bell, S. P. Von Duvillard, C. Cortis, and H. Wagner, "Effect of Differential Training on Female Volleyball Spike-Jump Technique and Performance," *International Journal of Sports Physiology and Performance*, vol. 15, no. 7, pp. 1019–1025, Aug. 2020, doi: 10.1123/ijspp.2019-0488.
[12] O. E. Atilgan, "Effects of Trampoline Training on Jump, Leg Strength, Static and Dynamic Balance of Boys. Sci. Gymnast. J.," pp. 15–25, 2013.
[13] M. M. Villalba *et al.*, "Effect of a plyometric training session on the ground vs on mini-trampoline on balance and jump performance in basketball player," *Sport Sci Health*, vol. 18, no. 1, pp. 97–105, Mar. 2022, doi: 10.1007/s11332-021-00779-y.
[14] H.-C. Heitkamp, T. Horstmann, F. Mayer, J. Weller, and H.-H. Dickhuth, "Gain in Strength and Muscular Balance After Balance Training," *Int J Sports Med*, vol. 22, no. 4, pp. 285–290, May 2001, doi: 10.1055/s-2001-13819.
[15] S. Vasto, A. Amato, P. Proia, R. Caldarella, C. Cortis, and S. Baldassano, "Dare to jump: The effect of the new high impact activity SuperJump on bone remodeling. A new tool to maintain fitness during COVID-19 home confinement," *bs*, vol. 39, no. 4, pp. 1011–1019, 2022, doi: 10.5114/biolsport.2022.108993.
[16] V. Contrò *et al.*, "Effects of different circuit training protocols on body mass, fat mass and blood parameters in overweight adults," *J Biol Res*, vol. 90, no. 1, Feb. 2017, doi: 10.4081/jbr.2017.6279.
[17] L. Steidl-Müller, C. Hildebrandt, E. Müller, C. Fink, and C. Raschner, "Limb symmetry index in competitive alpine ski racers: Reference values and injury risk identification according to age-related performance levels," *Journal of Sport and Health Science*, vol. 7, no. 4, pp. 405–415, Oct. 2018, doi: 10.1016/j.jshs.2018.09.002.
[18] A. Mannocci *et al.*, "International Physical Activity Questionnaire: Validation and assessment in an Italian sample," *Italian Journal of Public Health*, vol. 7, no. 4, pp. 369–376, 2010.
[19] A. Iannaccone *et al.*, "Stay Home, Stay Active with SuperJump®: A Home-Based Activity to Prevent Sedentary Lifestyle during COVID-19 Outbreak," *Sustainability*, vol. 12, no. 23, p. 10135, Dec. 2020, doi: 10.3390/su122310135.
[20] C. Cortis, G. Giancotti, A. Rodio, A. Bianco, and A. Fusco, "Home is the new gym: exergame as a potential tool to maintain adequate fitness levels also during quarantine," *Human Movement*, vol. 21, no. 4, pp. 79–87, 2020, doi: 10.5114/hm.2020.94826.
[21] A. Fusco *et al.*, "Dynamic Balance Evaluation: Reliability and Validity of a Computerized Wobble Board," *Journal of Strength and Conditioning Research*, vol. 34, no. 6, pp. 1709–1715, Jun. 2020, doi: 10.1519/JSC.0000000000002518.
[22] A. Fusco, G. F. Giancotti, P. X. Fuchs, H. Wagner, C. Varalda, and C. Cortis, "Wobble board balance assessment in subjects with chronic ankle instability," *Gait & Posture*, vol. 68, pp. 352–356, Feb. 2019, doi: 10.1016/j.gaitpost.2018.12.017.
[23] A. Fusco, P. X. Fuchs, M. De Maio, H. Wagner, and C. Cortis, "A novel approach to measuring wobble board performance in individuals with chronic ankle instability," *Heliyon*, vol. 6, no. 9, p. e04937, Sep. 2020, doi: 10.1016/j.heliyon.2020.e04937.
[24] M. De Maio, C. Cortis, A. Iannaccone, R. A. da Silva, and A. Fusco, "Association between Anthropometric Variables, Sex, and Visual Biofeedback in Dynamic Postural Control Assessed on a Computerized Wobble Board," *Applied Sciences*, vol. 11, no. 18, p. 8370, Sep. 2021, doi: 10.3390/app11188370.
[25] W. G. Hopkins, S. W. Marshall, A. M. Batterham, and J. Hanin, "Progressive Statistics for Studies in Sports Medicine and Exercise Science," *Medicine & Science in Sports & Exercise*, vol. 41, no. 1, pp. 3–12, Jan. 2009, doi: 10.1249/MSS.0b013e31818cb278.
[26] J. J. de Koning *et al.*, "Comparison of rating of perceived exertion scales during incremental and interval exercise," *Kinesiology*, vol. 51, no. 2, pp. 150–157, 2019, doi: 10.26582/k.51.2.1.
[27] D. Riebe, J. Ehrman, and G. Liguori, "ACSM's guidelines for exercise testing and prescription. Lippincott Williams & Wilkins: Philadelphia, PA, USA," 2021.
[28] P. V Komi and C. Bosco, "Utilization of stored elastic energy in leg extensor muscles by men and women.," *Medicine and science in sports*, vol. 10, no. 4, pp. 261–5, 1978.
[29] G. N. Gantchev and D. M. Dimitrova, "Anticipatory postural adjustments associated with arm movements during balancing on unstable support surface," *International Journal of Psychophysiology*, vol. 22, no. 1–2, pp. 117–122, Apr. 1996, doi: 10.1016/0167-8760(96)00016-5.
[30] A. Asadi, E. Saez de Villarreal, and H. Arazi, "The Effects of Plyometric Type Neuromuscular Training on Postural Control Performance of Male Team Basketball Players," *Journal of Strength and Conditioning Research*, vol. 29, no. 7, pp. 1870–1875, Jul. 2015, doi: 10.1519/JSC.0000000000000832.
[31] Y. Cherni *et al.*, "Eight Weeks of Plyometric Training Improves Ability to Change Direction and Dynamic Postural Control in Female Basketball Players," *Frontiers in Physiology*, vol. 10, Jun. 2019, doi:

10.3389/fphys.2019.00726.

[32] M. C. Jlid, G. Racil, J. Coquart, T. Paillard, G. N. Bisciotti, and K. Chamari, "Multidirectional Plyometric Training: Very Efficient Way to Improve Vertical Jump Performance, Change of Direction Performance and Dynamic Postural Control in Young Soccer Players," *Frontiers in Physiology*, vol. 10, Dec. 2019, doi: 10.3389/fphys.2019.01462.

[33] C. Cabrejas, J. Morales, M. Solana-Tramunt, A. Nieto-Guisado, A. Badiola-Zabala, and J. Campos-Rius, "Does 8 Weeks of Integrated Functional Core and Plyometric Training Improve Postural Control Performance in Young Rhythmic Gymnasts?," *Motor Control*, vol. 26, no. 4, pp. 568–590, Oct. 2022, doi: 10.1123/mc.2022-0046.

[34] H. Werfelli *et al.*, "Acute Effects of Different Plyometric and Strength Exercises on Balance Performance in Youth Weightlifters," *Frontiers in Physiology*, vol. 12, Sep. 2021, doi: 10.3389/fphys.2021.716981.

[35] R. Hammami *et al.*, "Acute effects of maximal versus submaximal hurdle jump exercises on measures of balance, reactive strength, vertical jump performance and leg stiffness in youth volleyball players," *Frontiers in Physiology*, vol. 13, Dec. 2022, doi: 10.3389/fphys.2022.984947.

[36] H. Topcu and R. Arabaci, "Acute Effect of Different Warm Up Protocols on Athlete'S Performance," *European Journal of Physical Education and Sport Science*, vol. 0, no. 0, pp. 35–50, 2017, doi: 10.5281/zenodo.833657.

[37] N. Rhouni, N. C. Dabbs, T. Gillum, and J. W. Coburn, "Acute Effect of Mini-Trampoline Jumping on Vertical Jump and Balance Performance," *International Journal of Kinesiology and Sports Science*, vol. 7, no. 2, p. 1, Apr. 2019, doi: 10.7575/aiac.ijkss.v.7n.2p.1.

[38] D. M. Hopper, T. L. Grisbrook, P. J. Newnham, and D. J. Edwards, "The Effects of Vestibular Stimulation and Fatigue on Postural Control in Classical Ballet Dancers," *Journal of Dance Medicine & Science*, vol. 18, no. 2, pp. 67–73, Jun. 2014, doi: 10.12678/1089-313X.18.2.67.

[39] I.-L. Wang *et al.*, "The Effect of Repetitive Drop Jumps among Different Heights on Bilateral Asymmetry of Countermovement Jumps," *Symmetry*, vol. 14, no. 2, p. 190, Jan. 2022, doi: 10.3390/sym14020190.

[40] C. Bishop, "Interlimb Asymmetries: Are Thresholds a Usable Concept?," *Strength & Conditioning Journal*, vol. 43, no. 1, pp. 32–36, Feb. 2021, doi: 10.1519/SSC.0000000000000554.

[41] C. Bishop, J. Lake, I. Loturco, K. Papadopoulos, A. Turner, and P. Read, "Interlimb Asymmetries: The Need for an Individual Approach to Data Analysis," *Journal of Strength and Conditioning Research*, vol. 35, no. 3, pp. 695–701, Mar. 2021, doi: 10.1519/JSC.0000000000002729.

[42] N. Šarabon, D. Smajla, N. A. Maffiuletti, and C. Bishop, "Strength, Jumping and Change of Direction Speed Asymmetries in Soccer, Basketball and Tennis Players," *Symmetry*, vol. 12, no. 10, p. 1664, Oct. 2020, doi: 10.3390/sym12101664.

[43] G. Wang *et al.*, "Association Analysis of ACE and ACTN3 in Elite Caucasian and East Asian Swimmers," *Medicine & Science in Sports & Exercise*, vol. 45, no. 5, pp. 892–900, May 2013, doi: 10.1249/MSS.0b013e31827c501f.

[44] C. Bishop, L. A. Pereira, V. P. Reis, P. Read, A. N. Turner, and I. Loturco, "Comparing the magnitude and direction of asymmetry during the squat, countermovement and drop jump tests in elite youth female soccer players," *Journal of Sports Sciences*, vol. 38, no. 11–12, pp. 1296–1303, Jun. 2020, doi: 10.1080/02640414.2019.1649525.

Changes of Brain-Derived Neurotrophic Factor (BDNF) levels after different exercise protocols: a systematic review of clinical studies in Parkinson's disease

Andrea Paterno[1*], Giovanni Polsinelli[1], Bruno Federico[1]

[1] Department of Human Sciences, Society and Health, University of Cassino and Southern Lazio, Via Folcara, 03043 Cassino, Italy

Email: andrea.paterno@unicas.it;

I. Introduction

Brain-Derived Neurotrophic Factor (BDNF) serum levels are reduced in patients with Parkinson's Disease (PD)(1).

II. Objective

This study aimed at assessing if exercise intensity, volume and type are associated with changes in BDNF in patients with PD.

III. Methods

We searched clinicaltrials.gov, CINAHL, Embase, PubMed, Scopus, Web of Science for both controlled and non-controlled studies with patients with PD, published between 2003 and 2022, which assessed BDNF before and after different exercise protocols. The quality of studies was assessed using the Cochrane Risk of Bias (2) and ROBINS-I tool. Exercise intensity was estimated with a time-weighted average of Metabolic Equivalent of Task (MET), while exercise volume was estimated by multiplying MET for the duration of exercise (3). Exercise types were classified as aerobic, resistance, balance and others. Meta-regression and linear regression were used to assess whether these effect measures were associated with intensity, volume and type (4). PROSPERO registration number: CRD42023418629.

IV. RESULTS

Sixteen studies (8 two-arm trials and 8 single-arm trials) including 384 patients with PD were eligible for the systematic review. Selected studies had low and moderate risk of bias and a large variability in terms of population and intervention characteristics. The meta-analysis showed a significant improvement in BDNF levels compared to the control group, Hedges' g = 0.70 (95% CI: 0.03, 1.38), with substantial heterogeneity (I^2 = 76.0%). Between-group differences in intensity were positively associated with change in BDNF over time in a subset of 5 controlled studies. In the analysis which included non-controlled studies, intensity and total exercise volume were both positively associated with BDNF change. No difference was found according to exercise type.

V. CONCLUSIONS

Exercise intensity and volume may increase BDNF levels in patients with PD, while the role of the type of exercise is to be further explored.

Index Terms

Brain-Derived Neurotrophic Factor, Exercise, Systematic review, Parkinson's disease

REFERENCE

1. Scalzo P, Kummer A, Bretas TL, Cardoso F, Teixeira AL. Serum levels of brain-derived neurotrophic factor correlate with motor impairment in Parkinson's disease. J Neurol. 2010;257(4):540-5.
2. Higgins JP, Altman DG, Gotzsche PC, Juni P, Moher D, Oxman AD, et al. The Cochrane Collaboration's tool for assessing risk of bias in randomised trials. Bmj. 2011;343:d5928.
3. Committee PAGA. Physical Activity Guidelines Advisory Committee Report. Washington, DC: U.S. Department of Health and Human Services2008.
4. Matthias Egger (Editor) JPTHE, George Davey Smith (Editor). June 2022 BMJ Books. Systematic Reviews in Health Research: Meta-Analysis in Context, 3rd Edition.2022.

Navigating the Social Media Landscape: Adolescents' Emotional Intelligence and Problematic Use

Lidia Piccerillo[1]

University of Cassino and Southern Lazio

[1] Dept. of Human Sciences, Society and Health

Email: lidia.piccerillo@unicas.it

Abstract

As our world becomes increasingly connected and digital, social media is central to young people' lives. Platforms such as Instagram, TikTok and WhatsApp serve as virtual bridges between generations. They allow young people to express themselves, share experiences and connect with the world. But a complex maze of emotions, challenges and educational opportunities lies behind this fascinating window into the cyber world. Teenage years are a critical period of growth and development, when people are still learning to navigate the complex waters of their feelings. In this context, emotional intelligence emerges as a crucial skill. This article explores the interplay between social media usage among adolescents, emotional intelligence, and the risk of developing problematic social media use. Through a study conducted on a sample of 530 adolescents in Italian schools, we analyzed patterns of social media usage, levels of emotional intelligence, and the propensity for problematic use. The results highlighted that the overwhelming majority of adolescents use social media and instant messaging applications as integral parts of their daily routines. However, excessive usage is positively correlated with problematic social media use. Furthermore, we found that higher levels of emotional intelligence are associated with a reduced tendency for problematic social media use. The article underscores the importance of promoting emotional intelligence among adolescents as part of strategies to prevent problematic social media use.

Index Terms

Social Media, Emotional Intelligence, Adolescence

I. INTRODUCTION

Social media uses mobile and internet-based technologies to create highly interactive platforms where individuals and communities can collaborate, share, discuss and contribute to user-generated content [1]. The term 'social media' describes websites and services that emerged in the early 2000s. The first identifiable social network site, SixDegrees.com, made its debut in 1997 [2]. These include social network sites, instant messaging Apps, video-sharing platforms, blogging and microblogging services, as well as related tools that enable users to generate and share their own content. In today's landscape, social media is a pervasive phenomenon in the lives of young people, with both positive and negative effects on their mental health and well-being [3]. These platforms now play an important role in helping individuals, particularly young people, to develop and express their identity. Identity formation begins in childhood and becomes increasingly important during adolescence. During this time, pre-teens and teenagers try to define who they are and what role they play in society. The concept of identity is at the centre of this search for self. According to Erikson's theory of developmental stages, the challenge of adolescence is represented by "identity versus role confusion" [4]. This stage involves exploring personal identity and experimenting with social identities, including digital identity. Digital platforms provide an environment for young people to explore different social identities, but it is important to note that online identity is not separate from offline identity, rather the two dimensions are intertwined [5].

Social networking sites are also an online space that provides more opportunities for young people to interact with other peers, and building meaningful friendships is an essential element of young people's psychosocial development, particularly for the overall well-being of pre-adolescents and adolescents. In addition, some research suggests that the formation and quality of friendships can be improved through online communication [6].

It is crucial to highlight that while social media offers young people opportunities to explore and develop their personal identity and to connect with friends, there is also a downside. Extended use of social media can replace other activities, such as face-to-face interactions and engagement in other leisure activities, such as sports or physical activities, which are known to be associated with improved well-being. Furthermore, the significant amount of time young people spend engaging in these online activities poses the risk of developing problematic social media use. Research conducted on 5961 adolescents highlighted that 4.5% of participants could be classified as at risk of developing problematic use of social media [7]. Emotional Intelligence (EI) represents a psychological trait of considerable importance, proving to play a fundamental role as a protective factor against various behavioral and health problems among adolescents. [8]. Adolescents with a higher level of EI may be better prepared to deal with the challenges that arise from the use of social media. Therefore, the primary objective of this study is to investigate the relationship between adolescents' social media usage patterns, emotional intelligence, and problematic social media usage. It also aims to identify potential strategies for promoting positive social media experiences and mitigating the risks associated with excessive and problematic use among young people.

II. METHODS

The study included 530 preadolescents (50% male, 50% female) aged between 11 and 14 years (M = 12.12, SD = .891) from various lower secondary schools in Italy.

An anonymous questionnaire was used to assess the study variables, consisting of a mixture of standardised questionnaires and questions.

To record daily time spent on social media, participants were asked to complete a table

indicating their daily usage duration for each platform, categorized into the following intervals: 15-30 minutes, 30-60 minutes, 1-2 hours, 2-4 hours, and more than 4 hours.
To assess social media addiction, the Bergen Social Media Addiction Scale (BSMAS) was employed. This scale consists of six items rated on a 5-point Likert scale, ranging from "very rarely" to "very often," measuring various addiction-like symptoms such as salience, withdrawal, mood modification, conflict, tolerance, and relapse [9].
For the evaluation of Emotional Intelligence, the "Trait Emotional Intelligence Questionnaire – Child Short Form" (TEIQue-CSF) was utilized [10]. This instrument is formed by 36 short statements answered on 5-point Likert scale, ranging from completely disagree to completely agree (e.g., I'm very good at understanding how other people feel).

III. RESULTS

Results from this study show that 98% of participants reported using an internet-connected device and 98.5% use instant messaging applications. Examining this data by gender, 98.1% of males and a slightly higher percentage of females, 99.2%, were active users of these apps. Approximately 86% of participants reported using social media platforms. Further analysis reveals some gender differences, with 89.4% of males and 82.5% of females using social media. The most used social media and instant messaging apps are WhatsApp (95%), YouTube (86%), TikTok (74%), Instagram (68%), Pinterest (44%) and Twitch (31%).

Time of use of main social media

Table 1 presents data on the time spent using the main social media platforms, divided into five categories corresponding to different time intervals (15-30 minutes, 30-60 minutes, 1-2 hours, 2-4 hours, and more than 4 hours).

TABLE I: Percentage Distribution of Daily WhatsApp Usage by Time Intervals *Correlation between TEI-Que, Bergen Social Media Addiction Scale and social media use*

Social Media	Time of use				
	1*	2*	3*	4*	5*
WhatsApp	26%	22%	20%	18%	14%
YouTube	19%	31%	25%	14%	11%
TikTok	9%	19%	29%	24%	19%
Instagram	37%	27%	17%	13%	6%

Pinterest	73%	17%	7%	3%	0.4%
Twitch	24%	24%	22%	19%	11%

*1=15-30 minutes, 2=30-60 minutes, 3=1-2 hours, 4=2-4 hours, 5= +4 hours.

Table II presents correlations between different study variables, with values represented at the top of the table. The variable Trait Emotional Intelligence has a moderate but significant negative correlation (-0.265) with the Bergen Social Media Addiction Scale. This suggests that a higher score on TEI-Que (a higher level of emotional intelligence) is associated with a slightly lower tendency to addiction to social media, as measured by the BSMAS scale. Furthermore, the BSMAS shows a significant positive correlation with the time spent using TikTok, Instagram, WhatsApp and YouTube.

TABLE II: Mean scores, standard deviations, and correlations of the study variables.

Correlation	1. TEI-Que	2. BSMAS	3. Instagram	4. Pinterest	5. Tiktok	6. WhatsApp	7. YouTube
1.	1	**-,265****	-0,028	-0,036	**-,172****	-0,026	-0,045
2.		1	**,376****	0,027	**,403****	**,341****	**,153****
3.			1	0,144	**,466****	**,459****	0,044
4.				1	**,154***	0,052	**,215****
5.					1	**,446****	**,139****
6.						1	**,143****
7.							1
Means	3.4	12.3	2.2	1.3	3.2	2.7	2.6
S.D	0.4	4.7	1.2	,7	1.2	1.3	1.2

*p <0.05 **p<0.01

IV. DISCUSSION

In today's society, the digital environment is an element that strongly characterises the contexts of everyday experience. This study aimed to contribute to the growing literature by deepening our understanding of how preadolescents are using digital technologies, especially social media platforms. The high usage percentages of instant messaging apps revealed by this study underscore how online communication has become a preferred mode of interaction among young individuals. Equally noteworthy are the substantial usage rates of social networking platforms. According to author Bozkurt, in today's world, similar to the cognitive stages of development proposed by Piaget or the psychosocial milestones proposed by Erikson, signing up for a social networking account has become a fundamental step in adolescents' psychosocial development [11].

Despite the many benefits of the Internet, some people may use it in ways that lead to negative consequences, and adolescents are particularly vulnerable to this risk. An aspect that deserves further investigation is the amount of time that adolescents and preadolescents spend on these platforms. For example, a significant group of 19% of the sample spend between 30 and 60 minutes daily on TikTok, while an even more significant group of 29% spend 1-2 hours daily on TikTok. It's important to note that TikTok is just one of the many social media platforms, substantial percentages of participants are also devoting significant time to other platforms like WhatsApp, YouTube, Instagram, and more. This indicates that pre-adolescents are actively using multiple social media platforms as integral parts of their daily routines. In addition, daily time spent on the most commonly used social media (TikTok, Instagram, WhatsApp and YouTube) is correlated with social media addiction, supporting previous findings that excessive and habitual use can lead to addiction [12].

Parents and professionals often find it challenging to provide young people with guidance on responsible online behaviour, help them navigate online content, teach them how to use digital media in a positive way, and give them advice on how to manage online situations. This challenge is partly due to the fact that young people, regardless of their socio-economic status, race or ethnicity, tend to be more immersed in the virtual world than adults [13].

The results of this study have also shown a negative correlation between emotional intelligence and problematic social media use. Adolescents with lower levels of emotive competence may face challenges in recognizing and effectively managing their own emotions. Emotional intelligence involves the ability to understand, express, and regulate emotions, both in oneself and in others [14]. When adolescents have decreased levels of emotional competencies, they may struggle to identify and cope with emotional distress in a healthy and adaptive manner. In such cases, they might turn to external sources for relief, and one common outlet can be excessive or problematic use of social media and smartphones. The lack of ability to identify one's own emotional states, to know how emotions can be channelled into thoughts and actions, as well as the lack of knowledge or ability to use effective strategies to regulate negative emotions, is what leads adolescents to resort to maladaptive strategies, such as problematic smartphone use (PSU), to cope with distress [15]. Social media platforms offer a convenient and easily accessible means of distraction and interaction, which can temporarily alleviate emotional discomfort. Developing better self-regulation skills might empower adolescents to manage their social media use more effectively [16].

The school represents one of the privileged contexts for promoting a "culture of health". It is an environment in which children and young people have the opportunity to develop their identity, critical thinking, self-awareness, as well as a sense of individual responsibility and autonomy. School-based programmes appear to be more effective in addressing this issue at this stage of development provide access to large numbers of students in a cost-effective way [17]. Incorporating programmes designed to develop emotional intelligence into schools could be crucial. These programmes would aim to improve young people's ability to cope with emotionally intense situations without resorting to excessive use of social media as an outlet, by teaching them how to recognise, understand and manage their emotions in a healthy way.

Several studies have demonstrated the potential of interventions aimed at emotional intelligence and emotional education in young people, highlighting the benefits both in terms of improving socio-emotional skills and academic performance [18]–[20].

This study contributes to a deeper understanding of how young people interact with social media and provides insights into addressing challenges related to this evolving form of digital communication. Understanding the complex interaction between emotional intelligence, social media use, and its impact on well-being should be the subject of future research. By gaining a more profound understanding of these relationships, we can better equip young individuals with the skills and knowledge needed to navigate the digital landscape in ways that enhance their well-being and promote positive online experiences.

References

[1] J. H. Kietzmann, K. Hermkens, I. P. McCarthy, and B. S. Silvestre, 'Social media? Get serious! Understanding the functional building blocks of social media', *Business Horizons*, vol. 54, no. 3, pp. 241–251, May 2011, doi: 10.1016/j.bushor.2011.01.005.

[2] D. M. Boyd and N. B. Ellison, 'Social Network Sites: Definition, History, and Scholarship', *Journal of Computer-Mediated Communication*, vol. 13, no. 1, pp. 210–230, Oct. 2007, doi: 10.1111/j.1083-6101.2007.00393.x.

[3] G. J. Hjetland, V. Schønning, R. T. Hella, M. Veseth, and J. C. Skogen, 'How do Norwegian Adolescents Experience The Role of Social Media in Relation to Mental Health and Well-Being: A Qualitative Study', In Review, preprint, Dec. 2020. doi: 10.21203/rs.3.rs-133641/v1.

[4] E. H. Erikson, *Identity and the life cycle*, 5. [print.]. New York: Norton, 1982.

[5] M. Dooly, 'Performing Identities in Social Media: Focusing on Language Learners' Identity Construction Online', *alsic*, no. Vol. 20, n° 1, Sep. 2017, doi: 10.4000/alsic.3005.

[6] M. A. Wood, W. M. Bukowski, and E. Lis, 'The Digital Self: How Social Media Serves as a Setting that Shapes Youth's Emotional Experiences', *Adolescent Res Rev*, vol. 1, no. 2, pp. 163–173, Jun. 2016, doi: 10.1007/s40894-015-0014-8.

[7] F. Banyai *et al.*, 'Problematic Social Media Use: Results from a Large-Scale Nationally Representative Adolescent Sample', *PLOS ONE*, vol. 12, no. 1, Jan. 2017, doi: 10.1371/journal.pone.0169839.

[8] M. T. Sánchez-López, P. Fernández-Berrocal, R. Gómez-Leal, and A. Megías-Robles, 'Evidence on the Relationship Between Emotional Intelligence and Risk Behavior: A Systematic and Meta-Analytic Review', *Front. Psychol.*, vol. 13, p. 810012, Feb. 2022, doi: 10.3389/fpsyg.2022.810012.

[9] C. S. Andreassen *et al.*, 'The relationship between addictive use of social media and video games and symptoms of psychiatric disorders: A large-scale cross-sectional study.',

Psychology of Addictive Behaviors, vol. 30, no. 2, pp. 252–262, Mar. 2016, doi: 10.1037/adb0000160.
[10] S. Mavroveli, K. V. Petrides, C. Shove, and A. Whitehead, 'Investigation of the construct of trait emotional intelligence in children', *Eur Child Adolesc Psychiatry*, vol. 17, no. 8, pp. 516–526, Dec. 2008, doi: 10.1007/s00787-008-0696-6.
[11] A. Bozkurt and C.-H. Tu, 'Digital identity formation: socially being real and present on digital networks', *Educational Media International*, vol. 53, no. 3, pp. 153–167, Jul. 2016, doi: 10.1080/09523987.2016.1236885.
[12] M. Zhitomirsky-Geffet and M. Blau, 'Cross-generational analysis of predictive factors of addictive behavior in smartphone usage', *Computers in Human Behavior*, vol. 64, pp. 682–693, Nov. 2016, doi: 10.1016/j.chb.2016.07.061.
[13] A. Mayhew and P. Weigle, 'Media Engagement and Identity Formation Among Minority Youth', *Child and Adolescent Psychiatric Clinics of North America*, vol. 27, no. 2, pp. 269–285, Apr. 2018, doi: 10.1016/j.chc.2017.11.012.
[14] P. Salovey and J. D. Mayer, 'Emotional Intelligence', *Imagination, Cognition and Personality*, vol. 9, no. 3, pp. 185–211, Mar. 1990, doi: 10.2190/DUGG-P24E-52WK-6CDG.
[15] C. Arrivillaga, L. Rey, and N. Extremera Pacheco, 'USO PROBLEMÁTICO DEL SMARTPHONE Y AJUSTE PSICOLÓGICO EN ADOLESCENTES: EL PAPEL CLAVE DE LA INTELIGENCIA EMOCIONAL', *KASP*, vol. 1, no. 4, Dec. 2020, doi: 10.25115/kasp.v1i4.4258.
[16] S. M. Coyne, L. M. Padilla-Walker, H. G. Holmgren, and L. A. Stockdale, 'Instagrowth: A Longitudinal Growth Mixture Model of Social Media Time Use Across Adolescence', *J of Research on Adolesc*, vol. 29, no. 4, pp. 897–907, Dec. 2019, doi: 10.1111/jora.12424.
[17] M. A. Throuvala, M. D. Griffiths, M. Rennoldson, and D. J. Kuss, 'School-based Prevention for Adolescent Internet Addiction: Prevention is the Key. A Systematic Literature Review', *CN*, vol. 17, no. 6, pp. 507–525, May 2019, doi: 10.2174/1570159X16666180813153806.
[18] R. Castillo, J. M. Salguero, P. Fernández-Berrocal, and N. Balluerka, 'Effects of an emotional intelligence intervention on aggression and empathy among adolescents', *Journal of Adolescence*, vol. 36, no. 5, pp. 883–892, Oct. 2013, doi: 10.1016/j.adolescence.2013.07.001.
[19] P. Luna, J. Cejudo, J. A. Piqueras, D. Rodrigo-Ruiz, M. Bajo, and J.-C. Pérez-González, 'Impact of the MooN Physical Education Program on the Socio-Emotional Competencies of Preadolescents', *IJERPH*, vol. 18, no. 15, p. 7896, Jul. 2021, doi: 10.3390/ijerph18157896.
[20] M.-J. Cantero, R. Bañuls, and P. Viguer, 'Effectiveness of an Emotional Intelligence Intervention and Its Impact on Academic Performance in Spanish Pre-Adolescent Elementary Students: Results from the EDI Program', *IJERPH*, vol. 17, no. 20, p. 7621, Oct. 2020, doi: 10.3390/ijerph17207621.

Exploring the Influence of Social Networks on Body Dissatisfaction among Preadolescents

Alessia Tescione[1]
[1]University of Cassino and Southern Lazio
Dept. of Human Sciences, Society and Health
Email:
alessia.tescione@unicas.it

Abstract

Social networks propose beauty standards that have dangerous implies on users' body satisfaction and multifaceted on body image of preadolescents, a vulnerable age group facing unique challenges in the digital era. With the proliferation of social media platforms, preadolescents are increasingly exposed to carefully curated images and ideals of beauty, which can significantly influence their self-perception and body image. This study examines the impact of social networks on body image in a sample of 92 preteens. An anonymous questionnaire was used to investigate the time spent on social networks and the role of sociocultural influences on body image. The findings from this research underscore the pressing need for targeted interventions and educational programs that equip preadolescents with the skills and knowledge to navigate social network use in a way that promotes a positive body image and psychological well-being.
Social Media, Body Image, Preadolescence

Index Terms

Social Media, Body Image, Preadolescence

I. Introduction

Body image constitutes a multifaceted concept encompassing three core domains: perception of our own bodies, the emotion intertwined with our physicality, and the thoughts and convictions we hold about our bodies [1]. Disruptions in one's body perception can significantly impact their mental well-being [2]. Research suggests that socio-cultural factors wield substantial influence in the development of body dissatisfaction [3]. Negative body image can originate from a variety of sources, including familial influences, peer dynamics, media portrayals, and societal pressures [4] ultimately affecting self-esteem, competence, and social functioning [1].

In recent times, the explosive growth of social media has exposed an ever-expanding user base to content that upholds beauty standards, emphasizes thinness, and champions the absence of imperfections. Consequently, body dissatisfaction can emerge as a result of internalizing these appearance ideals and struggling to conform to the beauty standards propagated by the media [5]. Adolescents who spend more time on social media platforms receive heightened feedback concerning their physical appearance [6]. Social media platforms open doors for young individuals to receive continuous evaluations of their physical appearance in the form of comments and "likes" [7].

Despite the extensive body of literature exploring the impact of social media on adolescents' body image, limited attention has been given to the youngest age group. Preadolescence is regarded as a vulnerable period that amplifies the risk of various issues, such as eating disorders, social anxiety, and depression [8]. The formation of preteens' body image commences during this developmental stage, and the constant comparisons with the beauty ideals promoted by social media may significantly influence their body satisfaction. Even though many platforms have set age restrictions, preadolescents often manage to access social networks. In this context, implementing educational initiatives centred around fostering positive body image and promoting the safe use of social media may offer a potential solution.

II. Methods

A group of 92 preadolescents, aged between 10 and 14 (comprising 55% females and 45% males, with an average age of 12 years old), participated in this study. They completed an anonymous self-administered questionnaire that aimed to investigate several aspects, including their use of social networks (including the types of platforms used, the average daily time spent on social media, addiction to social networks), as well as their level of body satisfaction.

Participants reported the amount of time they spent on each social network per day, ranging from 15 minutes to over 4 hours. To calculate the total time spent online, researchers derived an average based on participants' responses regarding their daily usage time and the number of social networks they used.

The degree of addiction to social networks was assessed using the Bergen Social Media Addiction Scale (BSMAS) [9], a six-item self-report scale. Respondents rated their behaviors on a 5-point scale, ranging from 0 (very rarely) to 5 (very often).

Lastly, participants' body dissatisfaction was evaluated using the Sociocultural Attitudes Towards Appearance Questionnaire-4-Revised (SATAQ-4R) [10]. This questionnaire consists of 31 items for females and 28 items for males, all rated on a 5-point Likert scale with response options ranging from 1 (definitely disagree) to 5 (definitely agree). The questionnaire is divided into two main sections: Internalization and Pressures. The Internalization section encompasses questions related to perceptions of thinness, body fat, muscularity, and overall attractiveness. The Pressures section explores the influence of family, peers, significant others, and media on body image. Mean scores were calculated for each section to analyze the participants' responses.

III. RESULTS

Out of the respondents, 80.4% (n=74, with a mean age of 12 years old) stated that they use social networks. This percentage increased to 93.5% for messaging apps (n=86). The most frequently used platforms were WhatsApp (89%), YouTube (78%), TikTok (67%), and Instagram (67%). On average, respondents used about 5.52 social networks (SD 3.16), and they spent an average of 2.21 hours daily (SD 0.68) on each social network. Notably, boys reported a higher mean daily usage time (mean 2.37; SD 1.32) compared to girls (mean 2.13; SD 1.25).

A. Descriptive statistics of BSMAS and SATAQ-4R

BSMAS and SATAQ-4R descriptive statistics for the entire sample and both gender groups are shown in Table I and II. In the overall sample, the range of means for the BSMAS item scores ranged from 1.68 to 2.57. In the female group, the means ranged from 1.66 to 2.56. In the male group, the means ranged from 1.70 to 2.59. The range of means for the SATAQ-4R, in the female group ranged from 1.67 to 3.49, in the male group ranged from 1.90 to 3.80. In the female group, media pressure score (2.23) is higher compared with the influence of family (2.00), peers (1.67) and significant others (1.78). In the male group the average of the scores is uniformly distributed (1.90-1.99).

TABLE I: Descriptive statistics of the BSMAS.

Sample	Item	Mean (SD)
Total (n=92)	1	2.38 (1.38)
	2	2.24 (1.28)
	3	2.57 (1.40)
	4	2.08 (1.47)
	5	1.97 (1.32)
	6	1.68 (1.00)
Female (n=51)	1	2.40 (1.37)
	2	2.32 (1.30)
	3	2.56 (1.43)
	4	2.22 (1.58)
	5	1.98 (1.38)
	6	1.66 (0.98)
Male (n=41)	1	2.35 (1.42)

	2	2.14 (1.25)
	3	2.59 (1.37)
	4	1.89 (1.30)
	5	1.95 (1.27)
	6	1.70 (1.05)

TABLE II: Descriptive statistics of the SATAQ-4R

		Mean (SD) Female	Mean (SD) Male
	Thin/Low Body Fat	2.70 (1.31)	2.40 (1.12)
Internalization	Muscular	1.80 (1.20)	2.26 (1.16)
	General attractiveness	3.49 (1.35)	3.80 (1.21)
	Family	2.00 (1.23)	1.99 (1.28)
Pressures	Peers	1.67 (1.09)	1.92 (1.14)

	Significant Others	1.78 (1.17)	1.95 (1.27)
	Media	2.23 (1.40)	1.90 (1.22)

B. Correlation between SATAQ 4-R, Time per day and BSMAS

Data screening suggested that data were normally distributed. Correlational analysis between body image (SATAQ-4R), amount of time spent on social networks and addiction to social media (BSMAS) are shown in Table 4. Body image showed a positive correlation with time spent on social media (r=0,417) and addiction to social network (r=0,537). Furthermore, there is also a positive correlation between time spent on platforms and addiction to social media (r=0,374).

TABLE III: Correlation table SATAQ-4R-Time per day- BSMAS

		SATAQ-4R	TIME PER DAY	BSMAS
SATAQ-4R	Pearson's Correlation	1	,417**	,537**
	p value		<,001	<,001
	N	92	88	87
TIME PER DAY	Pearson's Correlation	,417**	1	,374**
	p value	<,001		<,001

	N	88	88	84
BSMAS	Pearson's Correlation	,537**	,374**	1
	p value	<,001	<,001	
	N	87	84	87

IV. DISCUSSION

The primary objective of this study was to examine the correlation between the amount of time spent on social networks and individuals' body satisfaction. Our hypothesis that increased time spent on social media negatively impacts body satisfaction was confirmed. Additionally, we found that a higher score on a social network addiction scale had an adverse effect on body image, irrespective of the time spent online. Our findings suggest that social networks affect both males' and females' body image equally.

Notably, the use of social networks appears to have a detrimental impact on body satisfaction during this stage of life. According to the results from the SATAQ-4R questionnaire, among females, media influence on body image surpasses that of family, peers, and significant others.

This study has significant practical implications, with the most crucial being the necessity to implement educational approaches centered around fostering a positive body image and safe social network use. Schools are well-positioned to promote positive health behaviors, including body image development, and media literacy programs can counter unrealistic body representations in the media [11]. Long-term media education focusing on critical thinking, questioning, discussion, active participation, and key media competence concepts has been proven effective in addressing body dissatisfaction [12].

Intervention strategies should address key factors influencing body image, particularly emotions and feelings related to one's body [5]. Recent research indicates that children with a positive body image exhibit higher interpersonal intelligence, greater adaptability, and improved mood [13]. A collaborative approach involving schools, teachers, and parents is crucial. Schools, despite potential challenges, can play a vital role in both media education and promoting a positive body image. Physical education, if properly targeted, can be used to explore individuals' unique qualities. Additionally, education should start at home, with parents offering positive and supportive treatment to their children, emphasizing both appearance and personal qualities, and setting a positive example of body shape and fitness.

V. CONCLUSIONS

The current study revealed that the time spent online is linked to body dissatisfaction and addiction to social media. Preadolescents use social networks regardless the age restrictions settled by social media platforms. Social media companies must consider this aspect and develop strategies that limit exposure risks for young people. A new research area to explore might be related to the content and activities on social networks that most afflict the body image of preteens. Furthermore, it is necessary to develop interventions to promote positive body image in young people with the support of educators and parents.

The limitations of this study can be stated as follows. The sample analyzed were small, which may limit the generalizability of the results. Further, we were unable to model all the factors that lead to body image dissatisfaction. Measurements for social network use were self-reported and time spent on the platform might be underestimated or overestimated.

REFERENCES

[1] L. A. Ricciardelli and Z. Yager, *Adolescence and Body Image*, 0 ed. Routledge, 2015. doi: 10.4324/9781315849379.

[2] L. Tomas-Aragones and S. Marron, ‘Body Image and Body Dysmorphic Concerns’, *Acta Derm Venerol*, p. 0, 2014, doi: 10.2340/00015555-2368.

[1] [3] G. Cafri, Y. Yamamiya, M. Brannick, and J. K. Thompson, ‘The influence of sociocultural factors on body image: A meta-analysis.’, *Clinical Psychology: Science and Practice*, vol. 12, no. 4, pp. 421–433, 2005, doi: 10.1093/clipsy.bpi053.

[4] J. Shen, J. Chen, X. Tang, and S. Bao, ‘The effects of media and peers on negative body image among Chinese college students: a chained indirect influence model of appearance comparison and internalization of the thin ideal’, *J Eat Disord*, vol. 10, no. 1, p. 49, Dec. 2022, doi: 10.1186/s40337-022-00575-0.

[5] B. Jiotsa, B. Naccache, M. Duval, B. Rocher, and M. Grall-Bronnec, ‘Social Media Use and Body Image Disorders: Association between Frequency of Comparing One’s Own Physical Appearance to That of People Being Followed on Social Media and Body Dissatisfaction and Drive for Thinness’, *IJERPH*, vol. 18, no. 6, p. 2880, Mar. 2021, doi: 10.3390/ijerph18062880.

[6] D. A. De Vries, J. Peter, H. De Graaf, and P. Nikken, ‘Adolescents’ Social Network Site Use, Peer Appearance-Related Feedback, and Body Dissatisfaction: Testing a Mediation Model’, *J Youth Adolescence*, vol. 45, no. 1, pp. 211–224, Jan. 2016, doi: 10.1007/s10964-015-0266-4.

[7] D. A. De Vries, H. G. M. Vossen, and P. Van Der Kolk – Van Der Boom, ‘Social Media and Body Dissatisfaction: Investigating the Attenuating Role of Positive Parent–Adolescent Relationships’, *J Youth Adolescence*, vol. 48, no. 3, pp. 527–536, Mar. 2019, doi: 10.1007/s10964-018-0956-9.

[8] B. Khan and B. I. Avan, ‘Behavioral problems in preadolescence: Does gender matter?’, *PsyCh Journal*, vol. 9, no. 5, pp. 583–596, Oct. 2020, doi: 10.1002/pchj.347.

[9] C. S. Andreassen, S. Pallesen, and M. D. Griffiths, 'The relationship between addictive use of social media, narcissism, and self-esteem: Findings from a large national survey', *Addictive Behaviors*, vol. 64, pp. 287–293, Jan. 2017, doi: 10.1016/j.addbeh.2016.03.006.

[10] C. Stefanile, A. Nerini, C. Matera, L. M. Schaefer, and J. K. Thompson, 'Validation of an Italian version of the Sociocultural Attitudes Towards Appearance Questionnaire-4-Revised (SATAQ-4R) on non-clinical Italian women and men', *Body Image*, vol. 31, pp. 48–58, Dec. 2019, doi: 10.1016/j.bodyim.2019.08.005.

[11] Z. Yager, P. C. Diedrichs, L. A. Ricciardelli, and E. Halliwell, 'What works in secondary schools? A systematic review of classroom-based body image programs', *Body Image*, vol. 10, no. 3, pp. 271–281, Jun. 2013, doi: 10.1016/j.bodyim.2013.04.001.

[12] S. Conard, 'Best practices in digital health literacy', *International Journal of Cardiology*, vol. 292, pp. 277–279, Oct. 2019, doi: 10.1016/j.ijcard.2019.05.070.

[13] D. Amado Alonso, B. León-del-Barco, S. Mendo-Lázaro, and D. Iglesias Gallego, 'Examining Body Satisfaction and Emotional–Social Intelligence among School Children: Educational Implications', *IJERPH*, vol. 17, no. 6, p. 2120, Mar. 2020, doi: 10.3390/ijerph17062120.

Sub-micron particle number emission from residential heating systems: A comparison between conventional and condensing boilers fueled by natural gas and liquid petroleum gas, and pellet stoves

Elisa Caracci[1], Laura Canale[1], Giorgio Buonanno[1,2], Luca Stabile[1]
[1]Department of Civil and Mechanical Engineering, University of Cassino and Southern Lazio, Cassino, FR, Italy
[2]International Laboratory for Air Quality and Health, Queensland University of Technology, Brisbane

Abstract

Pollutant emissions from residential heating systems represent a main concern in terms of outdoor air quality. Differently from other pollutants, sub-micron particle emission from heating systems has not yet been exhaustively characterized by the scientific literature, with limited data available, in particular, for gas-fueled boilers. In the present paper, an experimental campaign to measure the sub-micron particle number concentrations and distributions at the stack of different automatically-fed small-scale heating systems (conventional and condensing boilers fueled by natural gas and liquid petroleum gas, and pellet stoves) was performed. Based on the measured concentrations, corresponding emission rates and emission factors were also estimated. The results of the experimental campaign revealed that the highest concentrations were measured for pellet stoves (median value $>10^7$ part. m^{-3}), whereas conventional (about 1×10^6 part. m^{-3}) and condensing boilers ($<10^6$ part. m^{-3}) presented much lower concentrations. No effect of the fuel (natural gas, liquid petroleum gas) on the total concentration measured at the stack of boilers was recognized, whereas a smaller distribution mode (at 10 nm) was measured for gas-fired boilers. Because of the particle concentration values, the highest particle emission rates and factors were the pellet stove ones (median values of 2.1×10^{15} part. h^{-1} and 8.4×10^{13} part. kWh^{-1}, respectively), whereas emission rates for conventional and condensing boilers were about 5×10^{13} part. h^{-1} and 2×10^{13} part. h^{-1}, respectively.

This work has already been published in the scientific journal “Science of the Total Environment” (Caracci, E., Canale, L., Buonanno, G., & Stabile, L. (2022). Sub-micron particle number emission from residential heating systems: A comparison between conventional and condensing boilers fueled by natural gas and liquid petroleum gas, and pellet stoves. *Science of The Total Environment*, *827*, 154288.).

Analysis of the performance of an orifice plate flowmeter in transient conditions for liquid fuels

Canale Christian[1],*, Arpino Fausto[1], Cortellessa Gino[1], Ficco Giorgio[1] and Grossi Giorgio[1]

1 Department of Civil and Mechanical Engineering, University of Cassino and Southern Lazio, Via Di Biasio 43, 03043 Cassino (FR), Italy

e-mail: chrstian.canale@unicas.it

Abstract. Nowadays, the need to reduce greenhouse gas emissions all over the industrial and transport sectors is clear. The rise of new alternative fuels and their increasing use in the industrial and transport sectors have also defined needs in the flow metrology sector, because the impact of these new alternatives, energy efficiency, and emissions factors, directly depend on the quality of the measurement. The rise of the new metrological infrastructure suitable for estimating the flow under variable operating conditions has defined the need to support flow metrology with the numerical approach.

Due to the solidity of the traditional infrastructure and the consolidated methodology of the measurement aspect, a small number of CFD applications have been conducted in the flow metrology sector to support measurement campaigns. To avoid the expensive experimental campaign and to get detailed fields and fluid behaviour, numerical simulations have been introduced in the metrological sector to intensively support the flow metrology goals. The CFD application is a very effective tool through which is possible to predict fluid behaviour and avoid configuration problems of the experimental setup.

The orifice flowmeters are widely used to measure the flow rate in pipelines and the problem has been deeply investigated through experimental and numerical tests. The effect of the release coefficient of the orifice plate on the water system (Hutagalung et al. 2019) has been investigated, analyzing the relationship between the Reynolds number, $\beta\beta$ ratio, and the discharge coefficient, concluding that the discharge coefficient values depend on the $\beta\beta$ ratio and the Reynolds number, all other factors affect the overall error in measuring the release coefficient CC_{dd}[1] . The differential pressure-based measuring instruments are widely used all over the sectors, due to simplicity, reliability and low maintenance costs. The differential pressure reflects an energy loss for the systems and the performance of a single-hole over a multi-hole orifice is compared (Bikic' et al. 2022). A comparison of the two systems is presented, showing the higher efficiency of MHO systems together with a lower sensitivity to flow fluctuation [2]. A comparison between a multi-hole orifice flow meter and the empirical formula of the ISO standard 5167-2 has been conducted (Tomaszewksi et al. 2020), aiming at investigating the mass flow and pressure drop dependency. The flow coefficient determined for the six-hole orifice flow meter has been compared with the flow coefficient of the conventional single-hole with the same contraction parameters. The results of the work show that empirical formulas included in ISO standard 5167-2 can be successfully used for multi-hole configuration and for a distance of 6D or higher the results of the two configurations are the same [3]. In the present study, numerical simulations have been realized, for a three-dimensional Reynolds-averaged Navier-Stokes (RANS) combined with the Realizable K-$\varepsilon\varepsilon$ turbulence model, to analyze the turbulent flow through a single-hole, sharped edge, orifice flow meter. In the present work, in the European SAFEST 203D project, the numerical model aims at testing a wide range of temperatures, density, viscosity and Reynolds number. A comparison of the numerical results with the empirical formula value through the ISO standard 5167-2 is conducted, aiming at the validation of the numerical model. Secondarily, the performance of the orifice flowmeter numerical model is tested with a variable flow rate at the inlet section, evaluating the flow rate calculated from numerical differential pressure across the orifice section.

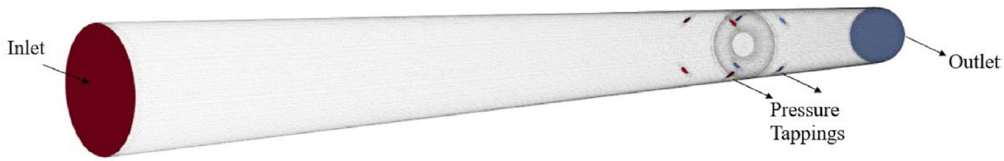

Figure 1: Computational domain of the orifice flowmeter and the main boundary patches

Keywords: *CFD, measurement, flowrate measuring, orifice flow meter, numerical simulations*

[1] S. S. Hutagalung, «Effect of Release Coefficient of Orifice Plate on Water Fluid Flow Systems», *J. Phys.: Conf. Ser.*, vol. 1230, fasc. 1, p. 012086, lug. 2019, doi: 10.1088/1742-6596/1230/1/012086.
[2] S. Bikić, M. Đurđević, M. Bukurov, e S. Tašin, «Comparison of single-hole and multi-hole orifice energy consumption», *Advances in Mechanical Engineering*, vol. 14, fasc. 1, p. 168781402210754, gen. 2022, doi: 10.1177/16878140221075461.
[3] A. Tomaszewski, T. Przybylinski, e M. Lackowski, «Experimental and Numerical Analysis of Multi-Hole Orifice Flow Meter: Investigation of the Relationship between Pressure Drop and Mass Flow Rate», *Sensors*, vol. 20, fasc. 24, p. 7281, dic. 2020, doi: 10.3390/s20247281.

Estimation of the operational limit of a spark ignition engine fueled by neat ammonia and ammonia hydrogen blend at low load conditions.

Gabriele D'Antuono[1]

[1] Department of Civil and Mechanical Engineering, University of Cassino and Southern Latium,03043
Cassino, Italy, 03043
Email: gabriele.dantuono1@unicas.it

Abstract

Carbon-free fuels, in particular ammonia and hydrogen, could play a significant role in the decarbonization of the mobility sector. In particular, ammonia, that can also be obtained starting from renewable energy sources, can be used as an hydrogen carrier. Ammonia is also a promising carbon-free fuel in combustion systems, then the behavior of internal combustion engines (ICEs) fueled by ammonia needs to be further investigated. The main disadvantage of this fuel is its low laminar flame speed especially when it is oxidized with air. On the other hand, considering a spark-ignition (SI) engine, the absence of knock phenomena could allow a performance improvement. In this work, a 15% of hydrogen by volume has been added to ammonia in order to investigate the behavior of small turbo-charged engine at low load conditions. The addition of the hydrogen to the mixture extends the exploitable region of the engine respect to neat ammonia propulsion. The efficiency icreases considering ammonia hydrogen blend. Ammonia-hydrogen blends also allow to explore a wider range engine load respect to ammonia fueling, guaranteeing compliance with some considered constraints. Running with neat ammonia the engine can reach 3000 rpm being able to vary the load very little, while for ammonia hydrogen blend engine supposed to run up to 5000 rpm.

Lift and Drag Coefficients for a NACA 63-412 near the Free Surface

Romolo Di Bernardo[1], Salman Ali[1], G. Spazzafumo[1,2] and Domenico Speranza[1]

[1]University of Cassino and Southern Lazio,
Via G. Di Biasio 43, Cassino (FR),
Italy.

[1]EnTraT s.r.l.s., Cassino (FR), Italy
Email: romolo.dibernardo@unicas.it

Index Terms

Hydrofoils, Multiphase Fluid Dynamics, CFD Simulation, NACA 63412 Wing Profile, Sustainable Boating, Control Systems, Drag Reduction.

Abstract

The marine sector is facing the need to find technology to reduce the resistance of boats to reduce gas emissions. One of the most promising is hydrofoil, which is applied for medium-sized vessels and allows a drastic decrease in drag, raising the boat's hull over the water. Despite these positive aspects, one of the challenges that the research is facing is the stability related to the behavior of the wings in a multiphase environment. In this paper, we performed simulations of a widely employed 2D wing profile in hydrofoil, the NACA 63-412, to verify how the lift and drag coefficients (respectively C_L, C_D) change with different submergences. The CFD software Star CCM+ was used to simulate the wing with a chord length (C) of 0.203 m and a Reynolds number (Re) of 159000. The simulations apply the RANS method, with k-epsilon turbulence and Volume of Fluid (VOF) model in accordance with the International Towing Tank Conference (ITTC) criteria. Results show that C_L presents a max value at the dimensionless submergence of h/C = 1.05, and as the wing gets closer to the free surface, C_D shows exponential growth. The data reported can be used in the design of hydrofoils to improve control systems and maximize the overall performance of these boats.

XIV. INTRODUCTION

The naval sector is aiming for carbon neutrality by 2050 as recommended by the International Maritime Organization [1], this effort is mandatory to enable a green transition as the shipping sector is fundamental to global trade and transport [3].

A key aspect on which research is working is to decrease the total drag of the boat and, consequentially, the fuel consumption and emissions. One of the most promising technologies that allow this goal is hydrofoil technology, applied on mid-small vessels [4]. Thanks to submerged wings, this technology can rise the hull from the surface of the sea and in some cases can half the drag of the boat with respect to a similar displacement or planing hull [6]. Against these positive effects, there are several problems related to this kind of boat still open to innovative solutions [7]. One of the most important is stability: this happens because the wings work in water very close to the free surface and, in addition to cavitation or ventilation [8], the lift and drag could change due the proximity of the less dense fluid (air).

In 1982 Duncan was one of the first to investigate the behaviour of a NACA 0012 close to the free surface [9]. Based on this experiment, after years, numerical analyses on NACA 0012 have verified that the lift coefficients and drag coefficients (respectively C_L and C_D) change with the submergence of the 2D hydrofoil [10].

To better understand this phenomenon and to broaden knowledge in the sector, the following work presents the methodology used to evaluate the hydrodynamic behaviour of one of the most used airfoils in hydrofoil projects: the NACA 63-412. Considering h as the submergence and C as the chord of the airfoil, the results were reported in terms of lift and drag coefficients (C_L and C_D) with respect the dimensionless submergence h/C under the hydrodynamic Duncan's experiment condition: Reynolds (Re) 159000, fresh water and 5° angle of attack for the airfoil.

The analyses were performed using the Reynolds Average Naviers-Stokes (RANS) equation solved by the STAR CCM+ by Siemens computational fluid dynamic (CFD) software, the Volume of Fluid (VOF) Wave method was employed to simulate the interaction between air and water and k-ε to model the turbulence.

I. METHODS

To facilitate comparison with other experiments or numerical analyses in the literature, this study was conducted validating the numerical model and replacing the NACA 0012 airfoil with the NACA 63-412 to evaluate its behaviour in terms of hydrodynamic coefficients (C_L and C_D) and free surface deformation (wave-cut). The C_L and C_D coefficients are defined below in equations (1, 2):

$$C_L = \frac{2L}{\rho v^2 S} \tag{1}$$

$$C_D = \frac{2D}{\rho v^2 S} \tag{2}$$

where ρ is the density, v is the speed of the fluid, S is the surface of the wing, L and D are respectively the lift and drag forces.
The VOF Wave method allows to simulate a virtual towing tank and in accordance with ITTC CFD requirements [11], we created a pseudo two-dimensional model to simulate the water-air interaction.

The airfoil leading edge was positioned within the reference system in accord to the literature to evaluate its submergence. The dimensions of the domain and geometry parameters used in the simulations are reported in Fig.1.

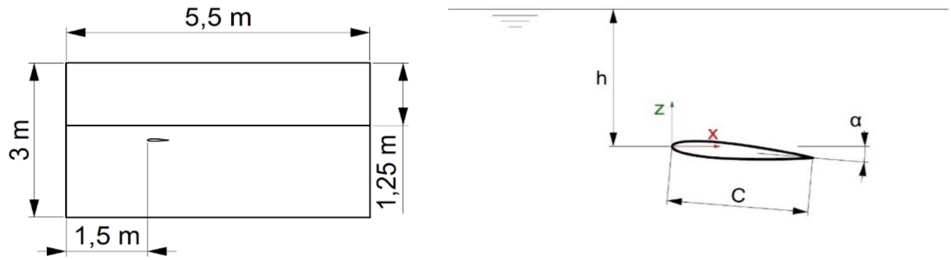

Figure 1. On the left side
the domain used in the simulations, on the right side the 2d.

A. Numerical Model

The Star CCM+ CFD software was used to solve numerically the evolution of incompressible viscous flow: in this case, we used the Reynolds Averaged Navier–Stokes (RANS) method using the Reynolds stress $-\rho\underline{u_i' u_j'}$. The governing equation of the flow field averaged for mass conservation and momentum are solved numerically. More information is described in Star CCM+ documentation [12].

On top and to the bottom of the domain we imposed the inlet condition to create a pseudo-B.C. that simulate the behaviour of a towing tank simulating the direction of the fluid in accord to the VOF Wave method.

In our work, we made an unstructured mesh refined only in the areas where necessary, with a total number of cells equal to 550 k and a max size of 0.01 m.

The results obtained using the mesh were compared with the literature [14] in terms of C_L and deformation of wave-cut verifying the accuracy of the numerical model.

In total we performed 10 simulations, to ensure the correct trend of the curve. The range of submersion simulated was from h/C = 0.8 to h/C = 1.8, one additional simulation was performed in a submergence h/C > 5 [15] to compare the results with the undisturbed condition.

II. Results

A. Lift coefficient – submergence curve

The lift coefficient – submergence curve and the percentage variation with respect to the undisturbed condition curves were reported in Fig. 2.

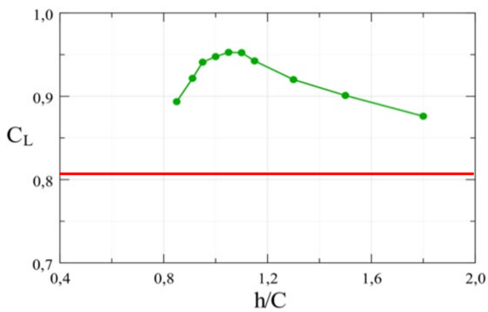

Figure 2. Lift coefficient – submergence curve for NACA 63-412 in Duncan conditions. In red undistrubed conditions.

Decreasing submergence of the hydrofoil (going to right-to-left in the diagram) the curves present a characteristic grow-peak-decrease trend, similar to the NACA 0012 case. For the NACA 63-412 the max value of $C_L = 0.952$ is measured at the h/C = 1.05.

B. C_D – h/C curve

In the same way as the lift coefficient, the C_D -h/C and the percentage variation with respect to the undisturbed condition curves were reported in Fig. 3.

In this case, C_D coefficient increases exponentially if the NACA 63-412 comes close to the free surface. In the condition of max C_L and submergence of h/C = 1.05, the drag coefficient is measured as $C_D = 0.0412$.

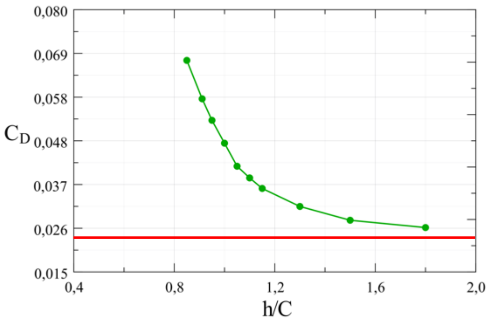

Figure 3. Lift coefficient – submergence curve for NACA 63-412 in Ducan conditions.
In red the value for the undisturbed condition.

III. Conclusions

The presented work expands the knowledge regarding the behaviour of the wings near the free surface presenting the methodology used to investigate the variation of the lift and drag coefficients for the NACA 63-412 at different submergences.

The lift and drag coefficient curves were obtained as a function of the dimensionless immersion on the hydrofoil chord.

Starting from a deep immersion condition and going to the free surface, the curve representing the lift coefficient is characterized by a grow-peak-decrease, with a peak of $C_L = 0.9523$ measured at h/C = 1.05. After this max value, the curve of lift coefficient rapidly decreases to the free surface.

In the case of the drag coefficient, its curve increases exponentially up to the free surface with a $C_D = 0.0412$ value in the condition of max C_L.

A future development regards the towing tank test of the NACA 63-412 2D hydrofoil in the same conditions analysed in the paper to verify the simulations also in an experimental way. Once the data has been verified, they can be used in the design of hydrofoil or to optimize the response of the automatic control system to improve the stability and the safety of the boats.

References

[1] International Maritime Organization - 2023 IMO Strategy on Reduction of GHG Emissions from Ships - https://www.imo.org/en/OurWork/Environment/Pages/2023-IMO-Strategy-on-Reduction-of-GHG-Emissions-

from-Ships.aspx
[2] Carić, H., Mackelworth, P.: Cruise tourism environmental impacts – The perspective from the Adriatic Sea. Ocean & Coastal Management. 102. 350-363 (2014). 10.1016/j.ocecoaman.2014.09.008
[3] Speranza, D., Di Bernardo, R., Martorelli, M., Gloria, A., Pensa, C., Papa, S.: Basic Design and Virtual Prototyping of a Hydrofoil Hybrid Daysailer. In: Gerbino, S., Lanzotti, A., Martorelli, M., Mirálbes Buil, R., Rizzi, C., Roucoules, L. (eds), Advances on Mechanics, Design Engineering and Manufacturing IV JCM2022, pp. 122-134. Springer (2023).
[4] Miranda S.: Architettura Navale. Elementi di dinamica della nave. Liguori, Napoli (2014)
[5] Speranza, D., Papa, S., Pensa, C., Di Bernardo, R.: Hydrofoil Technology: Current Applications and Future Developments for Sustainable Boating. ADM2023 (2023) Springer.
[6] M. Basic, B. Šarić, J. Basic, B. Blagojević, CFD Analysis of Surface-Piercing Hydrofoil Ventilation Inception, XXII Theory and Practice of Shipbuilding, Trogir Croatia, (2016).
[7] Brizzolara S., Federici A.: Super-Cavitating Profiles for Ultra High Speed Hydrofoils: a Hybrid CFD Design ApproachIX. HSMV Naples 25 - 27 May (2011).
[8] J. H. Duncan, The breaking and non-breaking wave resistance of a two-dimensional hydrofoil, J. Fluid Mech, vol. 126, pp. 507-520, (1983).
[9] International Towing Tank Conference (ITTC) – 7.5-03-01-02, Recommended Procedures: Uncertainty Analysis in CFD, Guidelines for RANS Codes.
[10] Siemens Star CCM+, Official documentation.
[11] Pernod, L., Matthieu, S., Jeroen, W., Benoit, A., Patrick, B. Free-Surface Effects on Two-Dimensional Hydrofoils by RANS-VOF Simulations (2022). 10.5957/CSYS-2022-012.
[12] Xing, T., Matveev, K.I. & Wheeler, M.P. Numerical study of high-lift hydrofoil near free surface at moderate Froude number. J Hydrodyn 32, 44–53 (2020). https://doi.org/10.1007/s42241-019-0095-0
[13] Md. Hoque A., Md. Karim M., Rahman A. Simulation of Water Wave Generated by Shallowly Submerged Asymmetric Hydrofoil, Procedia Engineering, Volume 194, 2017, Pages 38-43, ISSN 1877-7058, https://doi.org/10.1016/j.proeng.2017.08.114.

Optimizing Industrial Property Valorisation through Open Innovation: A Comprehensive Status Report

1st Antonio Giovanni Yury Di Russo
dept. Civil and Mechanical Engineering
Cassino, Italy
antoniogiovanniyury.dirusso1@unicas.it

Abstract

This article presents a comprehensive status report on a three-year PhD project focused on the intersection of Open Innovation (OI) and Intellectual Property (IP) Strategy. The study aims to develop a model that optimizes the valorisation of industrial property through OI and maximizes the effectiveness of OI initiatives through IP Strategy. The paper incorporates a literature review that highlights the gaps and challenges in the OI-IP relationship and presents a synthesized framework. It also includes findings from the research project, which utilized qualitative and quantitative research methods to identify overlooked factors and understand the experiences of individuals involved in OI projects. Additionally, the paper discusses insights from a scientific article published during the PhD and analyses the integration of the research project, literature review, and article. The article concludes with a progress report, future directions, and the potential practical applications of the developed model. This status report provides valuable insights into the evolving nature of the PhD project and its contributions to the field of OI and IP Strategy.

I. INTRODUCTION

Open Innovation (OI) is a paradigm that has gained significant scholarly and managerial attention due to its potential to promote knowledge flows and industrial property valorisation [1]–[3]. Unlike traditional closed innovation models, OI emphasizes the strategic exchange of knowledge and ideas with external partners, enabling organizations to access diverse expertise, resources, and technologies [4], [5]. By embracing OI, companies can accelerate innovation processes, expand their market reach, and effectively utilize their industrial property assets [6]. Through collaborations, licensing agreements, and joint ventures, organizations can tap into external innovation sources, enhancing their competitive advantage and maximizing the value of their intellectual property [7], [8]. Hence, OI holds substantial significance in facilitating knowledge flows and driving industrial property valorisation, enabling organizations to thrive in today's dynamic business environment.

The primary objective of this research project is to develop a model for optimizing industrial property valorisation through OI and Intellectual Property (IP) Strategy. OI, as proposed by Chesbrough [9], promotes the exchange of knowledge flows to accelerate innovation and expand markets for external use of innovation. However, many companies struggle with effectively utilizing their valuable patents and lack strategies in IP Strategy and Intellectual Property Protection, resulting in underutilization of industrial property [2], [5]. This research aims to address these challenges by developing a model that balances IP protection and Open Innovation to maximize the valorisation of industrial property and enhance the effectiveness of OI initiatives [6]. The model will incorporate strategic tools that enable companies and their partners to optimize industrial property valorisation through OI, thereby facilitating growth and success [10]. By integrating insights from the literature review and empirical research, this study aims to contribute to the advancement of OI and IP Strategy, providing practical guidance for companies in leveraging their intellectual property for innovation and market expansion.

The research project is planned to be conducted over a three-year timeline, encompassing a comprehensive investigation into optimizing the valorisation of industrial property through OI and IP Strategy. The timeline will include various stages and methodologies to achieve the research objectives. The methodologies employed in this study will comprise literature analysis, questionnaires, and interviews with key stakeholders in the field of IP and OI. These methods have been recognized as valuable tools for gathering relevant data, exploring insights, and understanding the experiences of individuals involved in OI projects [3], [8], [11], [12]. Through the integration of quantitative and qualitative research methods, this study aims to identify factors overlooked in previous studies and develop a model that provides strategic tools for companies to optimize industrial property valorisation and enhance the effectiveness of OI initiatives [10].

II. Theoretical Background

The literature review revealed several key findings regarding the relationship between OI and IP. OI, characterized by knowledge exchange and external collaboration, has the potential to leverage IP for innovation and market expansion. IP protection mechanisms play a vital role in facilitating knowledge sharing in an OI context, enabling companies with valuable patents to bring innovative products to market and promoting collaboration between companies lacking R&D resources and external inventors. However, the literature also highlighted challenges in strategic decision-making regarding IP and OI, with some companies adopting defensive behaviors and hindering innovation. The review identified a lack of clear transition from IP-focused to OI-focused strategies, calling for a comprehensive framework that synthesizes the literature. The findings emphasize the need to balance IP protection and OI to maximize the valorisation of industrial property and the effectiveness of OI initiatives [3], [6], [10], [13].

Existing literature on IP strategy in OI projects reveals several gaps and challenges that need to be addressed. Some studies have highlighted the lack of best practices or regulations for appropriating ideas from OI projects, leading to defensive behaviors and hindering innovation [10]. The fragmented nature of the literature creates a need for a clear transition from IP-focused to OI-focused strategies [14]. Furthermore, the impact of external factors such as industry and the external environment on OI strategies remains underexplored [15]. Individual factors, including perceived risks, tensions during technology transfers, and employee challenges, are also areas that require further investigation [16], [17]. Moreover, tensions related to knowledge ambiguity, fear of knowledge leaks, and the risk of revealing knowledge in OI projects have not been fully examined in the literature [18], [19]. To address these gaps, this study aims to develop a comprehensive framework synthesizing the literature on IP strategy and OI, contributing to a better understanding of the challenges and opportunities associated with IP management in OI projects.

A comprehensive framework has been synthesized from the literature, addressing the relationship between Open Innovation (OI) and IP and categorizing strategies [5], [9], [20]–[24]. This framework provides a structured overview of the OI-IP relationship, offering insights into how organizations can effectively navigate the tensions between knowledge sharing and protection. The framework categorizes strategies as IP Disassembly, IP Valorisation, Technology Transfer, Knowledge Exploitation, and Value Capture, capturing the diverse approaches adopted by organizations to balance IP protection and OI initiatives [22], [25]–[27]. By classifying strategies within these categories, the framework offers a valuable tool for organizations to analyse, understand, and strategically align their OI and IP practices to maximize the effectiveness of their innovation efforts while safeguarding their intellectual property assets.

III. Research Overview

The research project aims to address the gaps identified in the literature review regarding the relationship between OI and IP. As highlighted in the literature review [2], [3], [5], there is a lack of comprehensive frameworks and best practices for effectively integrating IP Strategy into OI initiatives. Building upon the synthesized framework proposed in the literature review [23], the research project seeks to develop a model that optimizes the valorisation of industrial property through OI and maximizes the effectiveness of OI initiatives through IP Strategy. By conducting thorough literature analysis, questionnaires, and interviews with key stakeholders in IP and OI, this research project aims to identify overlooked factors and understand the experiences of individuals involved in OI projects. The integration of the research project with the literature review will provide valuable insights and contribute to closing the existing gaps in knowledge.

The research methodology employed in this study encompasses various techniques to explore the relationship between OI and IP in the context of industrial property valorisation. A comprehensive literature analysis was conducted to gain a thorough understanding of the existing knowledge on OI and IP [2], [3], [5]. This analysis served as the foundation for developing research questions and identifying gaps in the literature. To gather primary data, questionnaires were administered to professionals involved in IP and OI initiatives, allowing for the collection of quantitative data on their experiences and perspectives. In addition, interviews were conducted with key stakeholders, including industry experts, IP managers, and OI practitioners, to obtain qualitative insights into their practices and challenges [8], [11], [12]. The combination of literature analysis, questionnaires, and interviews enabled a comprehensive investigation into the factors influencing the effectiveness of IP Strategy in OI projects and contributed to the development of a strategic model for industrial property valorisation through OI initiatives.

The expected outcome of the research project is the development of a strategic model for industrial property valorisation and effective OI initiatives. This model aims to address the underutilization of industrial property by optimizing its valorisation through OI and maximizing the effectiveness of OI initiatives through IP Strategy. By leveraging knowledge flows and collaborations, the model seeks to enable companies to exploit valuable patents that they possess but cannot fully utilize, as well as provide opportunities for companies lacking R&D resources to engage with external inventors. The strategic model is anticipated to offer a balanced approach that combines IP protection with OI, enabling companies and their partners to grow and thrive in the dynamic innovation landscape. It is envisioned that the model will incorporate key indicators of industrial property quantity, progress of OI initiatives, and numerical representations of IP Strategy, and provide strategic tools for decision-making, optimization, and integration with other models. The development of this model will contribute to the existing literature on OI and IP, offering practical implications for companies, such as Leonardo spa, to enhance their industrial property valorisation and advance their business analyses.

IV. Partial Findings

The research project has yielded significant findings and insights into the challenges and opportunities associated with industrial property valorisation through OI. Through literature analysis, questionnaires, and interviews with key stakeholders, the study has identified the lack of knowledge and strategies in IP Strategy and Intellectual Property Protection among many companies, resulting in the underutilization of valuable patents. Furthermore, the absence of best practices or regulations for appropriating ideas from OI projects often leads to defensive behaviours, hindering innovation and favouring closed paradigms. These findings reinforce the need for a model that optimizes industrial property valorisation through OI and maximizes the effectiveness of OI initiatives through IP Strategy, aligning with the insights provided in the literature review [2], [10].

The research project findings align and contribute to the existing insights from the literature review and the scientific article. The literature review highlighted the tension between knowledge sharing and protection in the context of OI and IP, and the research project findings further support this notion by demonstrating how companies can leverage OI to maximize the valorisation of their industrial property. Additionally, the literature review emphasized the lack of best practices or regulations for appropriating ideas from OI projects, hindering innovation. The research project findings address this gap by developing a model that optimizes IP Strategy in OI initiatives, balancing IP protection and OI effectiveness. Although not directly related to social media communication, the research project findings align with the challenges presented in the scientific article by providing strategic tools for industrial property valorisation and effective OI initiatives.

The progress made in the current study can be evaluated based on the data collection, analysis, and the development of insights. Through meticulous data collection efforts involving literature analysis, questionnaires, and interviews with key stakeholders, the research project has gained a comprehensive understanding of the factors overlooked in previous studies and captured the experiences of individuals involved in OI projects. The collected data has been analysed using quantitative and qualitative research methods, enabling the identification of key insights and patterns. The progress made in terms of data collection, analysis, and the development of insights serves as a solid foundation for the ongoing research, shaping its evolution and contributing to the advancement of the field.

V. OI and Marketing

The progress made in this study has been significant in terms of data collection, analysis, and the development of the proposed model. Data collection involved a comprehensive approach, incorporating literature analysis, questionnaires, and interviews with key stakeholders in the field of IP and OI. This multi-method approach allowed for a rich and diverse dataset, capturing a wide range of perspectives and experiences related to IP Strategy and OI. The collected data was rigorously analysed using both quantitative and qualitative research methods, enabling a thorough exploration of the factors overlooked in previous studies and a deeper understanding of the experiences of individuals involved in OI projects. Through this analysis, several key insights have emerged, shedding light on the challenges, opportunities, and best practices in IP Strategy and the effective implementation of OI initiatives. Building upon these findings, the development of the proposed model has been underway, aiming to optimize the valorisation of industrial property through OI and maximize the effectiveness of OI initiatives through IP Strategy. The model's design and refinement have been informed by the analysed data and insights gained from the literature review, ensuring its alignment with the existing knowledge base. The progress made in data collection, analysis, and model development lays a solid foundation for advancing the research and contributes to the growing body of literature on OI and IP Strategy.

The scientific article published during the PhD project, titled "Tweeting Open Innovation," provides valuable insights relevant to the ongoing research project. The article explores the role of Twitter in disseminating OI information. By employing semantic analysis of tweets and identifying OI project categories, the study examines the specificity and transparency of OI information shared on Twitter. The findings shed light on the challenges of conveying accurate and comprehensive OI information on Twitter and offer recommendations to enhance tweet content and improve the quality of OI information. This article's relevance to the research project lies in its focus on effective communication of OI information, which is crucial for maximizing the effectiveness of OI initiatives and aligning it with the developed model for industrial property valorisation.

Several insights and methodologies from the latter article have significantly influenced the ongoing research and its evolution. This article shed light on the role of OI initiatives as a marketing tool to enhance brand awareness and likability. This perspective broadened the understanding of the multifaceted nature of OI and its potential impact on the research project. Moreover, the article applied institutional theory [28], [29] to analyse the coercive, mimetic, and normative processes that shape organizations' adoption of OI practices. This theoretical framework has been instrumental in understanding the drivers and challenges influencing the implementation of OI initiatives in practice. Building upon these insights, the ongoing research project has incorporated a more comprehensive approach to analysing the specificity and transparency of OI information shared on social media platforms, including Twitter. The methodologies employed in the article, such as semantic analysis of tweets and categorization of OI project types, have been adapted and integrated into the research project to enhance the quality and effectiveness of communication in OI initiatives. The article's findings have provided valuable guidance for refining the research methodology and aligning the research project with real-world practices in OI communication and branding strategies.

VI. Integration and Evolution

The integration of the research project, literature review, and scientific article provides valuable insights into the evolution of the PhD project and its alignment with existing knowledge in the field. The literature review [2], [3], [5] highlighted the relationship between OI and IP, identified gaps in understanding, and presented a comprehensive framework synthesizing the literature [1], [30]. The research project aimed to develop a model for optimizing industrial property valorisation through OI and IP Strategy. The findings obtained from the research project were analysed in light of the literature review and the insights provided by the scientific article [3],

[31], [32]. This integration allowed for a comprehensive evaluation of the project's progress, identification of alignment or divergence with existing knowledge, and potential refinements to the research plan. The integrated knowledge has contributed to the ongoing evolution of the research project, enhancing its theoretical and practical significance within the context of OI and IP Strategy.

The research project has undergone significant evolution over time, informed by the comprehensive literature review and insights derived from the published scientific article. The literature review [2], [3], [5] highlighted the complex relationship between OI and IP, emphasizing the need for strategic IP protection and effective IP Strategy in OI initiatives. Furthermore, the literature review identified gaps in knowledge regarding the integration of IP and OI strategies. Informed by these insights, the research project aimed to develop a model that optimizes industrial property valorisation through OI while maximizing the effectiveness of OI initiatives through IP Strategy. The scientific article focused on the challenges of conveying accurate and comprehensive OI information on social media platforms, such as Twitter, and offered recommendations to enhance communication quality. Incorporating these findings, the research project adjusted its data collection methods and expanded the analysis to include social media platforms, aiming to explore effective communication strategies within the context of OI. Thus, the research project has evolved over time, incorporating insights from the literature review and the scientific article to enhance its methodology and address emerging aspects of OI and IP integration.

Considering the integrated knowledge derived from the research project, literature review, and scientific article, several modifications and adaptations have been made to the original research plan. Firstly, the literature review shed light on the importance of considering external factors, such as industry and the external environment, in shaping open innovation [15], [33]. Therefore, the research project has incorporated a deeper analysis of these factors to provide a more comprehensive understanding of their influence on open innovation initiatives. Additionally, the scientific article highlighted the challenges of conveying accurate and comprehensive open innovation information on Twitter. As a result, the research project has expanded its data collection methods to include an exploration of other social media platforms to capture a more diverse range of information sources and enhance the effectiveness of communication strategies. These modifications align the research project with the evolving understanding of open innovation dynamics and contribute to a more robust and holistic investigation of the research problem.

VII. Future Research

The current status of the project demonstrates significant progress in achieving its objectives and milestones. In terms of milestones, comprehensive literature analysis has been conducted, encompassing studies by Dahlander and Gann [2], Grimaldi et al. [5], and Pedersen [3], among others, to establish a solid theoretical foundation. Data collection has been successfully executed through the implementation of questionnaires and interviews involving key stakeholders in IP and Open Innovation. The gathered data provides valuable insights into the experiences of individuals involved in Open Innovation projects [16], [17], [34]. Additionally, quantitative and qualitative research methods have been employed to identify factors overlooked in previous studies and to uncover new dimensions in the relationship between IP Strategy and Open Innovation. These analyses align with the research conducted by Chesbrough [4], [21] and European Patent Office and European Union Intellectual Property Office [6], further deepening our understanding of the subject matter. The collected data and analyses conducted thus far form a solid foundation for the subsequent stages of the research project, laying the groundwork for the development of a model that optimizes industrial property valorisation through Open Innovation and IP Strategy.

The findings of this research project hold significant implications for industrial property valorisation and OI initiatives. The developed model for optimizing industrial property valorisation through OI and IP Strategy offers strategic tools that can enable companies to maximize the value of their intellectual assets and enhance the effectiveness of OI initiatives. By balancing IP protection and OI, companies can leverage their valuable patents and collaborate with external inventors, leading to accelerated innovation and expanded market opportunities. The model's ability to integrate IP Strategy with OI practices aligns with the growing interest in the relationship between OI and IP [2], [3], [5]. It provides a framework that enables companies to navigate the "OI paradox" by facilitating knowledge exchange while protecting intellectual property [1], [20], [30]. Thus, the research outcomes contribute to the existing literature by addressing the lack of best practices and regulations for appropriating ideas from OI projects, thereby promoting innovation and favouring open paradigms.

Moving forward, several important directions and next steps have been identified for the research project based on the integrated knowledge from the literature review and the scientific article. Firstly, additional data collection and analysis will be conducted to further validate and refine the developed model for industrial property valorisation through OI and IP Strategy. This will involve obtaining a more comprehensive set of data, including indicators of industrial property quantity, the progress of OI initiatives, and numerical representations of IP Strategy. Furthermore, the integration of machine learning-driven dashboards into the model will be explored to enhance its analytical capabilities and provide real-time insights. Additionally, collaborations with industry partners and stakeholders will be initiated to gather practical feedback and implement the model within their organizations. Finally, the research project aims to expand its scope by investigating the applicability of the developed model to other organizations and industries, beyond the initial focus on Leonardo spa. These future directions and adjustments will contribute to the ongoing evolution and refinement of the research project, ensuring its continued relevance and impact in the field of OI and IP Strategy.

VIII. CONCLUSIONS

The research project has made significant progress in investigating the optimization of industrial property valorisation through OI and IP Strategy. Through extensive literature analysis, questionnaires, and interviews with key stakeholders, several key findings have emerged. Firstly, the literature review highlighted the tension between sharing knowledge and protecting it in the OI-IP context, leading to the "OI paradox." The research project aims to address this paradox by developing a model that balances IP protection and OI to maximize the valorisation of industrial property and the effectiveness of OI initiatives. Secondly, the integration of insights from a scientific article emphasized the importance of transparency and specificity in conveying accurate OI information on social media platforms. The ongoing research project has incorporated these insights to enhance the quality and effectiveness of OI information dissemination on Twitter. The project is currently in the data collection and analysis phase, examining factors overlooked in previous studies and understanding the experiences of individuals involved in OI projects. The research project is on track and progressing towards the development of a comprehensive model that provides strategic tools for organizations to optimize industrial property valorisation and thrive in an OI ecosystem.

The research project makes significant contributions to the field of OI and IP Strategy. By developing a model that optimizes industrial property valorisation through OI and maximizes the effectiveness of OI initiatives through IP Strategy, this research fills a critical gap in the literature. The proposed model provides strategic tools for companies and their partners to grow and thrive in the context of OI. It offers a balanced approach that considers both IP protection and OI collaboration, thereby maximizing the value of industrial property and fostering innovation. The integration of OI and IP Strategy in the model aligns with the growing interest in understanding the relationship between these two areas [2], [5]. By addressing the lack of best practices and regulations in appropriating ideas from OI projects, the research project contributes to overcoming the defensive behaviors and closed paradigms that hinder innovation [3]. The model's analytical nature allows for optimization within constraints and integration with other models, indicating its potential to advance the field through machine learning-driven dashboards [6]. Overall, this research project significantly enhances the understanding of OI and IP Strategy, providing valuable insights for organizations aiming to leverage their industrial property and engage in effective OI initiatives.

The developed model for industrial property valorisation in the context of OI has significant practical applications and implications for organizations. By optimizing the utilization of industrial property through OI and integrating IP Strategy, the model offers strategic tools that can benefit companies and their partners. Firstly, it allows companies with valuable patents to unlock their untapped potential and bring innovative products to market through collaborative OI initiatives [6]. Secondly, for companies lacking internal R&D resources, the model enables them to leverage external inventors and collaborators to utilize their patents, thereby reducing time-to-market [8], [11], [12]. Furthermore, the model contributes to addressing the lack of best practices and regulations for appropriating ideas from OI projects, mitigating defensive behaviours, and promoting a more open and innovation-driven approach [10]. Overall, the developed model holds promise for organizations seeking to optimize the valorisation of their industrial property and enhance the effectiveness of their OI initiatives, ultimately fostering innovation and driving growth.

REFERENCES

[1] H. W. Chesbrough, *Open innovation: The new imperative for creating and profiting from technology*. Harvard Business Press, 2006.

[2] L. Dahlander and D. M. Gann, “How open is innovation?,” *Res. Policy*, vol. 39, no. 6, pp. 699–709, 2010, doi: 10.1016/j.respol.2010.01.013.

[3] K. Pedersen, “What can open innovation be used for and how does it create value?,” *Gov. Inf. Q.*, vol. 37, no. 2, Apr. 2020, doi: 10.1016/j.giq.2020.101459.

[4] H. Chesbrough, “The logic of open innovation: Managing intellectual property,” *Calif. Manage. Rev.*, vol. 45, no. 3, pp. 33–58, 2003, doi: 10.2307/41166175.

[5] M. Grimaldi, V. Corvello, A. De Mauro, and E. Scarmozzino, “A systematic literature review on intangible assets and open innovation,” *Knowl. Manag. Res. Pract.*, vol. 15, no. 1, pp. 90–100, Feb. 2017, doi: 10.1057/s41275-016-0041-7.

[6] European Patent Office and European Union Intellectual Property Office, “IPR-intensive industries and economic performance in the European Union,” *EPO Rep.*, no. September, 2019, [Online]. Available: http://documents.epo.org/projects/babylon/eponet.nsf/0/9208BDA62793D113C125847A00500CAA/$File/IPR-intensive_industries_and_economic_performance_in_the_EU_2019_en.pdf.

[7] H. Chesbrough and E. L. Chen, “Recovering abandoned compounds through expanded external IP licensing,” *Calif. Manage. Rev.*, vol. 55, no. 4, pp. 83–101, 2013, doi: 10.1525/cmr.2013.55.4.83.

[8] R. Lorenz, C. Benninghaus, T. Friedli, and T. H. Netland, “Digitization of manufacturing: the role of external search,” Int. J. Oper. Prod. Manag., vol. 40, no. 7–8, pp. 1129–1152, May 2020, doi: 10.1108/IJOPM-06-2019-0498.

[9] H. W. Chesbrough, *Open Innovation: The New Imperative for Creating and Profiting from Technology*. Boston, MA: Harvard Business School, 2003.

[10] M. Grimaldi, M. Greco, and L. Cricelli, “A framework of intellectual property protection strategies and open innovation,” *J. Bus. Res.*, vol. 123, pp. 156–164, 2021, doi: 10.1016/j.jbusres.2020.09.043.

[11] O. Alexy, P. Criscuolo, and A. J. Salter, “Does IP strategy have to cripple open innovation?,” *MIT Sloan Manag. Rev.*, vol. 51, no. 1, pp. 71–77, 2009, doi: 10.1177/1049731507302265.

[12] T. H. Clausen, T. Korneliussen, and E. L. Madsen, “Modes of innovation, resources and their influence on product innovation: Empirical evidence from R&D active firms in Norway,” *Technovation*, vol. 33, no. 6–7, pp. 225–233, 2013, doi: 10.1016/j.technovation.2013.02.002.

[13] H. W. Chesbrough, “Open Innovation: A New Paradigm for Understanding Industrial Innovation,” in *Open innovation: researching a new paradigm*, H. W. Chesbrough, W. Vanhaverbeke, and J. West, Eds. Oxford: Oxford University Press, 2006, pp. 1–19.

[14] M. Grimaldi, M. Greco, and L. Cricelli, “A framework of intellectual property protection strategies and open innovation,” *J. Bus. Res.*, vol. 123, pp. 156–164, Feb. 2020, doi: 10.1016/j.jbusres.2020.09.043.

[15] N. Kazemargi, C. Cerruti, and A. Appolloni, “Adopting open innovation in supply networks,” *Int. J. Manag. Enterp. Dev.*, vol. 15, no. 2–3, pp. 174–190, 2016, doi: 10.1504/IJMED.2016.078216.

[16] A. Salter, P. Criscuolo, and A. L. J. Ter Wal, “Coping with Open Innovation: Responding to the Challenges of External Engagement in R&D,” *Calif. Manage. Rev.*, vol. 56, no. 2, pp. 77–94, Feb. 2014, doi: 10.1525/cmr.2014.56.2.77.

[17] P. Ritala and I. Stefan, “A paradox within the paradox of openness: The knowledge leveraging conundrum in open innovation,” *Ind. Mark. Manag.*, vol. 93, pp. 281–292, 2021, doi: 10.1016/j.indmarman.2021.01.011.

[18] P. Trkman and K. C. Desouza, “Knowledge risks in organizational networks: An exploratory framework,” *J. Strateg. Inf. Syst.*, vol. 21, no. 1, pp. 1–17, 2012, doi: 10.1016/j.jsis.2011.11.001.

[19] C. Marullo, A. Di Minin, C. De Marco, and A. Piccaluga, “Is open innovation always the best for SMEs? An exploratory analysis at the project level,” *Creat. Innov. Manag.*, vol. 29, no. 2, pp. 209–223, 2020, doi: 10.1111/caim.12375.

[20] M. Bogers, “The open innovation paradox: Knowledge sharing and protection in R&D collaborations,” *Eur.*

J. Innov. Manag., vol. 14, no. 1, pp. 93–117, 2011, doi: 10.1108/14601061111104715.

[21] H. Chesbrough, "Open Innovation: Where We've Been and Where We're Going," *Res. Manag.*, vol. 55, no. 4, pp. 20–27, Jul. 2012, doi: 10.5437/08956308X5504085.

[22] H. W. Chesbrough and E. L. Chen, "Recovering abandoned compounds through expanded external IP licensing," *Calif. Manage. Rev.*, vol. 55, no. 4, pp. 83–101, 2013, doi: 10.1525/cmr.2013.55.4.83.

[23] O. Granstrand and M. Holgersson, "Managing the Intellectual Property Disassembly Problem," *Calif. Manage. Rev.*, vol. 55, no. 4, pp. 184–210, Jul. 2013, doi: 10.1525/cmr.2013.55.4.184.

[24] M. Holgersson and O. Granstrand, "Patenting motives, technology strategies, and open innovation," *Manag. Decis.*, vol. 55, no. 6, pp. 1265–1284, Jul. 2017, doi: 10.1108/MD-04-2016-0233.

[25] S. Anokhin, J. Wincent, and J. Frishammar, "A conceptual framework for misfit technology commercialization," *Technol. Forecast. Soc. Change*, vol. 78, no. 6, pp. 1060–1071, 2011, doi: 10.1016/j.techfore.2010.12.005.

[26] M. Bianchi and J. Lejarraga, "Learning to license technology: the role of experience and workforce's skills in Spanish manufacturing firms," *R D Manag.*, vol. 46, pp. 691–705, 2016, doi: 10.1111/radm.12211.

[27] J. Pénin and J. P. Wack, "Research tool patents and free-libre biotechnology: A suggested unified framework," *Res. Policy*, vol. 37, no. 10, pp. 1909–1921, 2008, doi: 10.1016/j.respol.2008.07.012.

[28] P. J. DiMaggio and W. W. Powell, "The Iron Cage Revisited: Institutional Isomorphism and Collective Rationality in Organizational Fields," *Am. Sociol. Rev.*, vol. 48, no. 2, p. 147, Apr. 1983, doi: 10.2307/2095101.

[29] M. S. Mizruchi and L. C. Fein, "The Social Construction of Organizational Knowledge: A Study of the Uses of Coercive, Mimetic, and Normative Isomorphism," *Adm. Sci. Q.*, vol. 44, no. 4, p. 653, 1999, doi: 10.2307/2667051.

[30] WIPO, "What is Intellectual property?," 2020. [Online]. Available: https://www.wipo.int/about-ip/en/.

[31] A. Kutvonen, "Strategic application of outbound open innovation," *Eur. J. Innov. Manag.*, vol. 14, no. 4, pp. 460–474, 2011, doi: 10.1108/14601061111174916.

[32] M. Hossain, K. M. Z. Islam, M. A. Sayeed, and I. Kauranen, "A comprehensive review of open innovation literature," *J. Sci. Technol. Policy Manag.*, vol. 7, no. 1, pp. 2–25, 2016, [Online]. Available: http://www.emeraldinsight.com/doi/10.1108/JSTPM-02-2015-0009.

[33] S. A. A. Tipu, "Open innovation process in developing-country manufacturing organisations: Extending the Stage-Gate model," *Int. J. Bus. Innov. Res.*, vol. 6, no. 3, pp. 355–378, 2012, doi: 10.1504/IJBIR.2012.046632.

[34] K. Abhari, E. J. Davidson, and B. Xiao, "A risk worth taking? The effects of risk and prior experience on co-innovation participation," *Internet Res.*, vol. 28, no. 3, pp. 804–828, 2018, doi: 10.1108/IntR-05-2017-0196.

Dynamic Tensile Extrusion response of Al2024-T351

Mirko Sgambetterra[1,2], Gabriel Testa[2], Gianluca Iannitti[2] and Nicola Bonora[2]

[1]Aeronautica Militare – Aeronautical and Space Test Division

[2]Università degli studi di Cassino e del Lazio Meridionale - Department of Civil and Mechanical Engineering

mirko.sgambetterra@unicas.it

Abstract

Al 2024-T351 is known to exhibit a significant shear effect on ductility. The dynamic tensile extrusion (DTE) test can probe material response under pressure and shear at large strain and high strain rates. In this work, DTE tests at different velocities were performed using a single stage light gas gun. Impact velocities were selected to deform the specimen with no extrusion, partial extrusion before fragment formation, and complete extrusion. Deformation and damage have been investigated by analysing the microstructure evolution and fracture in the recovered projectile fragment trapped in the extrusion die with optical microscopy and EBSD analysis. The material's propensity to fracture along localized shear bands, which limits the overall extrusion ductility, has been observed.

Index Terms

Dynamic tensile extrusion, EBSD, AA2024-T351, Texture

IX. Introduction

Aluminum is widely used in aerospace applications due to its high strength-to-weight ratio and good corrosion resistance [1]. Among these alloys, Aluminum 2024-T351 exhibits remarkable strength and superior fatigue resistance, making it widely employed in the aerospace and automotive industries. This alloy also exhibits a significant shear effect on ductility, an effect emphasized at high strain rates and large deformation [2]. Understanding this alloy's dynamic behavior and microstructural evolution under extreme conditions is crucial for ensuring its reliable performance in demanding applications.

AA2024 is an aluminum-based alloy containing copper, magnesium, manganese, and iron with a complex microstructure characterized by the presence of intermetallic particles. The T351 thermal treatment consists of a solution heat treatment, a quenching, and cold working, followed by natural aging and stress relief. In this state, the typical intermetallic particle is composed of micrometric q-phase Al_2Cu, S-phase Al_2CuMg, second phase $(AlCu)_{11}(FeMn)_3Si$, and nanometric dispersoid composed of AlCuMn [3]. Cold working treatment (e.g. lamination) leads to a "*pancake*" grain structure, in which the lengths and widths of individual grains are large compared to their thicknesses (Fig. 1).

In this work, an investigation of the dynamic tensile extrusion (DTE) behavior of Aluminum 2024-T351 is presented, analyzing the resulting fragments via electron backscattered diffraction (EBSD) technique. The dynamic tensile extrusion test, proposed by Gray III et al. [4], is a powerful experimental method that allows the evaluation of the material response under high strain rates, reproducing real-life extreme scenarios such as impact, collision, and explosion events. In this experiment, a projectile-shaped sample is forcedly extruded in a conical die, with an exit hole diameter narrower than the projectile diameter, using a gas gun. This research explores the deformation mechanisms and microstructural evolution exhibited by Aluminum 2024-T351 during dynamic tensile extrusion, considering the orthotropic behavior of this alloy in case of cold work. In this regard, the projectiles were manufactured, aligning the extrusion and lamination axes. EBSD analyses were performed in points of the fragments with different degrees of total plastic strain, estimated with a numerical analysis using implicit FEM code. The impact velocities were selected to deform the specimen with no extrusion, partial extrusion before fragment formation, and complete extrusion.

X. Material and Methods

DTE testing was conducted with a single stage system light gas gun, 3.50 m long with a 7.62 mm bore, with a maximum pressure of 300 bar, tunable with the thickness of a Mylar® disk used for firing the gun. Further detail of the DTE test is given in previously published work [5]. The investigation on DTE samples was conducted using Optical Microscopy (OM, LEICA DM 6000 M) and Scanning Electron Microscopy (SEM, ZEISS Ultra Plus) equipped with an energy dispersive X-ray spectroscopy (EDS, Oxford Instrument X-Max) and an Electron Back Scattered Diffraction (EBSD, Oxford Instrument C-nano) apparatuses. Numerical simulations were used to estimate material total plastic strain using implicit FEM code MSC MARC v2013; detail can be found elsewhere [5].

XI. Experimental

DTE fragments were sectioned along the symmetry axis, taking good care of a normal-rolling section, as shown in Fig. 2. Before cutting, a metallography analysis was carried out using lapping and etching with Keller solution to reveal the grain structure present at the base of the cone. This analysis aimed to accurately section the cone perpendicular to the direction of the grain to obtain a normal-rolling section.

Using the implicit Finite Element Method (FEM) code MSC MARC v2013, numerical simulations were carried out to estimate material total plastic strain. More detailed information about this methodology can be found in [5]. Points of the sample with 30%, 100%, and 400% total plastic strain have been analyzed using EBSD in the case of non-extruded and partially extruded samples.

The threshold value of the misorientation angle used in EBSD tests to distinguish two different grains was 10° for high-angle grain boundaries (HAGBs) and 2° for low-angle grain boundaries (LAGBs). Due to the elongation of grains, grain size was estimated by a fit with ellipses. Grain size decreases slightly, increasing deformation, with a further increase of grain elongation in the rolling direction. It can be seen a bending of the grains and the formation of new grains in the grain boundaries due to fragmentation and recrystallization (Fig. 4).

Analyzing the inverse pole figure maps, Fig 5, it is possible to observe a strong texture evolution of a dual {001} and {111} fiber in the rolling direction. This evolution is already present at lower deformation, and only a slight change (a few points against random) is observed, increasing the total plastic strain.

In Fig. 6, the percentage of the ratio LAGB/HAGB is reported. A pronounced increase in LABs can be observed, moving from pristine material to 30% total plastic strain point, and a slight decrease of this ratio with further increase. Such boundaries consist mainly on an array of dislocations, induced by stress [6]. In the pristine material subjected to a stress relief treatment, LABs are substantially absent. Moving to 30% deformation location, stress-induced dislocations accumulate, and their numbers slightly decrease with a further increase in total plastic strain. The hypothesis is that in points subjected to DTE stress where no plastic strain is present, the quantity of dislocation is even higher, but EBSD in such zones has shown poor quality.

Fig. 8 shows a fracture surface of a fragment recovered after DTE test, confirming the same fracture mechanism typical of this alloy in case of static load conditions. The fracture mechanism is characterized by intermetallic particle breaking (brittle features at the center of Fig. 8) and shear dimples typical of a shear fracture of an aluminum alloy.

XII. Conclusions

In conclusion, the present study investigated the effect of a dynamic tensile extrusion in the rolling direction of an AA2024-T351 sample on grain elongation, texture development, and formation of LABs. The EBSD findings demonstrate that grains further elongate in the rolling/extrusion direction. Moreover, a notable development of a {001} and {111} dual fiber texture was observed, indicating a strong crystallographic alignment along these specific planes. It was also observed that LABs formation occurred at low levels of deformation, which transformed into High Angle Boundaries (HABs) as the deformation increased, causing fragmentation of grains. Additionally, a higher concentration of LABs, therefore dislocations, was found in {001} grains compared to {111} grains, being the {111} direction the preferred slip plane. Furthermore, crack formation and propagation were observed, which can be attributed to a void growth, void sheet, and void shear mechanism.

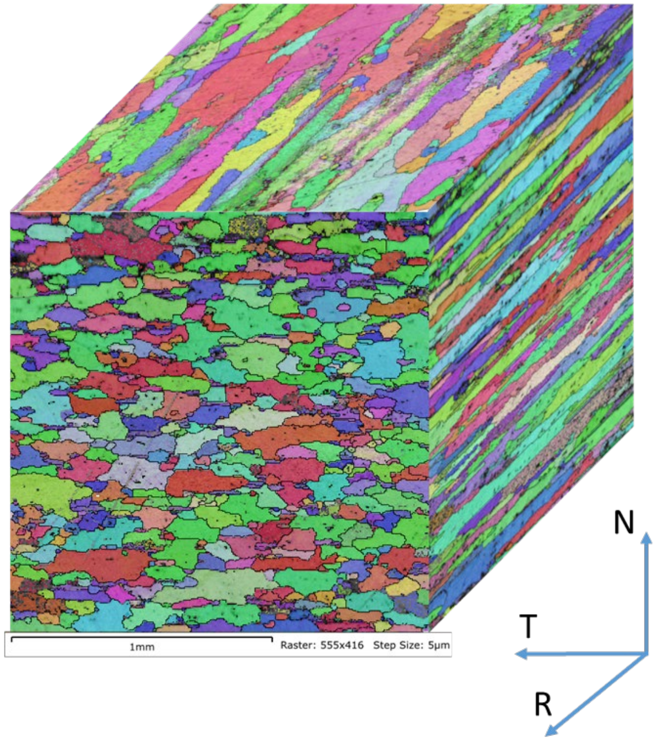

Fig. 1: Example of a typical pancake structure, with R rolling direction, T transverse direction, and N normal direction.

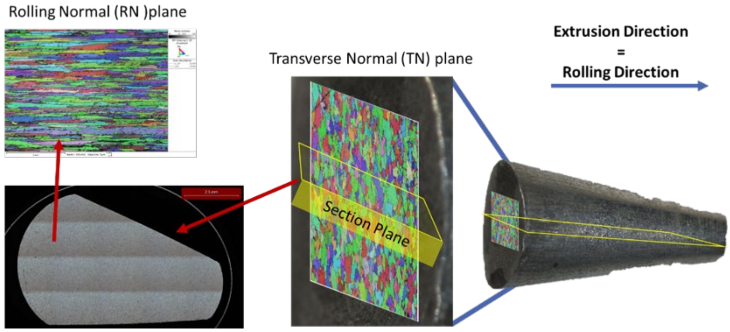

Fig. 2: DTE sample preparation for EBSD analysis.

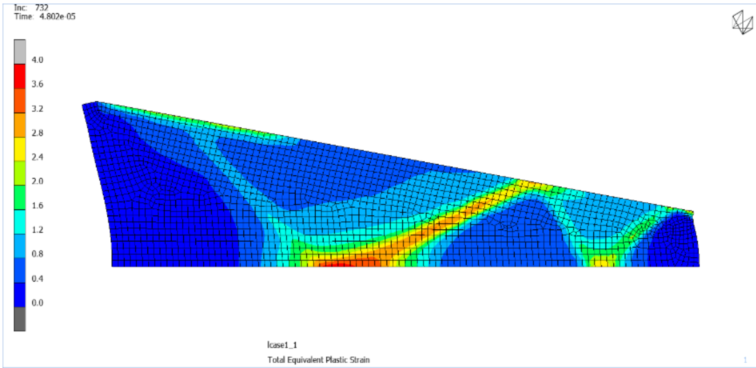

Fig. 3: Numerical analysis of a DTE sample.

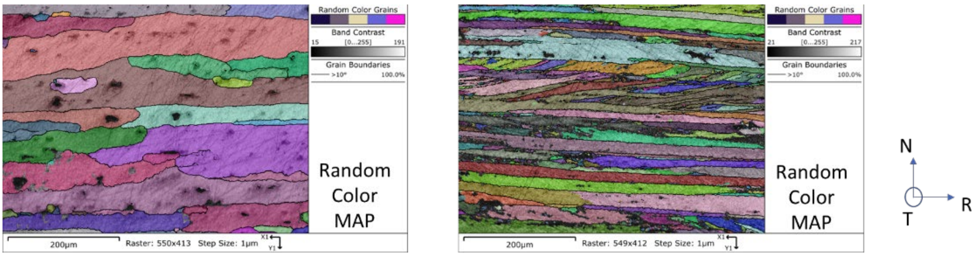

Fig. 4: Grain analysis, on the left pristine material, on the right a point at 100% total plastic strain.

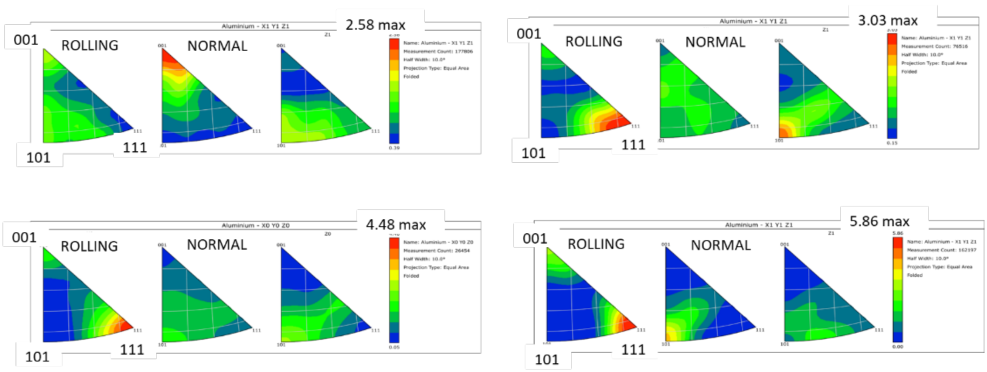

Fig. 5: Inverse pole figure maps of pristine (top left), 30% total plastic strain (top right), 100% total plastic strain (bottom left), and 400% total plastic strain.

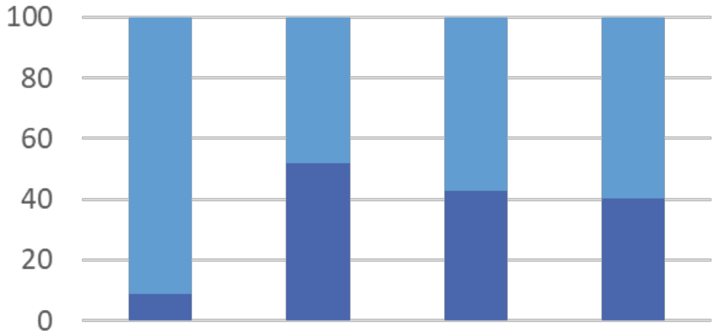

Fig. 6: High angle boundaries (light blue) and low angle boundaries (dark blue) ratio in the sample with increasing plastic strain from left to right (no plastic strain, 30%, 100%, and 400%).

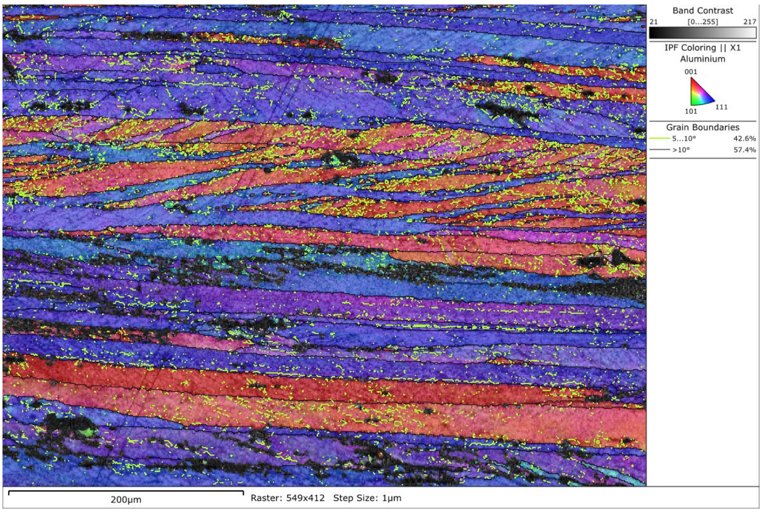

Fig. 7 LABs (yellow) in 100% total plastic strain

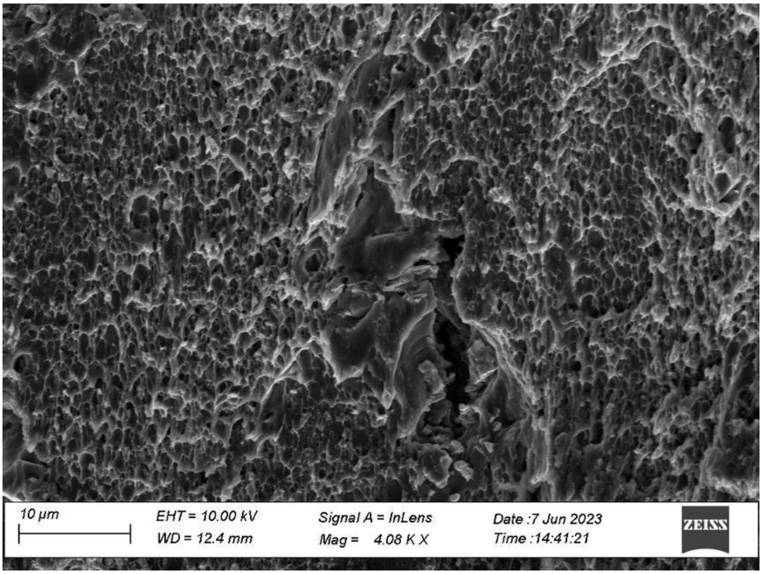

Fig. 8 SEM image of fracture surface of a fragments.

REFERENCES

[1] A.E. Hughes, R. Parvizi, M. Forsynth Corros Rev 33(1-2):1-30 2015
[2] I. Barsoum, J. Faleskog. International Journal of Solids and Structures, 322:5481–5498, 2007
[3] L.K. Ives, L.J. Swartzendruber, W.J. Boettinger, M. Rosen, S.D. Ridder, F.S. Biancaniello, R.C. Reno, D.B. Balliard, R. Mehrabian: NBSIR 83-2669, 1983
[4] G.T. Gray III, E. Cerreta, C.A. Yablinsky, L.B. Addessio, B.L. Henrie, B.H. Sencer, M. Burkett, P.J. Maudlin, S.A. Maloy, C.P. Trujillo, M.F. Lopez: Shock Compression of Condensed Matter-2005, M.D. Furnish, ed., AIP Conf. Proc., American Institute of Physics Press, Woodbury, New York (2006), pp. 725-728. "Influence of Shock Prestraining and Grain Size on the Dynamic-Tensile-Extrusion
[5] M. Hornqvist, N. Mortazavi, M. Halvarsson, A. Ruggiero, G. Iannitti and N. Bonora, Acta Materialia 89:163-180 2015
[6] A.T. Lim , D.J. Srolovitz, M. Haataj Acta Materialia 57:5013–5022 2009